NASA TECHNICAL MEMORANDUM

NASA TM X-3438

NASA TM X-3438

SIDE FORCES ON FOREBODIES AT HIGH ANGLES OF ATTACK AND MACH NUMBERS FROM 0.1 TO 0.7: TWO TANGENT OGIVES, PARABOLOID AND CONE

Earl R. Keener, Gary T. Chapman, Lee Cohen, and Jamshid Taleghani

Ames Research Center
Moffett Field, Calif. 94035

NATIONAL AERONAUTICS AND SPACE ADMINISTRATION • WASHINGTON, D. C. • FEBRUARY 1977

1. Report No.	2. Government Accession No.	3. Recipient's Catalog No.
NASA TM X-3438		

4. Title and Subtitle	5. Report Date
SIDE FORCES ON FOREBODIES AT HIGH ANGLES OF ATTACK AND MACH NUMBERS FROM 0.1 TO 0.7: TWO TANGENT OGIVES, PARABOLOID AND CONE	February 1977
	6. Performing Organization Code

7. Author(s)	8. Performing Organization Report No.
Earl R. Keener, Gary T. Chapman, Lee Cohen, and Jamshid Taleghani	A-6670
	10. Work Unit No.
9. Performing Organization Name and Address	505-06-95
Ames Research Center, NASA Moffett Field, California 94035	11. Contract or Grant No.
	13. Type of Report and Period Covered
12. Sponsoring Agency Name and Address	Technical Memorandum
National Aeronautics and Space Administration Washington, D. C. 20546	14. Sponsoring Agency Code

15. Supplementary Notes

16. Abstract

An experimental investigation was conducted in the Ames 12-Foot Wind Tunnel to determine the subsonic aerodynamic characteristics of four forebodies at high angles of attack. The forebodies tested were a tangent ogive with fineness ratio of 5, a paraboloid with fineness ratio of 3.5, a 20° cone, and a tangent ogive with an elliptic cross section. The investigation included the effects of nose bluntness and boundary-layer trips. The tangent-ogive forebody was also tested in the presence of a short afterbody and with the afterbody attached. Static longitudinal and lateral/directional stability data were obtained at Reynolds numbers ranging from 0.3×10^6 to 4.6×10^6 (based on base diameter) at a Mach number of 0.25, and at Mach numbers ranging from 0.1 to 0.7 at a Reynolds number of 0.8×10^6 (nominal). Angle of attack was varied from 0° to 88° at zero sideslip, and the sideslip angle was varied from -10° to 30° at angles of attack of 40°, 55°, and 70°

The investigation was conducted to investigate the existence of large side forces and yawing moments at high angles of attack and zero sideslip. It was found that all of the forebodies experience steady side forces that start at angles of attack of from 20° to 35° and exist to as high as 80°, depending on forebody shape. The side force is as large as 1.6 times the normal force and is generally repeatable with increasing and decreasing angle of attack and, also, from test to test. The side force is very sensitive to the nature of the boundary layer, as indicated by large changes with boundary trips. The maximum side force varies considerably with Reynolds number and tends to decrease with increasing Mach number. The direction of the side force is sensitive to the body geometry near the nose. The angle of attack of onset of side force is not strongly influenced by Reynolds number or Mach number but varies with forebody shape. Maximum normal force often occurs at angles of attack near 60°. The effect of the elliptic cross section is to reduce the angle of onset by about 10° compared to that of an equivalent circular forebody with the same fineness ratio. The short afterbody reduces the angle of onset by about 5°

17. Key Words (Suggested by Author(s))	18. Distribution Statement
Aerodynamic characteristics Subsonic Bodies High angle of attack Side forces	Unlimited STAR Category – 02

19. Security Classif. (of this report)	20. Security Classif. (of this page)	21. No. of Pages	22. Price*
Unclassified	Unclassified	141	$5.75

*For sale by the National Technical Information Service, Springfield, Virginia 22161

NOMENCLATURE

The data are presented in the body axis coordinate system with the moment center located at the base of the forebody models. Since the data were computer-plotted, the corresponding plot symbol, where used, is given together with the conventional symbol.

Conventional symbol	Plot symbol	
b		span of elliptic forebody at base (major or minor axis of base depending on orientation of model; major or minor axis horizontal)
C_A	CA	axial-force coefficient, $\frac{\text{balance axial force}}{qS}$
C_{AF}	CAF	axial-force coefficient adjusted for base pressure equal to free-stream static pressure, $C_A + C_{p,b}$
C_m	CLM	pitching-moment coefficient, $\frac{\text{pitching moment}}{qSd}$
$C_{m,R}$	CRM	resultant-moment coefficient in the body axis system, $C_n \sin \Psi + C_m \cos \Psi$
C_N	CN	normal-force coefficient, $\frac{\text{normal force}}{qS}$
C_n	CYN	yawing-moment coefficient, $\frac{\text{yawing moment}}{qSd}$
C_ℓ	CBL	rolling-moment coefficient, $\frac{\text{rolling moment}}{qSd}$
$C_{p,b}$	CPB	base pressure coefficient, $\frac{p_b - p}{q}$
CP_R	CPR	resultant-force center of pressure location, fraction of length ℓ from nose tip, $1 - \left(\frac{C_{m,R}}{C_R}\right)\left(\frac{d}{\ell}\right)$
C_R	CR	resultant-force coefficient in body axis system, $\sqrt{C_N^2 + C_Y^2}$
C_Y	CY	side-force coefficient, $\frac{\text{side-force}}{qS}$
$\lvert C_Y \rvert$	ACY	absolute value of C_Y
d	D	base diameter (for an elliptic body it is taken to be the span b at the base)

Conventional symbol	Plot symbol	
ℓ	L	length of forebody
M	MACH	free-stream Mach number
p		free-stream static pressure
p_b		base pressure
q		free-stream dynamic pressure
R_d	R	Reynolds number based on base diameter, d
S	S	base reference area (circular bodies: area of base; elliptic body: area of an equivalent circular base with a diameter equal to span b of base)
x		distance behind forebody apex along body axis of symmetry
α	ALPHA	angle of attack, deg
β	BETA	angle of sideslip, deg
Θ	THETA	meridian angle measured from bottom center line, right side is positive looking upstream, deg
ϕ_B	PHI-B	roll angle of model forebody about axis of symmetry, clockwise is positive looking upstream, deg
ϕ_N	PHI-N	roll angle of removable nose alone about axis of symmetry, clockwise is positive looking upstream, deg
Ψ	PSI	angle between the resultant and normal forces, resultant force inclined to the right is positive angle looking upstream, $\tan^{-1}\left(\frac{C_Y}{C_N}\right)$, deg
		Model Configuration Code
	AA	afterbody attached to forebody
	AD	afterbody detached from forebody (separated by 0.16 cm gap), but attached to sting
	FC	conical forebody

Plot symbol	
FEH	elliptic tangent-ogive forebody, major axis horizontal
FEV	elliptic tangent-ogive forebody, major axis vertical
FP	parabolic forebody
FT2	tangent-ogive forebody, $\frac{\ell}{d} = 5.0$
NS	sharp nose, radius = 0
NB1	blunt nose, radius = 0.317 cm
NB2	blunt nose, radius = 0.635 cm
NB3	blunt nose, radius = 1.27 cm
NP	parabolic nose
T1	boundary-layer transition strip along forebody meridians at $\Theta = \pm 15°$, full length
T2	boundary-layer transition strip along forebody meridians, $\Theta = \pm 30°$, full length
T2R	boundary-layer transition strip along forebody meridian on right side, $\Theta = 30°$, full length
T3	boundary-layer transition strip encircling model, $\frac{x}{\ell} = 0.03$
T4	boundary-layer transition strip encircling model, $\frac{x}{\ell} = 0.10$
T5	boundary-layer transition strip encircling model at junction of nose and forebody, $\frac{x}{\ell} = 0.20$
T6	boundary-layer transition strip encircling model, $\frac{x}{\ell} = 0.33$

SIDE FORCES ON FOREBODIES AT HIGH ANGLES OF ATTACK AND MACH NUMBERS FROM 0.1 TO 0.7: TWO TANGENT OGIVES, PARABOLOID AND CONE

Earl R. Keener, Gary T. Chapman, Lee Cohen, and Jamshid Taleghani

Ames Research Center

SUMMARY

An experimental investigation was conducted in the Ames 12-Foot Wind Tunnel to determine the subsonic aerodynamic characteristics of four forebodies at high angles of attack. The forebodies tested were a tangent ogive with fineness ratio of 5, a paraboloid with fineness ratio of 3.5, a 20° cone, and a tangent ogive with an elliptic cross section. The investigation included the effects of nose bluntness and boundary-layer trips. The tangent-ogive forebody was also tested in the presence of a short afterbody and with the afterbody attached. Static longitudinal and lateral/directional stability data were obtained at Reynolds numbers ranging from 0.3×10^6 to 4.6×10^6 (based on base diameter) at a Mach number of 0.25, and at Mach numbers ranging from 0.1 to 0.7 at a Reynolds number of 0.8×10^6 (nominal). Angle of attack was varied from 0° to 88° at zero sideslip, and the sideslip angle was varied from −10° to 30° at angles of attack of 40°, 55°, and 70°.

The investigation was conducted to investigate the existence of large side forces and yawing moments at high angles of attack and zero sideslip. It was found that all of the forebodies experience steady side forces that start at angles of attack of from 20° to 35° and exist to as high as 80°, depending on forebody shape. The side force is as large as 1.6 times the normal force and is generally repeatable with increasing and decreasing angle of attack and, also, from test to test. The side force is very sensitive to the nature of the boundary layer, as indicated by large changes with boundary trips. The maximum side force varies considerably with Reynolds number and tends to decrease with increasing Mach number. The direction of the side force is sensitive to the body geometry near the nose. The angle of attack of onset of side force is not strongly influenced by Reynolds number or Mach number but varies with forebody shape. Maximum normal force often occurs at angles of attack near 60°. The effect of the elliptic cross section is to reduce the angle of onset by about 10° compared to that of an equivalent circular forebody with the same fineness ratio. The short afterbody reduces the angle of onset by about 5°.

INTRODUCTION

When bodies of revolution are pitched at high angles of attack, a side force can occur at zero sideslip angle. This side force results when the separation-induced vortex flow field on the lee side of the body becomes asymmetric. This is a well-known phenomenon (refs. 1 and 2) and one on which research has focused in recent years, particularly with the advent of highly maneuverable aircraft, because the side force and yawing moment might contribute to the onset of aircraft spin (ref. 3). To date, much of the research on asymmetric forces has been directed toward determining fixes for specific configurations and on studies of vortex flow fields on long slender bodies (e.g., refs. 4-9). However, a recent test of three forebody models at low Mach number and Reynolds

number (ref. 10) showed that large side forces can be generated on the forebody alone at zero sideslip.

Since the configuration of the forebody might play an important role in the spin characteristics of the aircraft, a comprehensive wind tunnel test program has been undertaken at Ames Research Center to obtain static aerodynamic data for forebody-alone models, covering a wide range of forebody shapes and a wide range of Reynolds numbers and Mach numbers. The objective was to determine the effect of forebody shape on the forces and moments so that criteria could be established for aircraft and missiles with good, high angle-of-attack, aerodynamic characteristics. Reports thus far generated from this test program are listed in references 11 to 14.

As part of the forebody test program, aerodynamic force and moment characteristics were measured at subsonic speeds over a large Reynolds number range for five forebody models. Test data for one of the forebody models, a tangent ogive having a fineness ratio of 3.5, were reported in reference 12, and selected results were reported in reference 11. The present report presents experimental data for the four forebody models: a tangent ogive having a fineness ratio of 5, a paraboloid having a fineness ratio of 3.5, a 20° cone, and a tangent ogive having an elliptic cross section whose major and minor axes at the base results in fineness ratios of 5 and 3.5, respectively.

Tests prior to the present investigation (ref. 10) at low speed and low Reynolds numbers showed that side forces and yawing moments occurred at zero sideslip (asymmetric forces and moments) for a tangent ogive and a cone, each having fineness ratios of 3.5. On the other hand, test results for a paraboloid did not exhibit side forces and yawing moments. Test results for the tangent ogive with fineness ratio of 3.5 from the present investigation (refs. 11 and 12) showed asymmetric forces similar to those of reference 10 at high angles of attack. The side force was as large as 1.5 times the maximum normal force, varied considerably with Reynolds number, and decreased with Mach number. The side forces were reduced or eliminated by bluntness, nose strakes, or nose booms.

The objectives of the present investigation were to determine the effects on the asymmetric forces due to forebody geometry, hysteresis, repeatability, Reynolds number, roll angle, sideslip, boundary-layer trips, nose bluntness, and Mach number. To determine the effects of flow around the base of the forebody-alone configuration, the fineness-ratio 5 tangent ogive was tested in the presence of an $\ell/d = 3.5$ cylindrical afterbody. The forebody was also tested with the afterbody attached to determine the effect of a short afterbody on the side force.

This investigation was conducted in the Ames 12-Foot Pressure Wind Tunnel at Mach numbers ranging from 0.1 to 0.7 and at Reynolds numbers ranging from 0.3×10^6 to 4.6×10^6. Six-component static forces and moments were measured at angles of attack from 0° to 88°.

This report presents the basic data that show the effects on the aerodynamic characteristics due to model configuration, Reynolds number, and subsonic Mach numbers up to 0.7. Selected results from this investigation were reported in reference 11.

TEST FACILITY

The aerodynamic data presented here were obtained from wind tunnel tests conducted in the Ames 12-Foot Pressure Wind Tunnel. This wind tunnel is a variable-pressure, low-turbulence facility with a Mach number range from 0.1 to about 0.9 and a unit Reynolds number capability up to about 26×10^6/m at a Mach number of 0.25. Eight fine-mesh screens in the settling chamber, together with a contraction ratio of 25 to 1, provide the airstream of exceptionally low turbulence.

MODEL DESCRIPTION

Test results are presented for four forebody models. Sketches of the models are presented in figure 1, model dimensions are given in table 1, and photographs of the models and wind-tunnel installation are presented in figure 2. The models were designed to represent forebodies of aircraft fuselage or missiles. Three of the forebodies were bodies of revolution: an $\ell/d = 5$ tangent ogive, an $\ell/d = 3.5$ paraboloid, and a 20° cone. All of these bodies were designed with removable nose sections of various nose radii up to 1.27 cm. The paraboloid was provided with a pointed nose (resulting in a short conical tip) with an apex angle of 32.9°; identical to that of the $\ell/d = 3.5$ tangent ogive (ref. 12). A fourth forebody was designed with an elliptic cross section that could be tested with either the major or the minor axis perpendicular to the crossflow velocity. The major and minor axes of the base were selected so that the respective ℓ/b (length/base span) ratios were 3.5 and 5.0 to coincide with the circular tangent-ogive model fineness ratios. In addition, an $\ell/d = 3.5$ afterbody was designed to be clamped to the sting behind the $\ell/d = 5$ tangent ogive but free of the forebody (approximately 0.16 cm gap) so that forebody forces could be measured in the presence of the afterbody. The afterbody could also be attached to the forebody so that the forebody plus afterbody force could be measured. The junctions between the removable nose and the forebody and afterbody were carefully machined so that the surface discontinuity was less than 0.025 mm and had rearward facing steps. The removable nose sections were held by a set screw located on the leeward side and covered with smoothed dental plaster. A balance pin access hole was located on the leeward side, covered with dental plaster, and smoothed. The afterbody was built in two halves; the parting surface was oriented perpendicular to the windward side so that the retaining bolts were located on the windward side. The bolt holes and the small gap on each side between the cylindrical halves were filled with dental plaster and smoothed.

TESTING AND PROCEDURE

The investigation was conducted over a Reynolds number range from 0.3×10^6 to 4.6×10^6 (nominal, based on model base diameter) at a Mach number of 0.25, and over a Mach number range from 0.1 to 0.7 at a Reynolds number of 0.8×10^6 (nominal). The models were mounted from a floor support system that provides a high angle-of-attack range. Since it was not possible to pitch the model continuously from 0° to 88°, two different sting supports were used. The sting support systems shown in figures 2(c) and 2(d) were used for angle-of-attack ranges of 0° to 45° and 36° to 88°, respectively. Angle of sideslip was varied from -10° to 30° at $\alpha = 40°$, 55°, and 70°.

Aerodynamic forces and moments on the model were measured using an internal six-component strain-gage balance. The model base pressure was measured using a pressure tube that was attached to the sting and open in the balance cavity in the base of the model. For tests of the forebody in the presence of the afterbody, the open end of the pressure tube was located in the gap between the forebody and afterbody.

The $\ell/d = 5.0$ tangent-ogive forebody was first tested without the afterbody. Tests were made with pointed and blunt noses and with several positions of boundary-layer transition strips. The transition strips were 0.32 cm wide and composed of 0.021-cm-diam glass spherules (no. 80 mesh). This trip size was selected from sublimation tests, which indicated that this size was effective in causing boundary-layer transition to turbulent crossflow over the rear third of the body length. Further increase in trip size was rejected because the particles near the nose might have acted to separate rather than trip the flow. The boundary-layer transition strips were tested in the positions listed in the figures and described in the Nomenclature section. In order to determine the effects of model asymmetries, both the forebody and its removable pointed nose tip were tested at several fixed roll-angle positions, generally in 90° increments. Next, several tests of the forebody were made in the presence of the $\ell/d = 3.5$ afterbody (afterbody clamped to the sting). Finally, the effect of the $\ell/d = 3.5$ afterbody was determined by testing the forebody with the afterbody attached.

The paraboloid and cone forebodies were tested with the pointed and blunt noses. The elliptic tangent ogive was tested with its major axis both horizontal and vertical.

DATA REDUCTION AND ACCURACY

The six-component force and moment data were reduced about the model moment-reference center in the body axis system. The moment center was located on the model centerline at the base of the forebody. The angle of attack and angle of sideslip were corrected for deflection of the sting and balance under aerodynamic load. Appropriate aerodynamic coefficients were constructed for model weight tares. Stream angles as large as 2° are known to exist in the vicinity of the model due to the influence of the support system fairing on the tunnel floor (see fig. 2). No stream angle corrections were applied to the data. Mean values of the forces and pressures were recorded by electronic filtering, and in addition, three samples of all balance and tunnel static pressure data were averaged for each data point and then reduced to coefficient form. The model base pressure was used to compute an approximate base axial force, which was subtracted from the total balance axial-force measurement so that the coefficient presented (C_{AF}) is for the axial force ahead of the body base.

Data repeatability was estimated by reviewing repeat points and is presented as follows:

α	$= \pm 0.03°$	C_N	$= \pm 0.04$
β	$= \pm 0.03°$	C_A	$= \pm 0.02$
R	$= \pm 0.02 \times 10^6$	C_Y	$= \pm 0.03$
M_∞	$= \pm 0.005$	C_m	$= \pm 0.04$
C_{p_b}	$= \pm 0.01$	C_ℓ	$= \pm 0.004$

PRESENTATION OF RESULTS

The experimental results are presented in figures 3 through 27 showing the effects of the various configurations and of Reynolds number on the aerodynamic characteristics at $M = 0.25$, and the effects of Mach numbers up to 0.7. The results for the $\ell/d = 5$ tangent ogive are presented in figures 3 to 16. Figure 3 compares the data for the forebody tested alone to the data for the forebody tested in the presence of the afterbody. Figures 4 to 14 present the aerodynamic characteristics for the forebody, showing the effects of hysteresis, repeatability, Reynolds number, roll angle, sideslip angle, boundary-layer trips, and bluntness at $M = 0.25$, and the effect of Mach numbers up to 0.7. Figures 15 and 16 present the data for the forebody with the $\ell/d = 3.5$ cylindrical afterbody attached, showing the effects of Reynolds number and Mach number. This is followed by the test results for the $\ell/d = 3.5$ paraboloid (figs. 17 to 21), the 20° cone (figs. 22 and 23), and the elliptic tangent ogive tested with the major axis horizontal (figs. 24 and 25) and vertical (figs. 26 and 27), showing the effects of Reynolds number and bluntness at $M = 0.25$ and the effect of Mach numbers up to 0.7.

The following coefficients were plotted and faired using a computerized data plotting program:

C_Y	CP_R and Ψ
C_N	C_n, C_m, and $C_{m,R}$
$\lvert C_Y \rvert / C_N$ and $C_R - C_N$	$C_{p,b}$ and C_{AF}

Most of the data are plotted versus angle of attack at zero sideslip angle; however, some data are plotted versus sideslip angle. Since the results for $\lvert C_Y \rvert / C_N$ and CP_R are spurious at low angles of attack and undefined at $\alpha = 0$, these results have been deleted for $\alpha < 10°$. Also, the results from the low-α sting support for $\alpha = 35°$, 40°, and 45° were deleted in order to provide a smooth computerized fairing of the data from the low-α and high-α support systems. It was determined that the overlapping data were usually in close agreement so that the plotted data are a good representation of the results.

Many of the tests were limited to the high-α sting support where the principal effect of the many configurations on the side forces could be determined, such as the tests for roll and sideslip angles, boundary-layer trips, and bluntness. For these figures, only C_Y, C_N, C_n, C_m, and sometimes C_{AF} are shown.

DISCUSSION

The primary purpose of this investigation was to determine the forebody configurations and test conditions for which a side force develops at zero sideslip. The results are discussed in the following sections, starting with the results of the investigation at low speed ($M = 0.25$).

Comparison of the results of forebody alone and forebody in the presence of afterbody– There was some concern that data measured with the forebody alone might not represent adequately the contribution of the forebody to the asymmetric side force and moment on a forebody-afterbody configuration because of possible interference of the flow around the base on the upper surface flow field (see also ref. 12). To investigate this effect, additional tests were made with the forebody mounted on the balance and the afterbody attached to the sting but separated slightly from the forebody (forebody forces in the presence of the afterbody). A comparison of the results is presented in figure 3 for the forebody tested alone and for the forebody tested in the presence of the afterbody (indicated by AD for afterbody detached) at $M = 0.25$.

The side forces from the two configurations are in close agreement throughout most of the angle-of-attack range for which a side force exists. At very high angles ($\alpha = 65°$ to $75°$) the data show a disagreement that could be a base flow effect. At these high angles, the balance inputs were more unsteady for the forebody-alone tests. The normal forces are 15 to 20 percent lower for the forebody-alone data, indicating that reduction in normal force may be attributed to the end effect of the base. The base pressures ($C_{p,b}$) show a small difference at $\alpha < 55°$ that does not greatly affect the forebody axial force (C_{AF}). However, at $\alpha > 55°$ both Cp,b and C_{AF} are greatly affected by the base flow, which was an expected result.

Since the side forces were not greatly affected by the base flow, many tests were made with the forebody alone because it was more convenient. Consequently, in the following sections, the results with the forebody alone and with the forebody in the presence of afterbody are used interchangeably to describe the force and moment characteristics of the $\ell/d = 5$ forebody. The distinction between the two configurations is indicated in the configuration description at the top of each plot (AD indicates the presence of the afterbody detached from the forebody). Likewise, the side-force data for the remaining three forebodies, tested with no afterbodies, should not be appreciably affected by the base flow, except at very high angles of attack.

Hysteresis– Aerodynamic forces that are related to boundary-layer separation may exhibit a hysteresis effect, that is, the variation of the forces with increasing flow angle might be different from that with decreasing angle. The possible effect of hysteresis was investigated by making many of the test runs with both increasing and decreasing flow angles and some of the results are presented in figure 4. In general, the results are repeatable with increasing and decreasing angles of attack, indicating little or no hysteresis effect. Similar results were obtained with the $\ell/d = 3.5$ tangent ogive (ref. 12).

Repeatability– During the investigation, repeated test runs were made with the basic pointed configuration. Figure 5 shows that at $M = 0.25$ the results are generally repeatable from test to test. Similar results were obtained with the $\ell/d = 3.5$ tangent ogive (ref. 12).

Reynolds number ($M = 0.25$)– In figure 6 the forebody results are presented for a wide range of Reynolds numbers from 0.3×10^6 to 3.8×10^6 (based on base diameter) at $M = 0.25$. At the lowest Reynolds numbers of 0.3×10^6 and 0.8×10^6, a large side force develops at zero sideslip, starting at $\alpha \approx 25°$ and extending to $\alpha \approx 70°$. The angle of attack at which the side force first becomes significant (generally within the $\pm2.5°$) is called the "angle of onset" herein. The direction of the side force has been shown by previous studies to depend primarily on small geometric

asymmetries in the models, especially in the machining of the nose tip (refs. 1 and 10). The maximum magnitude of the side force at the lower Reynolds number is as large as 1.2 times the normal force (see $|C_Y|/C_N$) so that the inclination angle of the resultant force, Ψ is as large as 50°. Increasing the Reynolds number progressively reduces the magnitude of the side force, which is similar to the effect of tests with boundary-layer trips. However, the maximum side force increases again at the higher Reynolds number, and the direction is opposite to that of the side forces at low Reynolds number. This means that the inclination angle Ψ of the resultant force changes from left to right with increasing Reynolds number. This effect of Reynolds number is not entirely understood, except that the boundary layer on the windward side of the forebody is tending towards more turbulent flow. The possibility that the change with Reynolds number could be an effect of the flow in the 12-ft wind tunnel was considered; however, the 12-ft wind tunnel is known to have a very low free-stream turbulence, and the known effect of increasing noise level with increasing Reynolds number should only increase the effective Reynolds number of the test. Also, the effect of possible small changes in free-stream angle, such as the possible 2° flow angle due to the sting support fairing, should be negligible according to the tests with sideslip (fig. 9). Finally, note that the effect of increasing Reynolds number on the angle of onset is small.

The maximum normal force varies considerably with Reynolds number. The maximum value for C_N is greater than 4 at the lowest Reynolds number of 0.3×10^6, drops to about 1.8 at $R_d = 0.8\times10^6$, then increases to about 3 at $R_d = 3.8\times10^6$. Also, the maximum value of the normal force occurs at angles of attack between 45° and 55°. At angles between 55° and 75° the normal force decreases appreciably so that at $\alpha = 88°$ the value of C_N is considerably lower than the maximum. Note also that there is an apparent increase in the normal-force curve slope in the angle-of-attack range where the side force increases ($\alpha > 25°$). This increase in C_N curve slope implies that the normal force and, hence, the resultant force are increased by the flow asymmetry that causes the side force. In reference 12, the results for the $\ell/d = 3.5$ tangent ogive are similar for the effects of normal force.

The center of pressure CP_R of the resultant normal force is located at $x/\ell \approx 0.5$ at angles of attack up to 20°. This is close to the slender-body theory value of $x/\ell = 0.47$ for this forebody. As the angle of attack increases, the center of pressure ranges from 0.45ℓ to 0.65ℓ; at $\alpha = 88°$ it is close to the center of the planform area, $x/\ell = 0.623$.

A small rolling moment was recorded that occurred at high angles of attack when the side force was large. Since the asymmetric pressures that produce the side force do not produce a rolling moment for a circular body, the small recorded rolling moment was probably due to an asymmetry in the boundary-layer skin friction forces. Evidently, a small rolling moment due to an asymmetry in the skin friction forces should be anticipated for bodies at high angles of attack when large side forces exist. The data are not presented because the measured rolling moment was small ($|C_\ell| < 0.02$) and relatively inaccurate from the particular strain-gage balance used.

Roll– Previous investigations (refs. 5, 10, and 12) have shown that when a body is tested in various positions of roll angle about the axis of symmetry, the side force can change direction (sign) for a range of roll angles. The effect of roll angle on the present results (fig. 7) is to change the direction of the side force for a range of roll angles near $\phi_B = 180°$. When the removable nose tip (length of 0.20ℓ) was rolled to several fixed positions (fig. 8), the effect was partly, but not entirely, similar to that of rolling the complete forebody. This is because the side forces are in opposite directions at $\phi_N = 90°$ and 180° to those of $\phi_B = 90°$ and 180°. On the other hand, for the

$\ell/d = 3.5$ tangent ogive (ref. 12), the effects of rolling the nose tip to fixed positions were quite similar to the effects of rolling the complete forebody.

These roll tests indicate that body models should be tested in several positions of roll, if possible, when determining the asymmetric characteristics at high angles of attack. In addition, the orientation of model parts and of surface discontinuities, such as junctions and set screws should be noted. Some insight into the possible effect of the junction of the removable nose section may be obtained from the results of the tests that were made with a ring of roughness elements located at the junction (fig. 13). The side force was greatly reduced; hence, it was believed that the effect of a large discontinuity at the junction would have acted as a boundary-layer trip and would likewise have reduced the side force. Since the side force is large with the present junction, it is believed that the junction effect is negligible.

Sideslip– Figure 9 shows the effect of sideslip angle for $\alpha = 40°$, 55°, and 70° at $R_d = 0.8 \times 10^6$. At sideslip angles between 10° and 15°, the side force changes direction (sign). These results indicate that the direction of the side force for the present data is not sensitive to small variations in the free-stream flow angles such as those produced by the model support system fairing on the floor of the wind tunnel. The range of sideslip angles where the change occurs (10° to 15°) is generally repeatable. The data show nearly identical results for both increasing and decreasing angles of sideslip.

Note that the effect of sideslip on a body at a given angle of attack is identical to testing at zero sideslip at a slightly higher angle of attack and at a roll angle of both the body and the balance.

The change in direction of side force from left to right between $\beta = 10°$ and 15° indicates that a change in direction occurs between the corresponding roll angles of 12° to 18°. On the other hand, the side-force data at roll angles of 0° and 45° (figs. 7 and 8) are in the same direction, which indicates that the side force must change direction twice in the roll range between 0° and 45°, and this was not tested. These results indicate that testing in 90° increments could be insufficient to adequately describe the effect of roll.

Boundary-layer trips– Boundary-layer transition trips have been shown in previous investigations (refs. 2 and 5) to reduce the asymmetric force, by an amount that depends on the location of the trips. At high angles of attack, longitudinal boundary-layer transition strips were partially effective. Surprisingly, a ring of roughness elements around the body behind the nose was also effective; this was also true when roughness elements were applied over a large part of the nose surface area (ref. 2).

Results of the present investigation at $M = 0.25$ with boundary-layer transition strips show that longitudinal strips at $\Theta = \pm 15°$ (T1 in fig. 10) reduce the magnitude of the side force by 50 percent or more; the longitudinal strips at $\Theta = \pm 30°$ (fig. 11), however, were not so effective. It was thought that a single transition strip on the right side (T2R, fig. 11) might change the direction of the side force from left (-) to right (+), which it did, but only for part of the angle-of-attack range (45° to 55°). It is interesting to note that for T2R at $\alpha > 55°$ a strong side force develops to the left (-), and it is maintained through $\alpha = 88°$ ($C_Y = -1.6$). Figure 12 shows that the side force is also reduced by a ring of roughness elements around the forebody located at $x/\ell = 0.10$, 0.20, and 0.30.

These results with boundary-layer trips show that the asymmetric forces are sensitive to the nature of the boundary layer (laminar, transitional, or turbulent), especially near the forebody apex.

Nose bluntness– Two nose radii were tested at $M = 0.25$ and $R_d = 0.8 \times 10^6$ (fig. 13). The smallest nose radius of 8.4 percent of the base radius (NB2) reduces the side force to nearly zero. However, the side force for the nose radius of 16.7 percent base radius (NB3) was larger than for the NB2 nose and, in addition, was noticeably unsteady. Similar effects were found for the $\ell/d = 3.5$ tangent ogive, except that the forces were not so unsteady for the larger bluntness. In addition, the side force was higher at the higher Reynolds numbers for the 8.4 percent blunt nose (NB2). Evidently, some caution should be exercised in the use of nose bluntness to reduce side forces. It is possible that there is an optimum nose radius for a particular configuration.

Mach number– Figure 14 presents the results for $M = 0.1$, 0.25, 0.4, 0.6, and 0.7 at $R_d = 0.8 \times 10^6$. The magnitude of the maximum side force does not decrease appreciably with Mach number. This is noticeably different from the side force for the $\ell/d = 3.5$ tangent ogive, (ref. 12) for which the magnitude of C_Y decreased from -2.8 at $M = 0.25$ to about -0.3 at $M = 0.7$. Note that the angle of onset does not vary much with Mach number.

Afterbody attached– Results for the $\ell/d = 5$ tangent-ogive forebody attached to the $\ell/d = 3.5$ afterbody are presented in figures 15 and 16 for the Reynolds number and Mach number range of the test. The data are limited to angles of attack below 46° on the low-angle support system because large dynamic forces and moments occurred at $\alpha > 30°$. The magnitude of the side force is as large or larger than that for the forebody alone, but it is a smaller fraction of the normal force in the test range of $\alpha < 46°$. The side force changes direction with increasing angle of attack, indicating that additional vortices might be forming and shedding over the increased length of the afterbody. The angle of onset of side force is about 20°; this is about 5° lower than for the forebody alone. The angle of onset does not change much with either Reynolds number or Mach number.

Similar to the forebody results, the slope of the normal-force curve increases noticeably when the side force increases. This is also true for the resultant force (compare the curves for C_N, $|C_Y|/C_N$, and $C_R - C_N$). The resultant CP_R ranges between 70 percent and 100 percent of the forebody length at angles of attack below 46°.

In figure 16 the available test data are limited to angles of attack below 46° so that the variation with Mach number of the maximum magnitude of the side forces with the afterbody attached cannot be determined. However, it is observed that the angle of onset is essentially constant with Mach number.

$\ell/d = 3.5$ Paraboloid

The results in reference 10 for an $\ell/d = 3.5$ paraboloid of a size identical to the present model with a parabolic nose showed that the asymmetric force is much smaller than that for a pointed $\ell/d = 3.5$ tangent ogive or for a pointed 8.13° semiapex angle cone.

Figures 17 and 18 present the results for the present model with a parabolic nose for several Reynolds numbers at $M = 0.1$ (for comparison with ref. 10) and at $M = 0.25$. The parabolic nose is

similar in bluntness to the 16.7 percent bluntness ratio of the other forebodies (NB3). The side forces are small, similar to the results in reference 10. There is a small variation with Reynolds number.

Since pointed noses were suspected of producing an appreciable asymmetric force, the present paraboloid was provided with a pointed nose that had the same apex angle as that of the $\ell/d = 3.5$ tangent ogive. The results for the pointed nose are presented in figures 19 to 21 for the Reynolds number and Mach number ranges tested. At the lowest Reynolds numbers of 0.3×10^6 and 0.8×10^6, a large side force develops for the pointed paraboloid at angles of attack between 35° and 70°; this is similar to the results for the $\ell/d = 3.5$ tangent ogive. The maximum magnitude of $|C_Y|$ is about 3.0, which is about 1.6 times the maximum normal-force coefficient. The maximum side force decreases with increasing Reynolds number; however, at $R_d = 3.8\times10^6$ the pointed paraboloid experienced heavy dynamics at $\alpha = 45°$ to 55°, at which angles data could not be obtained. At $M = 0.4$ the side force changes direction from right to left (negative in fig. 21), and as Mach number increases, the side force decreases to near zero at $M = 0.7$. The angle of onset of about 35° does not vary strongly with Reynolds number or Mach number. The resultant center of pressure location CP_R varies with angle of attack and Reynolds number between $x/\ell = 0.46$ and 0.62.

20° Cone

The results for the 20° cone with pointed nose are presented in figure 22 for the Reynolds number range tested. At low Reynolds numbers, a large side force develops at angles of attack between 20° and 75°. The side force changes from side to side as the angle of attack increases, which is the most erratic variation of all the forebodies tested. The changes in side force with increasing angle of attack are accompanied by dynamic oscillations. The maximum magnitude of $|C_Y|$ is 1.3 at $M = 0.25$, and the maximum value of the ratio $|C_Y|/C_N$ is about 0.9. The magnitude of the side force decreases with increasing Reynolds number. The angle of onset of about 20° is not strongly affected by Reynolds number. The resultant center of pressure CP_R ranges between $x/\ell = 0.60$ and 0.65 at angles of attack up to 70°; above $\alpha = 70°$ the CP_R moves rearward to $x/\ell \approx 0.70$ at $\alpha = 90°$. The slender-body theory location for a cone is $CP_R = 0.667$; this location is the center of the planform area, which is also the theoretical crossflow location of CP_R at $\alpha = 90°$.

Shown in figure 23 are the results for two blunt noses with radii of 8.4 percent (NB2) and 16.7 percent (NB3) of the base radius at $M = 0.25$ and $R_d = 1.0\times10^6$. Both blunt noses reduce the asymmetric force considerably. The effect of Reynolds number was not tested.

$\ell/b = 3.5$ Elliptic Tangent Ogive, Major Axis Horizontal

The major axis of the tangent ogive with the elliptic cross section was selected so that the fineness ratio (ℓ/b) of the planform was identical to the fineness ratio of the $\ell/d = 3.5$ circular tangent ogive (ref. 12). This was done so that the coefficients of the elliptic and circular cross section could be compared. Accordingly, the reference area used in the aerodynamic coefficients was the equivalent (not the actual) base area for a circle with diameter equal to the span of the major axis of the elliptic base. (By using the equivalent base area, the coefficients of the circular and elliptic forebodies can be compared in the same manner as if the planform were used as the reference areas.) The results are presented in figures 24 and 25 for the Reynolds number and Mach

number ranges tested. A large side force develops at angles of attack between 20° and 70° and changes considerably with Reynolds number. The maximum magnitude of $|C_Y|$ is 2.4 at $M = 0.25$, and the maximum value of the ratio $|C_Y|/C_N$ is about 0.8. Moderate model oscillations were encountered at the highest Reynolds number. The angle of onset of about 25° compares to about 33° for the $\ell/d = 3.5$ circular tangent ogive (ref. 12), so that the effect of the elliptic cross section is to reduce the angle of onset by about 10°. The magnitude of the side-force coefficient decreases with increasing Mach number so that maximum $|C_Y|$ is about 0.6 at $M = 0.7$. The resultant center of pressure CP_R ranges between $x/\ell \approx 0.48$ at low angles of attack to $x/\ell \approx 0.62$ at $\alpha = 88°$. Since the model is noncircular in cross section, a large rolling moment occurs when a large side force exists.

$\ell/b = 5$ Elliptic Tangent Ogive, Major Axis Vertical

The minor axis of the tangent ogive with the elliptic cross section was selected so that the fineness ratio (ℓ/b) of the planform was identical to the fineness ratio of the $\ell/d = 5.0$ circular tangent ogive (fig. 2); this permits the results for tangent ogives with the elliptic and circular cross sections to be compared. Accordingly, the reference area used in the aerodynamic coefficients was the equivalent (not the actual) base area for a circle with diameter equal to the span of the minor axis of the elliptic base. The results are presented in figures 26 and 27 for the Reynolds number and Mach number ranges tested. At zero sideslip a large side force develops at angles of attack between 15° and 80°, and a residual side force exists at $\alpha = 88°$; this may be due to model-geometric or flow-angle asymmetries. The maximum magnitude of $|C_Y|$ is 3.4 at $M = 0.25$, and the maximum value of the ratio $|C_Y|/C_N$ is about 1.4. The side force varies considerably with Reynolds number. The angle of onset of about 15° compares to about 25° for the $\ell/d = 5.0$ circular tangent ogive (fig. 6) so that the effect of the elliptic cross section is to reduce the angle of onset by about 10°. This is similar to the effect for the elliptic tangent ogive when tested with the major axis horizontal, $\ell/b = 3.5$. The magnitude of the side force remains large as the Mach number increases to 0.7. The resultant CP_R ranges between $x/\ell = 0.40$ and 0.62 at $M = 0.25$. Since the model is noncircular in cross section, a large rolling moment occurs when a large side force exists.

CONCLUSIONS

The following conclusions are made from the data from a wind-tunnel investigation to determine the effect of forebody shape on the asymmetric forces and moments at high angles of attack and zero sideslip of four forebodies: an $\ell/d = 5.0$ tangent ogive, an $\ell/d = 3.5$ paraboloid, a 20° cone, and an elliptic tangent ogive tested with the major axis horizontal and vertical. Data were obtained over a wide range of angles of attack and sideslip, Reynolds number, and Mach numbers up to 0.7. The results can be summarized as follows:

1. All of the forebodies experience steady side forces at high angles of attack at zero sideslip when the noses are pointed.

2. The variation of side force is repeatable with increasing and decreasing angle of attack and also from test to test for all of the forebodies; this is generally true except for the cone and for the elliptic tangent ogive with major axis vertical, for which the variation is erratic.

3. The maximum side force varies from 0.8 to 1.6 times the normal force, depending on forebody shape.

4. The side force is sensitive to the nature of the boundary layer, as indicated by large changes with boundary trips.

5. The maximum side force varies considerably with Reynolds number and tends to decrease with increasing Mach number.

6. The slope of the normal-force curve increases in the angle-of-attack range in which the side force increases, and the maximum normal force often occurs at angles of attack near 60°, rather than at 90°.

7. The direction and magnitude of the side force is sensitive to the body geometry; rotating the nose tip changes the direction of the side force, and small bluntness greatly reduces the side force.

8. The angle of attack of onset of side force varies with forebody shape from about 20° for the cone to about 35° for the pointed paraboloid and the side forces exist at angles of attack up to 80°. The angle of onset is not strongly influenced by Reynolds number or Mach number.

9. The elliptic cross section reduces the angle of onset by about 10° when compared to that of the equivalent circular forebody with the same fineness ratio.

10. The short $\ell/d = 3.5$ afterbody reduces the angle of onset of side force by about 5°.

Ames Research Center
National Aeronautics and Space Administration
Moffett Field, Calif. 94035, August 4, 1976

REFERENCES

1. Allen, H. J.; and Perkins, E. W.: A Study of the Effects of Viscosity on Flow Over Slender Inclined Bodies of Revolution. NACA TR 1048, 1951.

2. Letko, W.: A Low-Speed Experimental Study of the Directional Characteristics of a Sharp-Nosed Fuselage Through a Large Angle-of-Attack Range at Zero Angle of Sideslip. NACA TN 2911, 1953.

3. Chambers, J. R.; Anglin, E. L.; and Bowman, J. S., Jr.: Effects of a Pointed Nose on Spin Characteristics of a Fighter Airplane Model Including Correlation with Theoretical Calculations. NASA TN D-5921, 1970.

4. Thomson, K. D.; and Morrison, D. F.: The Spacing, Position, and Strength of Vortices in the Wake of Slender Cylindrical Bodies at Large Incidences. J. Fluid Mech., vol. 50, part 4, 1971, pp. 751-783.

5. Pick, G. S.: Investigation of Side Forces on Ogive-Cylinder Bodies at High Angles of Attack in the $M = 0.5$ to 1.1 Range. AIAA Paper 71-570, June 1971.

6. Clark, W. H.; and Peoples, J. R.: Occurrence and Inhibition of Large Yawing Moments During High Incidence Flight of Slender Missile Configurations. AIAA Paper 72-968, Sept. 1972.

7. Jorgensen, Leland H.; and Nelson, Edgar R.: Experimental Aerodynamics Characteristics for a Cylindrical Body of Revolution With Various Noses at Angles of Attack From 0° to 58° and Mach Numbers From 0.6 to 2.0. NASA TM X-3128, 1974.

8. Jorgensen, Leland H.; and Nelson, Edgar R.: Experimental Aerodynamic Characteristics for a Cylindrical Body of Revolution With Side Strakes and Various Noses at Angles of Attack From 0° to 58° and Mach Numbers From 0.6 to 2.0. NASA TM X-3130, 1975.

9. Jorgensen, Leland H.; and Nelson, Edgar R.: Experimental Aerodynamic Characteristics for Bodies of Elliptic Cross Section at Angles of Attack From 0° to 58° and Mach Numbers From 0.6 to 2.0. NASA TM X-3129, 1975.

10. Coe, P. L., Jr.; Chambers, J. R.; and Letko, W.: Asymmetric Lateral-Directional Characteristics of Pointed Bodies of Revolution at High Angles of Attack. NASA TN D-7095, 1973.

11. Keener, Earl R.; and Chapman, Gary T.: Onset of Aerodynamic Side Forces at Zero Sideslip on Symmetric Forebodies at High Angles of Attack. AIAA Paper 74-770, Aug. 1974.

12. Keener, Earl R.; Chapman, Gary T.; Cohen, Lee; and Taleghani, Jim: Side Forces on a Tangent Ogive Forebody With Fineness Ratio of 3.5 at High Angles of Attack and Mach Numbers From 0.1 to 0.7. NASA TM X-3437, 1976.

13. Keener, Earl R.; and Taleghani, Jamshid: Wind Tunnel Investigation of the Aerodynamic Characteristics of Five Forebody Models at High Angles of Attack at Mach Numbers From 0.25 to 2. NASA TM X-73,076, 1975.

14. Keener, E. R.; Chapman, G. T.; and Kruse, R. L.: Effects of Mach Number and Afterbody Length on Onset of Asymmetric Forces on Bodies at Zero Sideslip and High Angles of Attack. AIAA Paper 76-66, Jan. 1976.

TABLE 1.– MODEL CHARACTERISTICS AND REFERENCE MEASUREMENTS

Forebody shape		Reference measurements[a]				Removable noses	
Planform	Cross section	ℓ/d	ℓ, cm	d, cm	S, cm^2	Sharp nose apex angle, cm	Nose radius, cm
Tangent ogive	Circular	5.0	76.2	15.24	182.4	22.8	0, 0.635, 1.27
Tangent ogive	Elliptic						
	Major axis horizontal	3.5	66.0	18.87	279.6	32.9	0
	Major axis vertical	5.0	66.0	13.21	137.0	22.8	0
Cone	Circular	2.84	53.3	18.82	278.2	20.0	0, 0.635, 1.27
Paraboloid	Circular	3.5	53.3	15.24	182.4	32.9	0, 0.635, parabolic

[a]Reference diameter (d) and area (S): for circular bodies, base diameter and base area; for elliptic bodies, span at the base and area of an equivalent circular base with a diameter equal to base span.

REMOVABLE NOSES
POINTED AND BLUNT

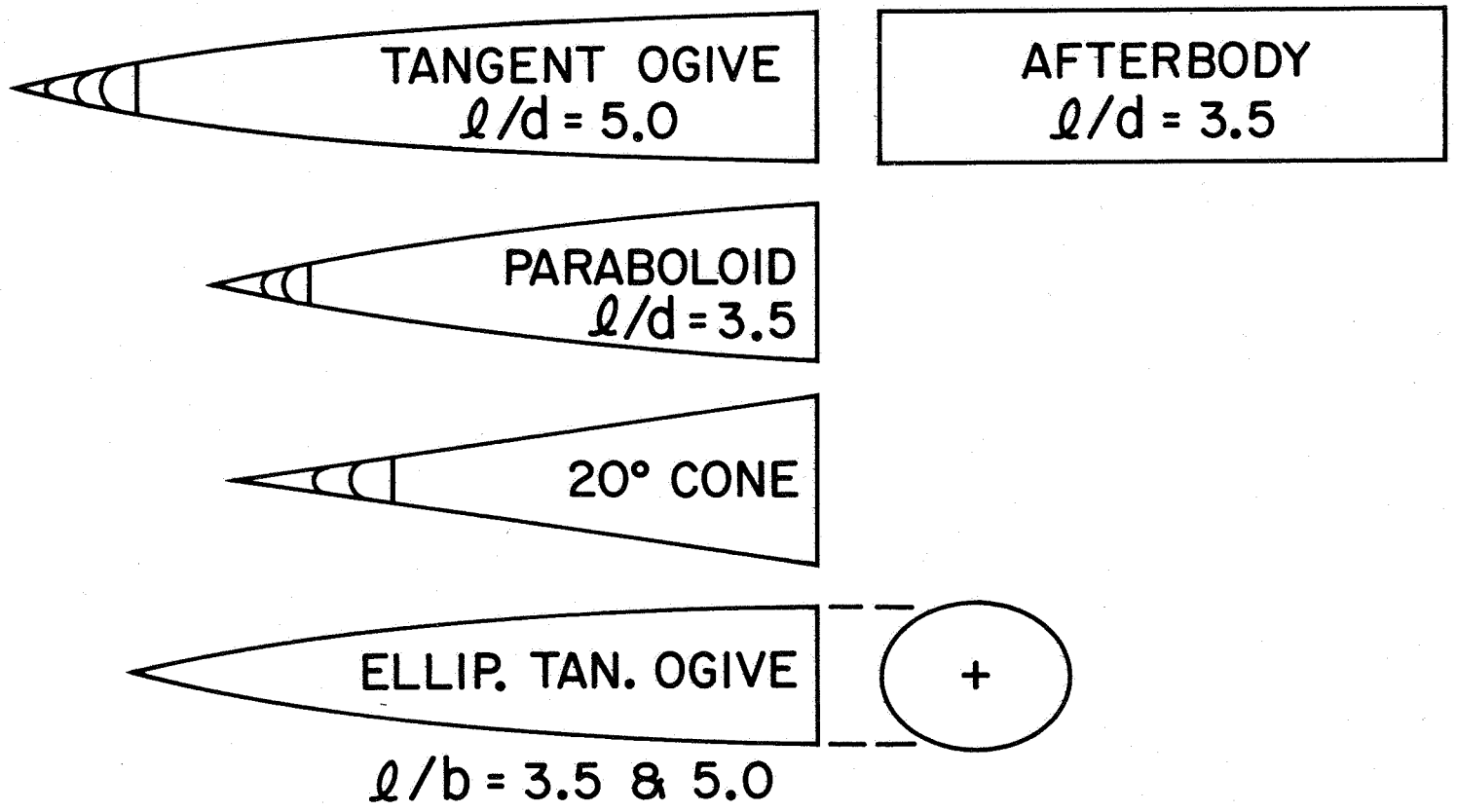

Figure 1.– Sketch of models.

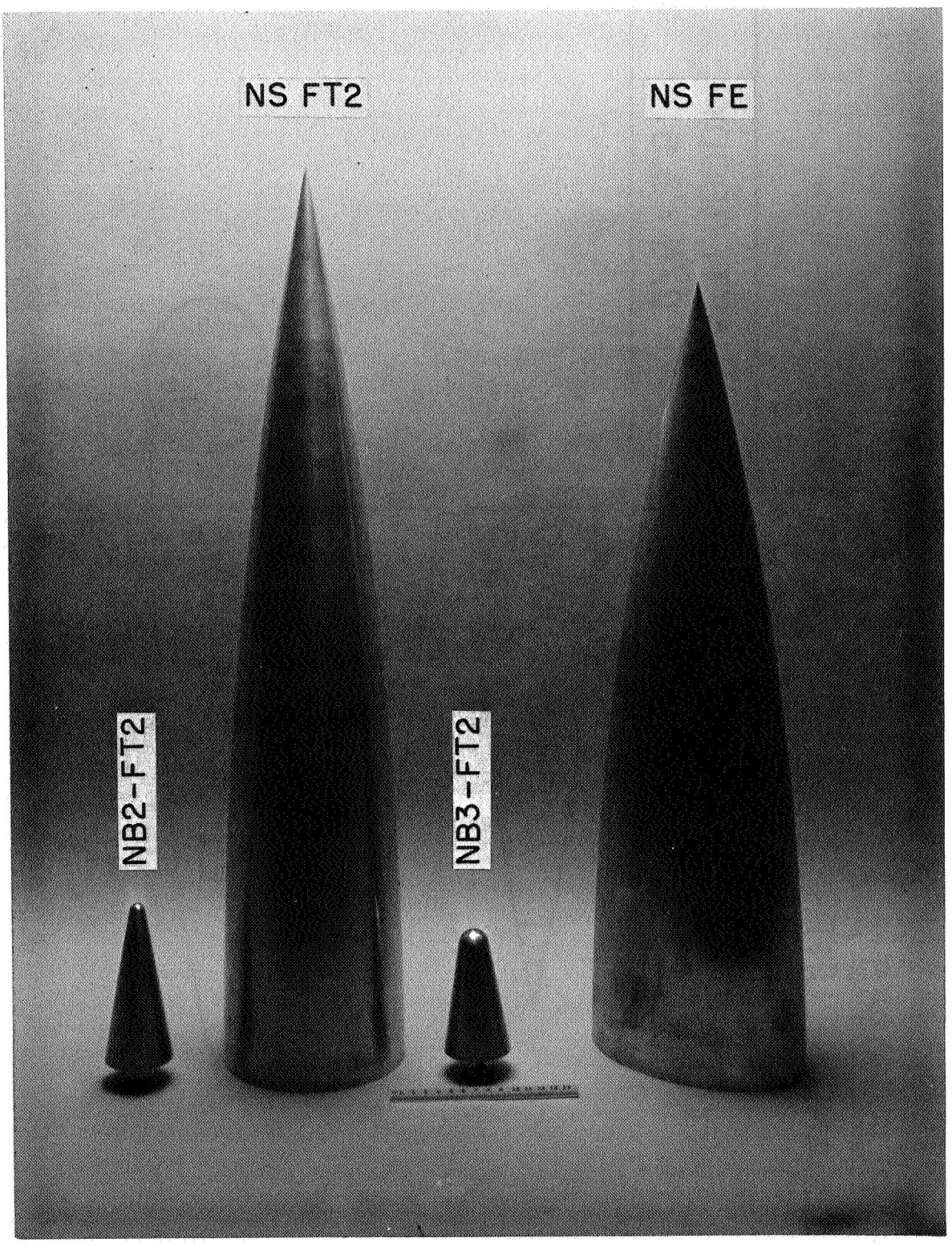

(a) ℓ/d = 5 tangent ogive and elliptic tangent ogive.

Figure 2.– Photograph of models and tunnel installation.

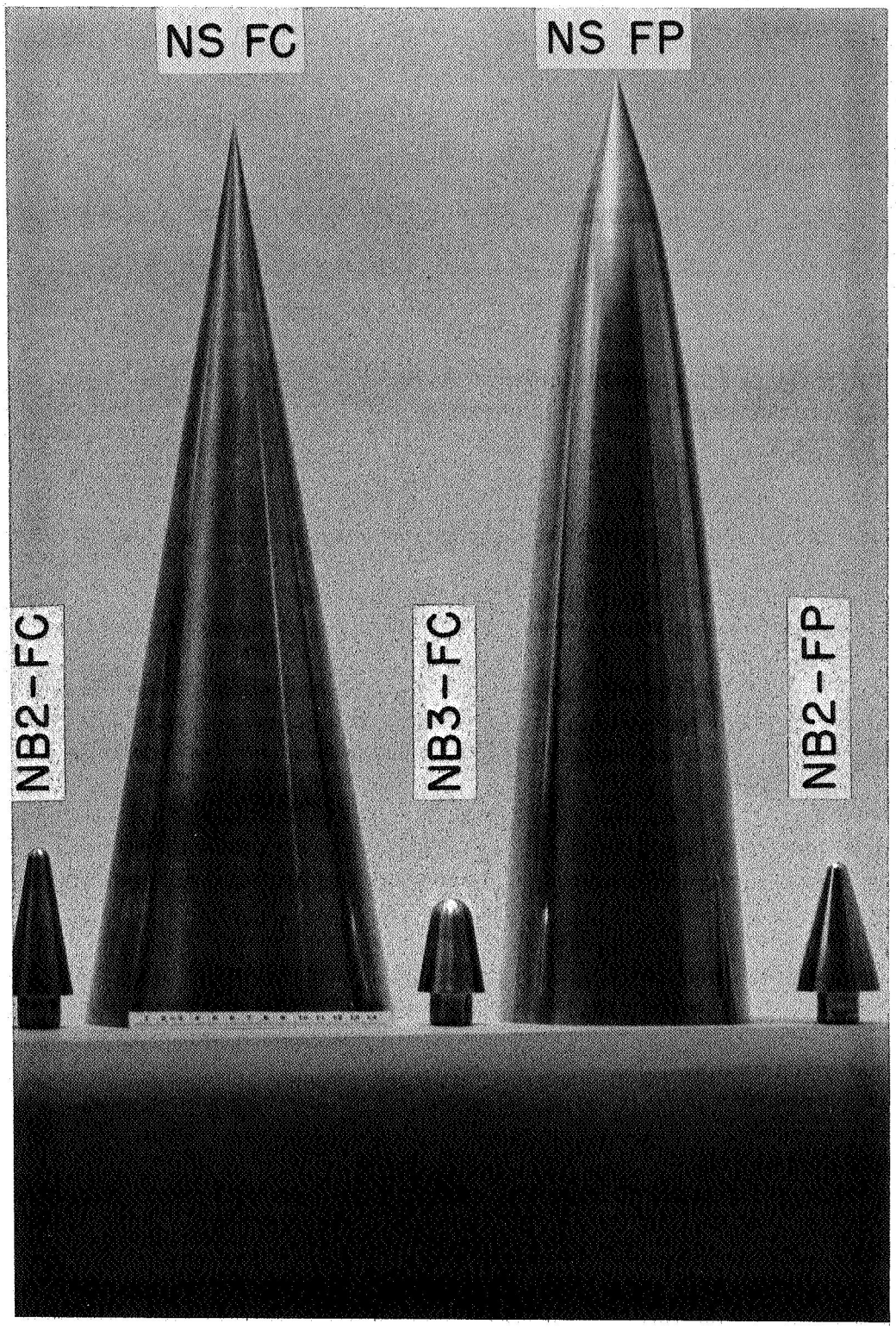

(b) 20° cone and ℓ/d = 3.5 paraboloid.

Figure 2.– Continued.

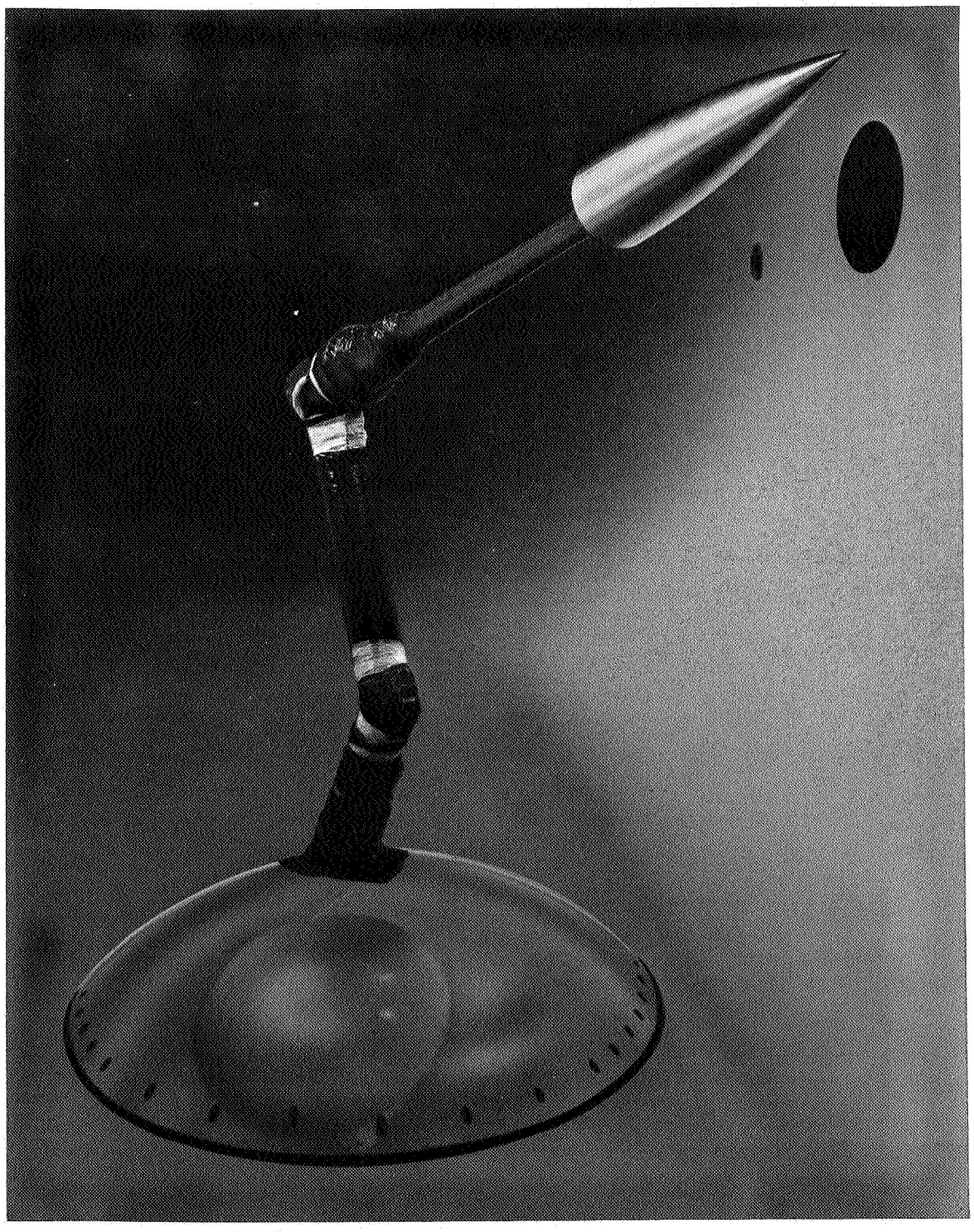

(c) Installation of tangent ogive on floor support system, $\alpha = 0°$ to 45°.

Figure 2.– Continued.

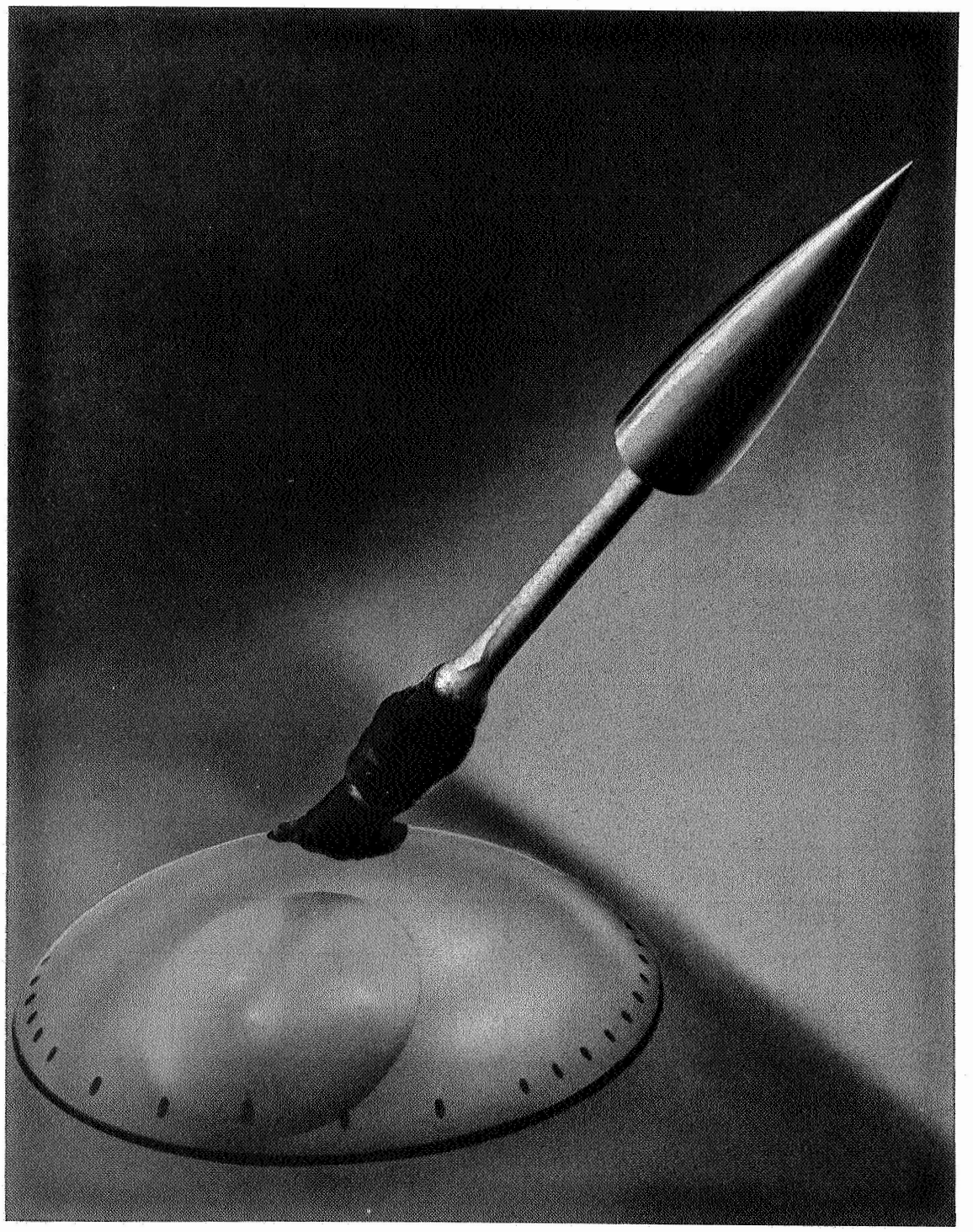

(d) Installation of tangent ogive on floor support system, $\alpha = 36°$ to $88°$.

Figure 2.– Concluded.

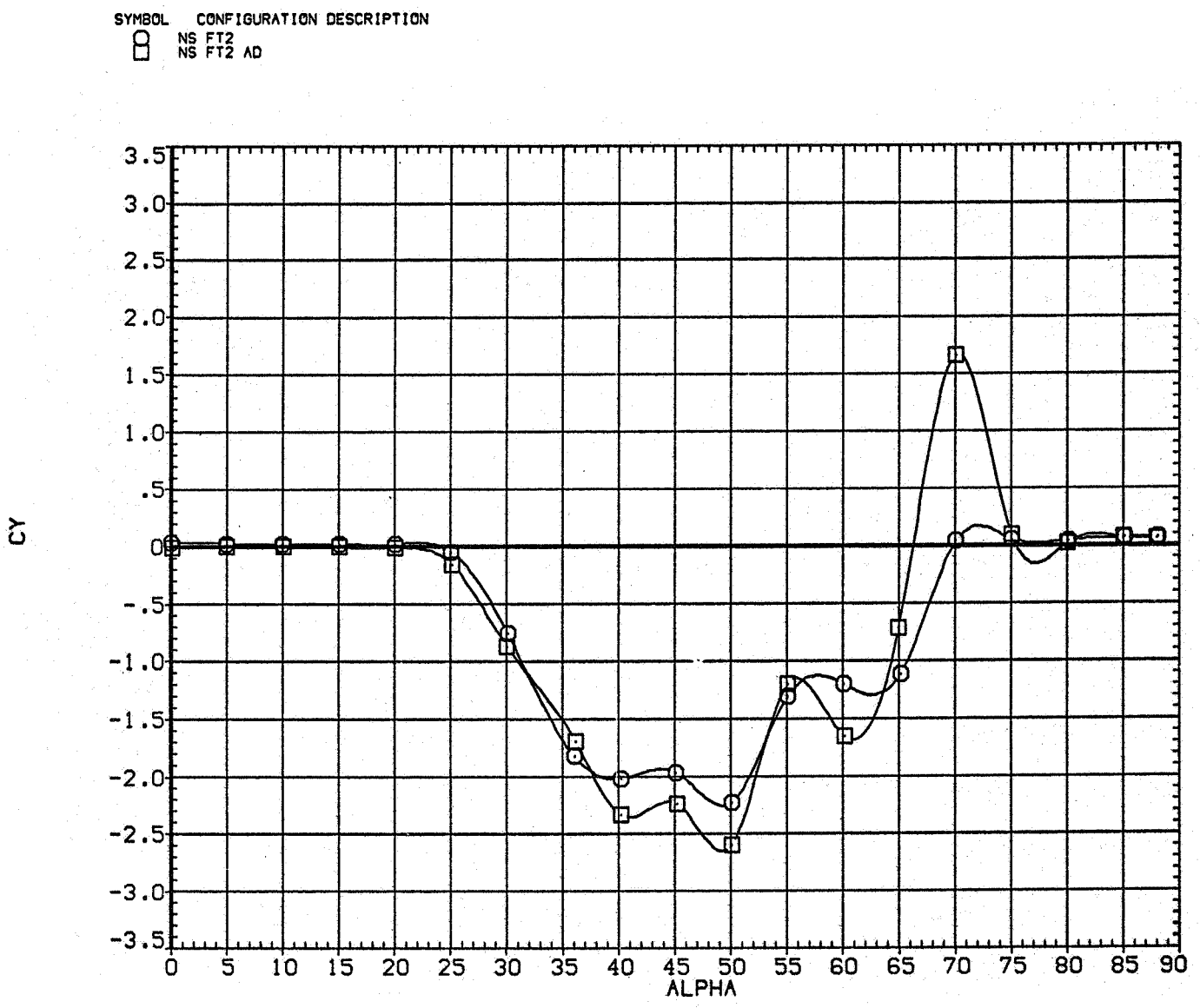

(a) C_Y vs α

Figure 3.– Comparison of forebody alone to forebody in the presence of afterbody for the $\ell/d = 5$ tangent ogive, $M = 0.25$, $R_d = 0.8 \times 10^6$.

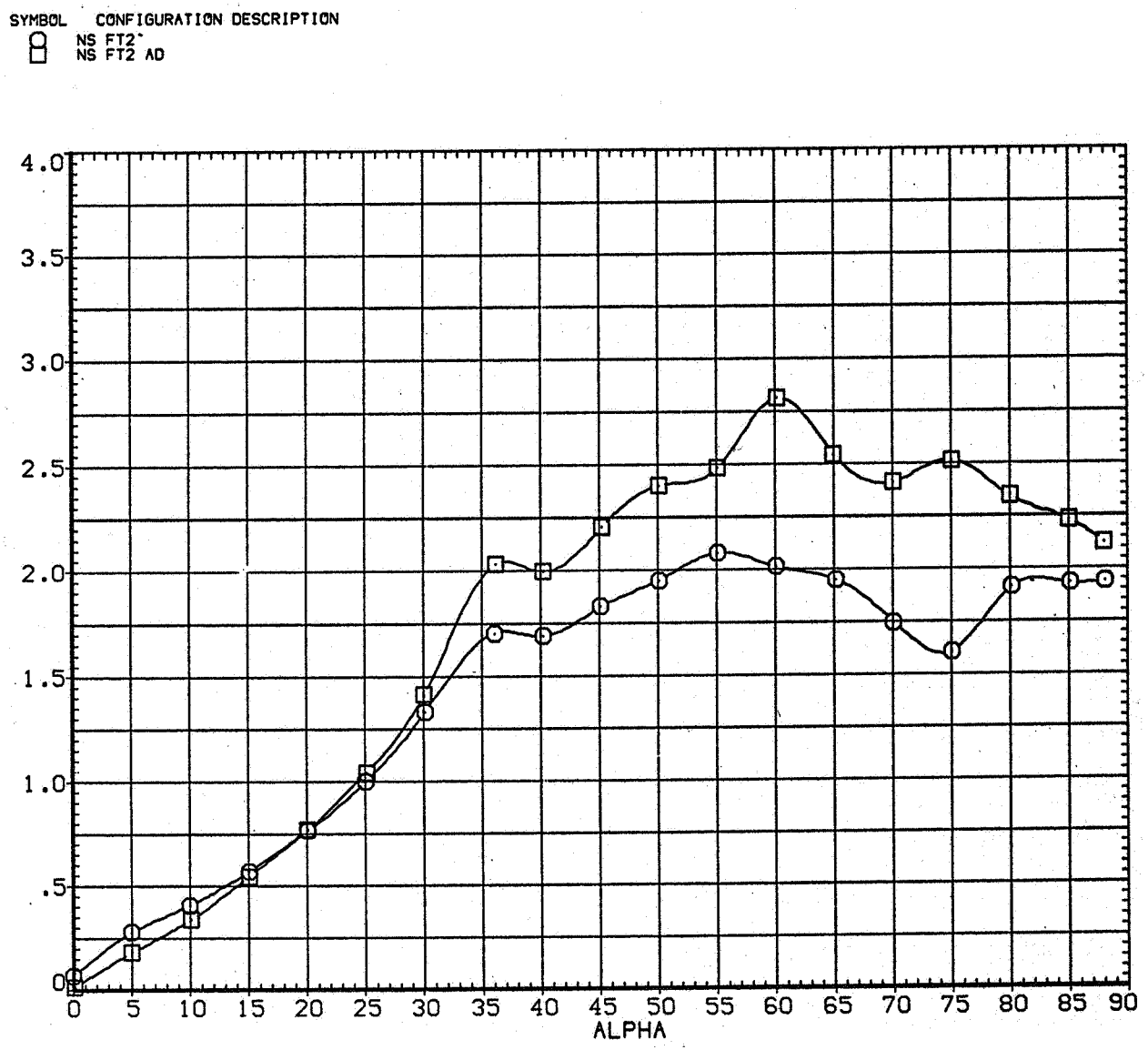

(b) C_N vs α

Figure 3.– Continued.

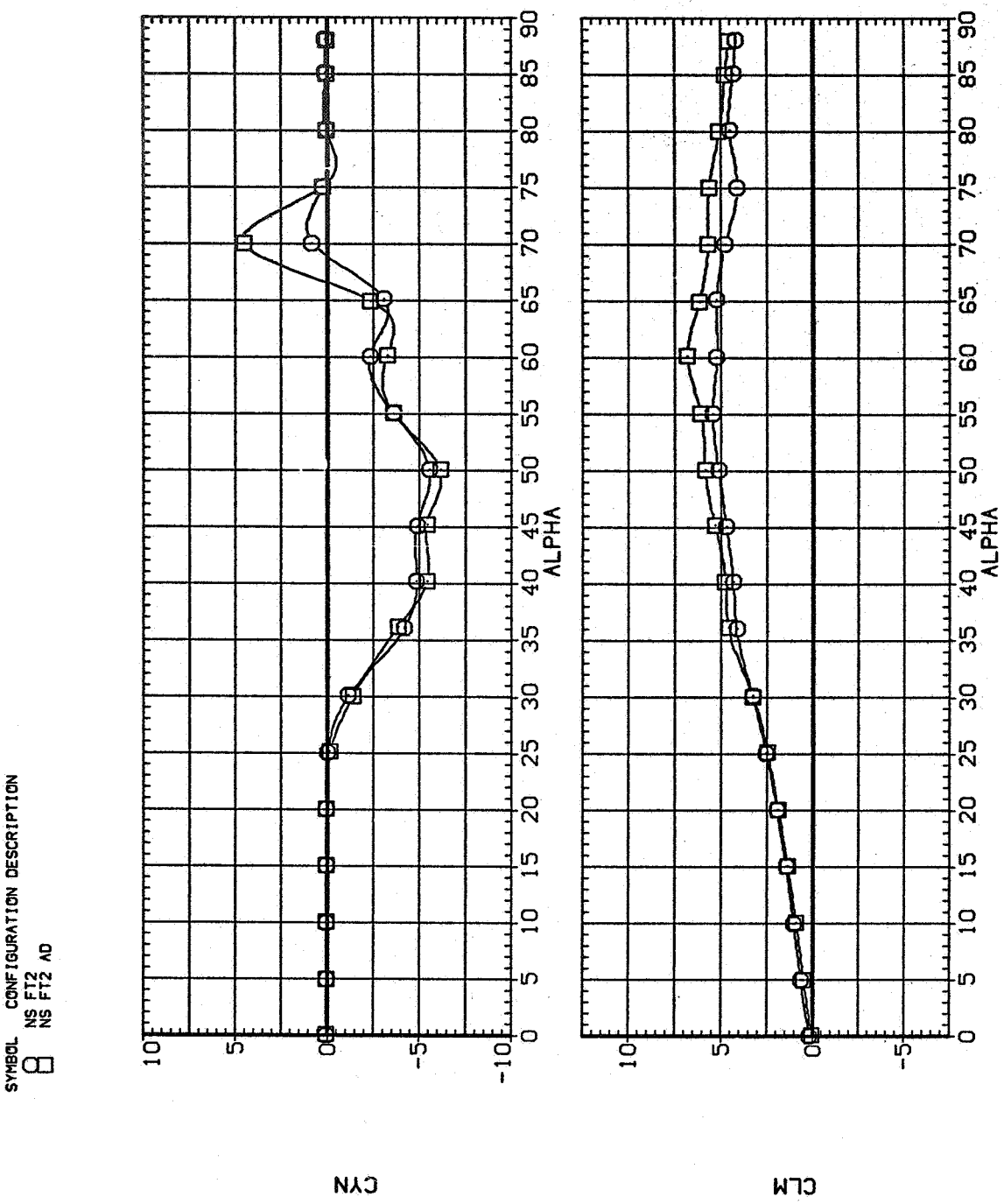

(c) C_n and C_m vs α

Figure 3.– Continued.

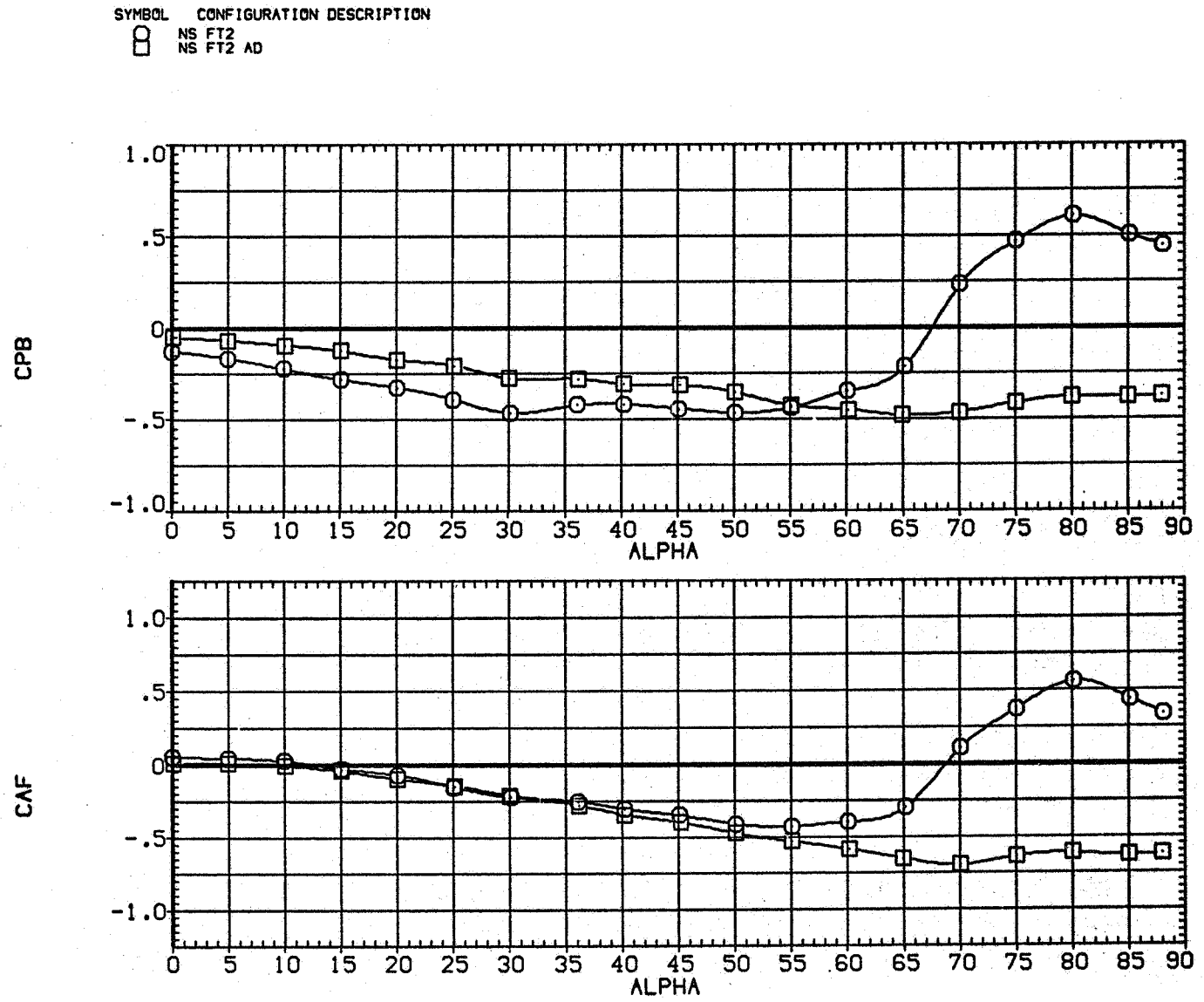

(d) $C_{p,b}$ and C_{AF} vs α

Figure 3.– Concluded.

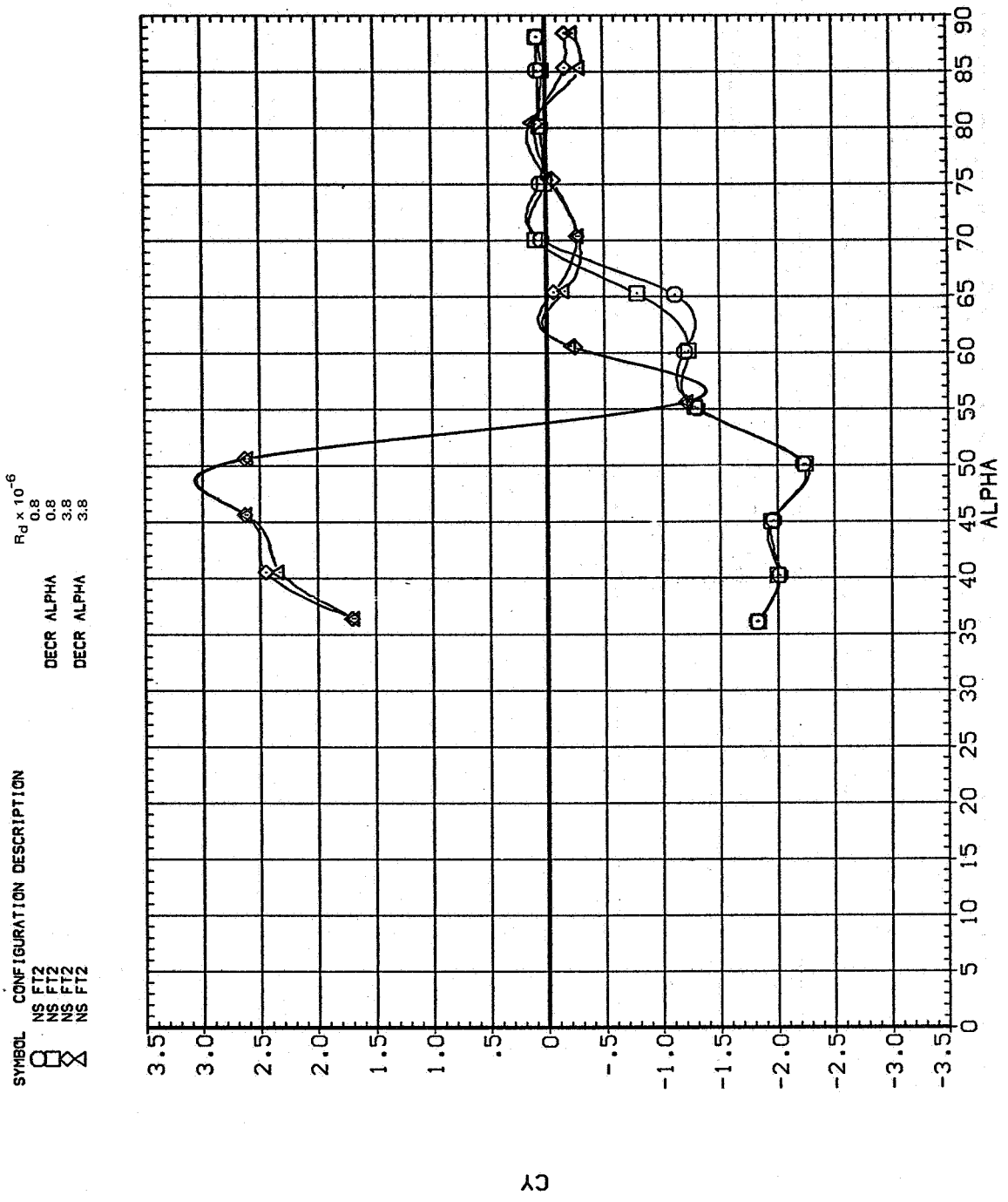

(a) C_Y vs α

Figure 4.– Effect of hysteresis for the $\ell/d = 5$ tangent ogive, $M = 0.25$.

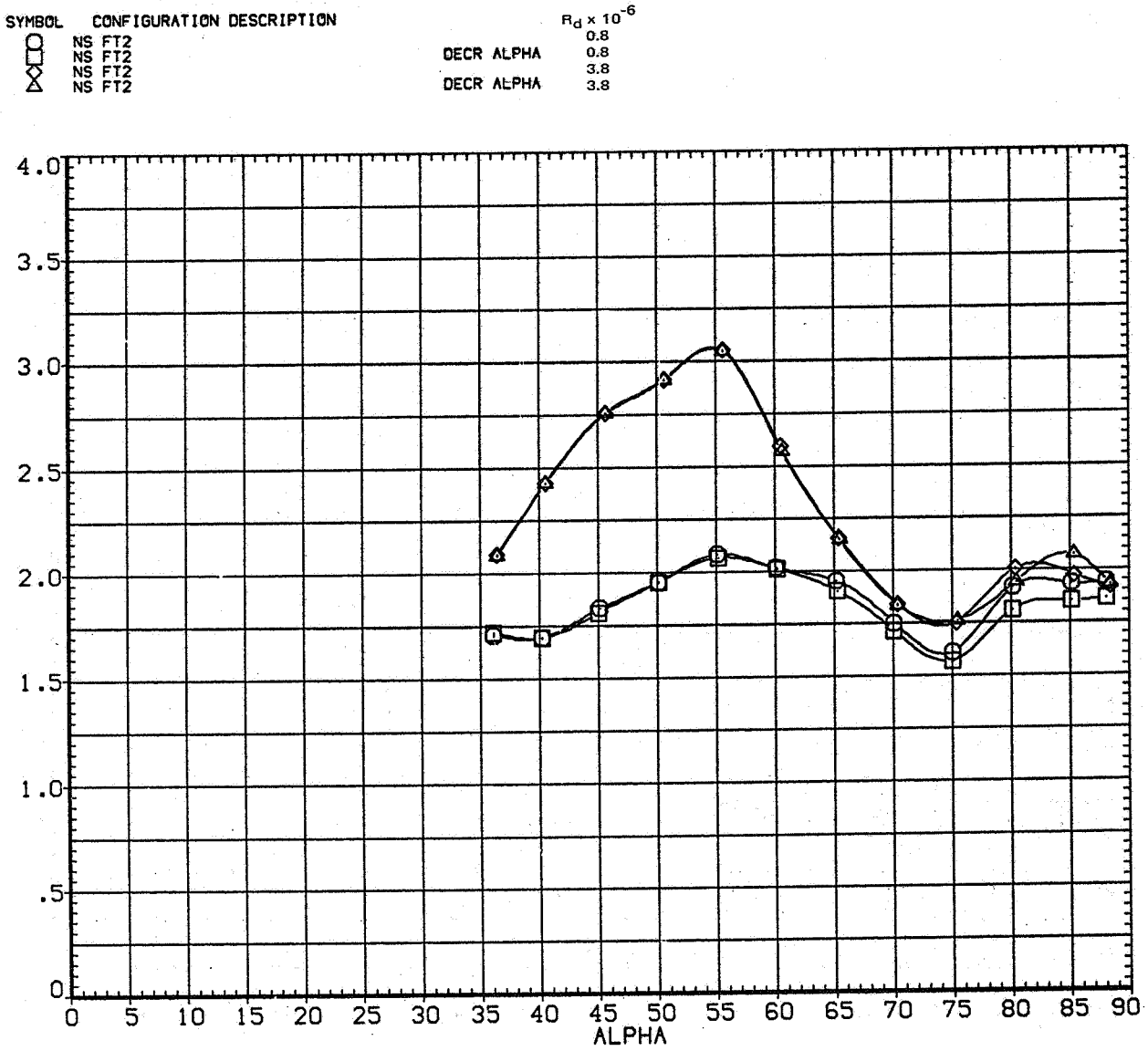

(b) C_N vs α

Figure 4.– Continued.

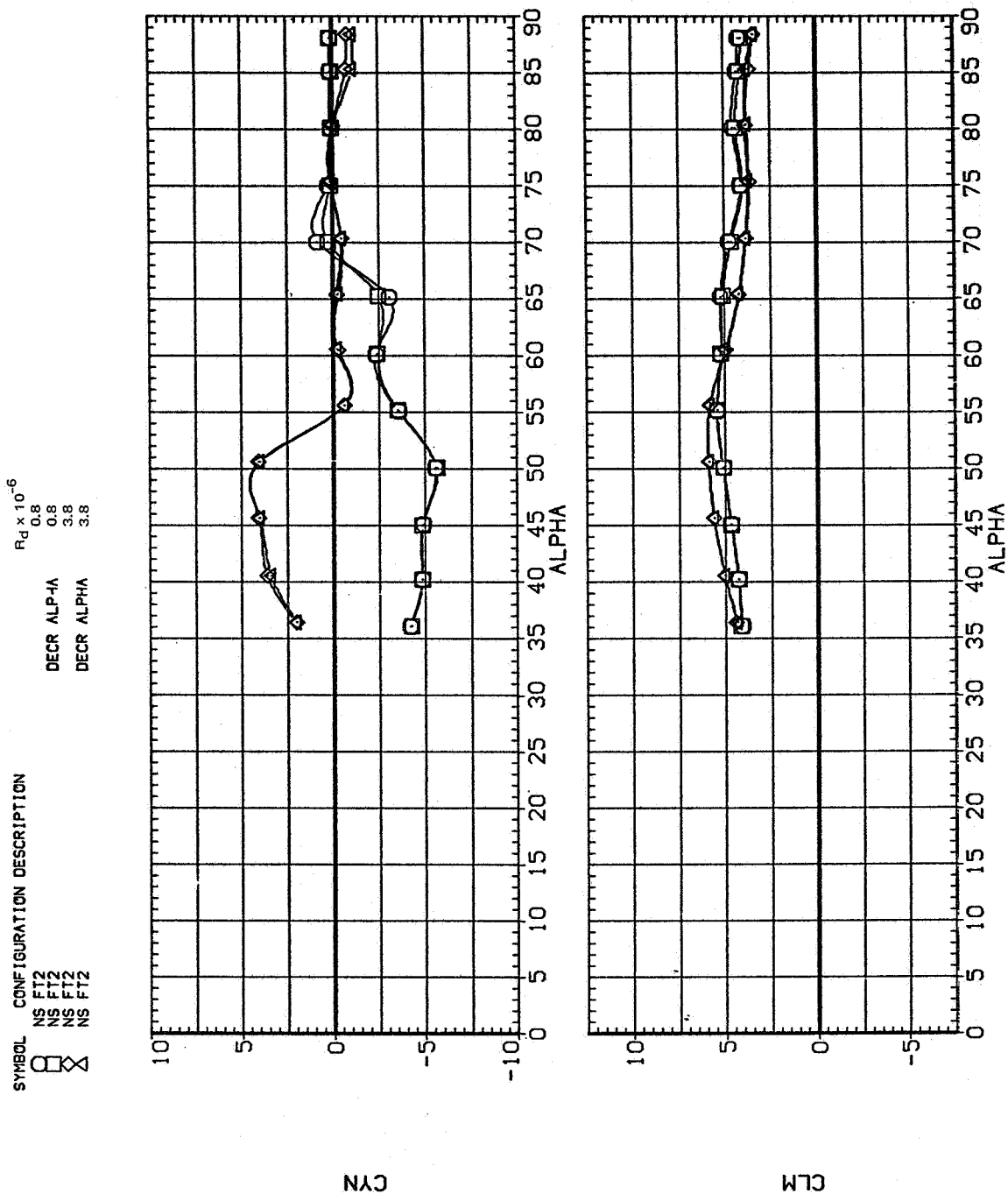

(c) C_n and C_m vs α

Figure 4.– Concluded.

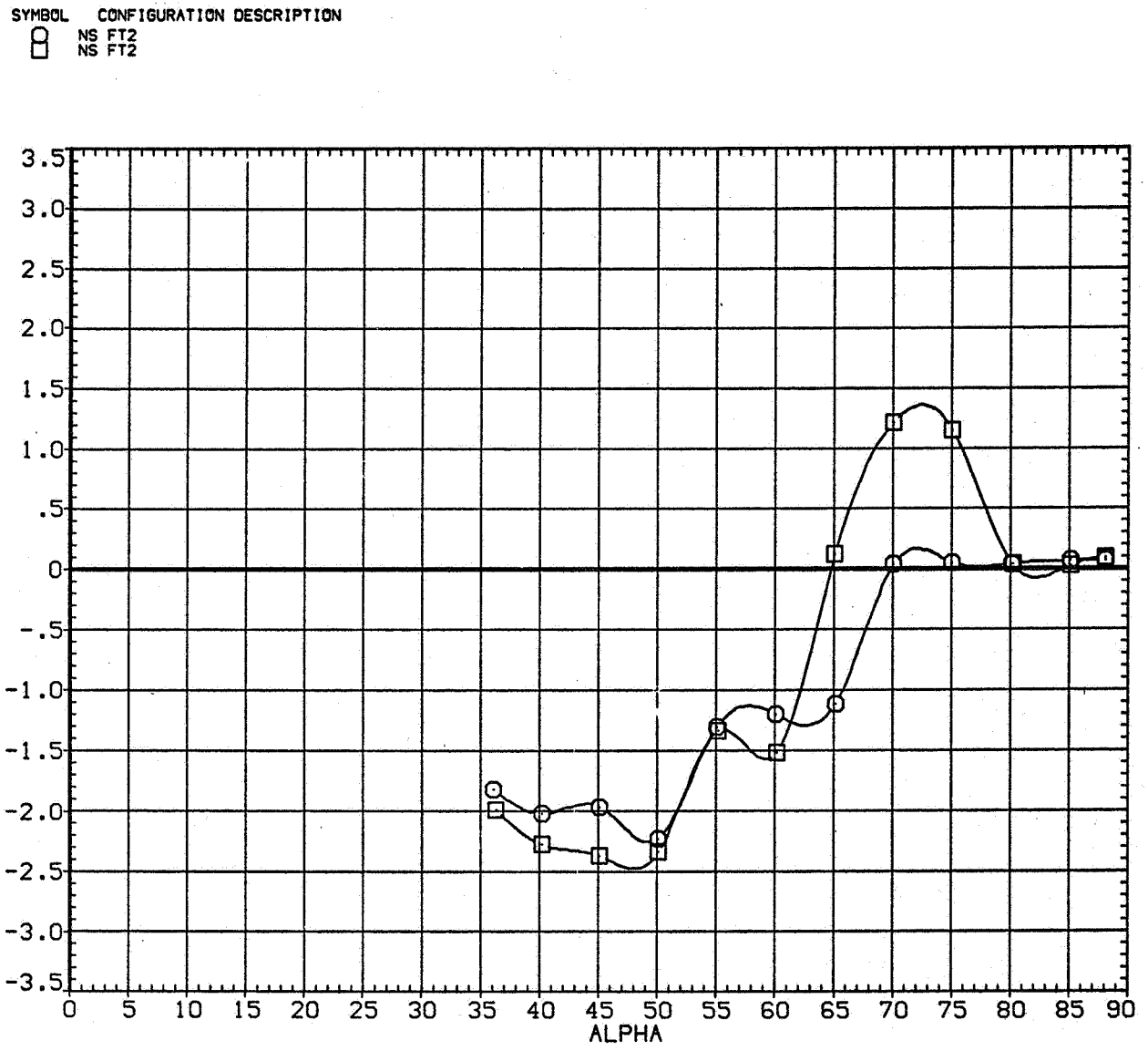

(a) C_Y vs α

Figure 5.– Effect of repeatability for the $\ell/d = 5$ tangent ogive, $M = 0.25$, $R_d = 0.8 \times 10^6$.

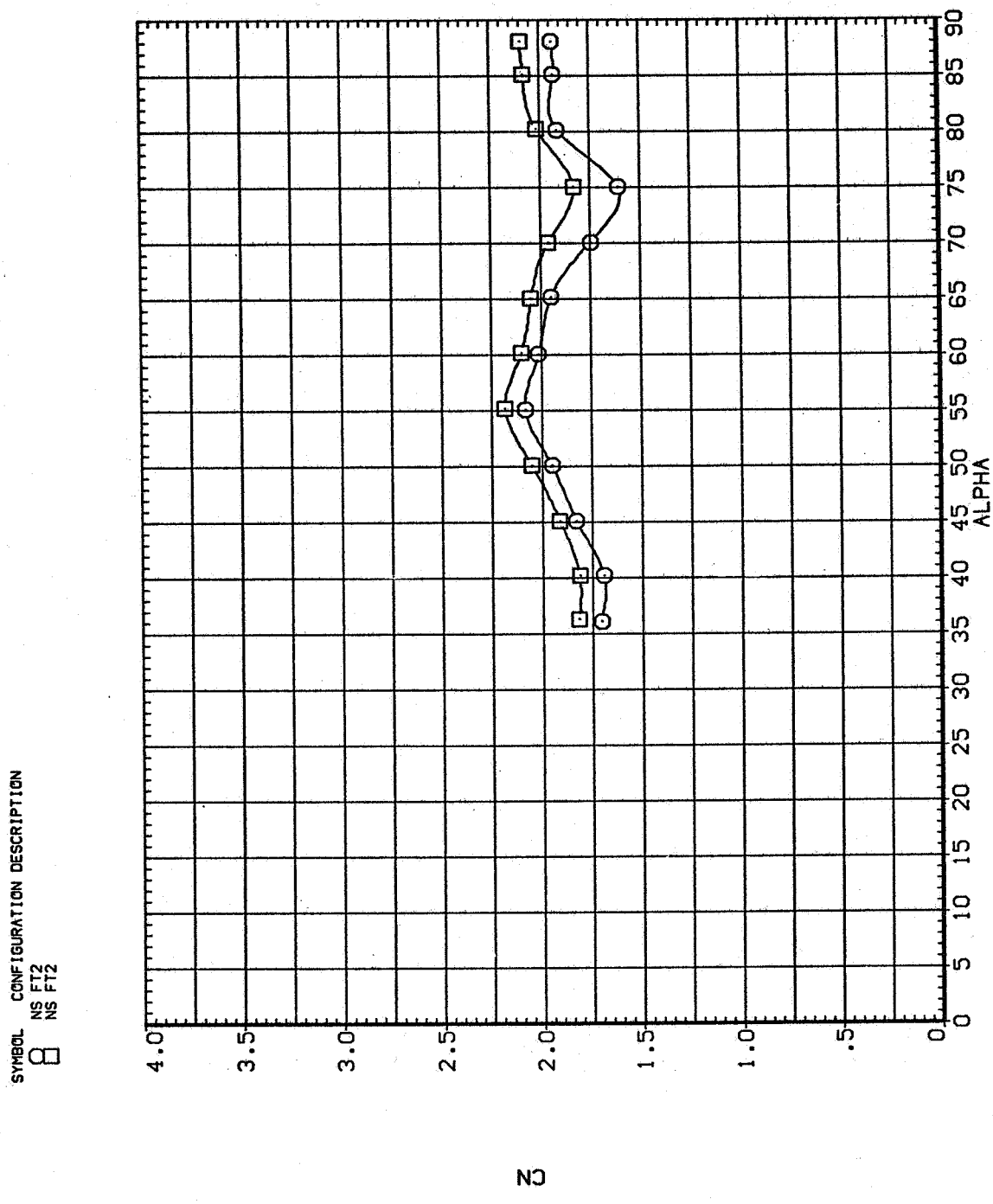

(b) C_N vs α

Figure 5.– Continued.

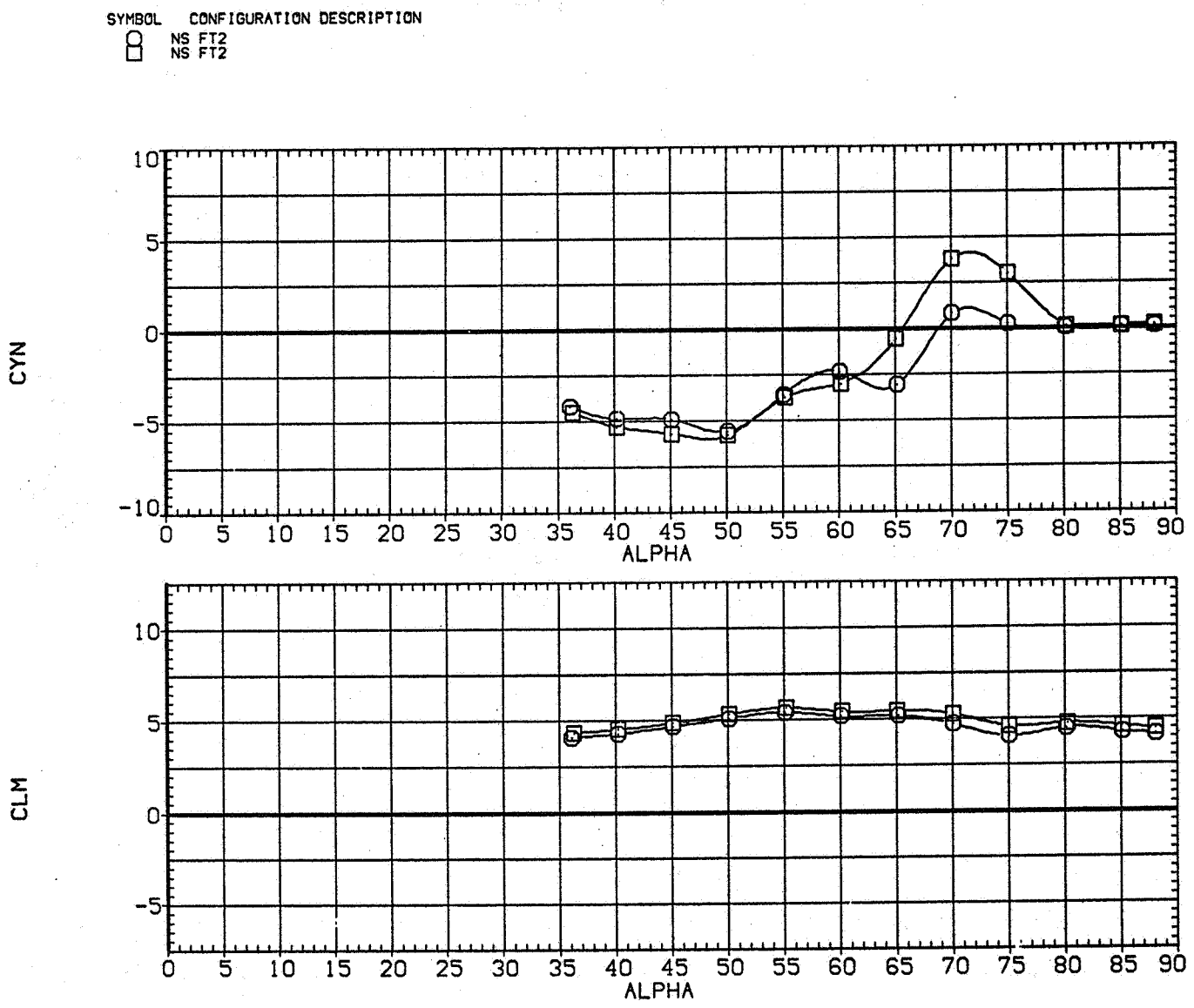

(c) C_n and C_m vs α

Figure 5.– Concluded.

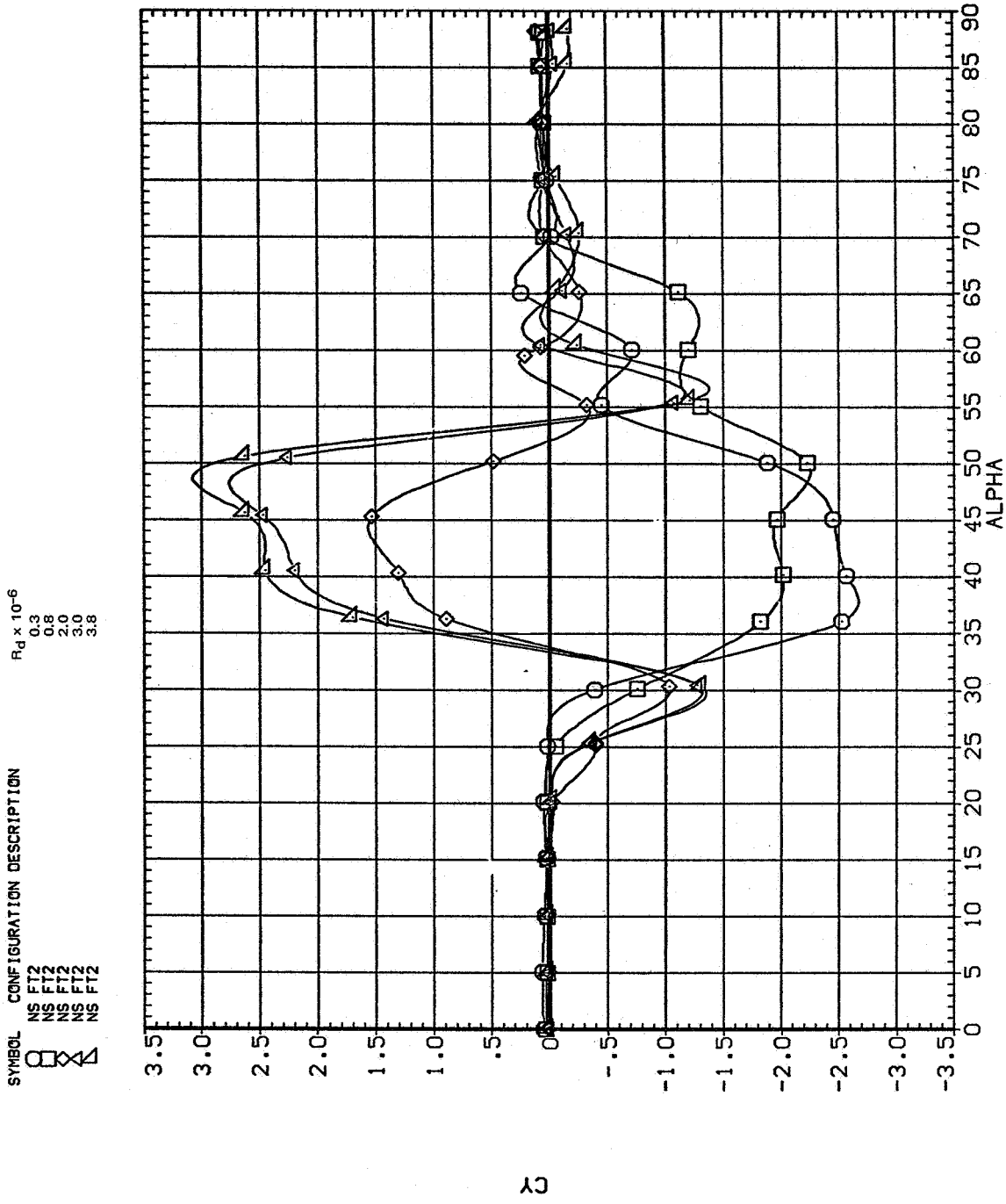

(a) C_Y vs α

Figure 6.– Effect of Reynolds number for the $\ell/d = 5$ tangent ogive, $M = 0.25$.

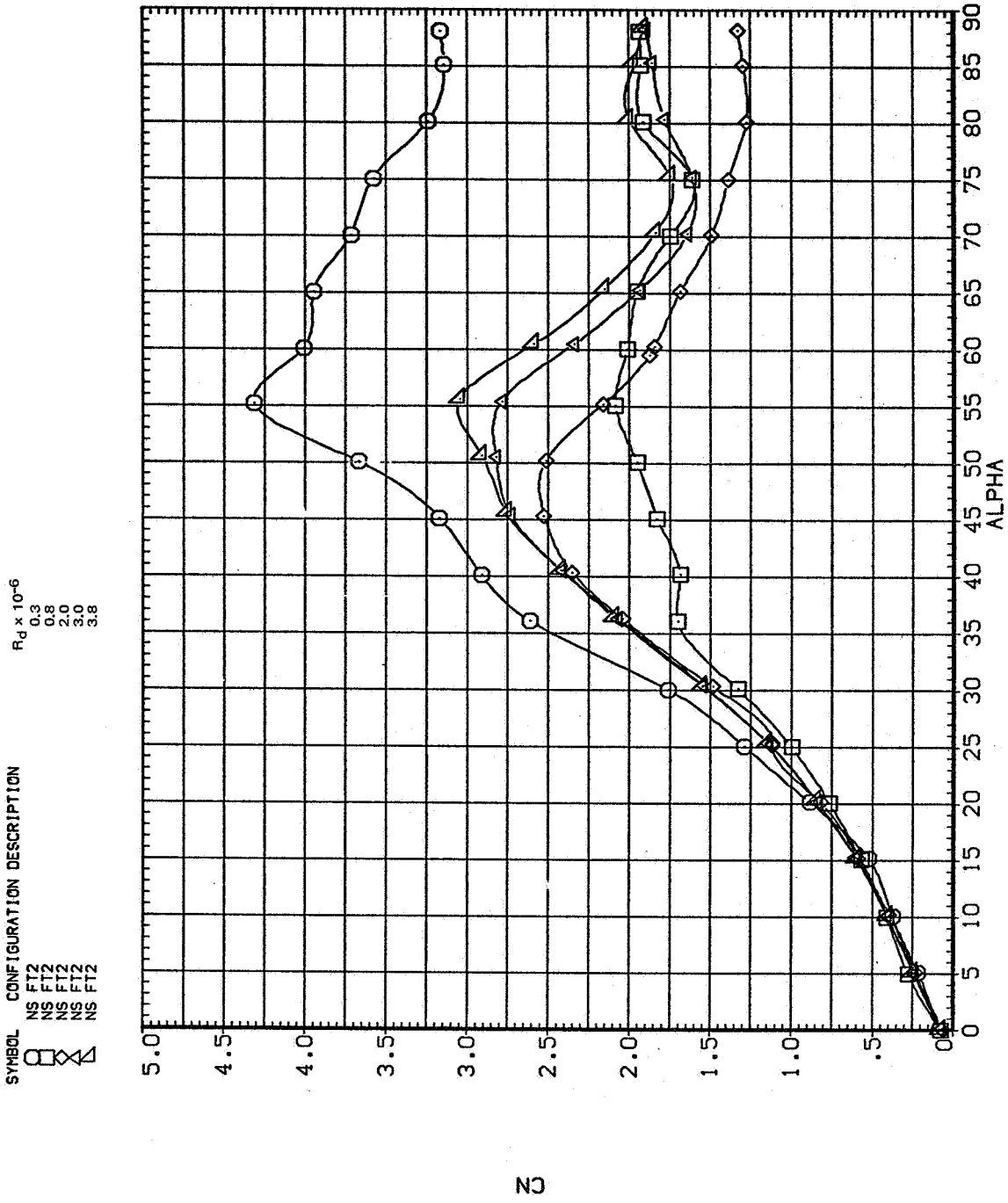

(b) C_N vs α

Figure 6.– Continued.

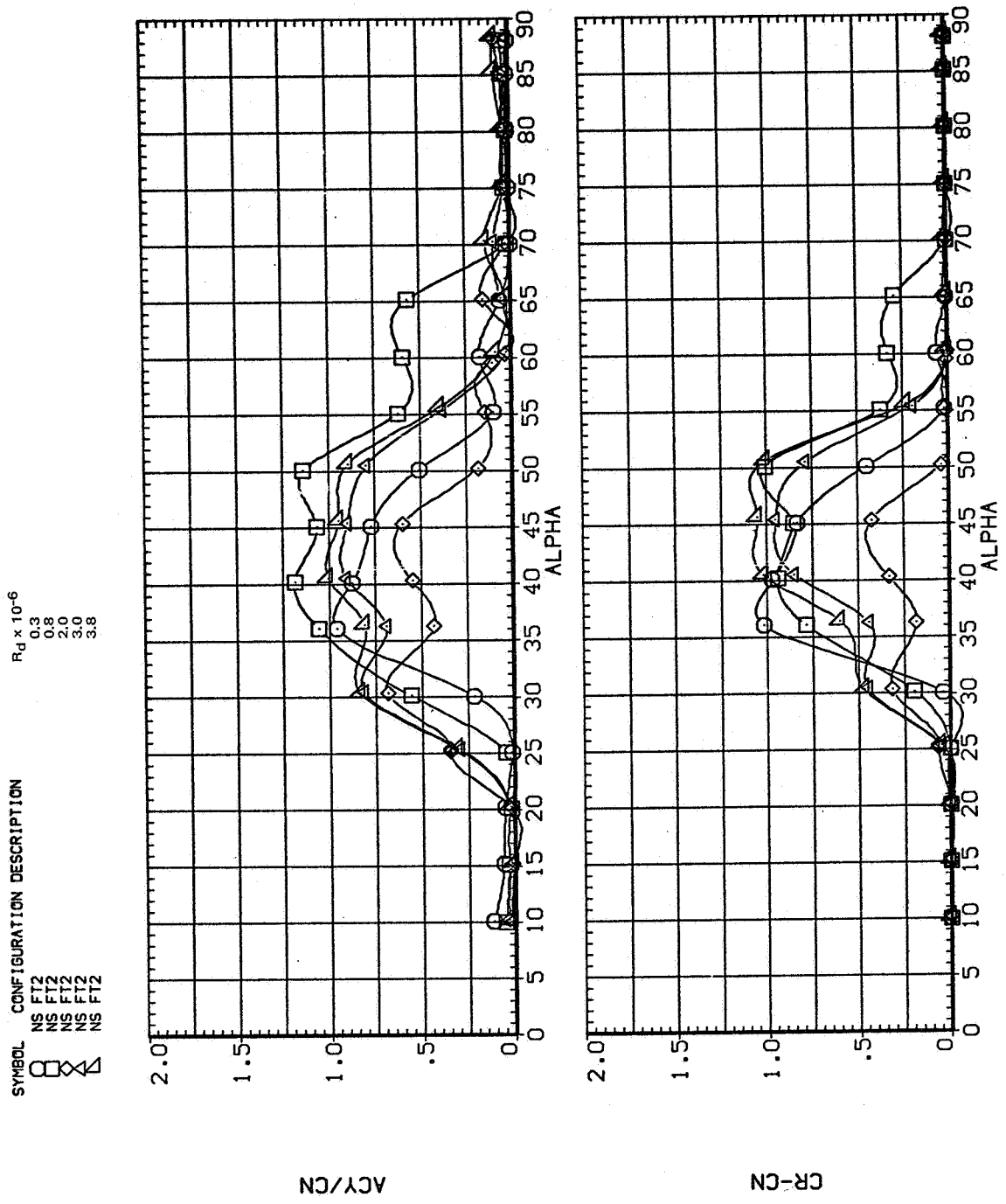

(c) $C_Y/|C_N|$ and $C_R - C_N$ vs α

Figure 6.– Continued.

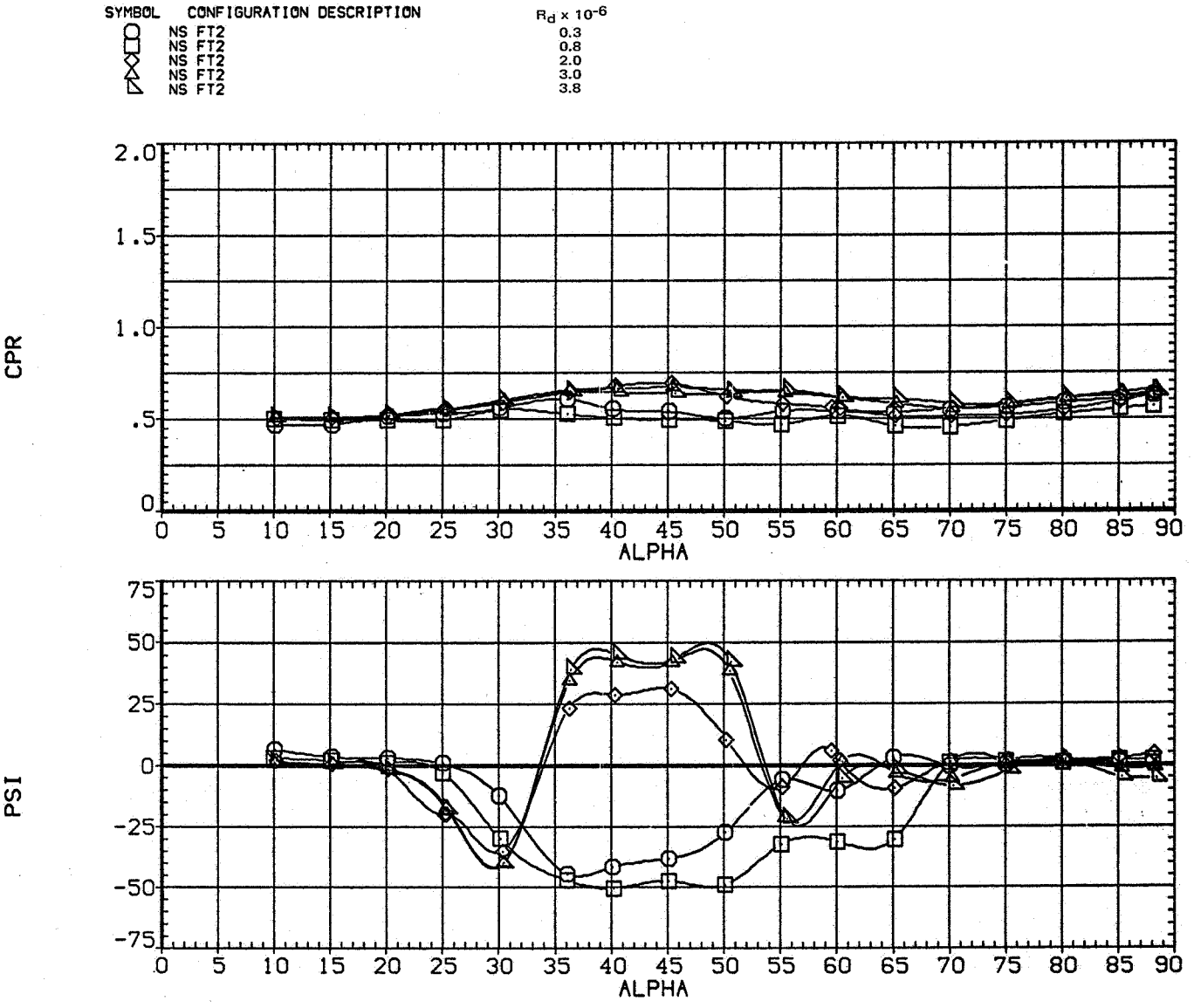

(d) CP_R and Ψ vs α

Figure 6.– Continued.

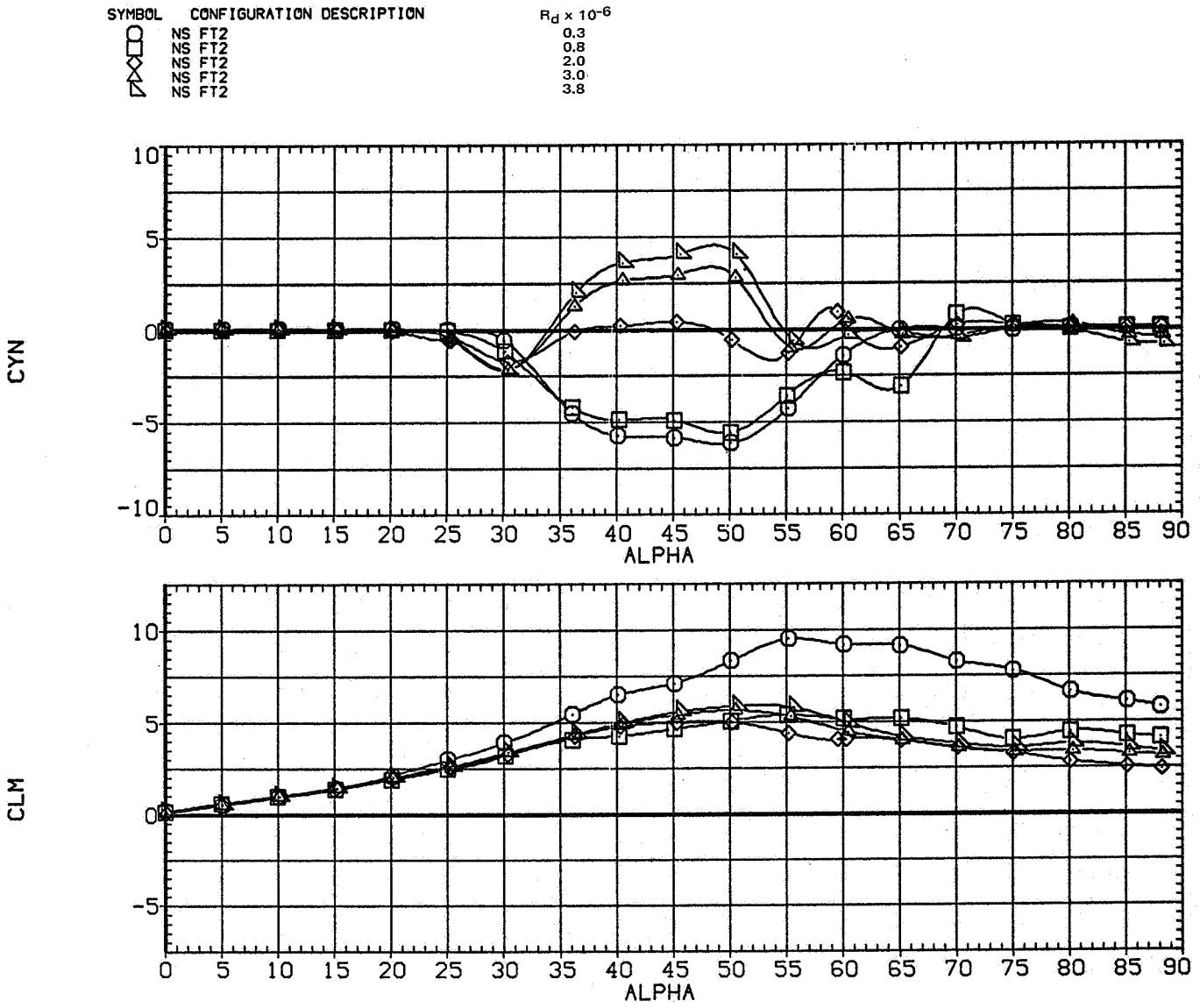

(e) C_n and C_m vs α

Figure 6.– Continued.

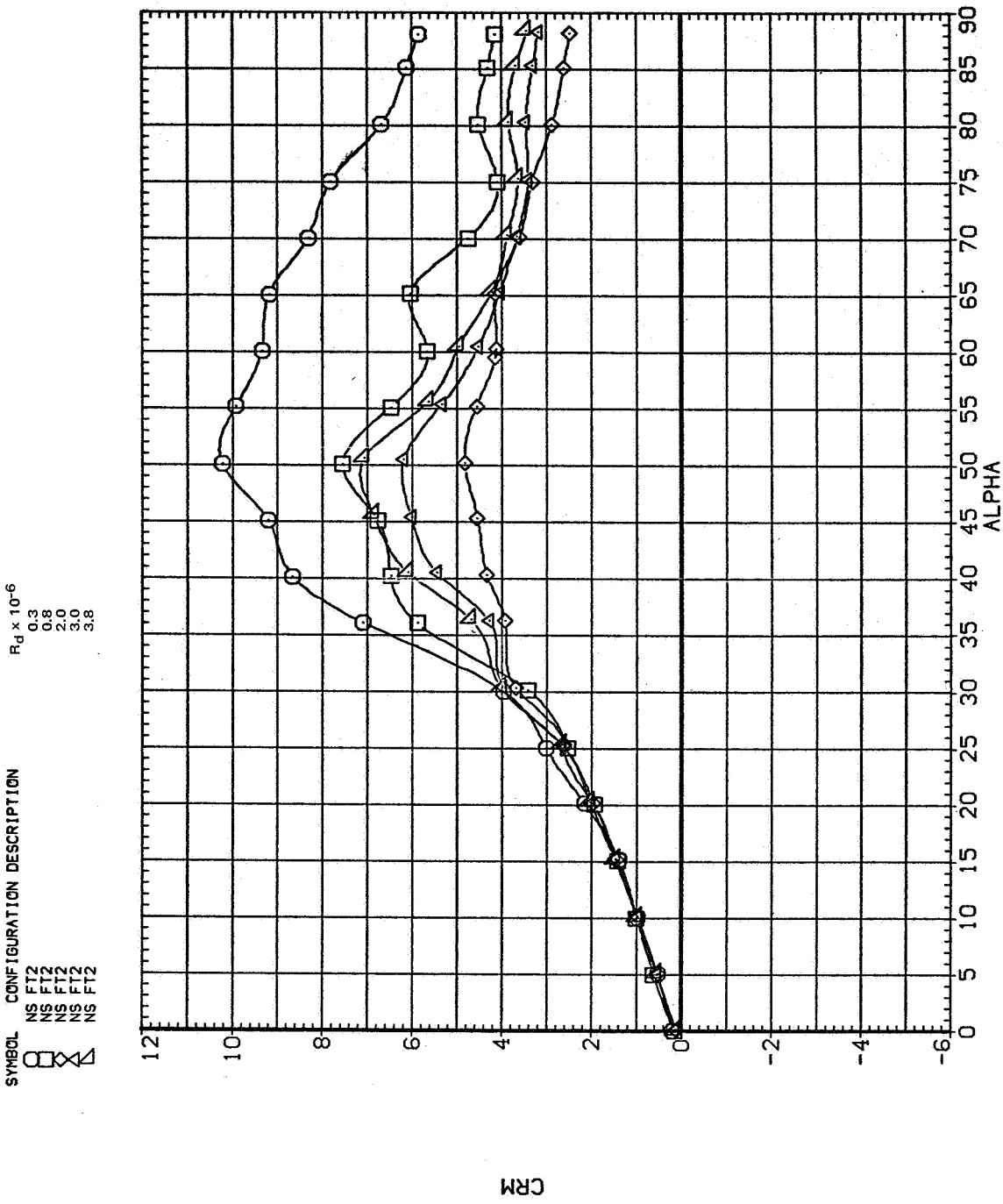

(f) $C_{m,R}$ vs α

Figure 6.– Continued.

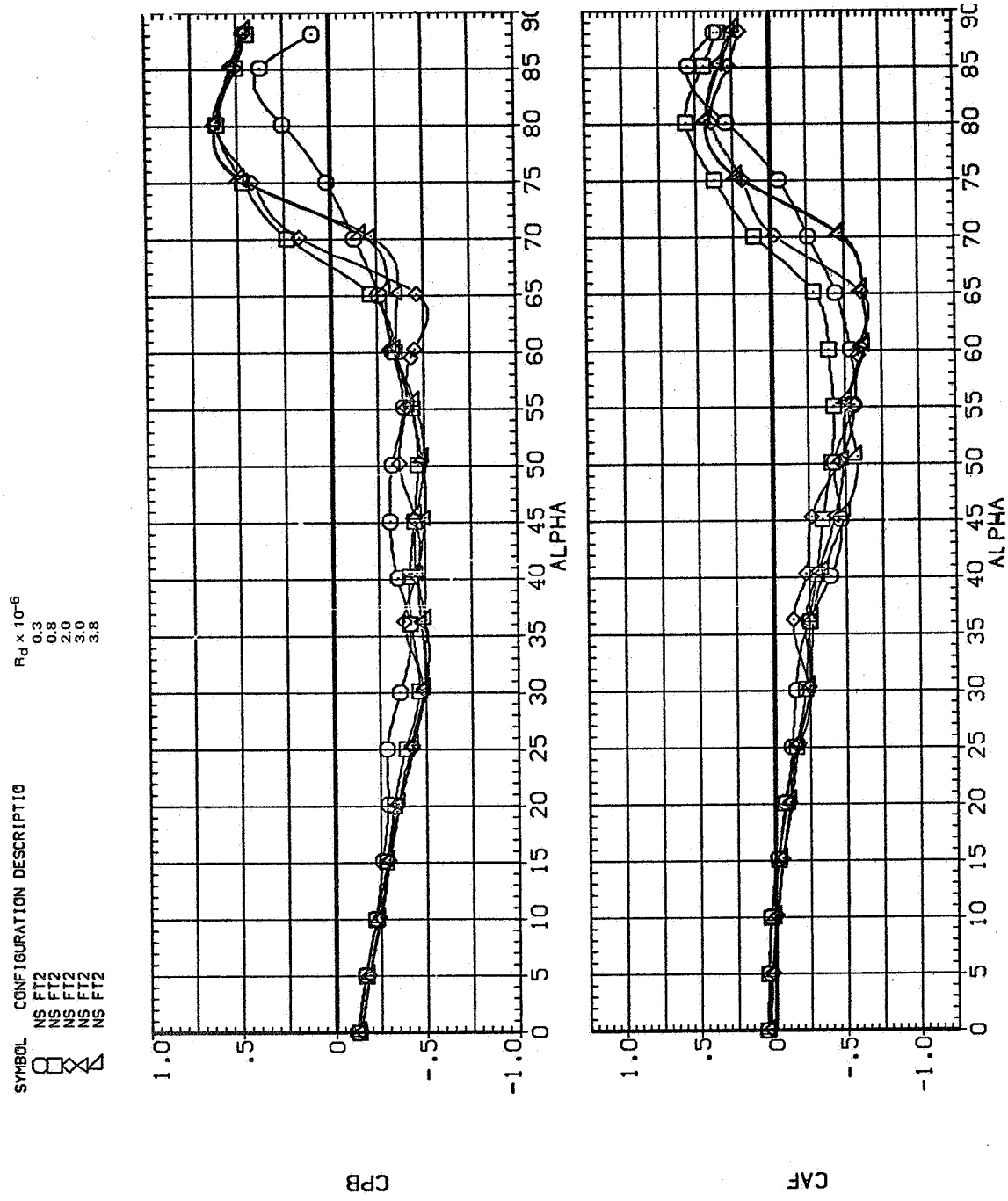

(g) $C_{p,b}$ and C_{AF} vs α

Figure 6.– Concluded.

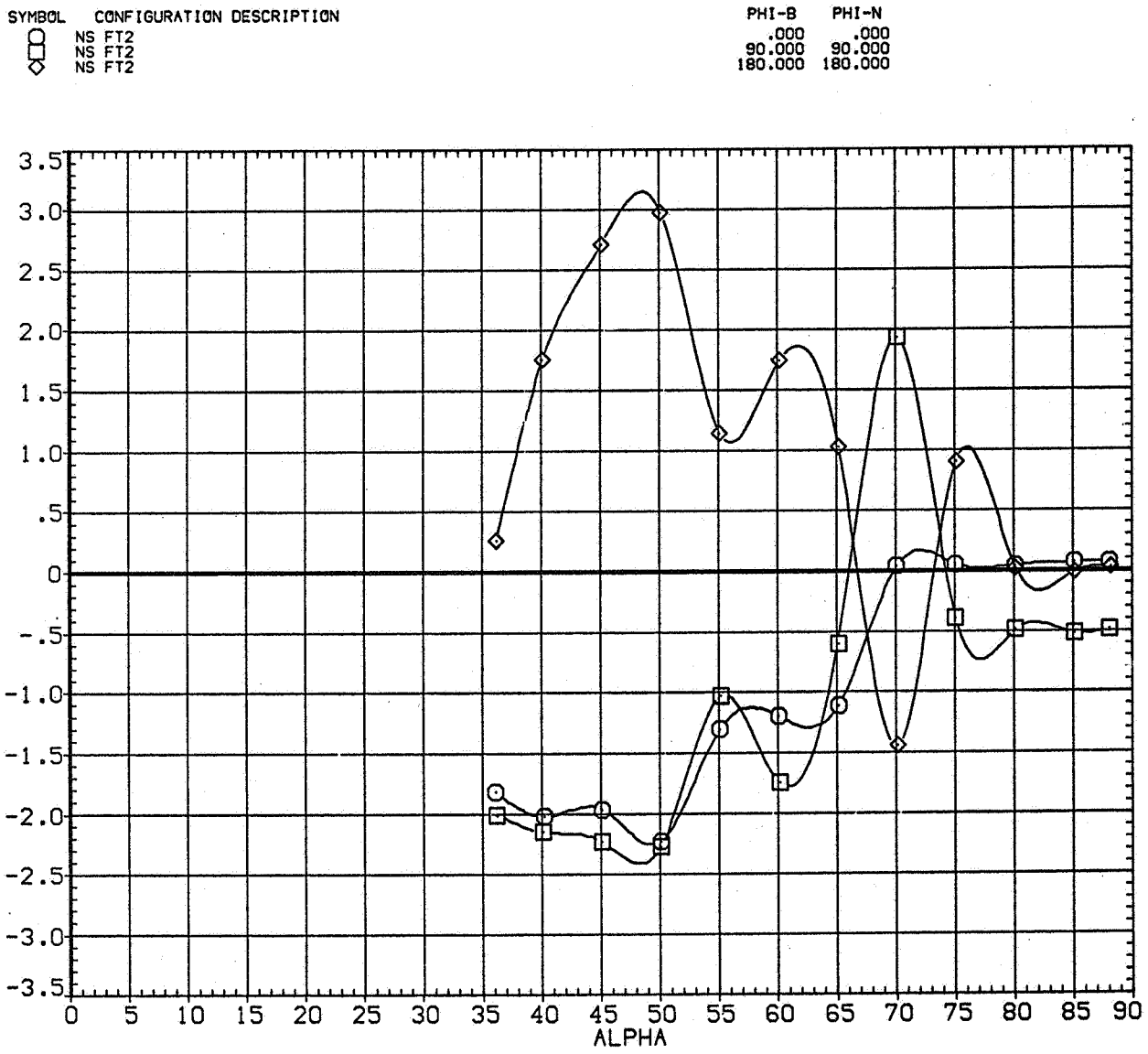

(a) C_Y vs α

Figure 7.– Effect of roll angle of forebody for the $\ell/d = 5$ tangent ogive, $M = 0.25$, $R_d = 0.8 \times 10^6$.

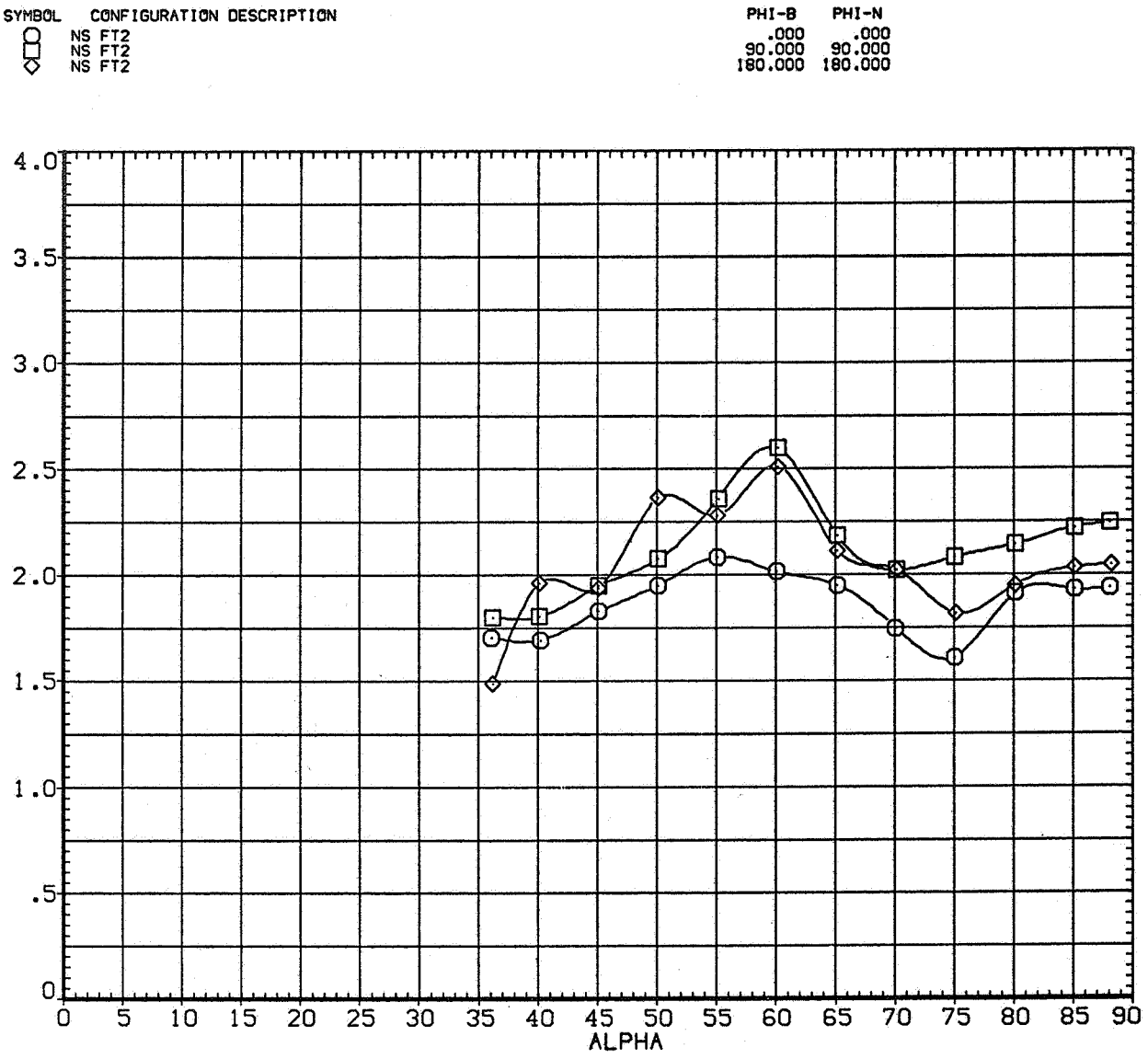

(b) C_N vs α

Figure 7.– Continued.

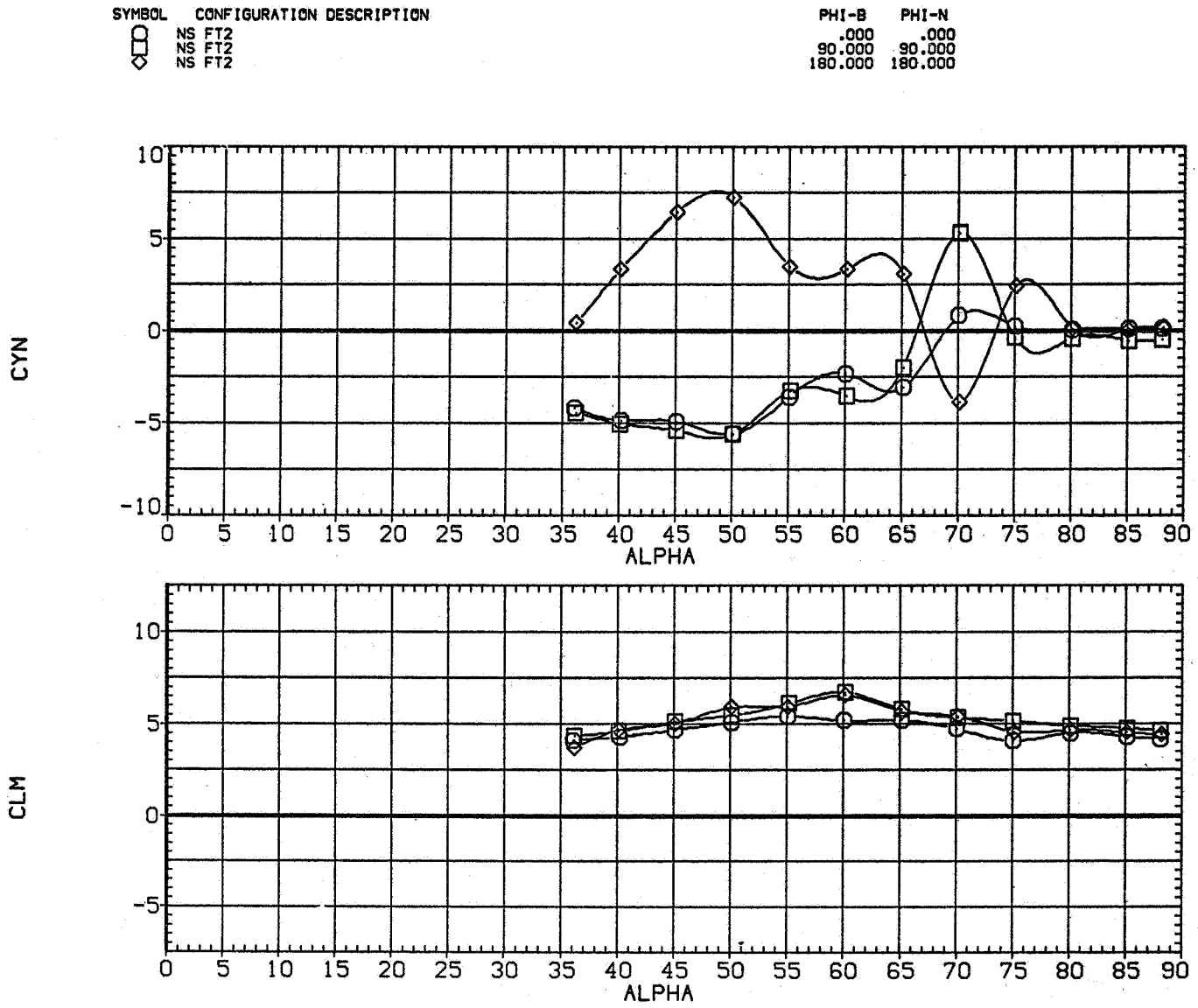

(c) C_n and C_m vs α

Figure 7.– Concluded.

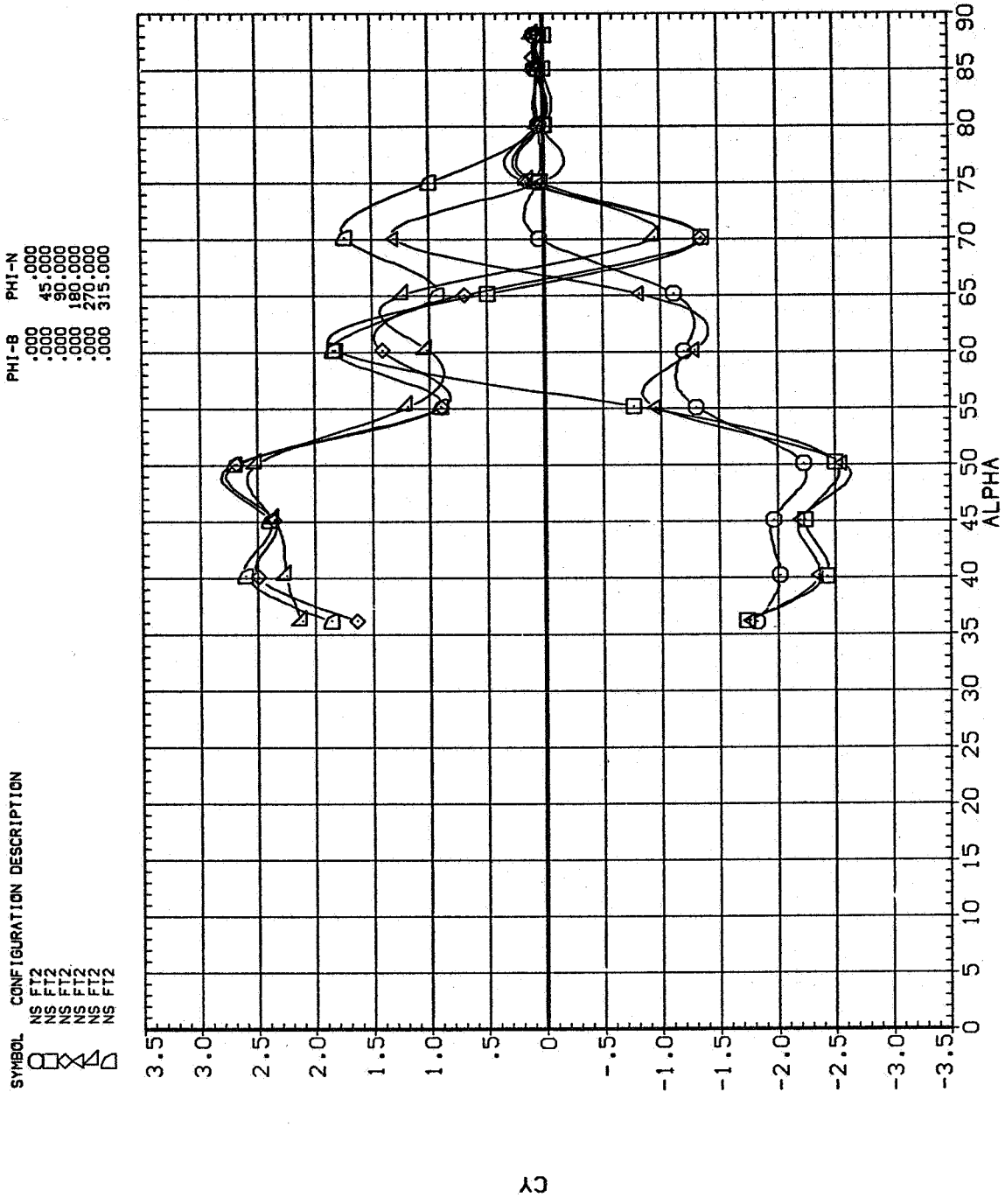

(a) C_Y vs α

Figure 8.– Effect of roll angle of nose tip section for the $\ell/d = 5$ tangent ogive, $M = 0.25$, $R_d = 0.8 \times 10^6$.

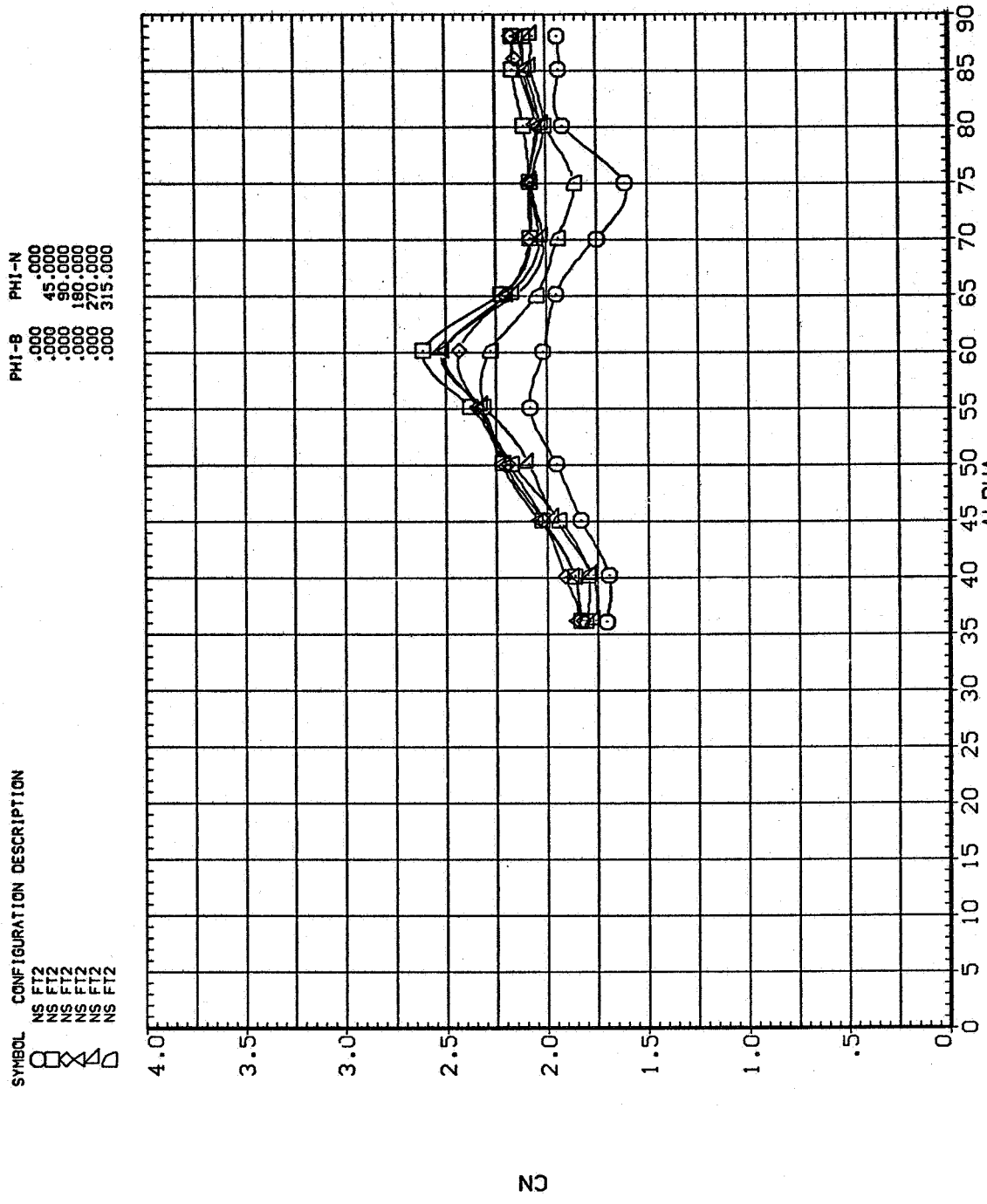

(b) C_N vs α

Figure 8.– Continued.

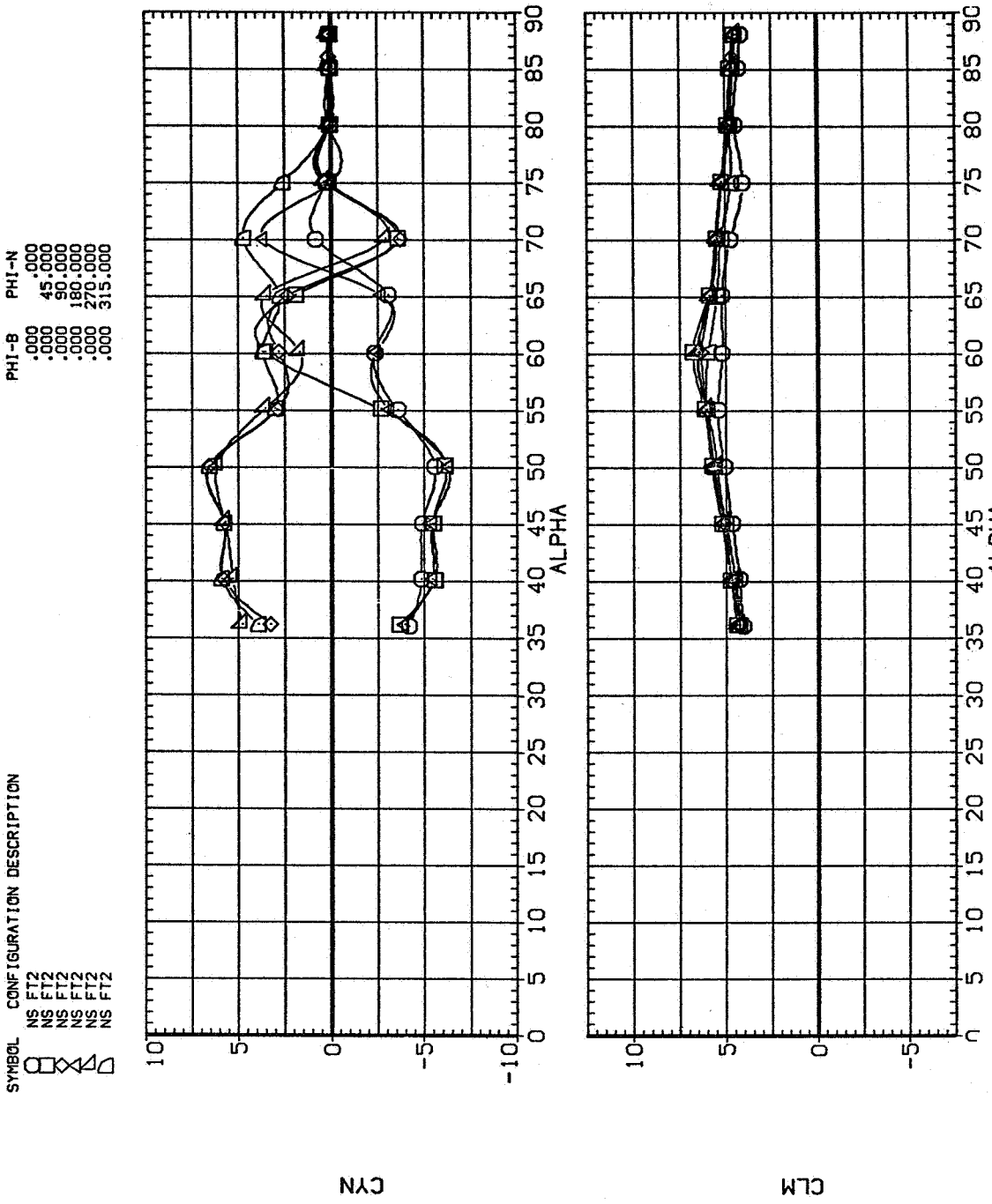

(c) C_n and C_m vs α

Figure 8.– Concluded.

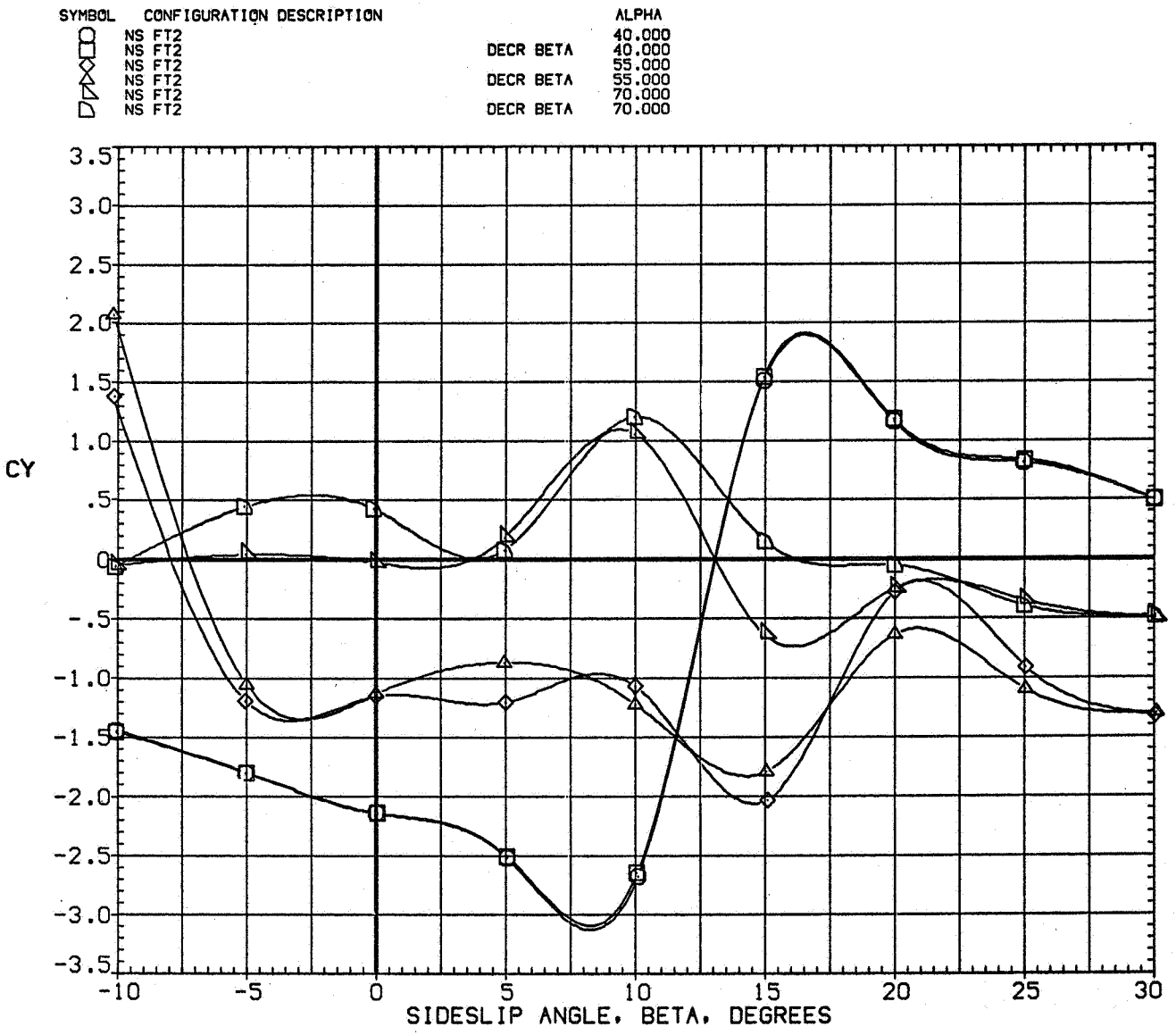

(a) C_Y vs α

Figure 9.– Effect of angle of sideslip for the $\ell/d = 5$ tangent ogive, $M = 0.25$, $R_d = 0.8 \times 10^6$.

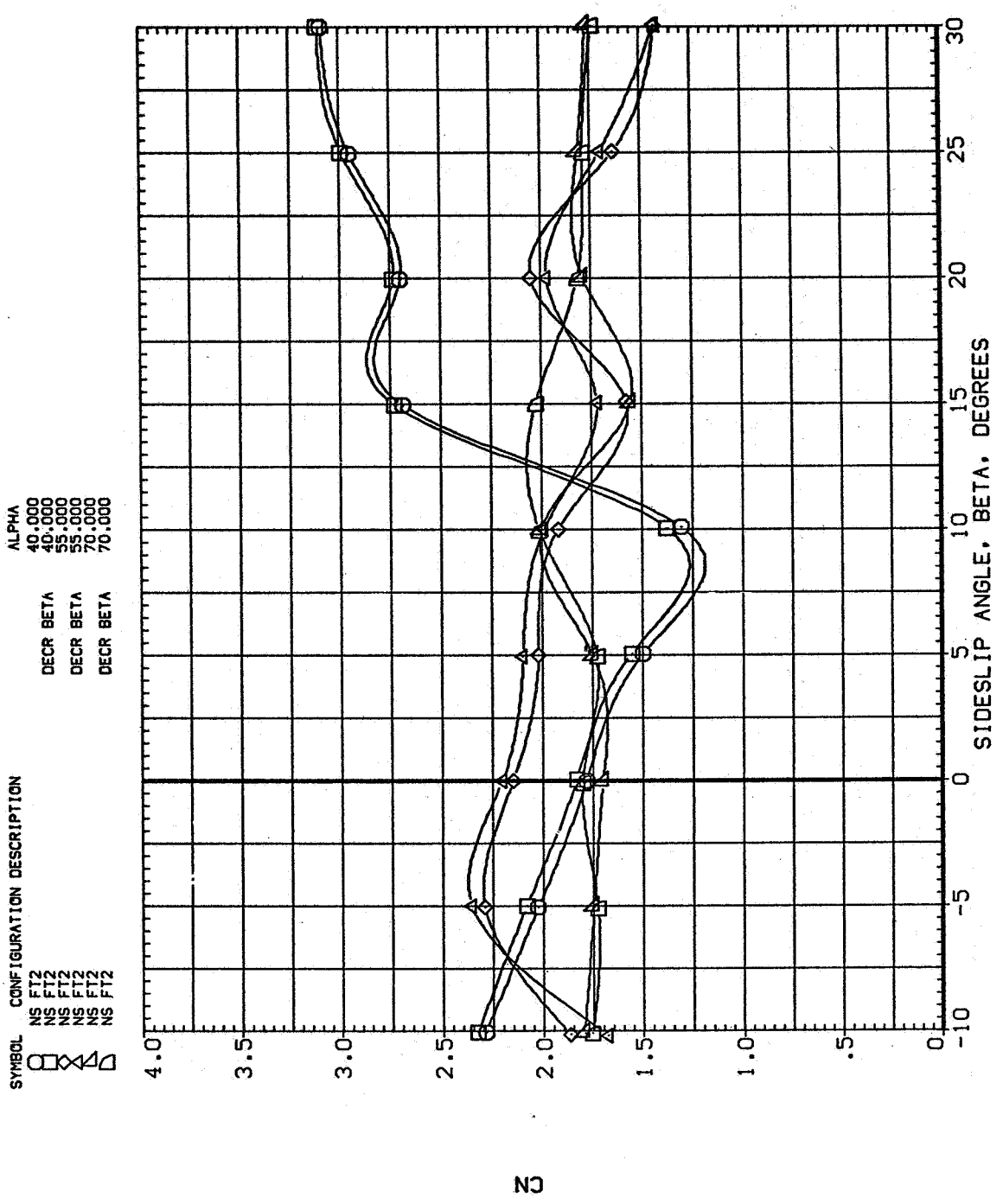

(b) C_N vs α

Figure 9.– Continued.

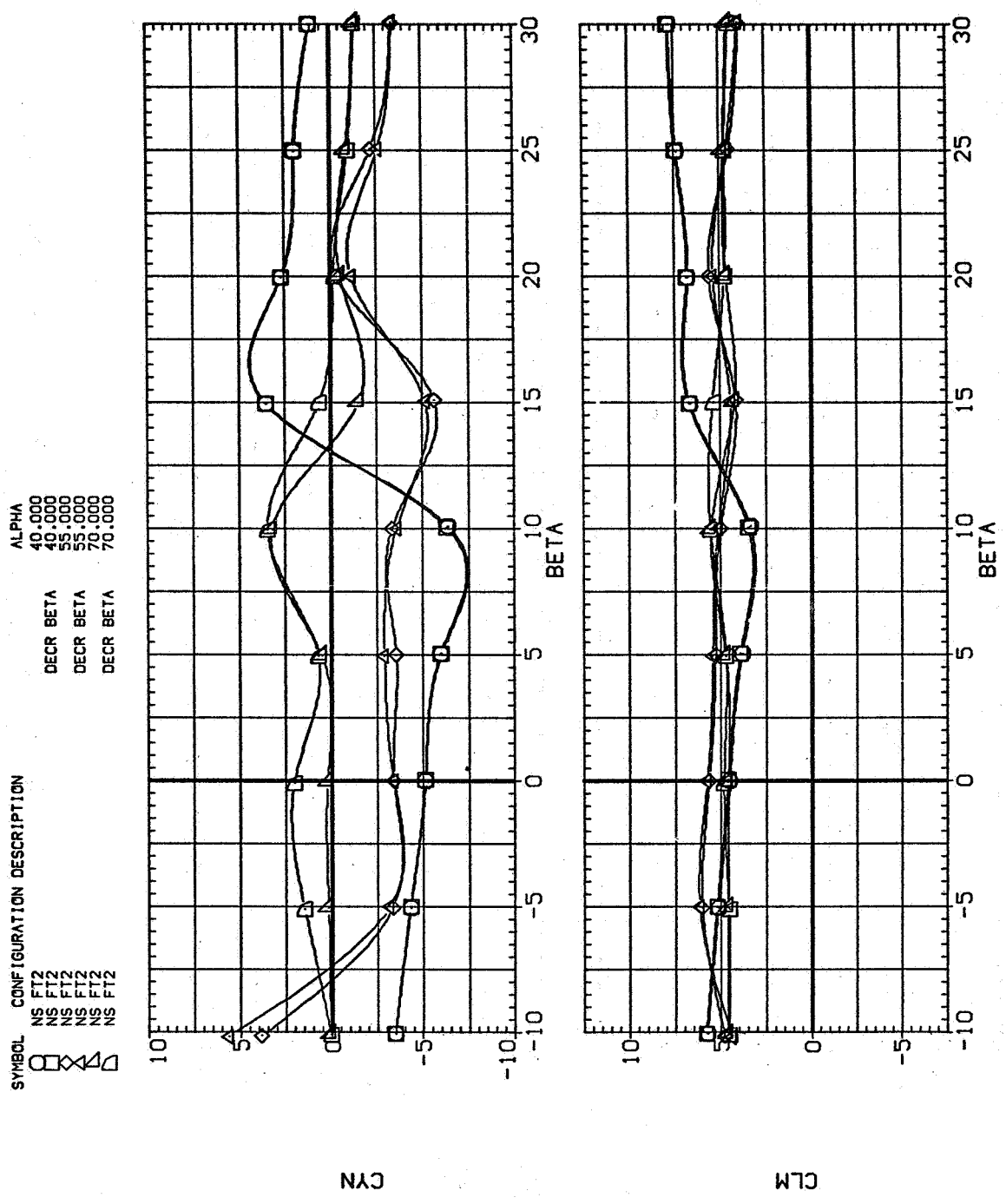

(c) C_n and C_m vs α

Figure 9.– Concluded.

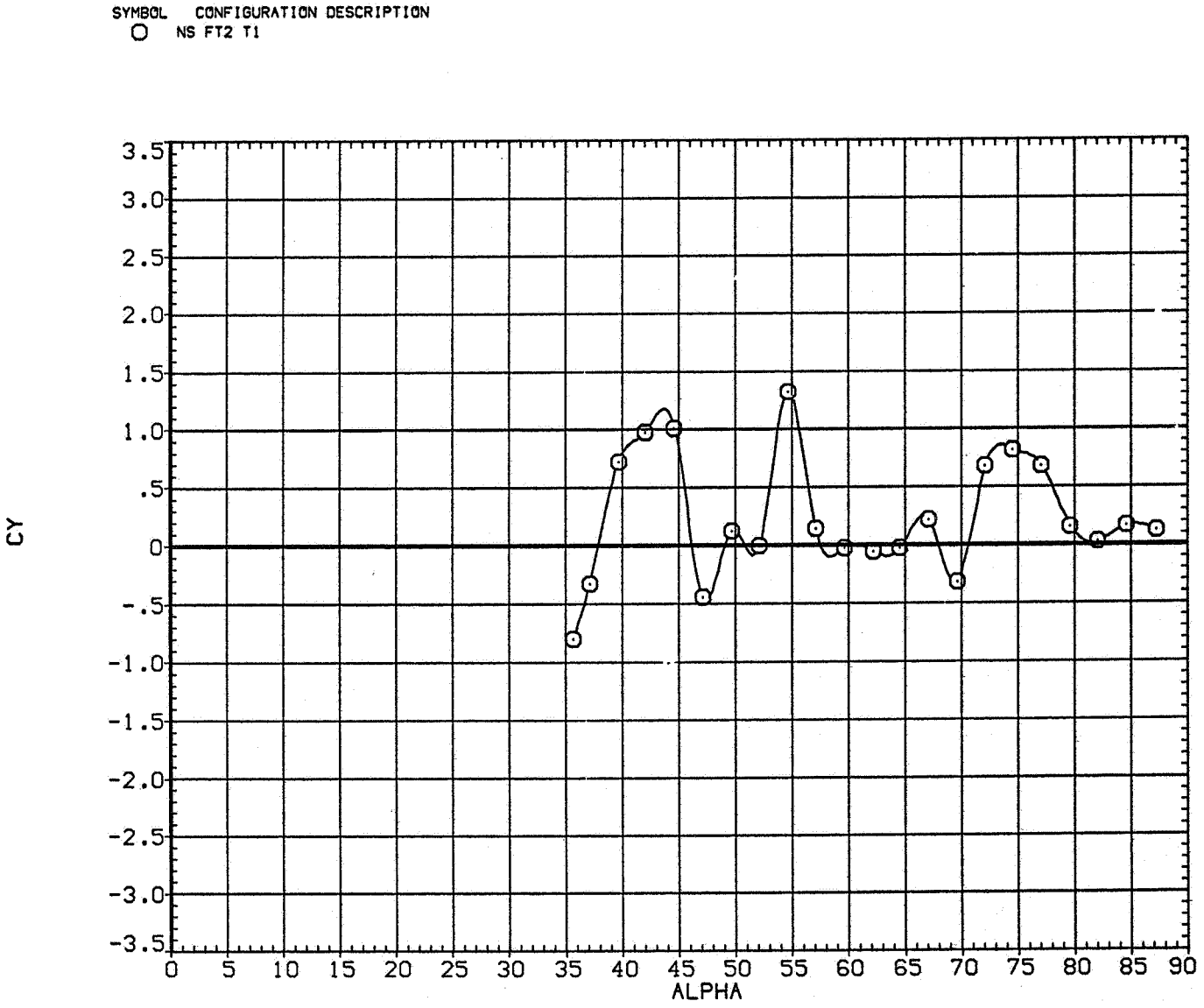

(a) C_Y vs α

Figure 10.– Effect of boundary-layer transition strips for the $\ell/d = 5$ tangent ogive, $M = 0.25$, $R_d = 0.8 \times 10^6$, $\Theta = \pm 15°$.

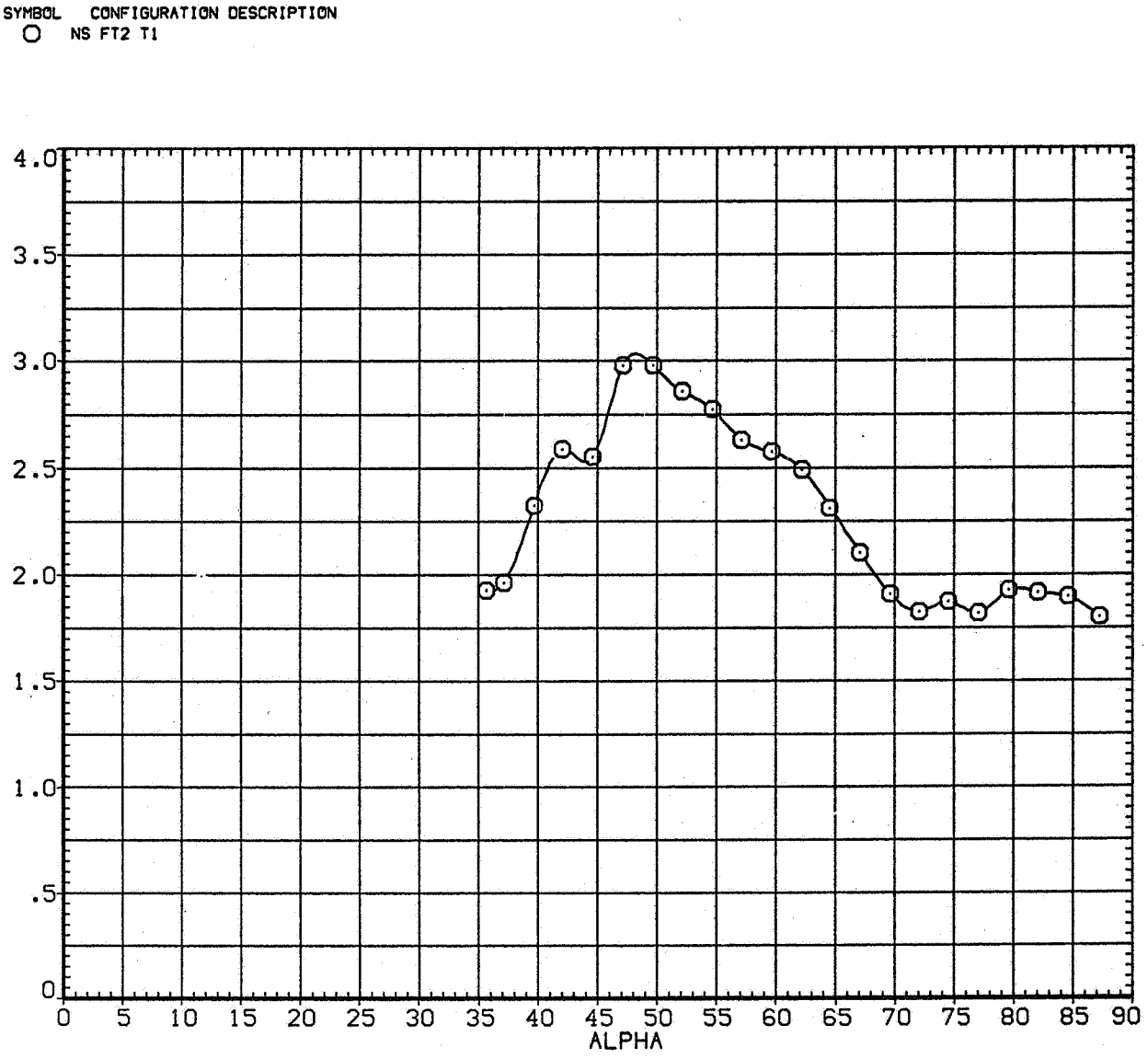

(b) C_N vs α

Figure 10.– Continued.

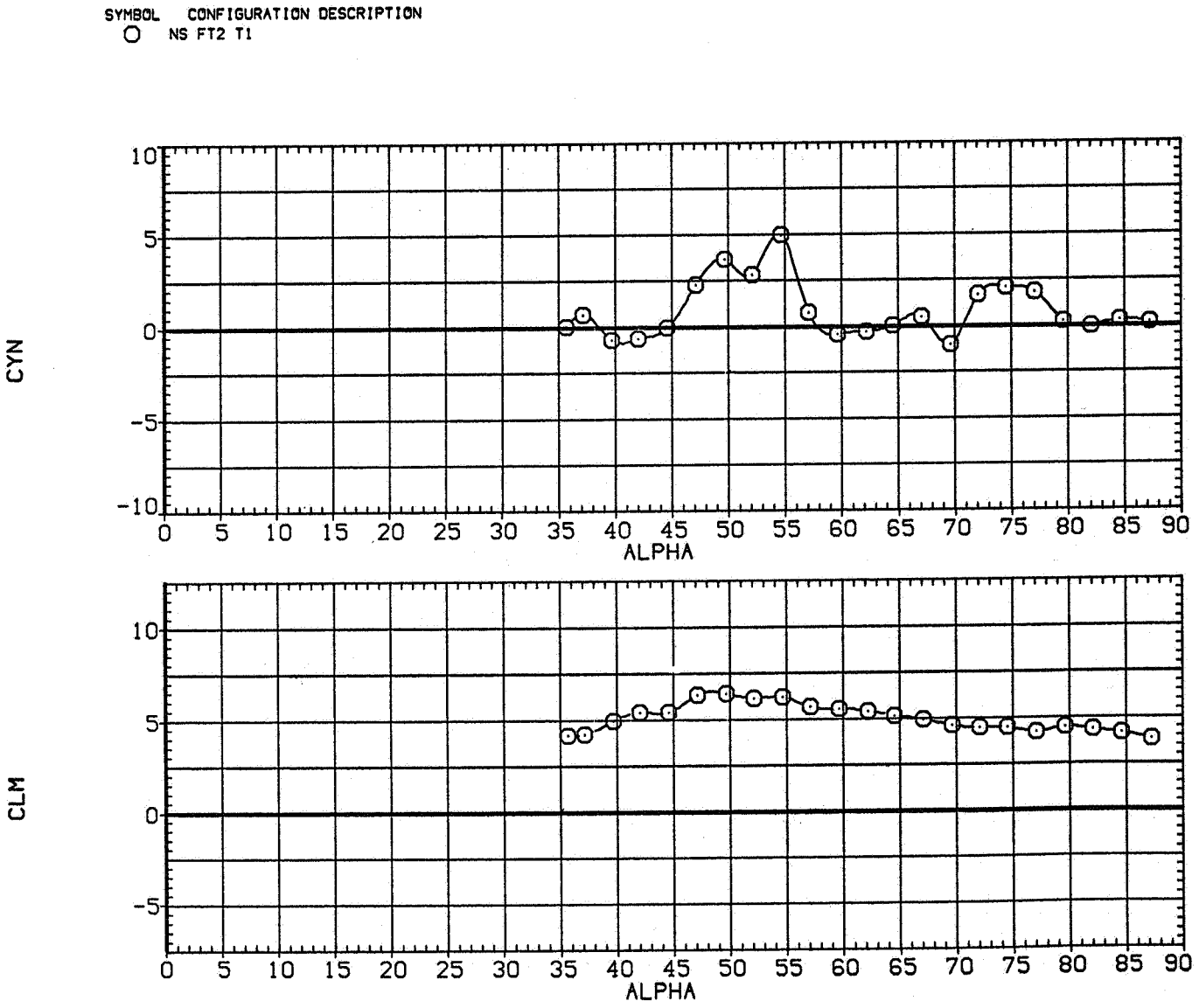

(c) C_n and C_m vs α

Figure 10.– Concluded.

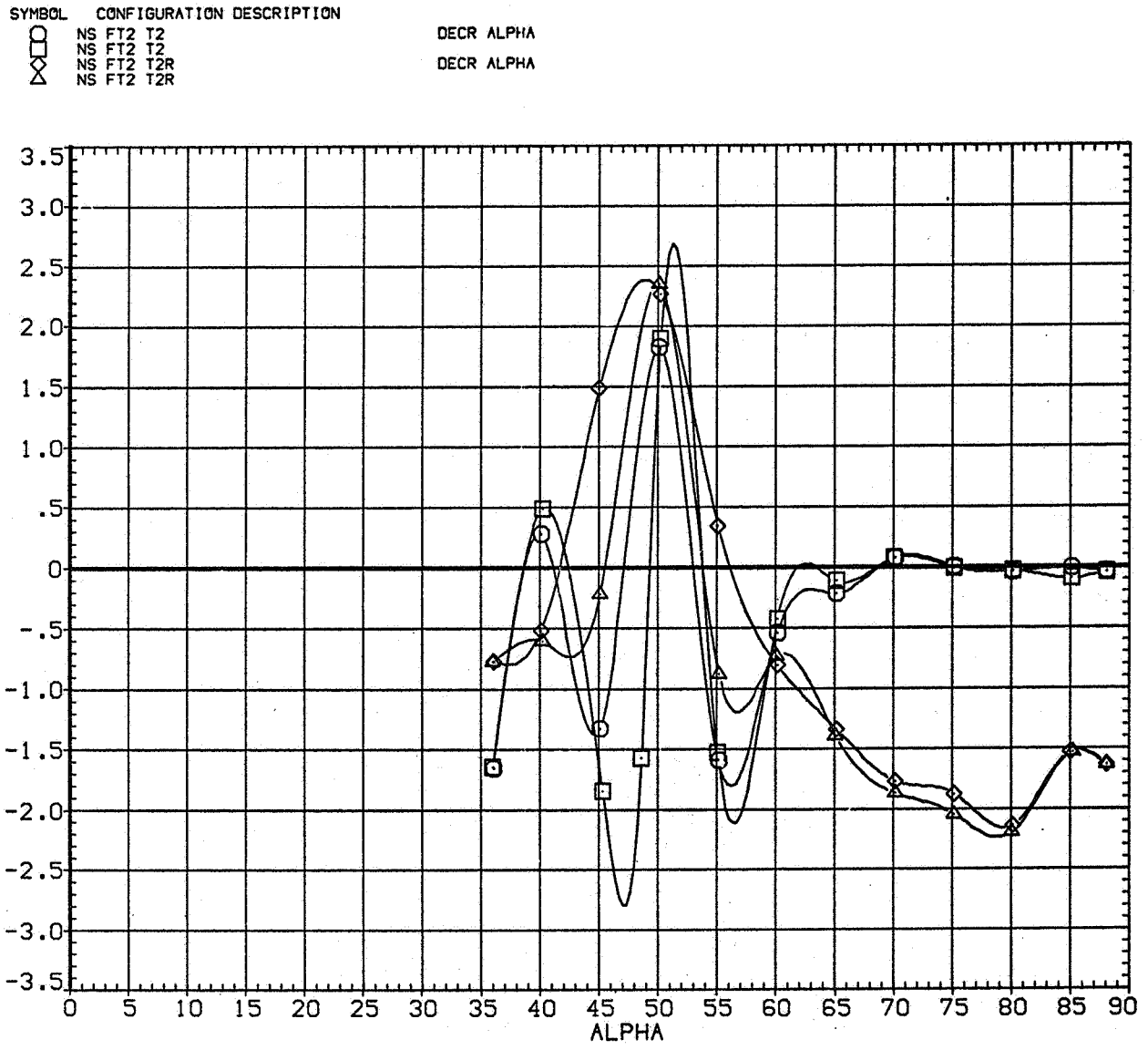

(a) C_Y vs α

Figure 11.– Effect of boundary-layer transition strips for the $\ell/d = 5$ tangent ogive, $M = 0.25$, $R_d = 0.8 \times 10^6$, $\Theta = \pm 30°$.

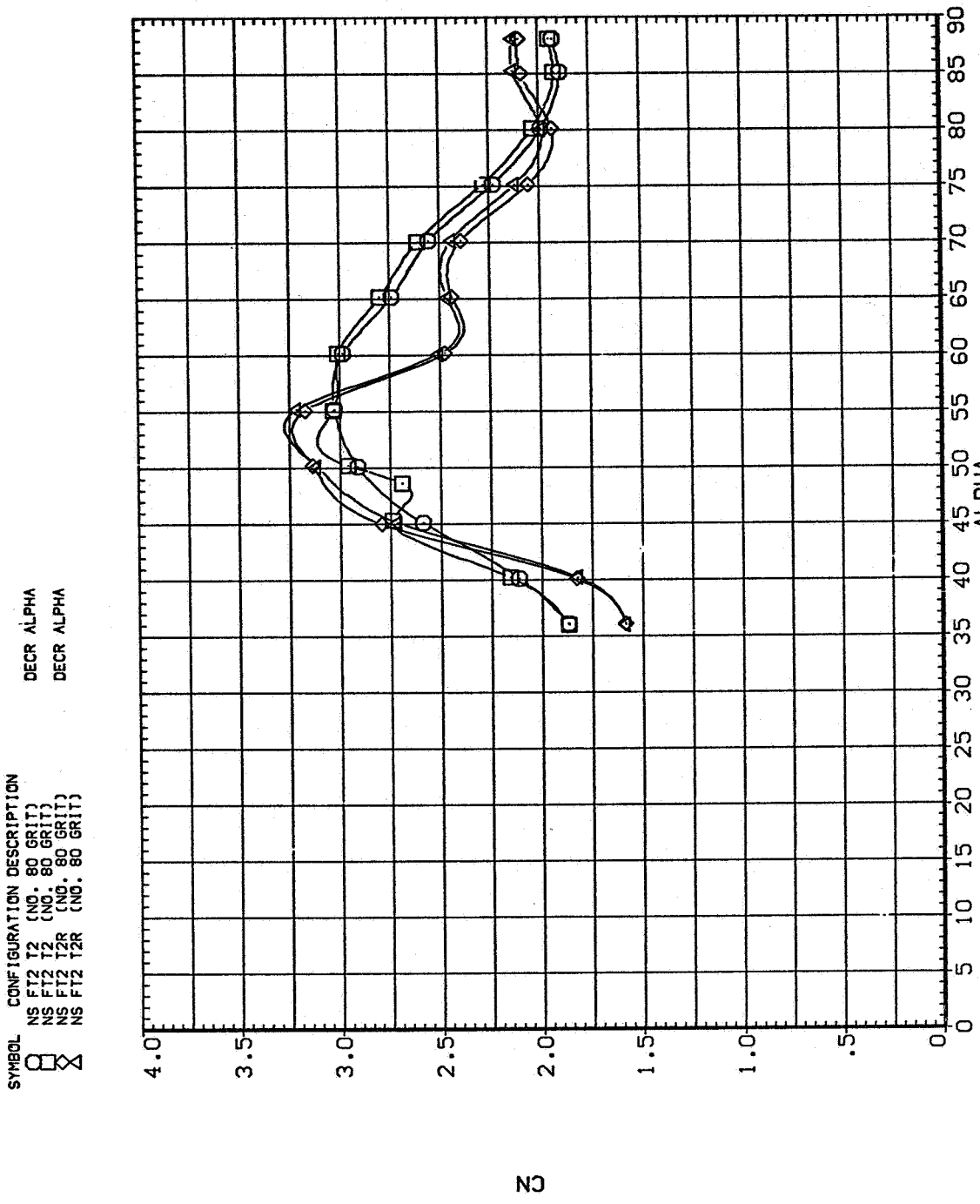

(b) C_N vs α

Figure 11.– Continued.

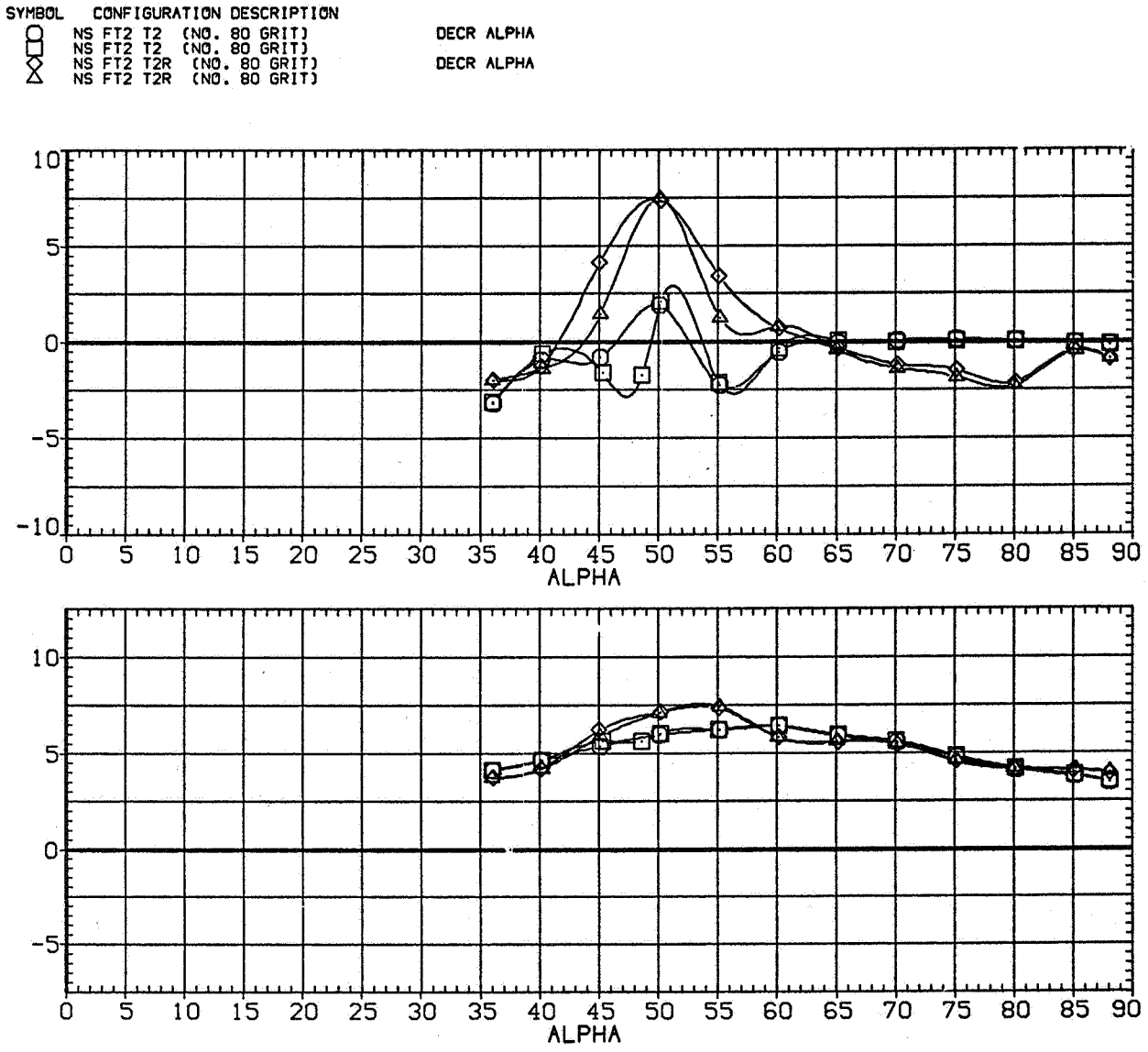

(c) C_n and C_m vs α

Figure 11.– Concluded.

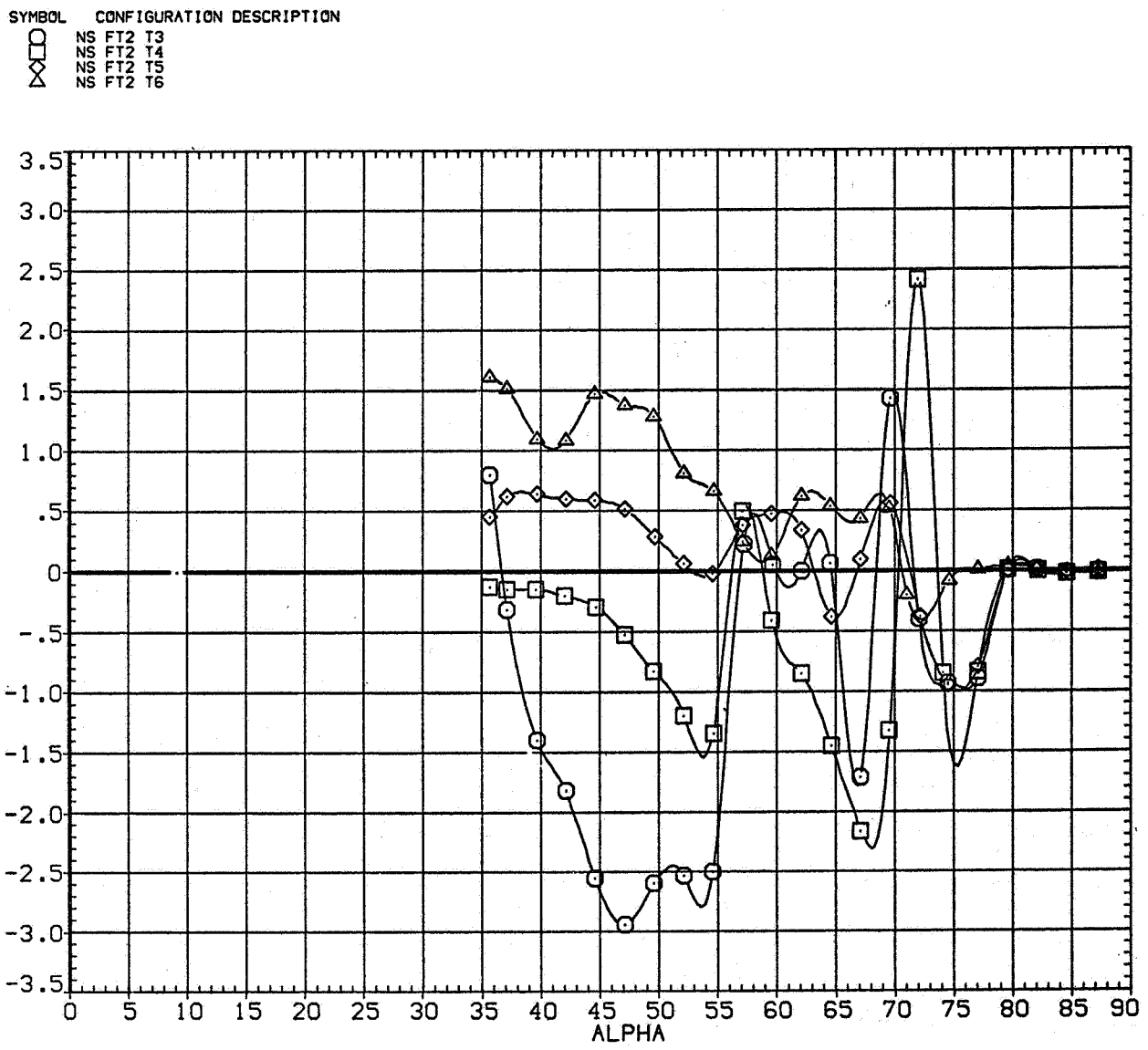

(a) C_Y vs α

Figure 12.– Effect of boundary-layer transition-strip ring around the forebody at various locations for the $\ell/d = 5$ tangent ogive, $M = 0.25$, $R_d = 0.8 \times 10^6$.

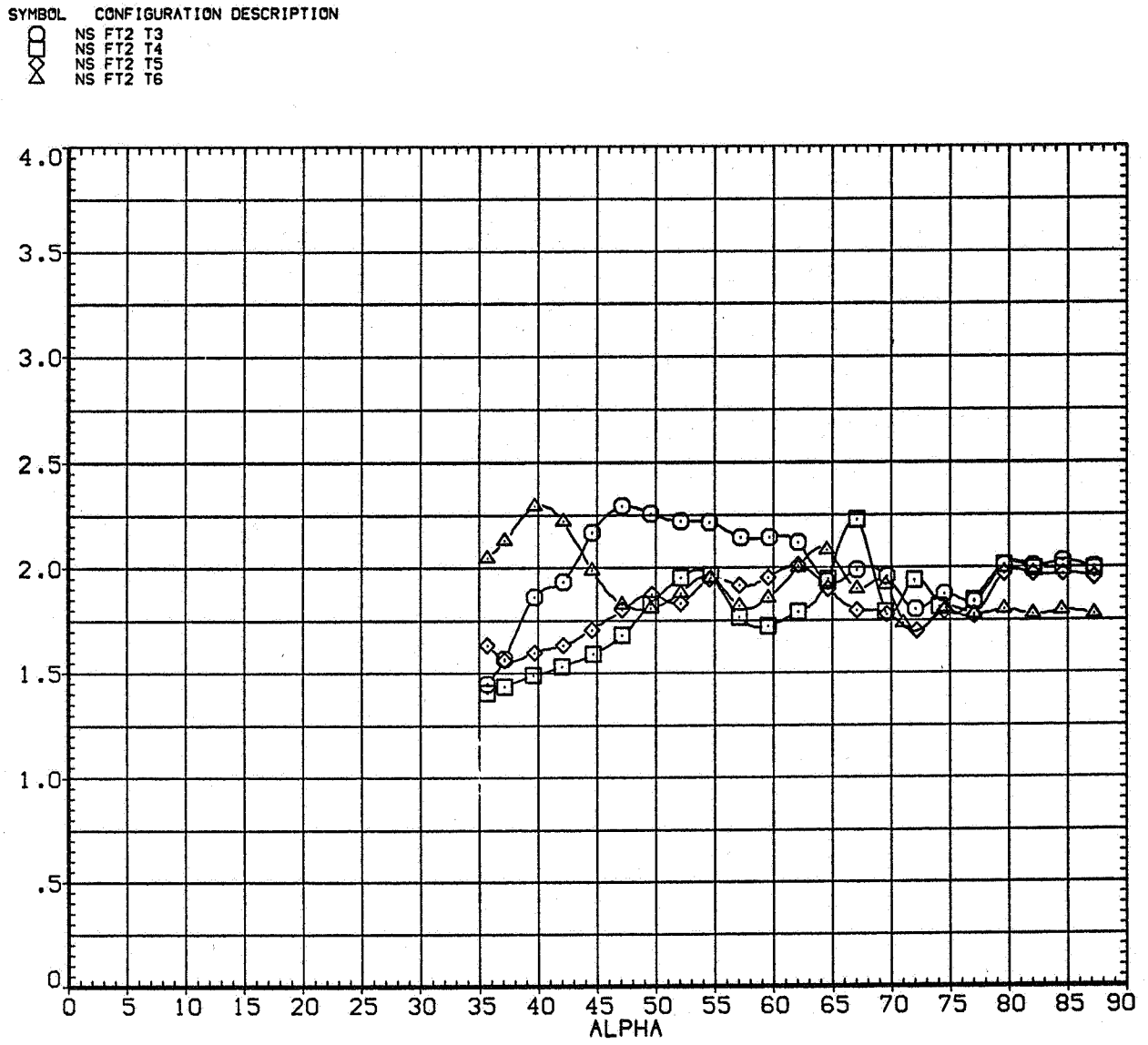

(b) C_N vs α

Figure 12.– Continued.

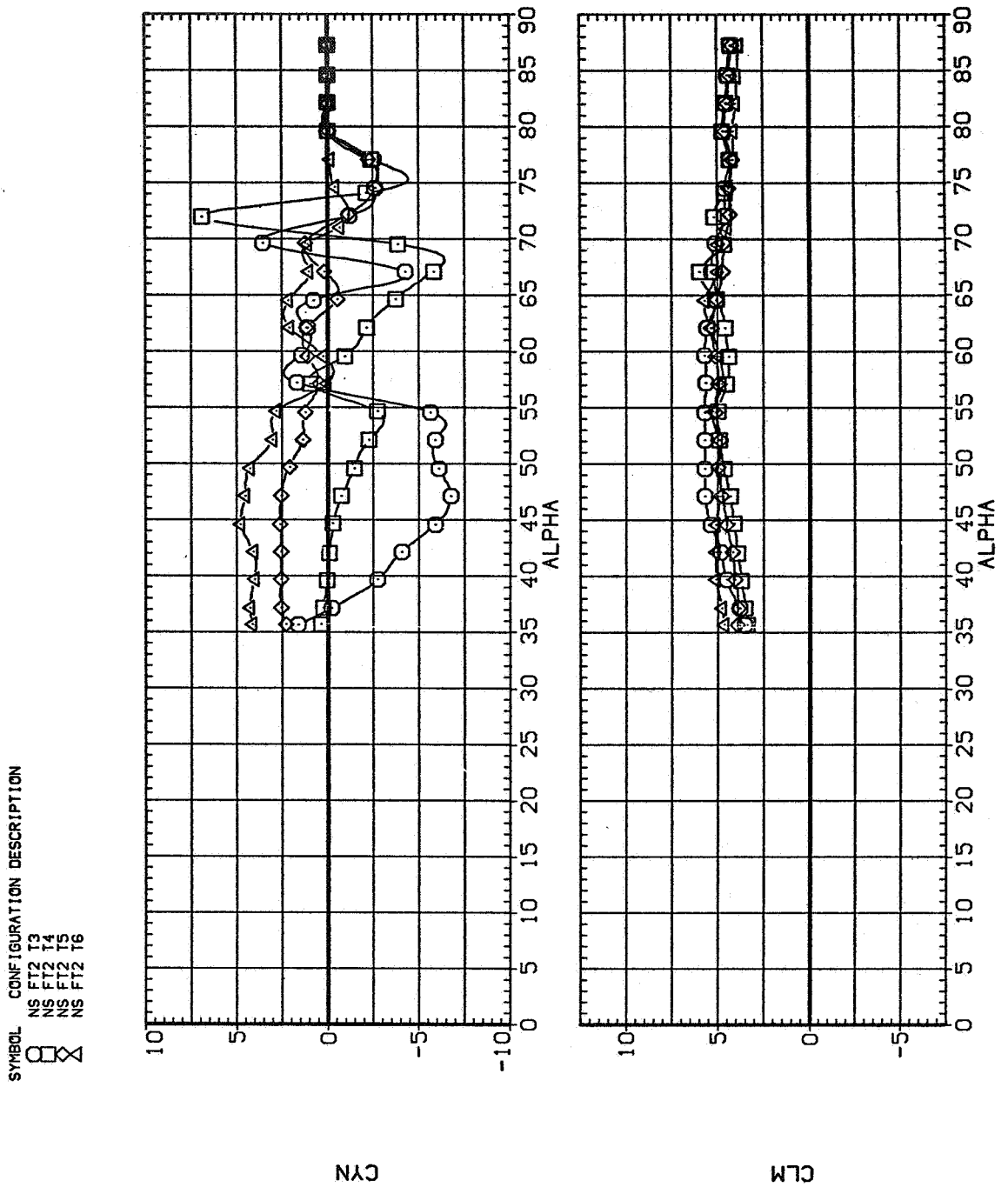

(c) C_n and C_m vs α

Figure 12.– Concluded.

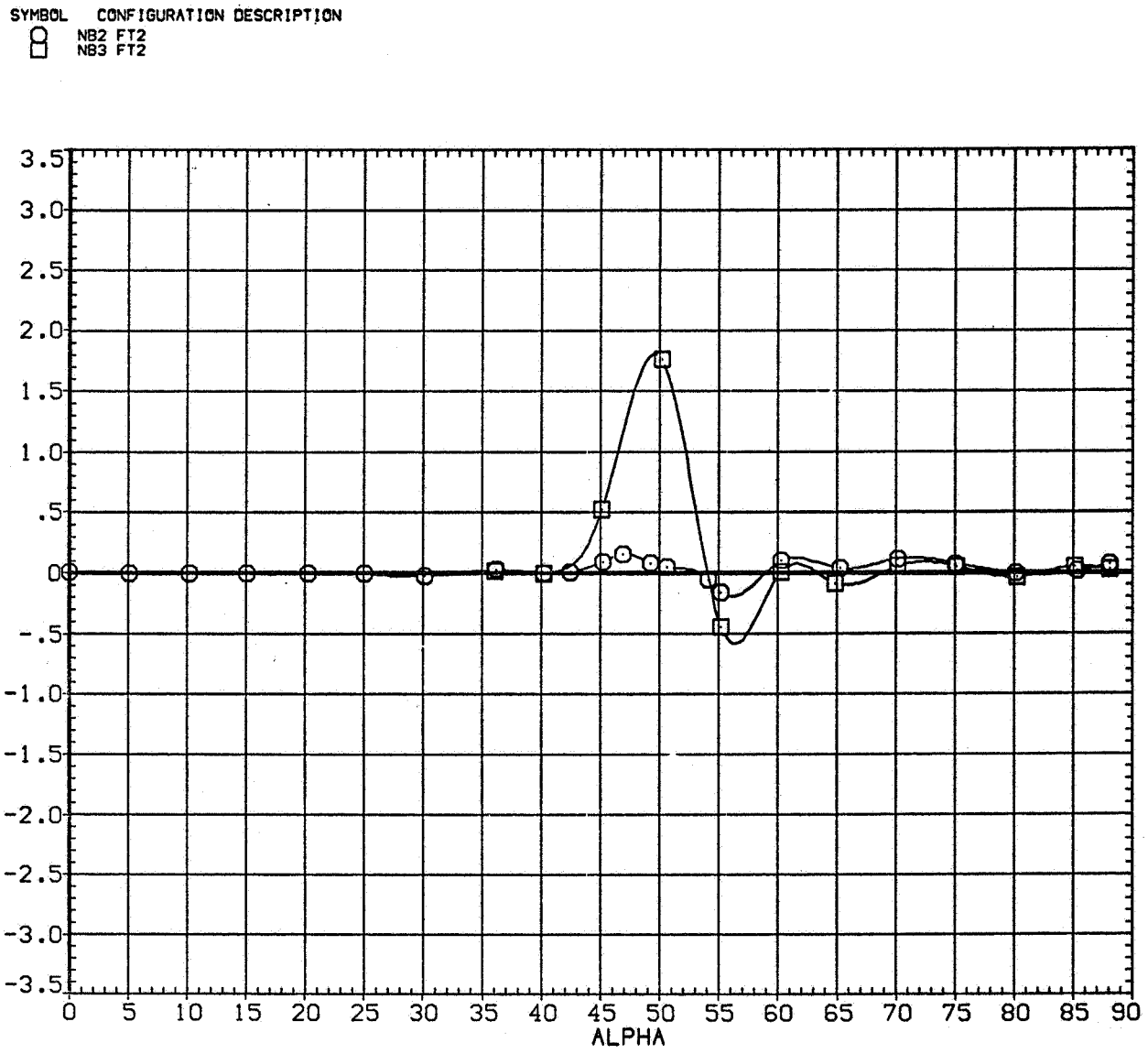

(a) C_Y vs α

Figure 13.– Effect of nose radius for the $\ell/d = 5$ tangent ogive, $M = 0.25$, $R_d = 0.8 \times 10^6$.

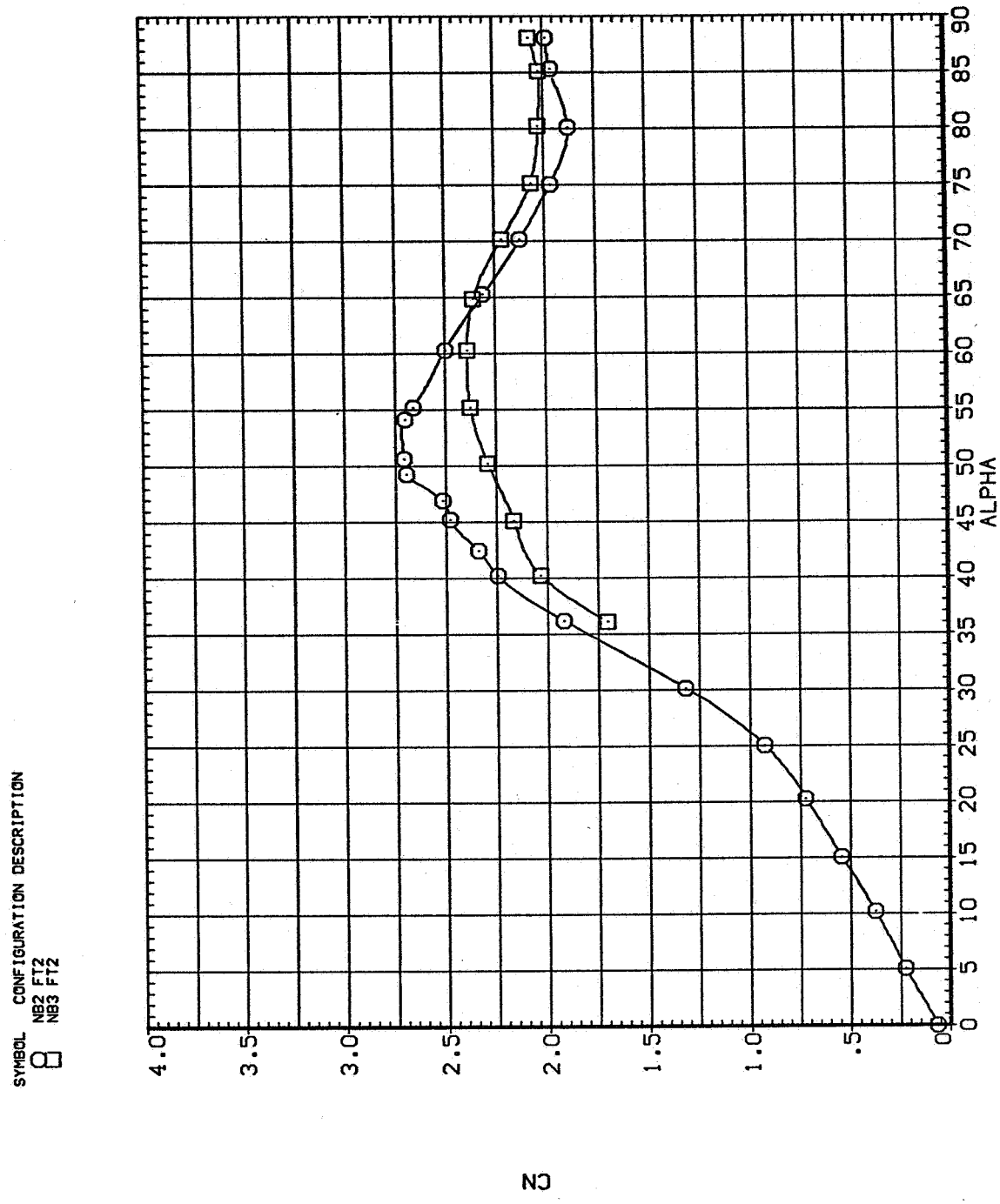

(b) C_N vs α

Figure 13.– Continued.

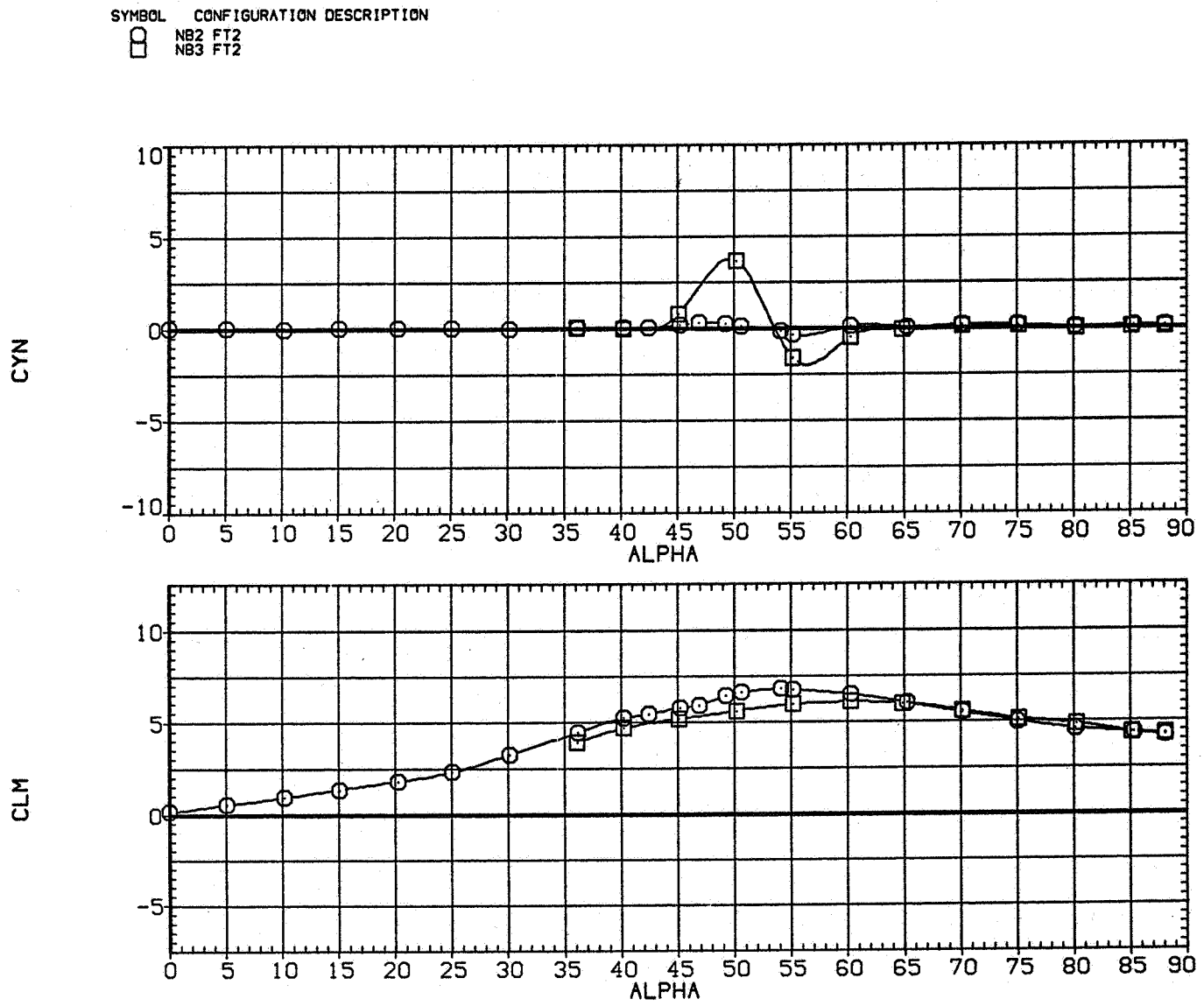

(c) C_n and C_m vs α

Figure 13.– Concluded.

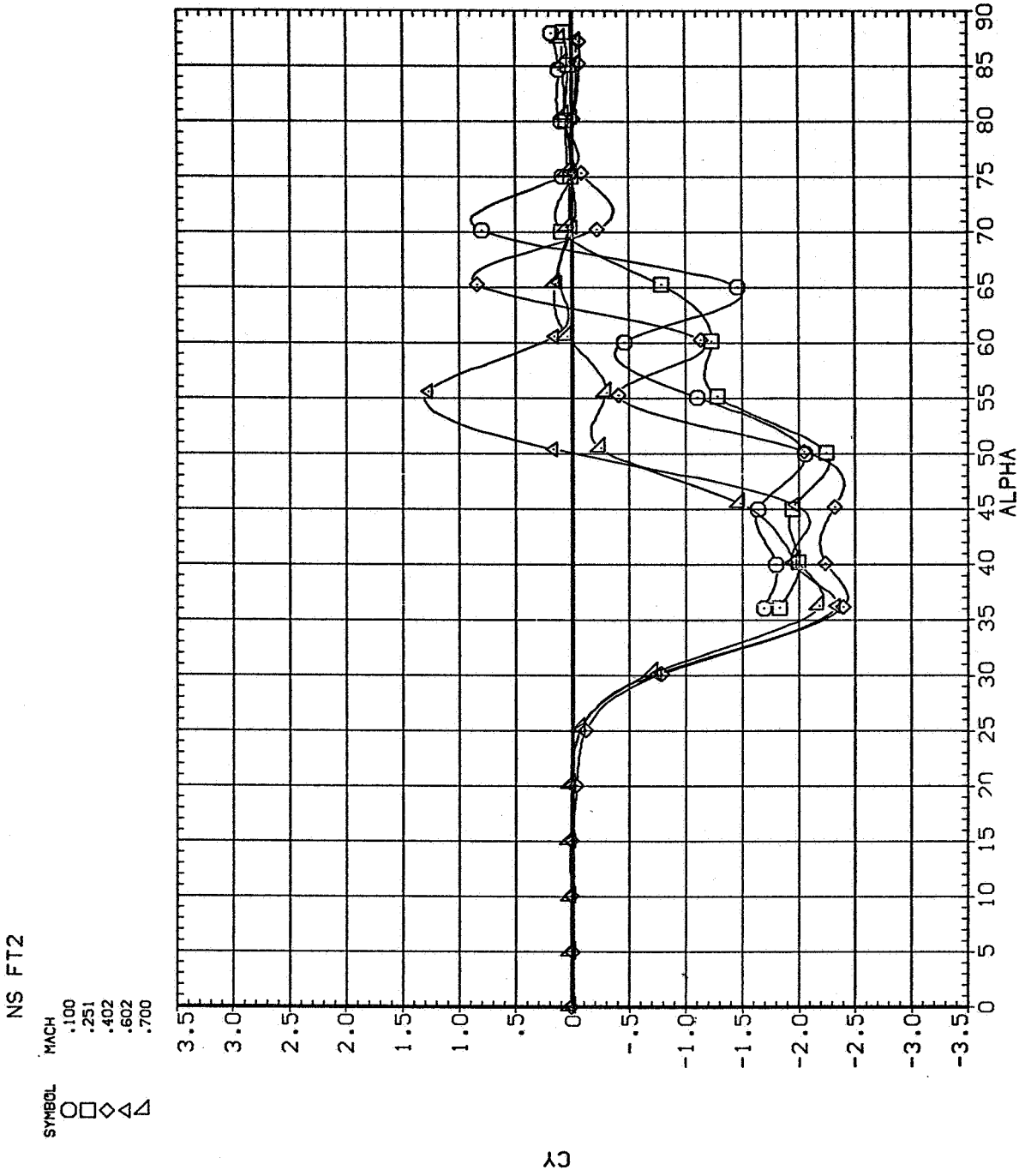

(a) C_Y vs α

Figure 14.– Effect of Mach number for the $\ell/d = 5$ tangent ogive, $R_d = 0.8 \times 10^6$.

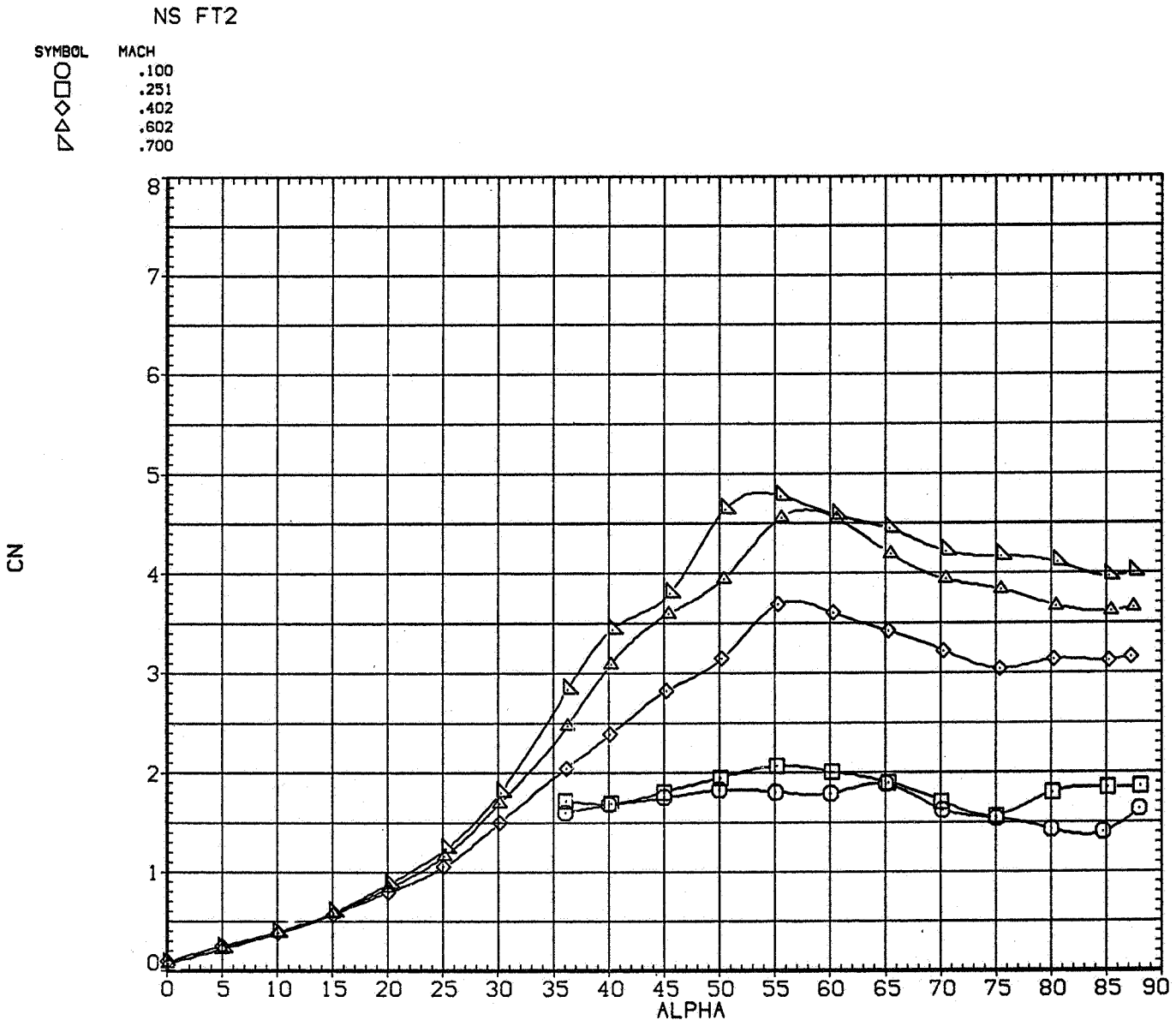

(b) C_N vs α

Figure 14.– Continued.

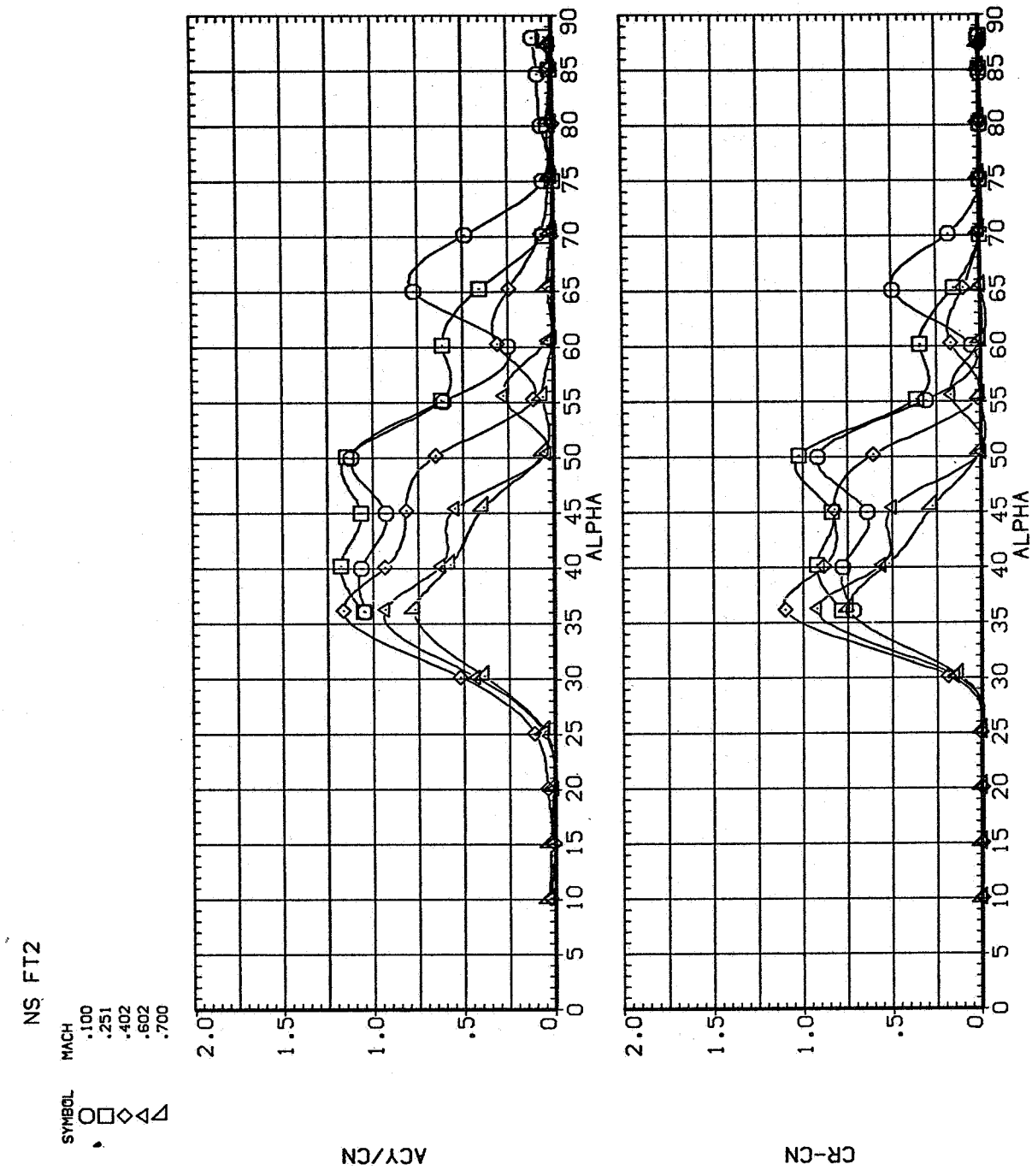

(c) $|C_Y|/|C_N$ and $C_R - C_N$ vs α

Figure 14.– Continued.

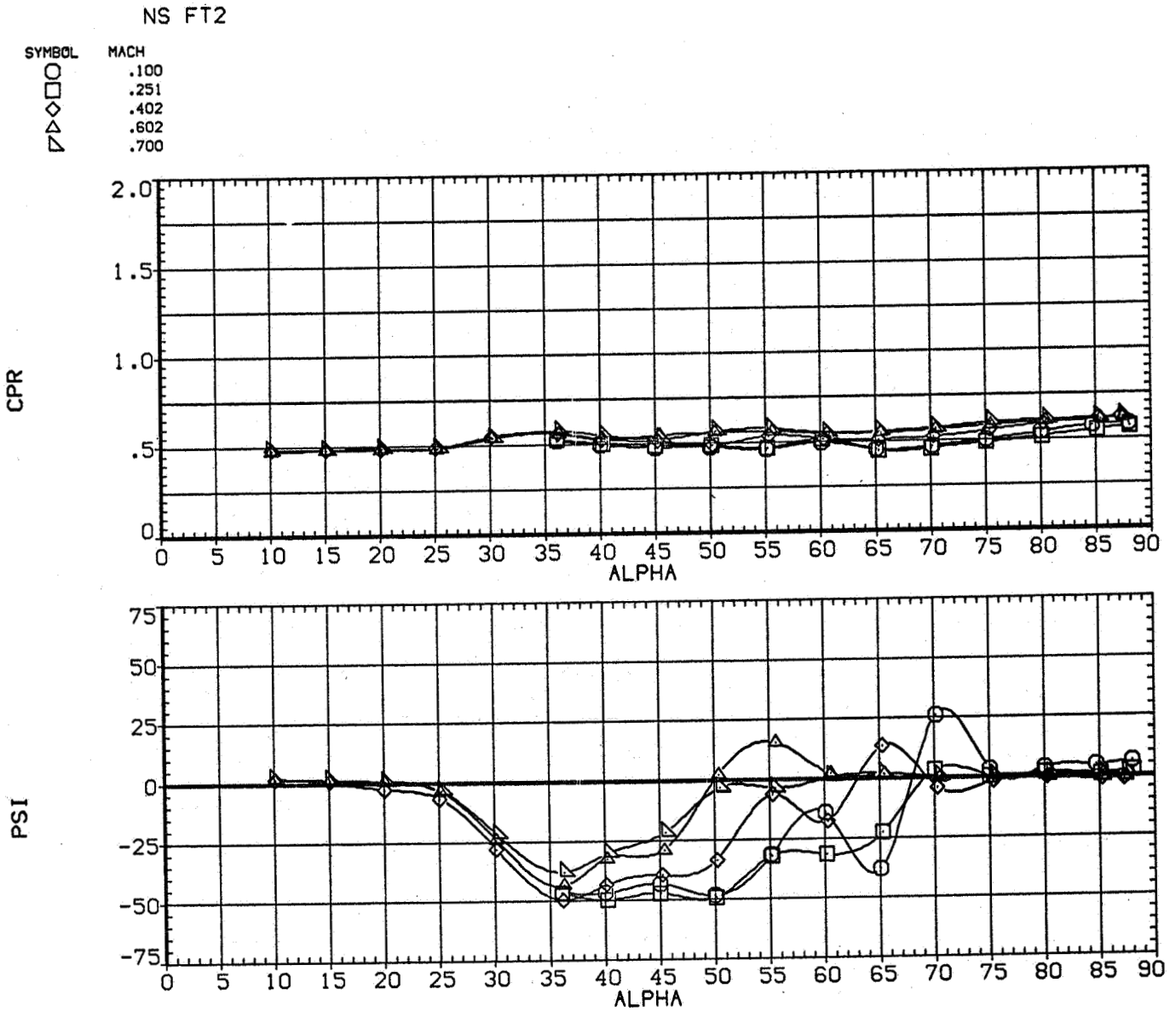

(d) CP_R and Ψ vs α

Figure 14.– Continued.

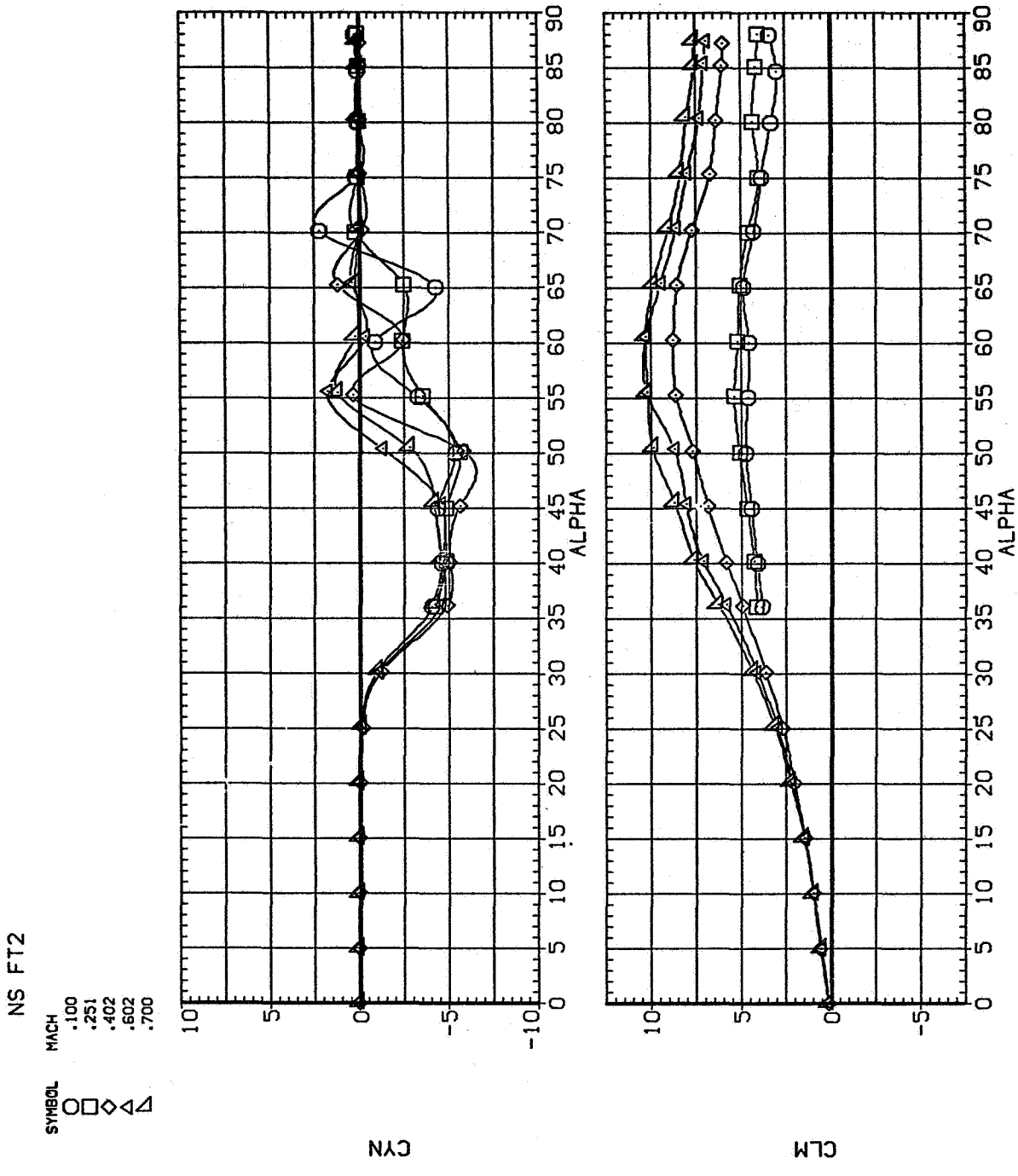

(e) C_n and C_m vs α

Figure 14.– Continued.

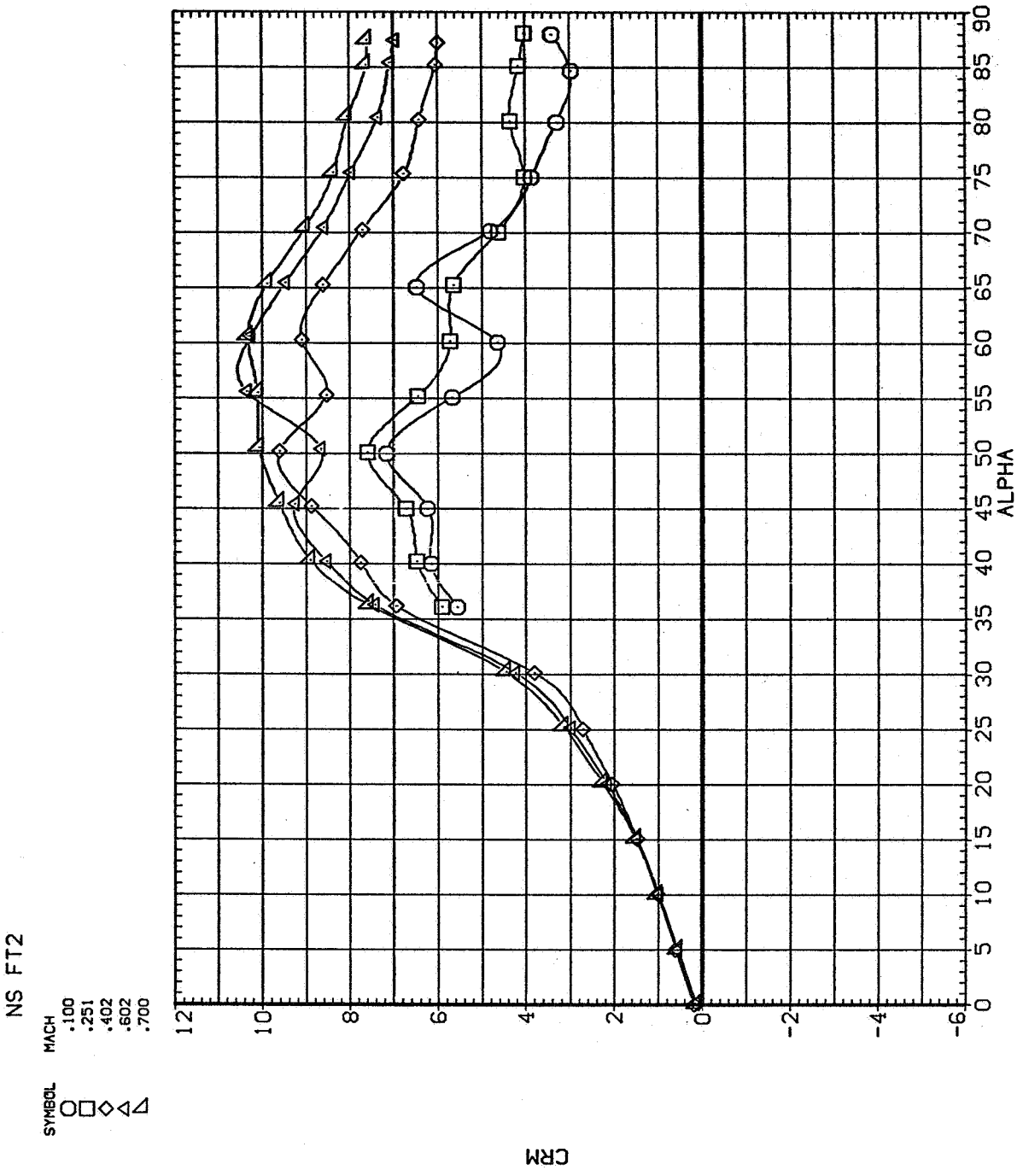

(f) $C_{m,R}$ vs α

Figure 14.– Continued.

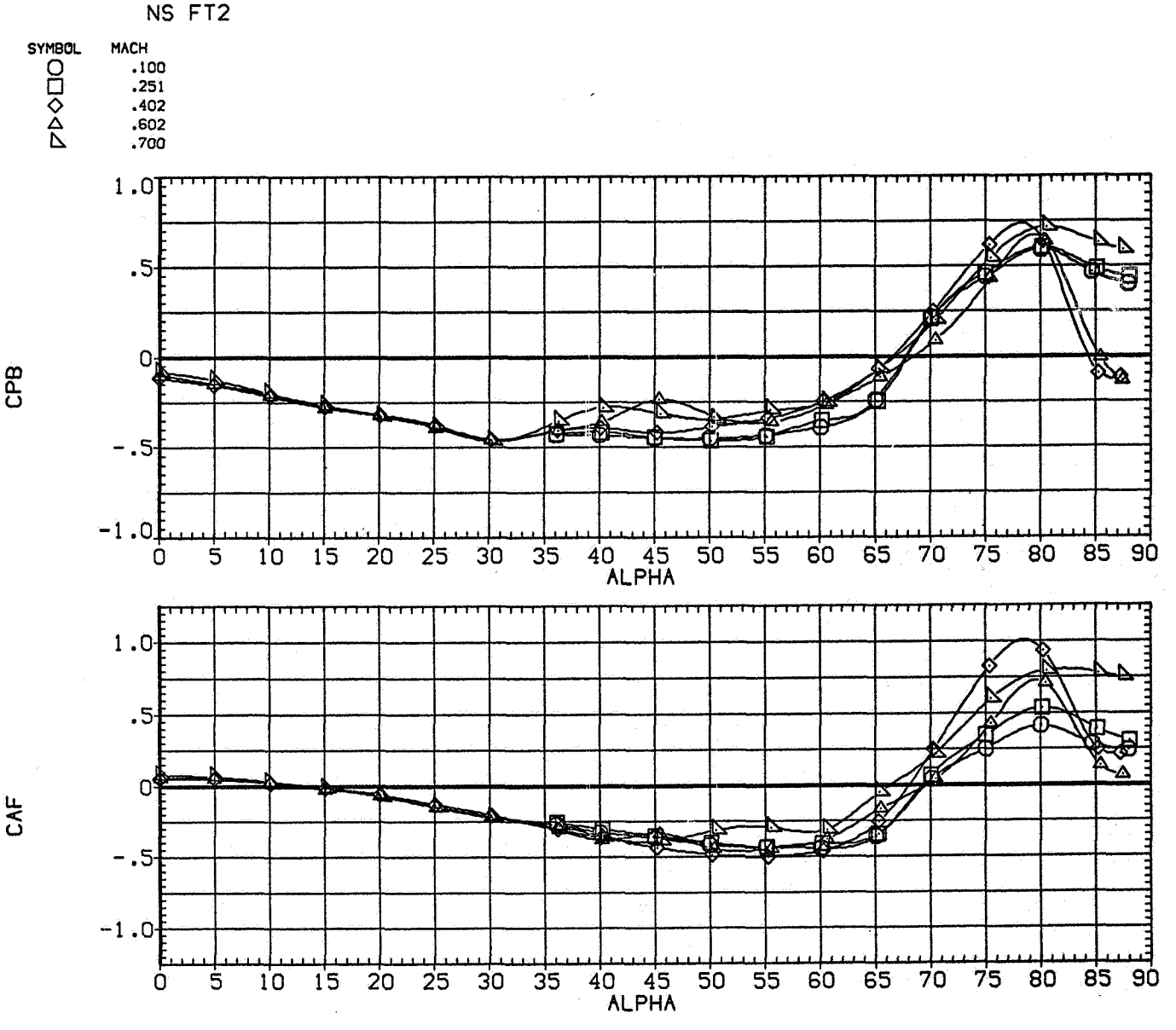

(g) $C_{p,b}$ and C_{AF} vs α

Figure 14.– Concluded.

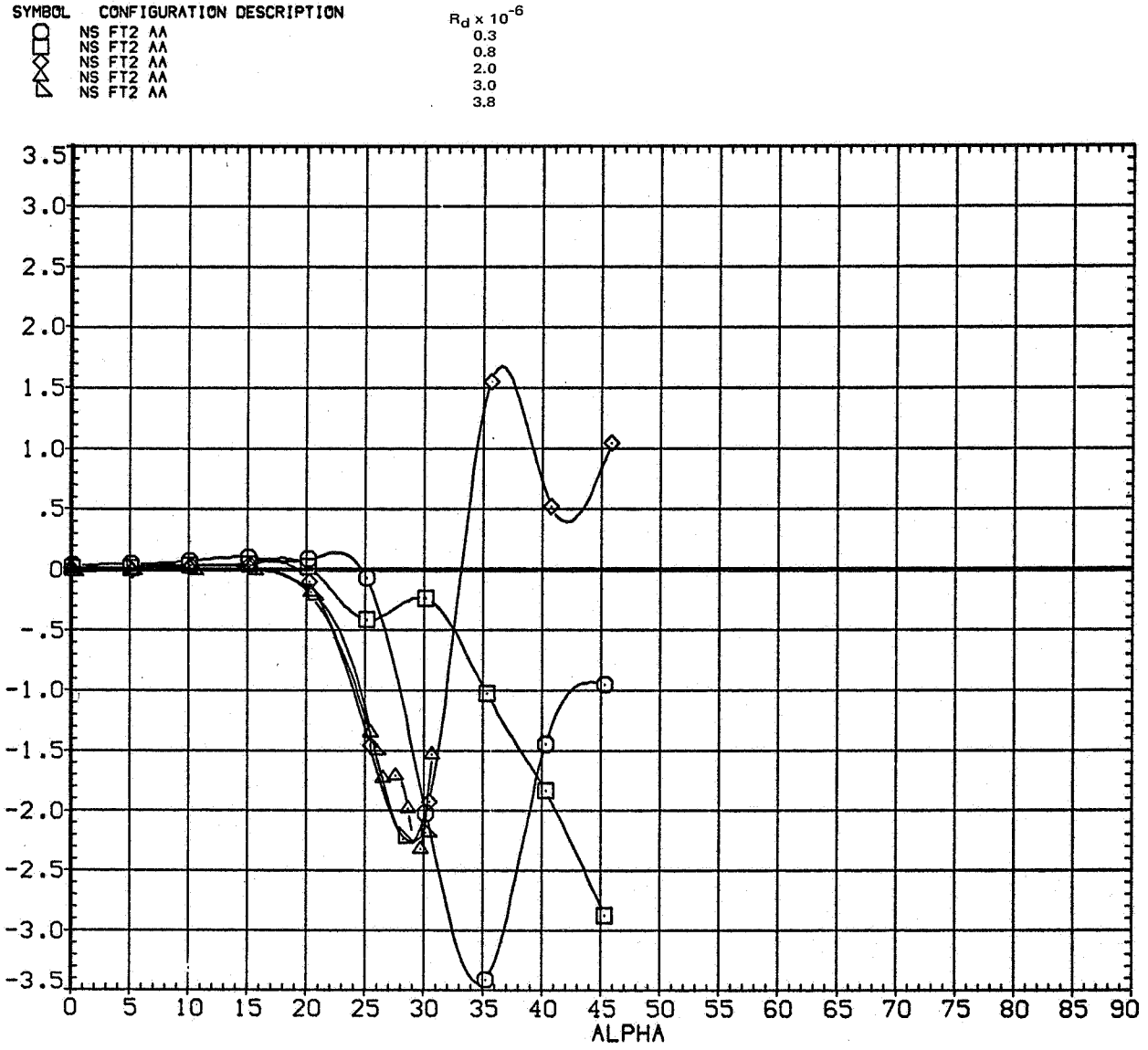

(a) C_Y vs α

Figure 15.– Effect of Reynolds number for the $\ell/d = 5$ tangent ogive with afterbody, $M = 0.25$.

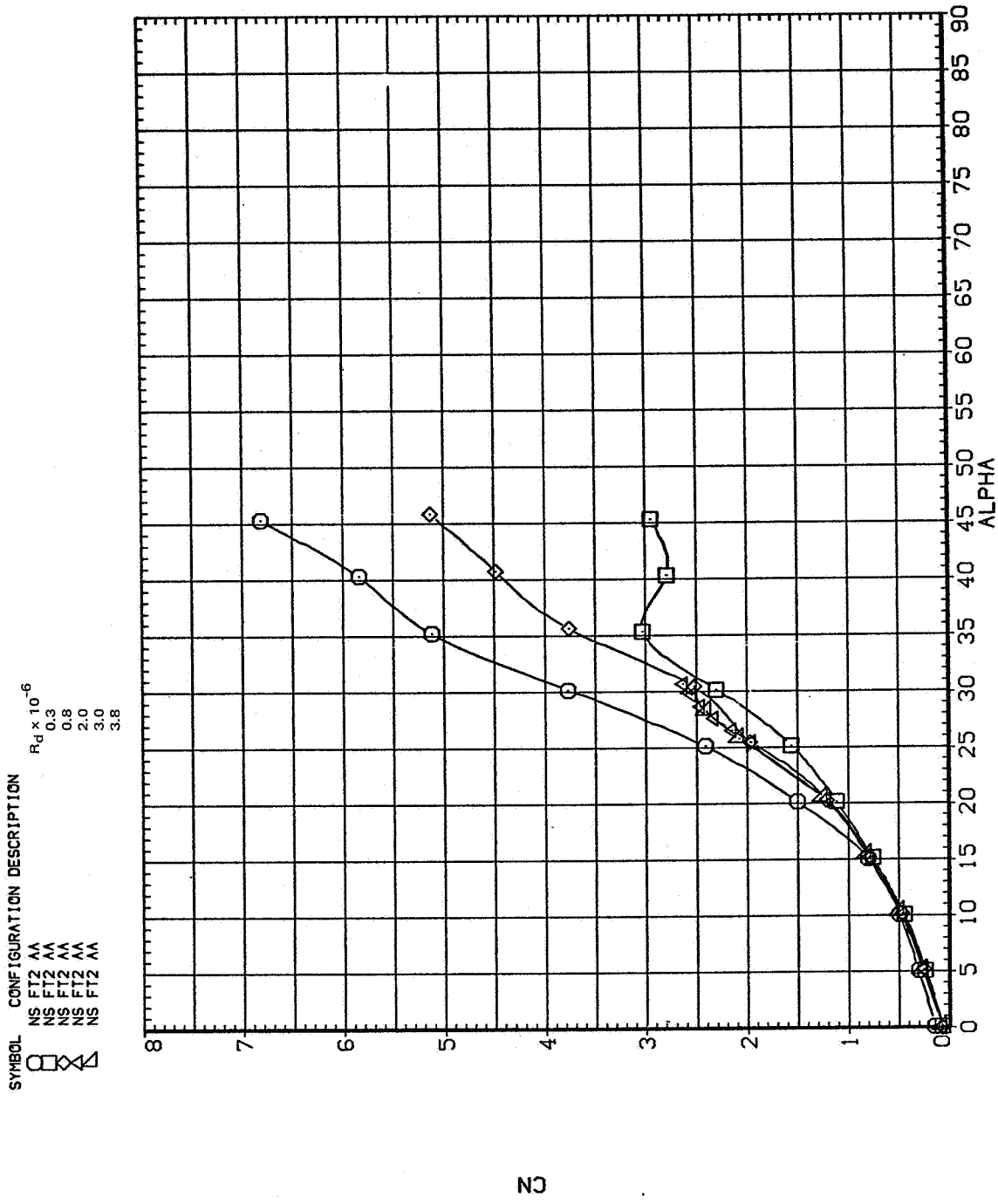

(b) C_N vs α

Figure 15.– Continued.

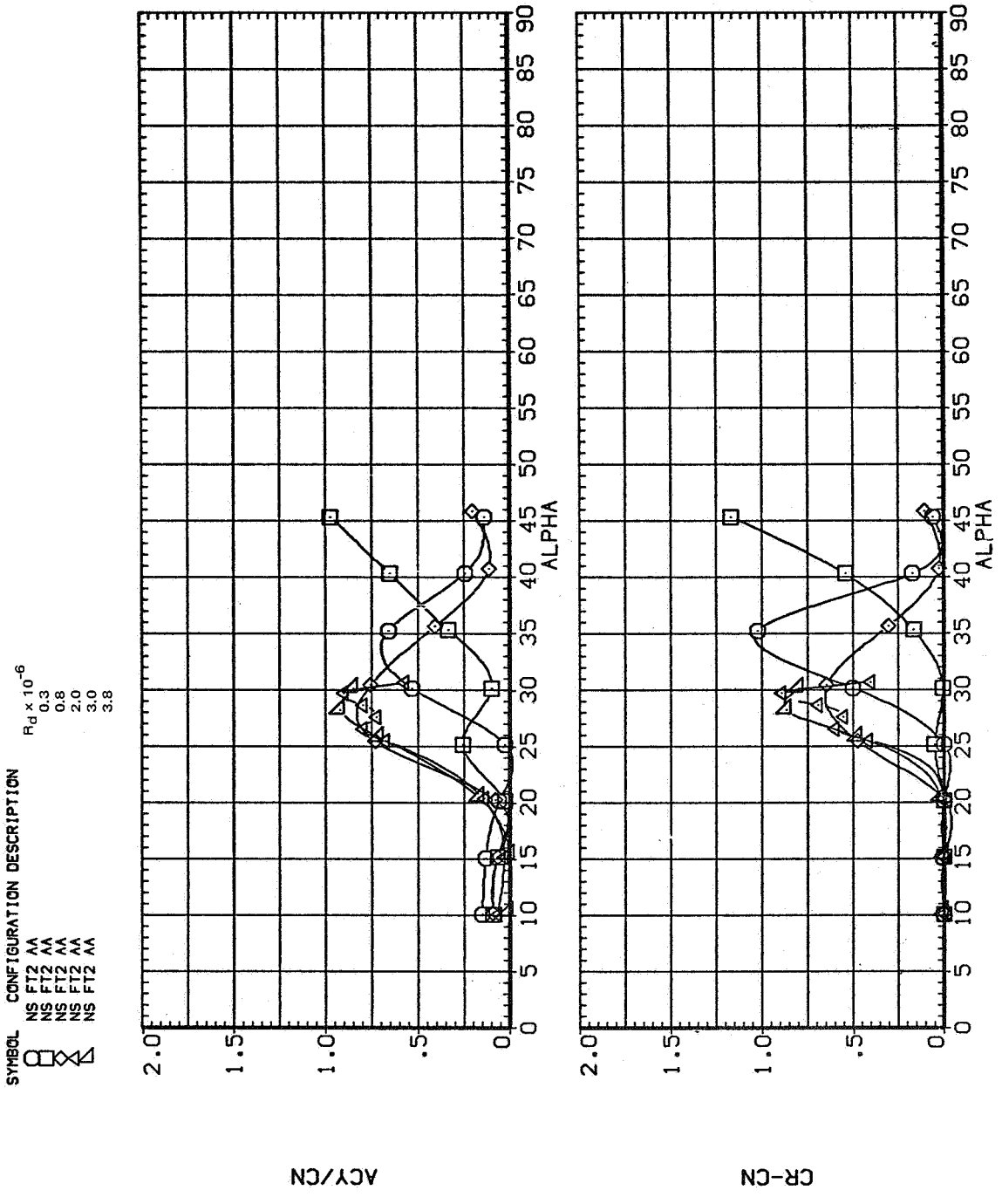

(c) $|C_Y|/|C_N|$ and $C_R - C_N$ vs α

Figure 15.– Continued.

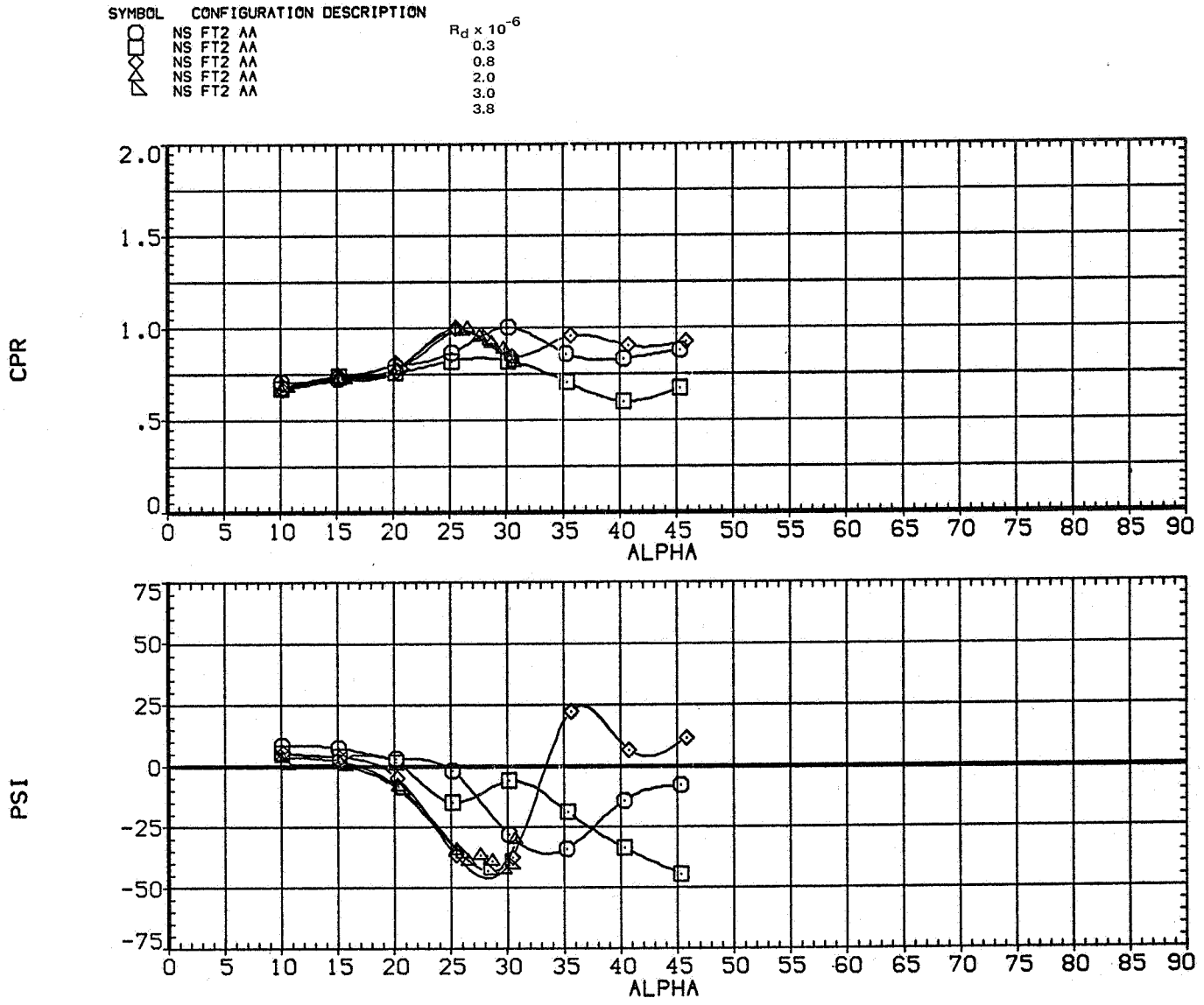

(d) CP_R and Ψ vs α

Figure 15.– Continued.

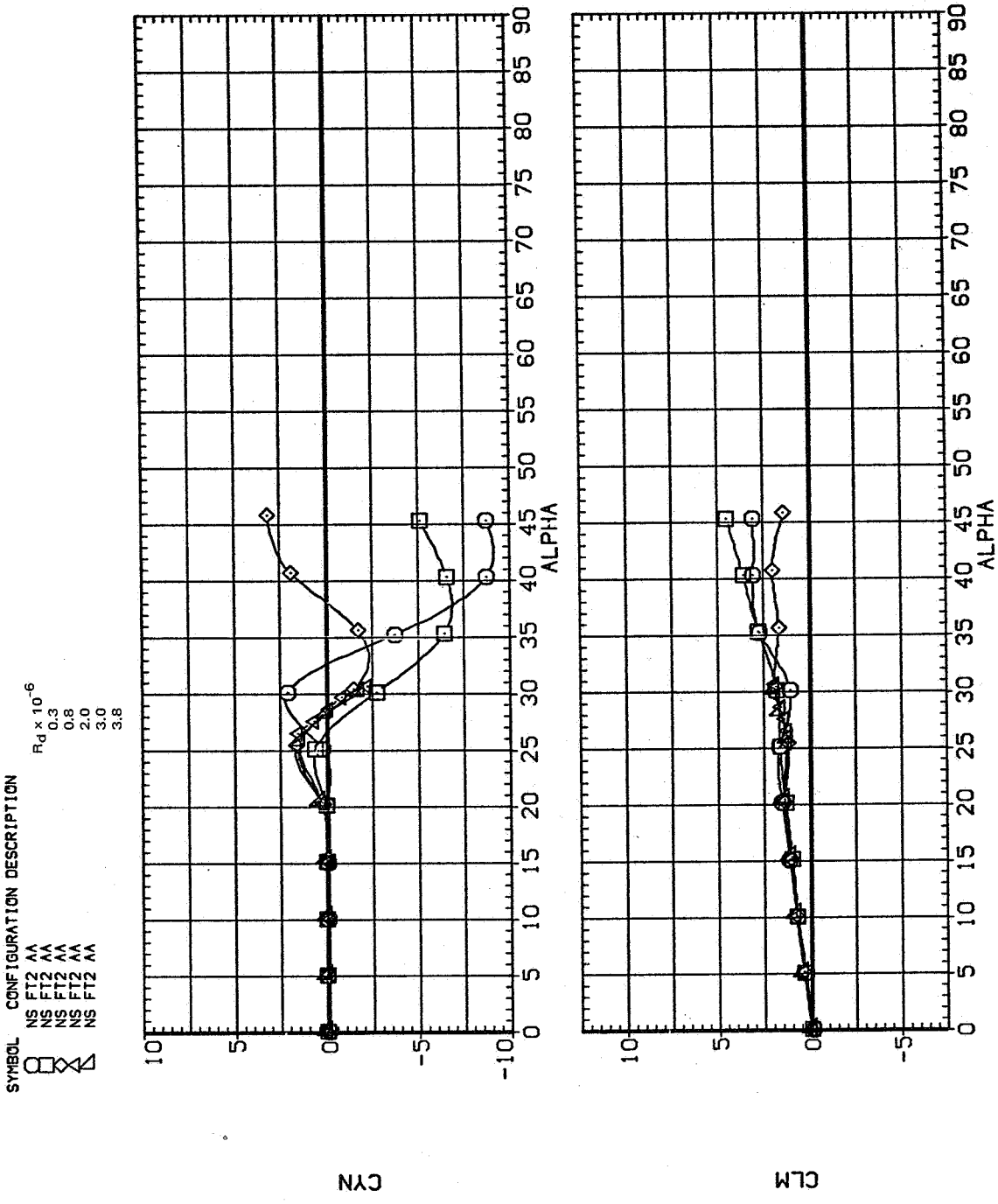

(e) C_n and C_m vs α

Figure 15.– Continued.

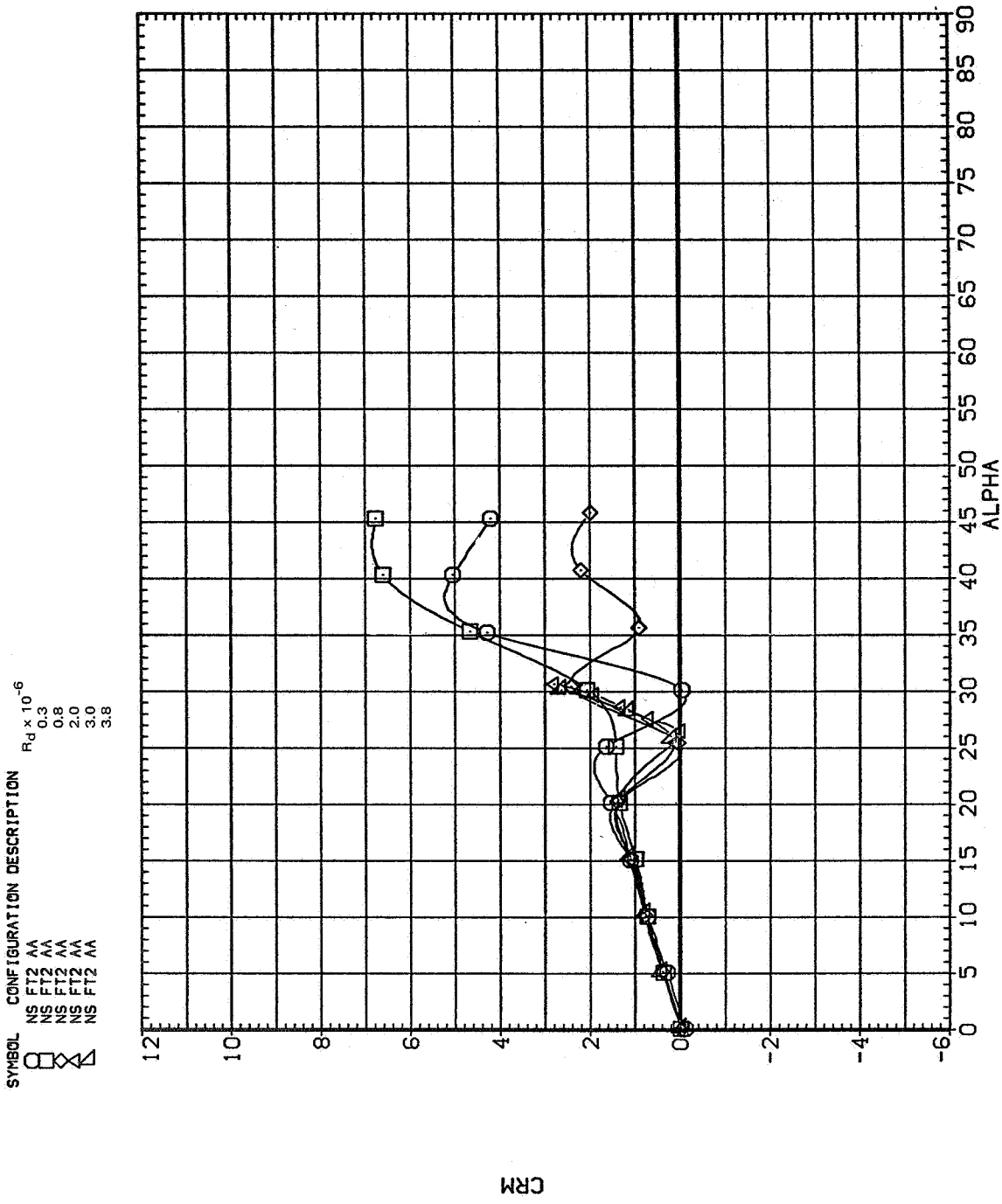

(f) $C_{m,R}$ vs α

Figure 15.– Continued.

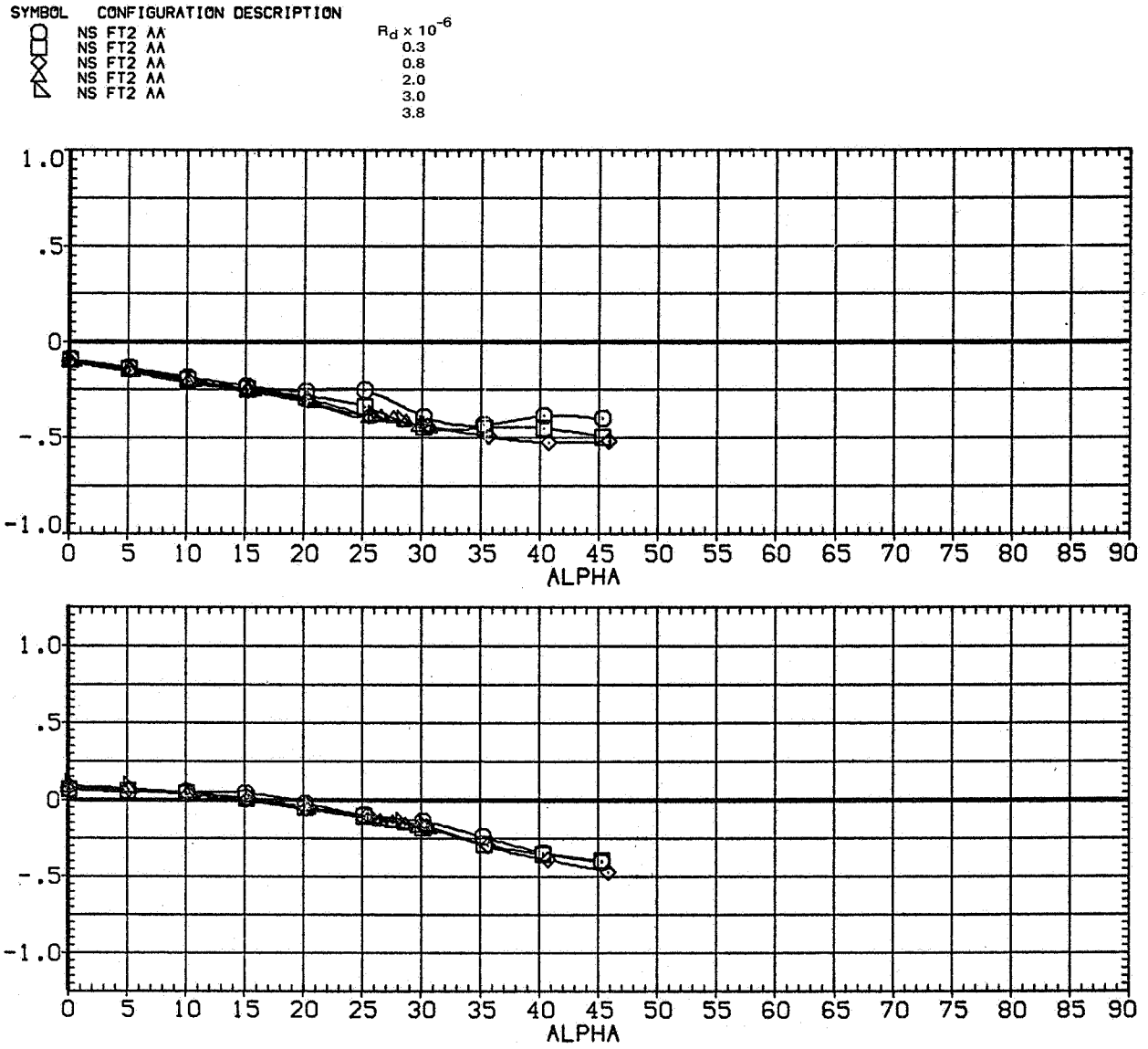

(g) $C_{p,b}$ and C_{AF} vs α

Figure 15.– Concluded.

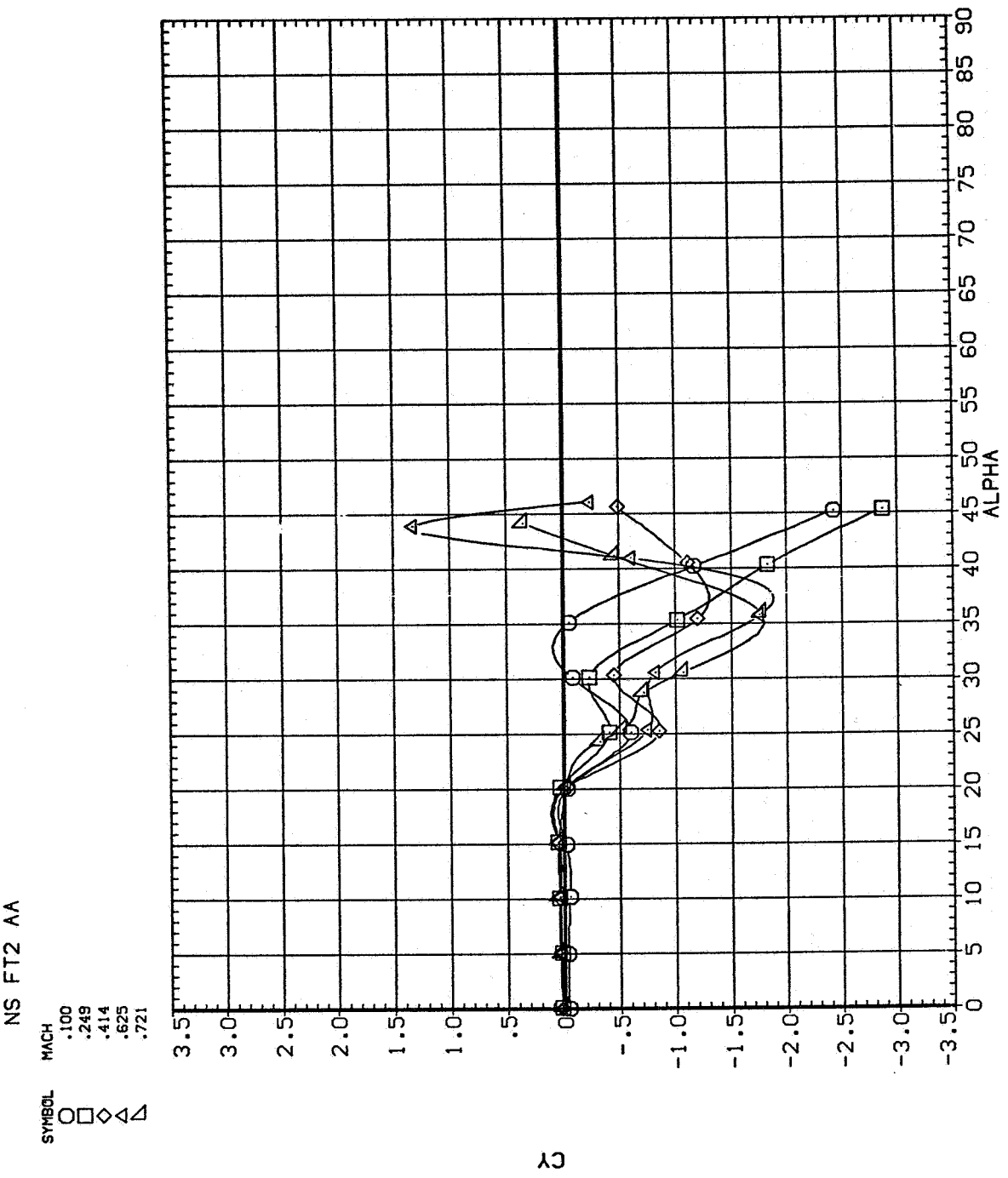

(a) C_Y vs α

Figure 16.– Effect of Mach number for the $\ell/d = 5$ tangent ogive with afterbody, $R_d = 0.8 \times 10^6$.

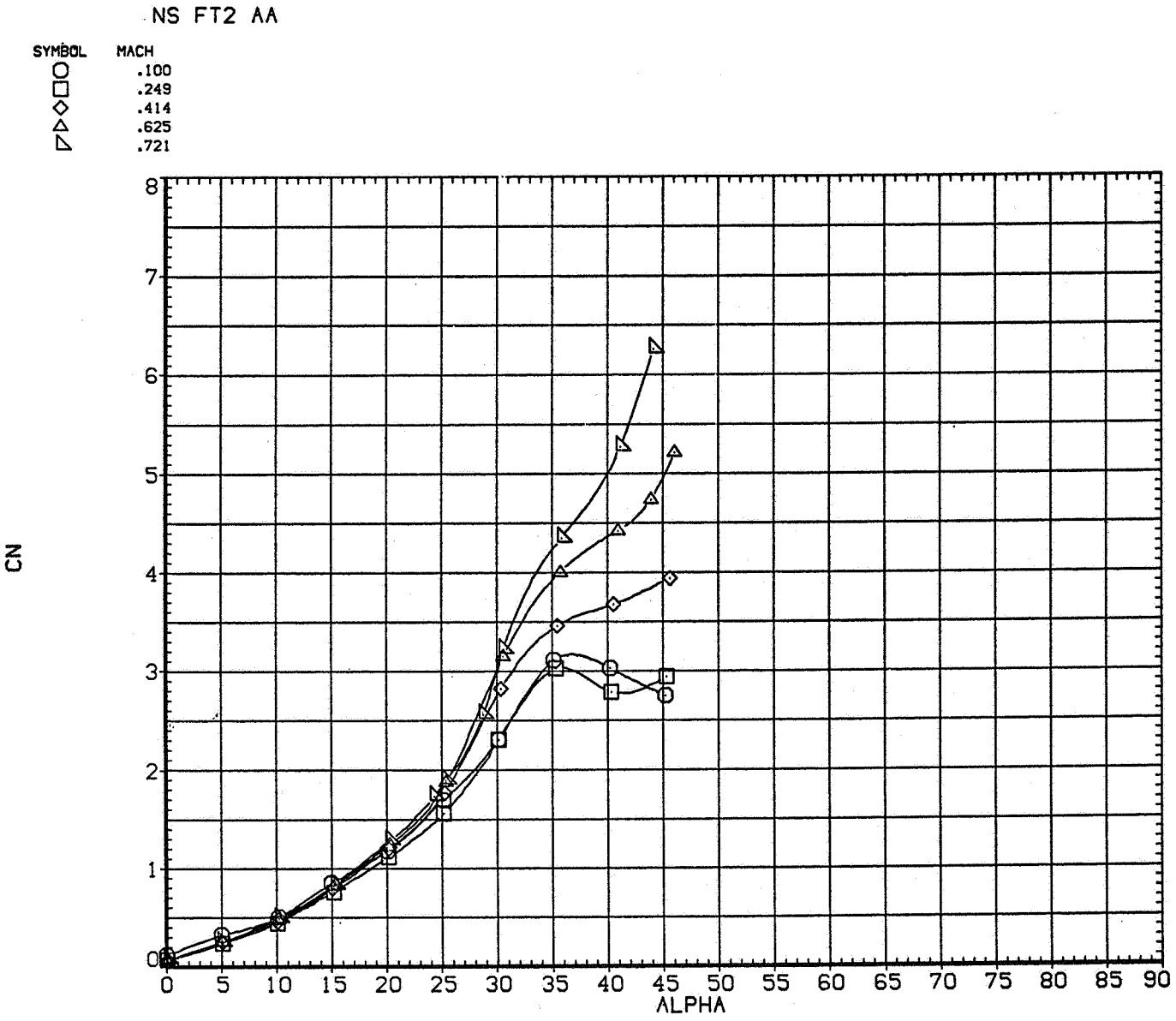

(b) C_N vs α

Figure 16.– Continued.

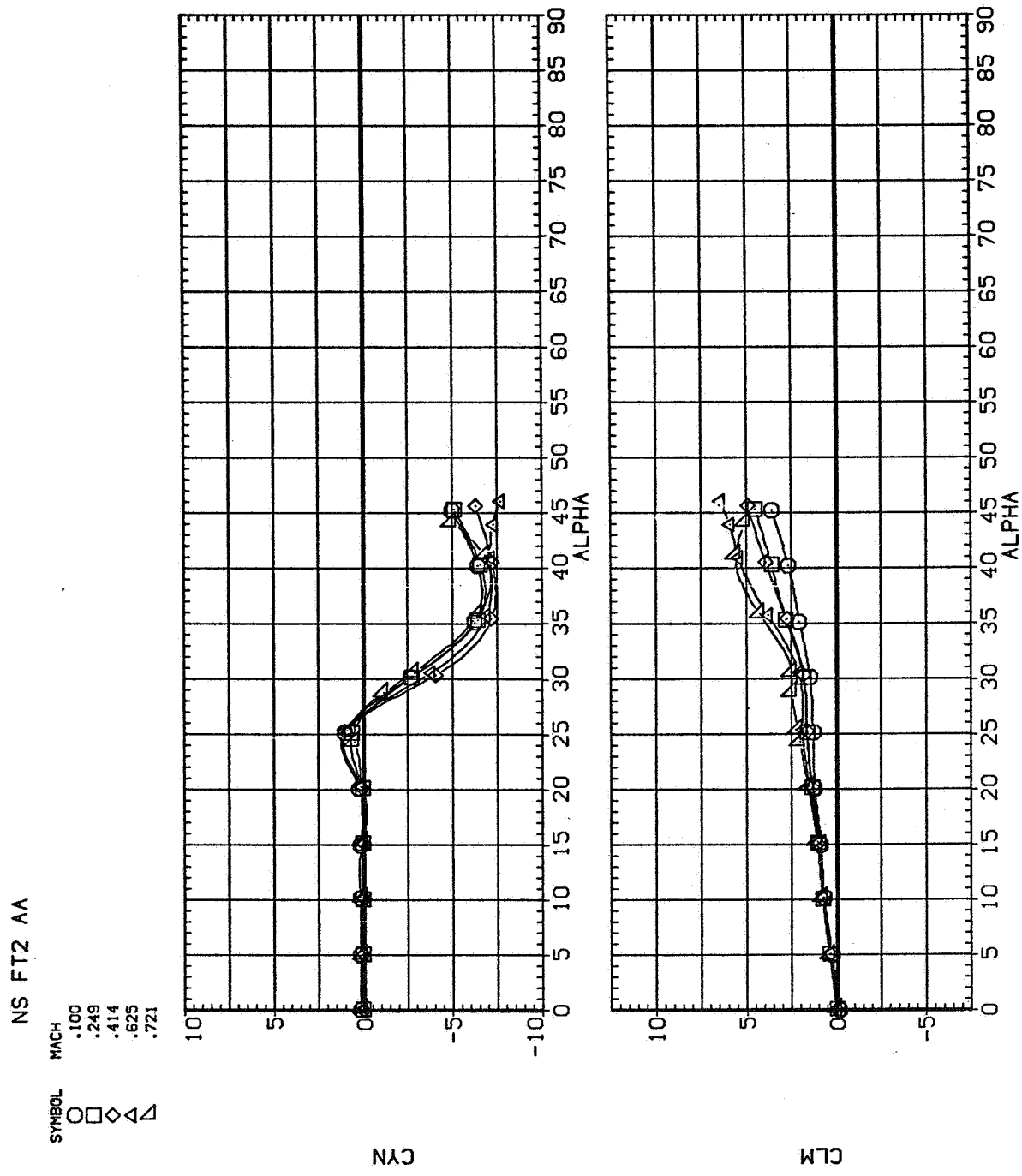

(c) C_n and C_m vs α

Figure 16.– Concluded.

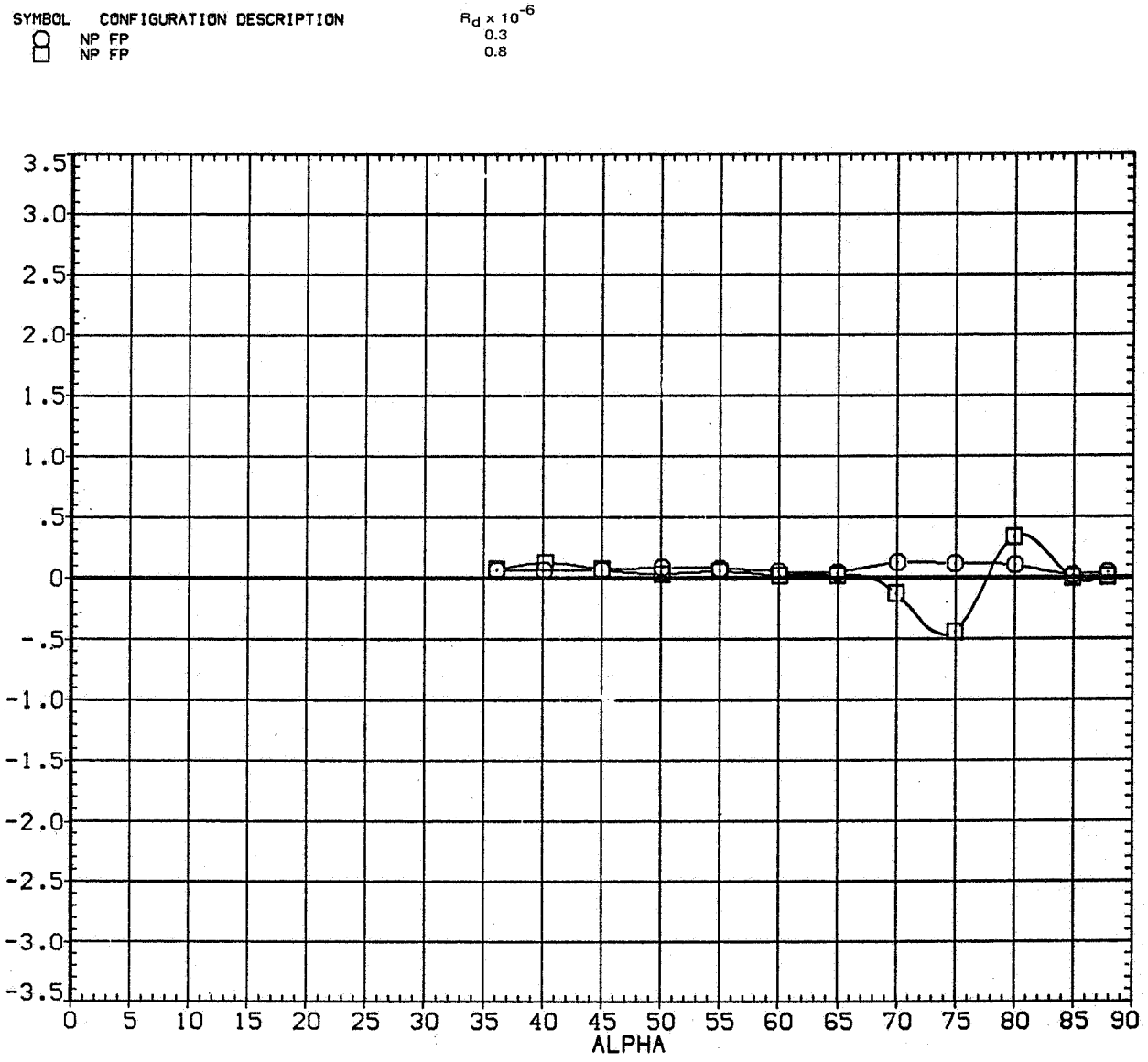

(a) C_Y vs α

Figure 17.– Effect of Reynolds number for the blunt $\ell/d = 3.5$ paraboloid, $M = 0.1$.

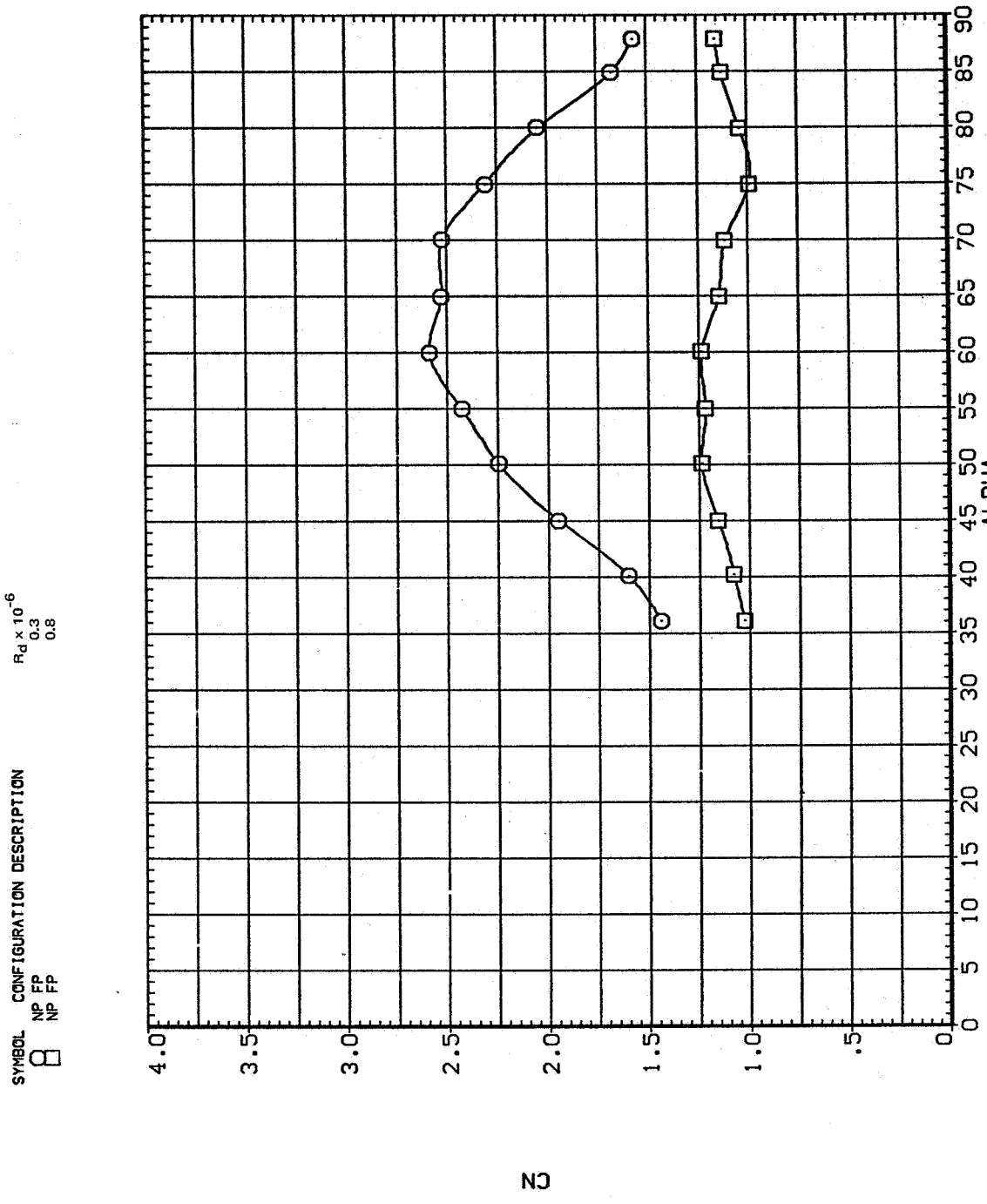

(b) C_N vs α

Figure 17.– Continued.

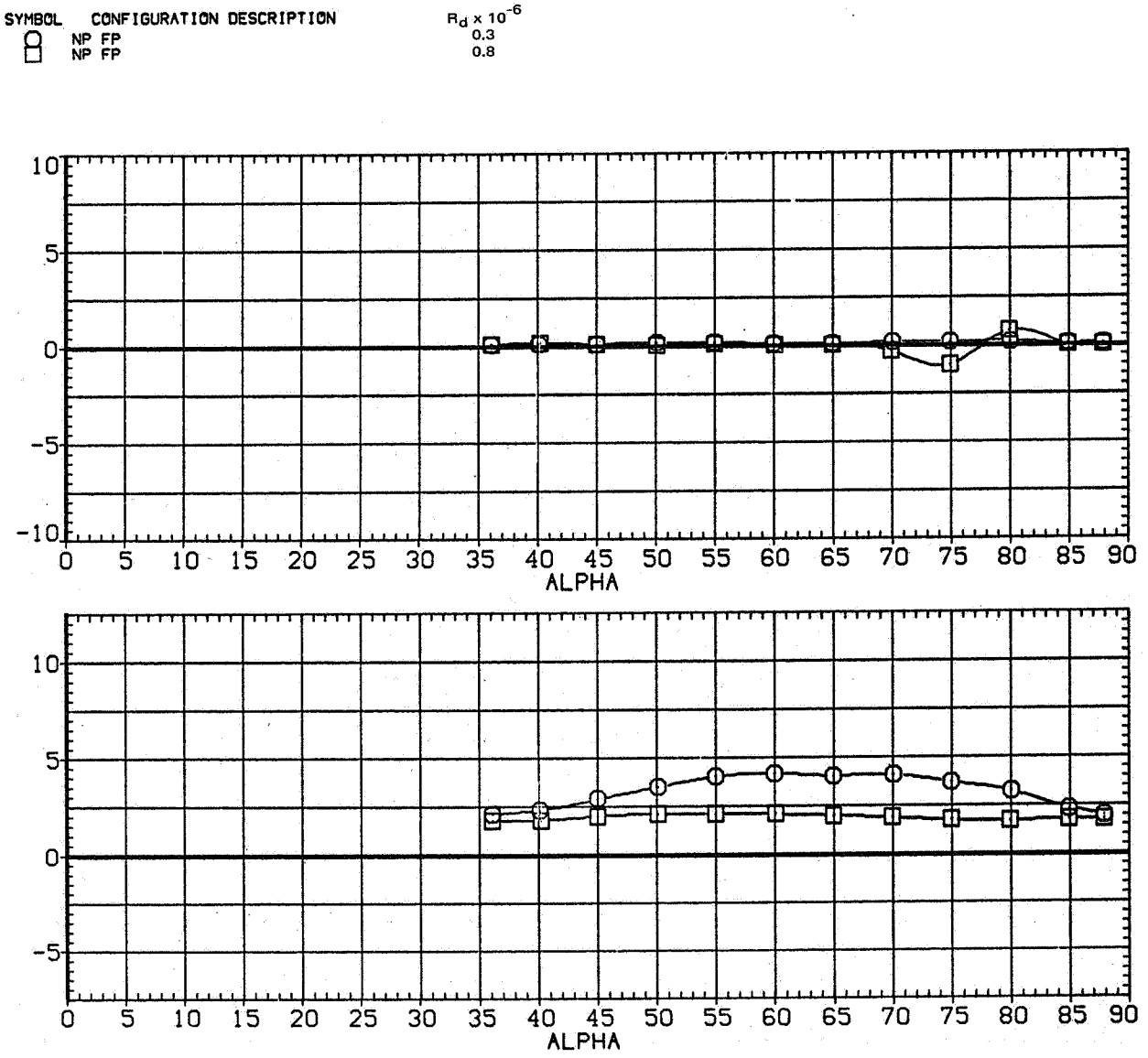

(c) C_n and C_m vs α

Figure 17.– Concluded.

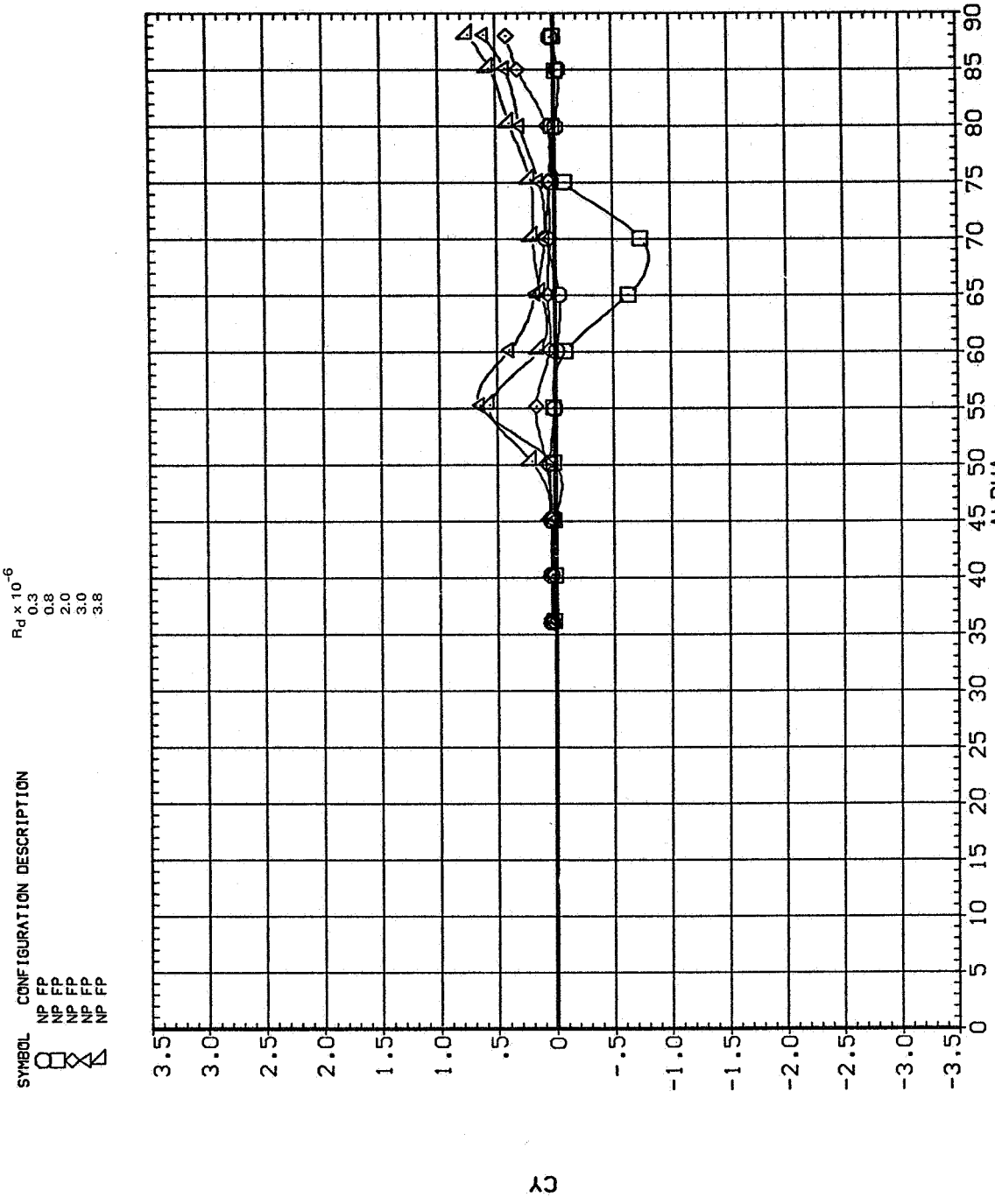

(a) C_Y vs α

Figure 18.– Effect of Reynolds number for the blunt $\ell/d = 3.5$ paraboloid, $M = 0.25$.

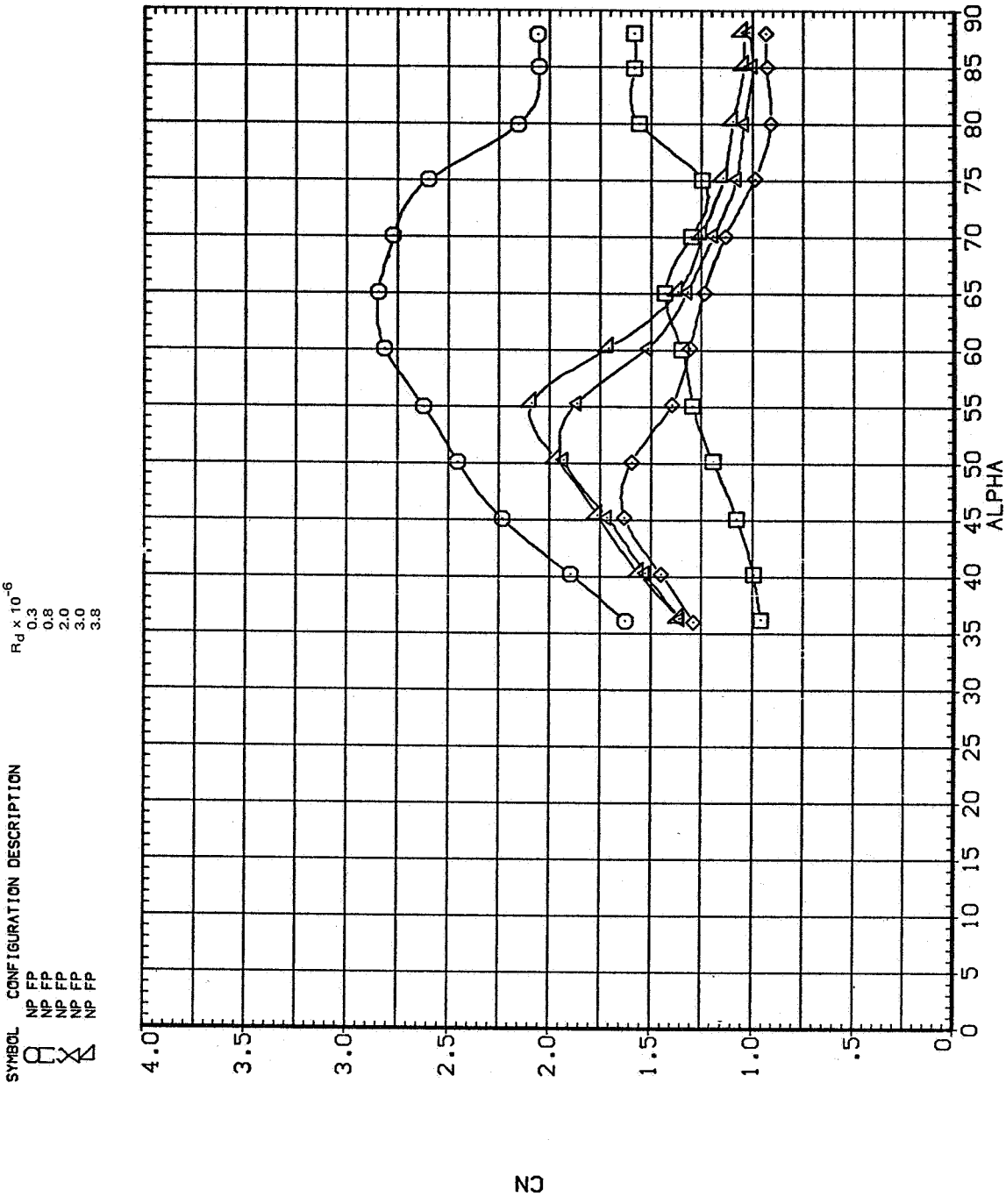

(b) C_N vs α

Figure 18.– Continued.

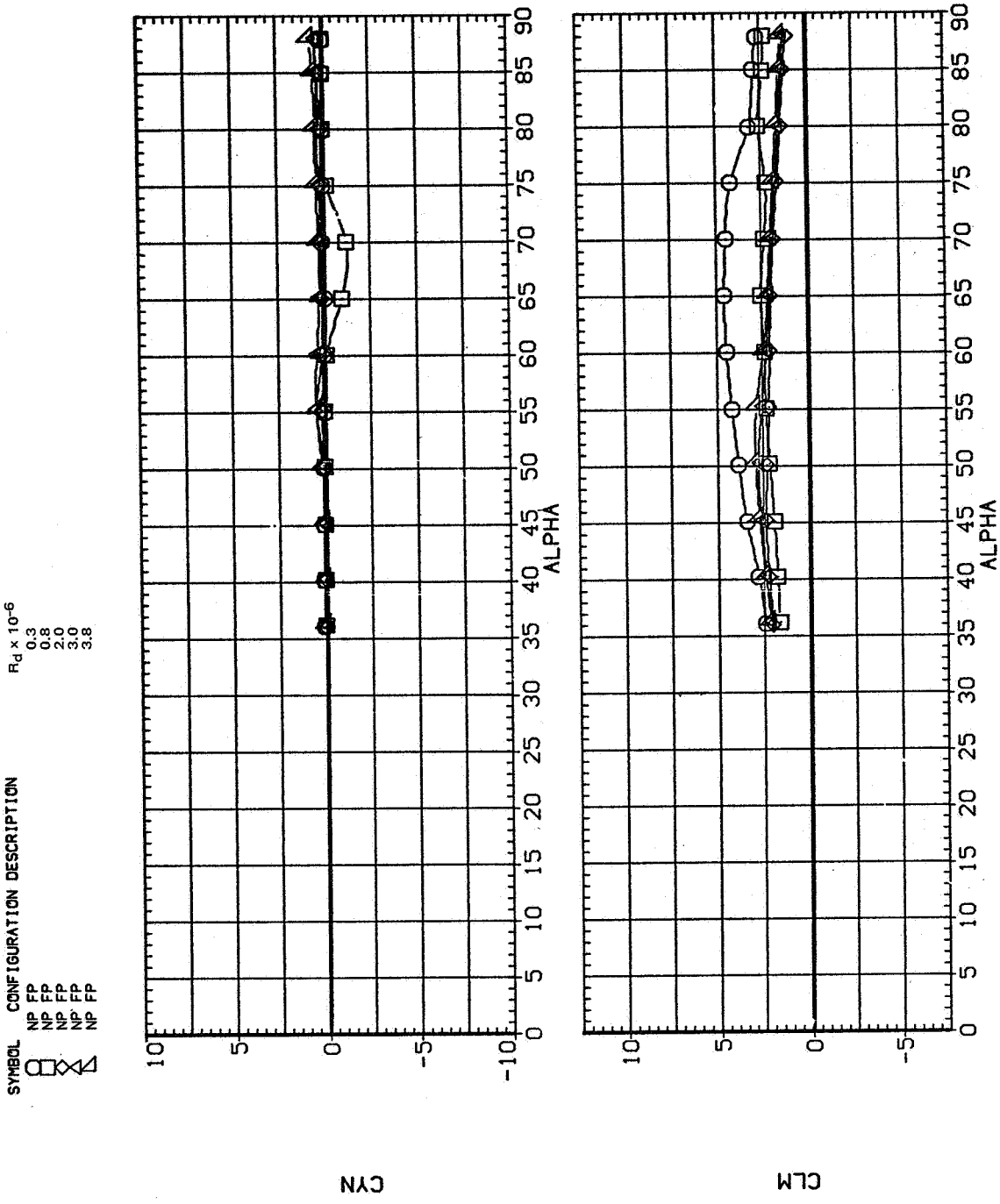

(c) C_n and C_m vs α

Figure 18.– Concluded.

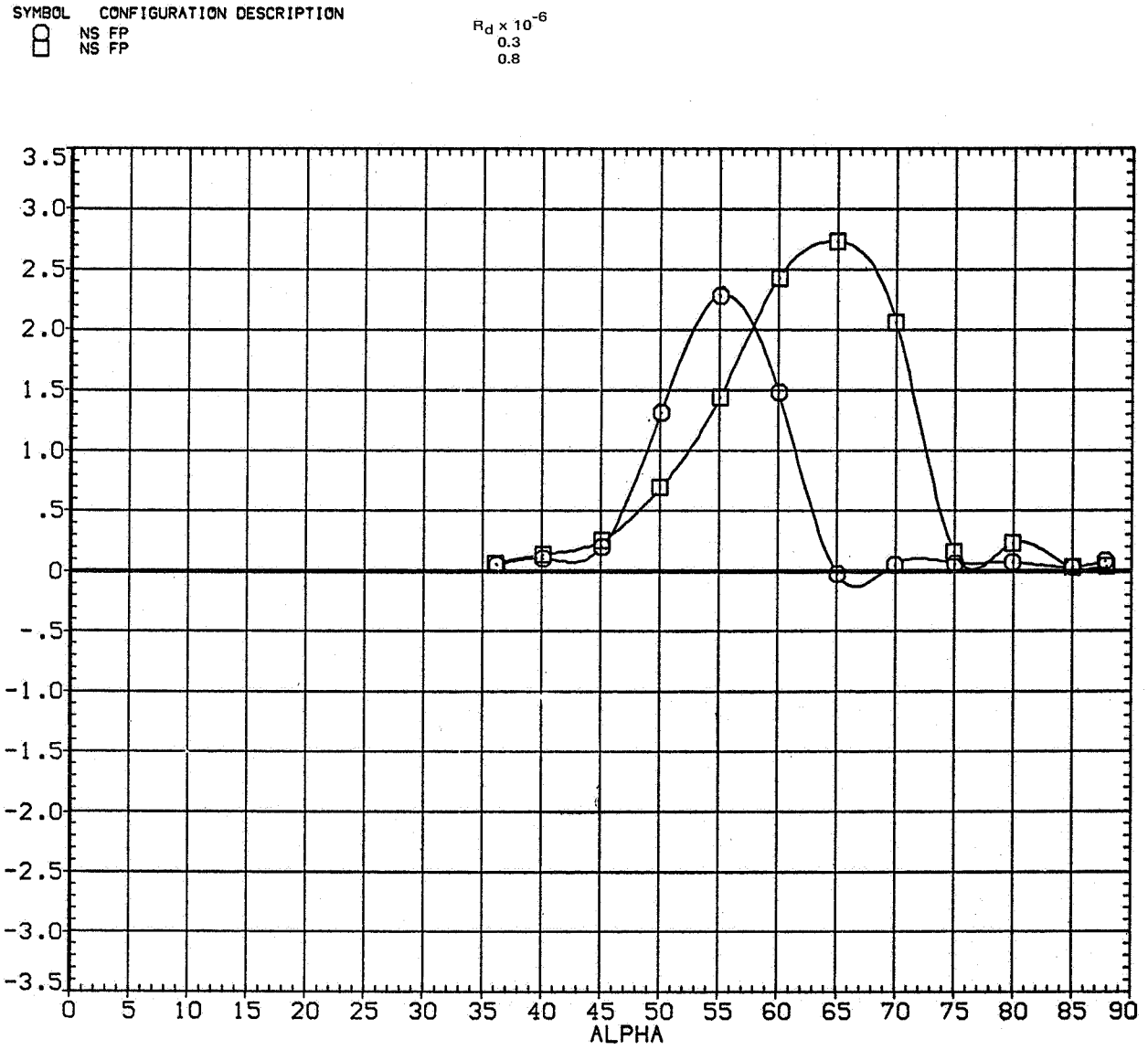

(a) C_Y vs α

Figure 19.– Effect of Reynolds number for the pointed $\ell/d = 3.5$ paraboloid, $M = 0.1$.

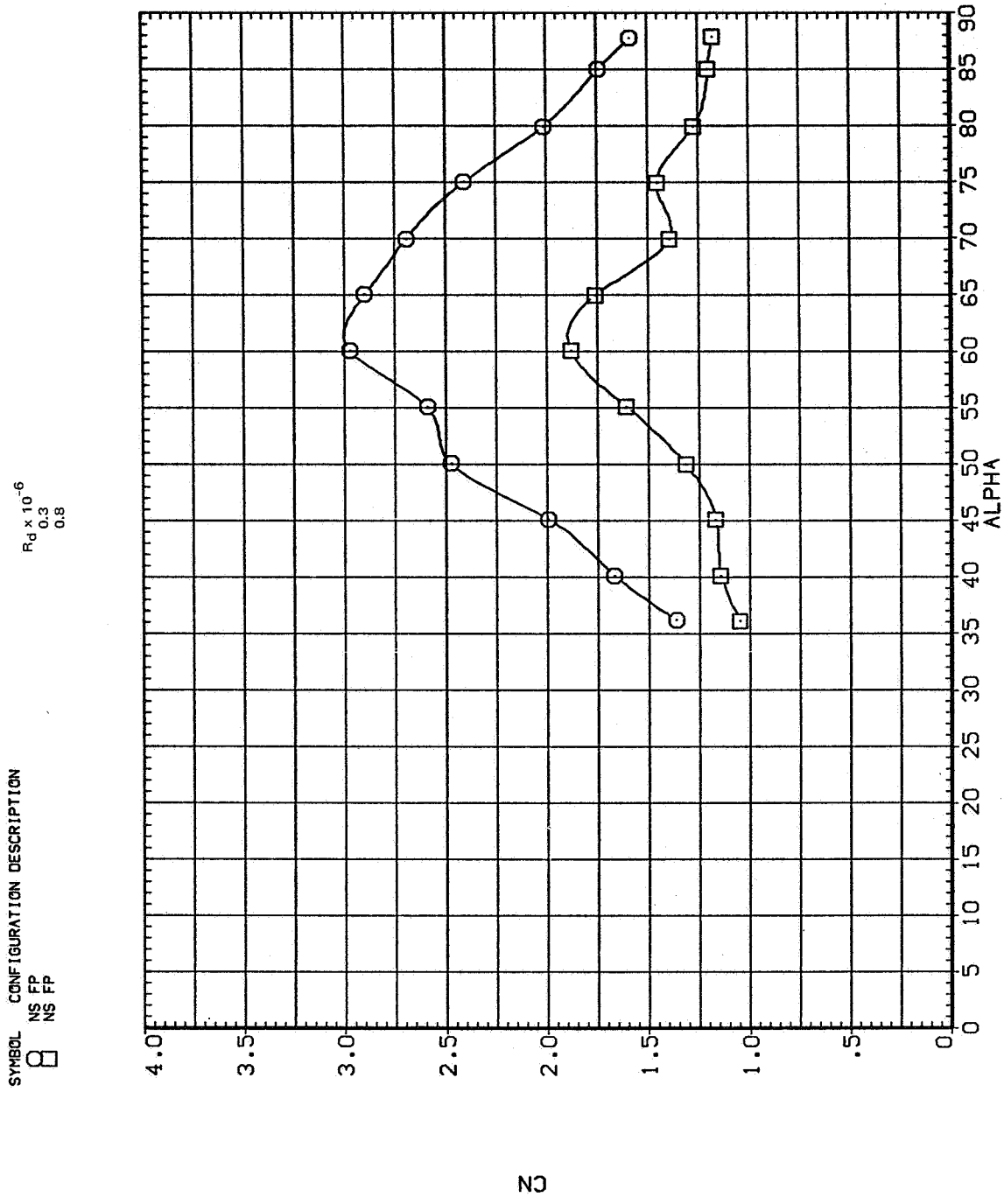

(b) C_N vs α

Figure 19.– Continued.

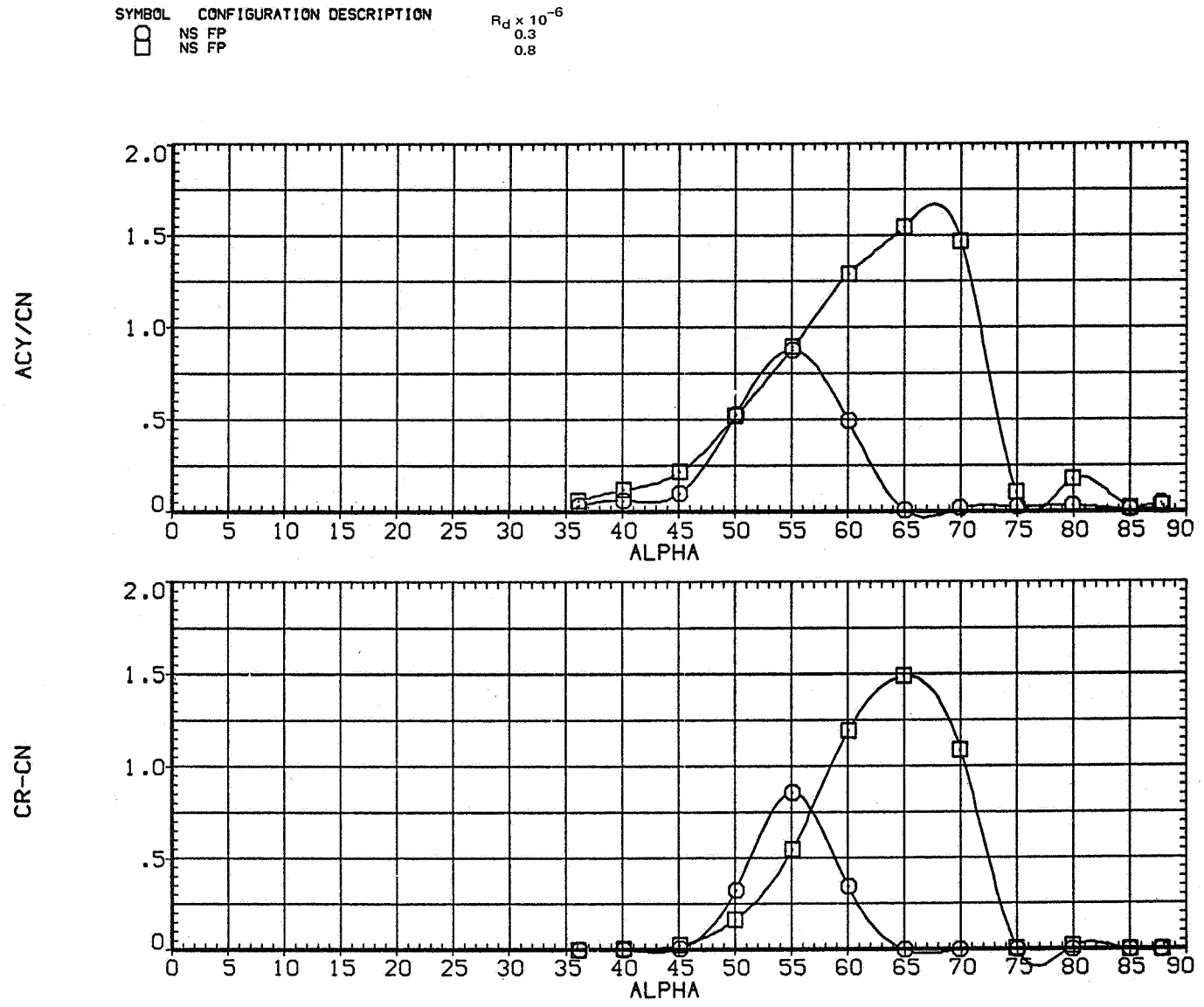

(c) $|C_Y|/|C_N|$ and $C_R - C_N$ vs α

Figure 19.– Continued.

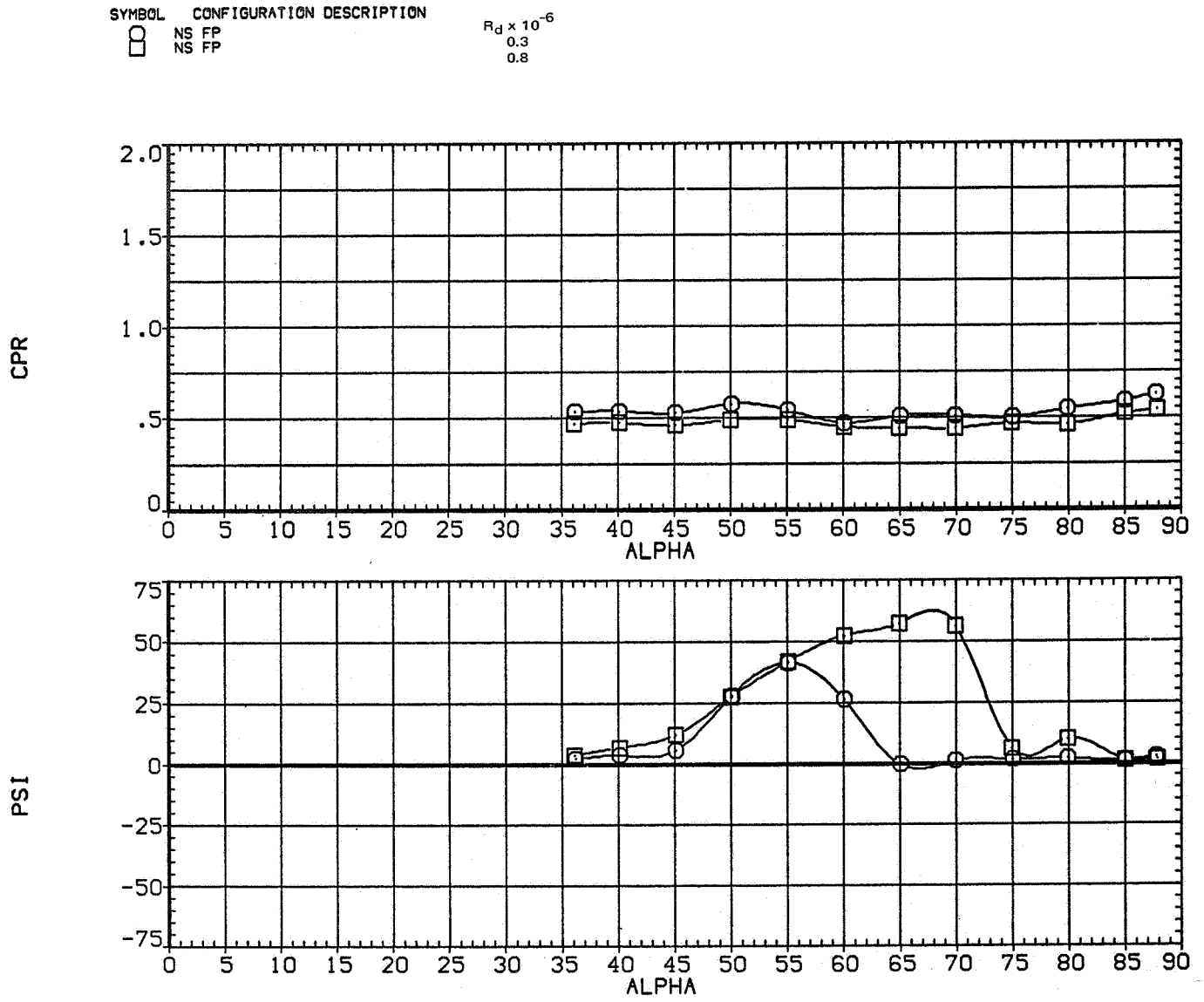

(d) CP_R and Ψ vs α

Figure 19.– Continued.

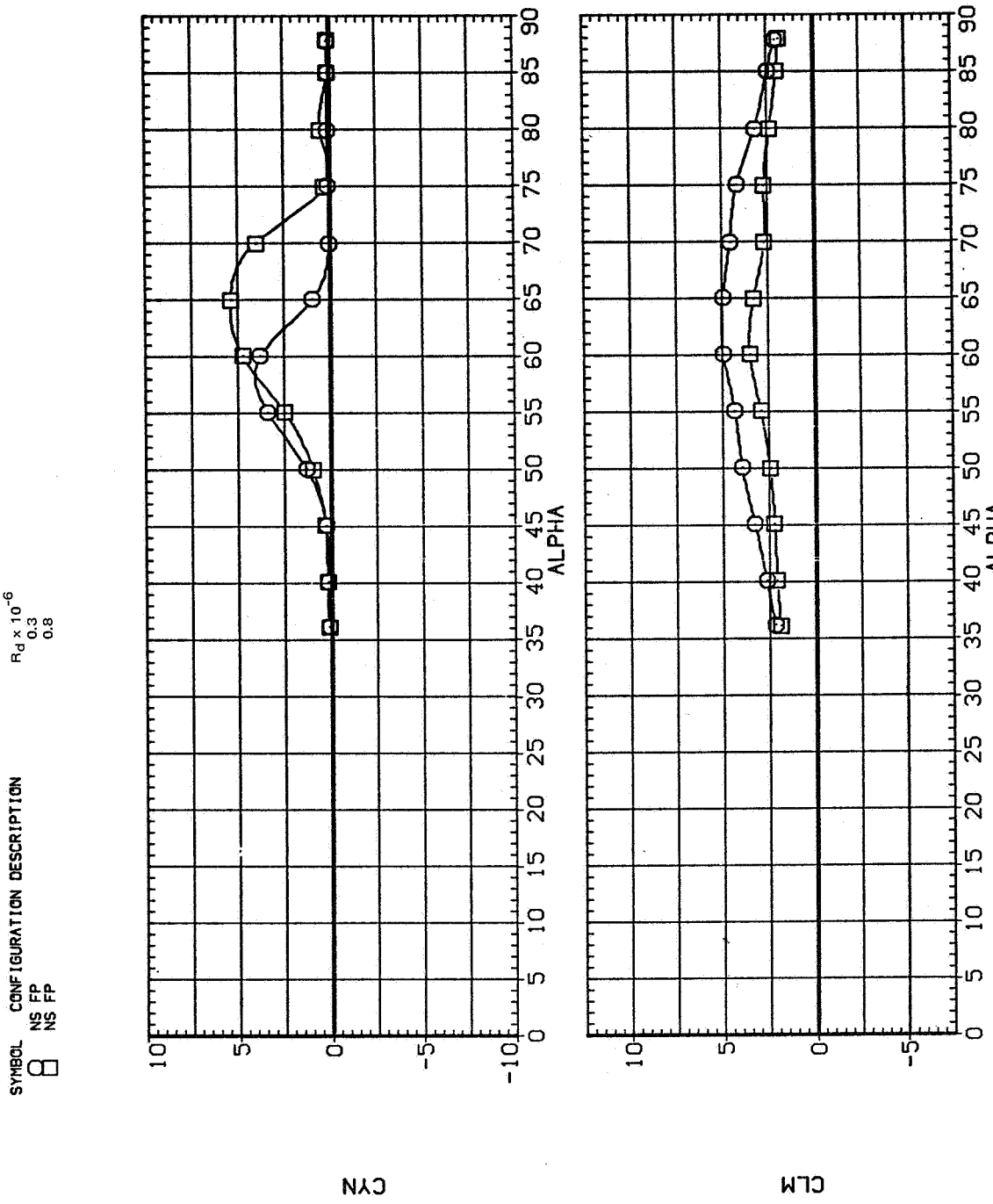

(e) C_n and C_m vs α

Figure 19.– Continued.

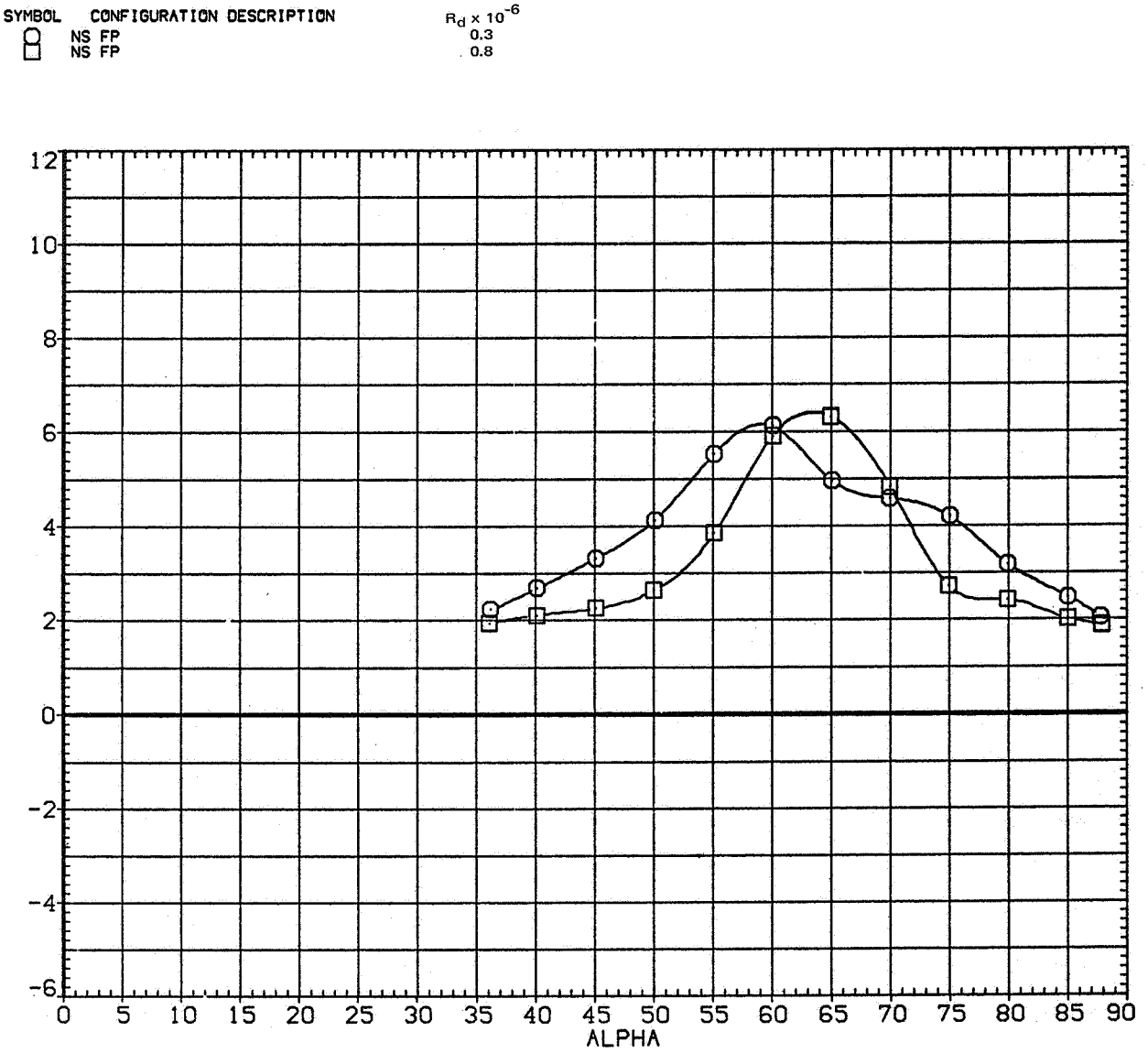

(f) $C_{m,R}$ vs α

Figure 19.– Concluded.

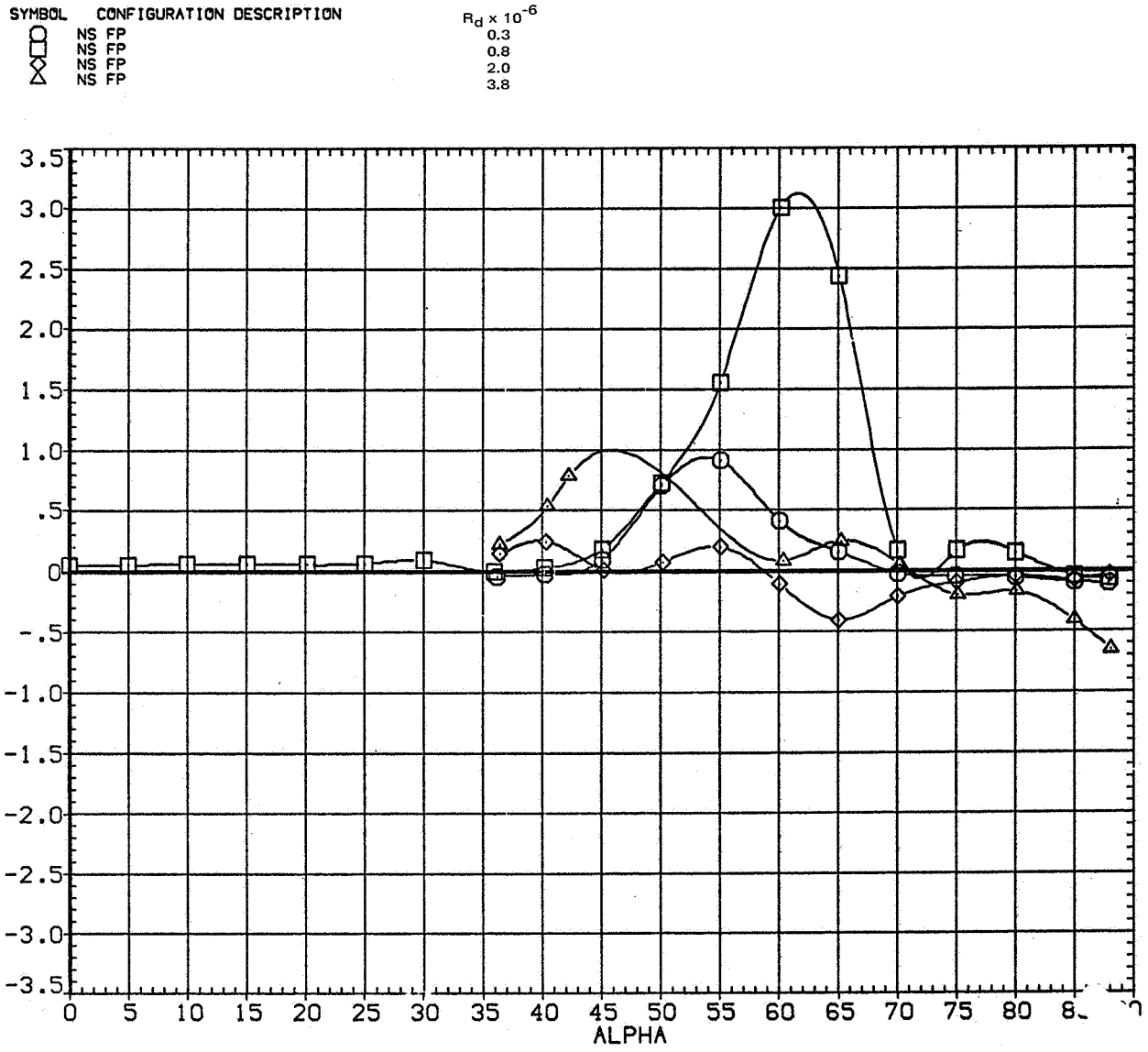

(a) C_Y vs α

Figure 20.– Effect of Reynolds number for the pointed $\ell/d = 3.5$ paraboloid, $M = 0.25$.

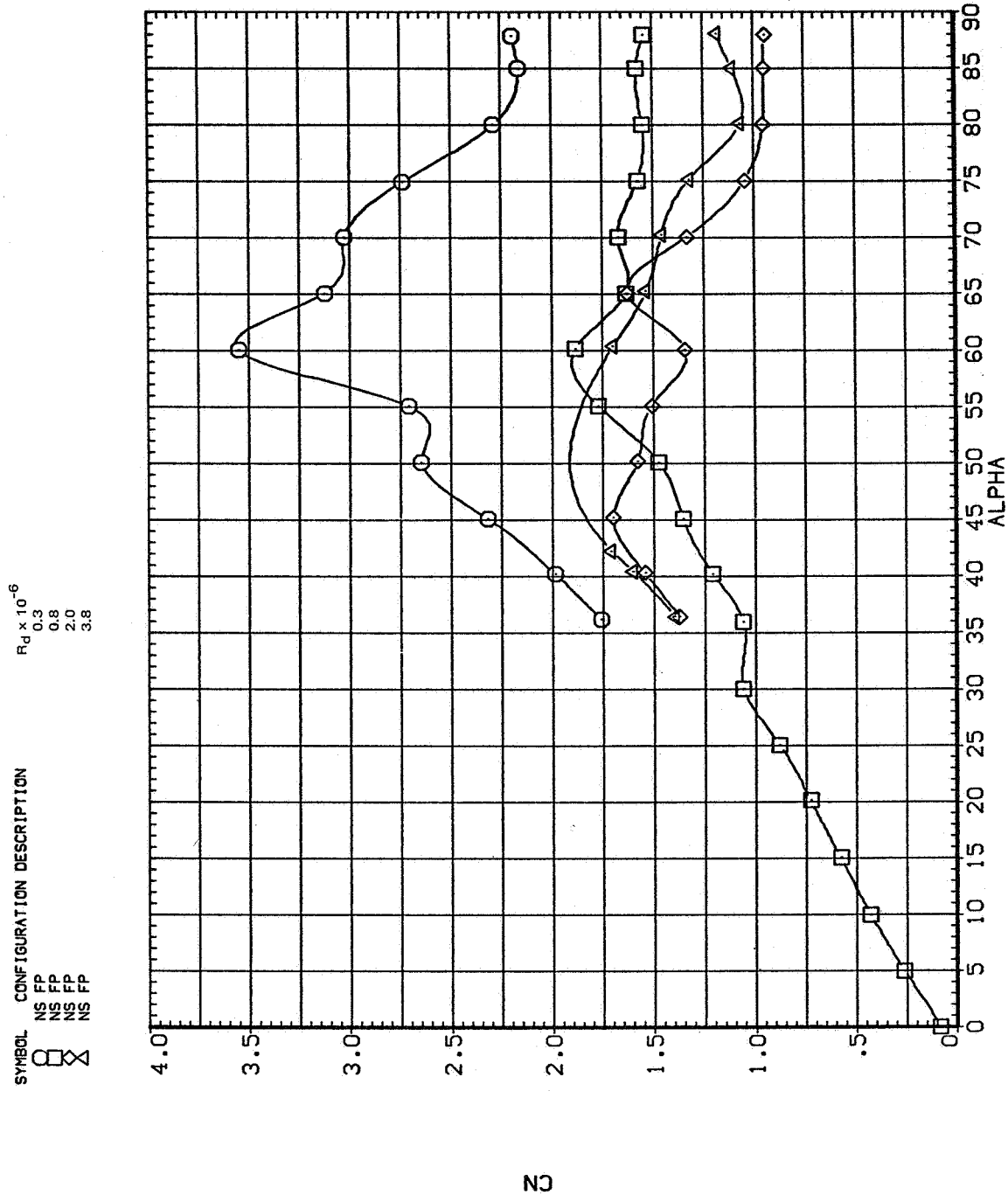

(b) C_N vs α

Figure 20.– Continued.

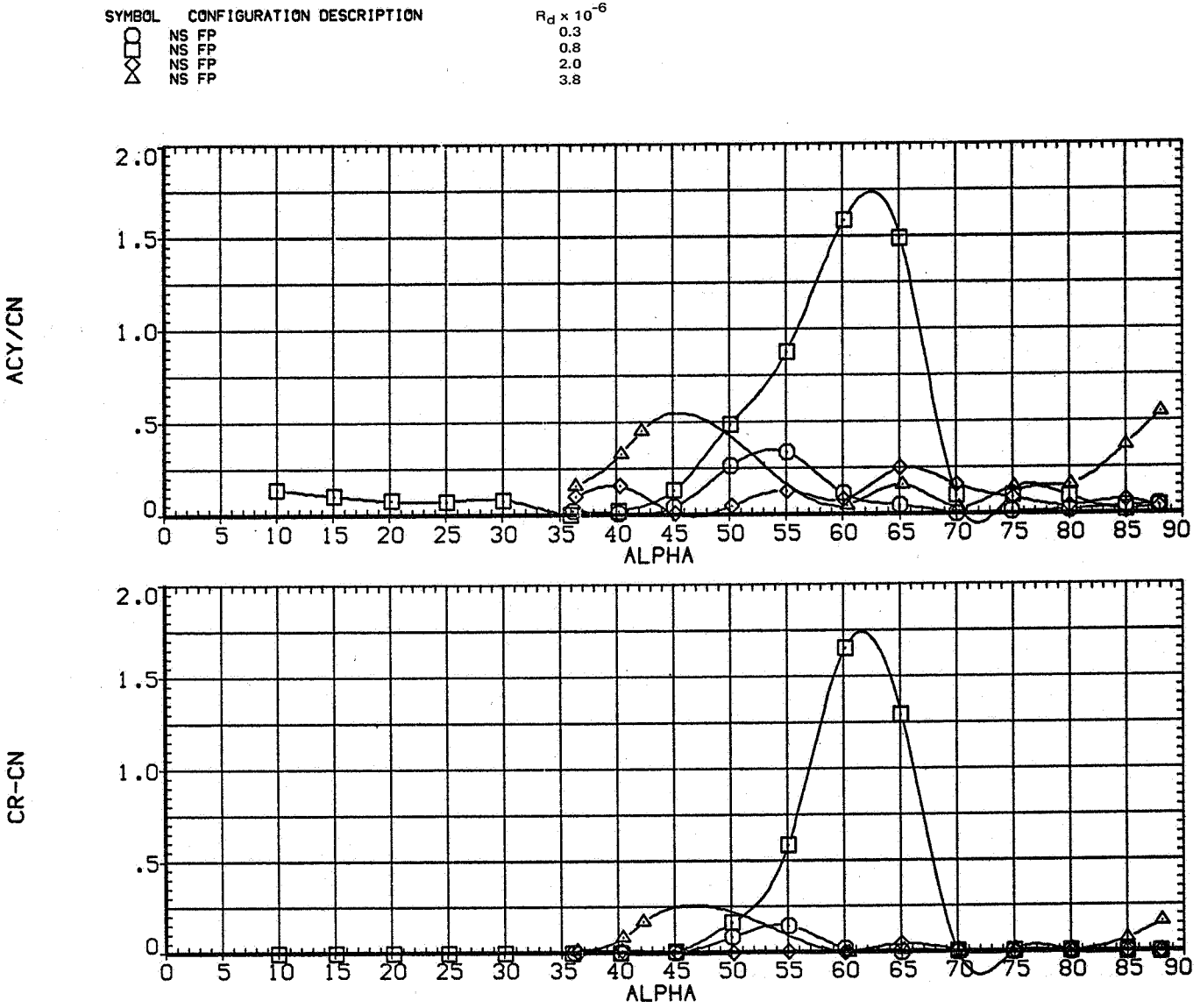

(c) $|C_Y|/|C_N|$ and $C_R - C_N$ vs α

Figure 20.– Continued.

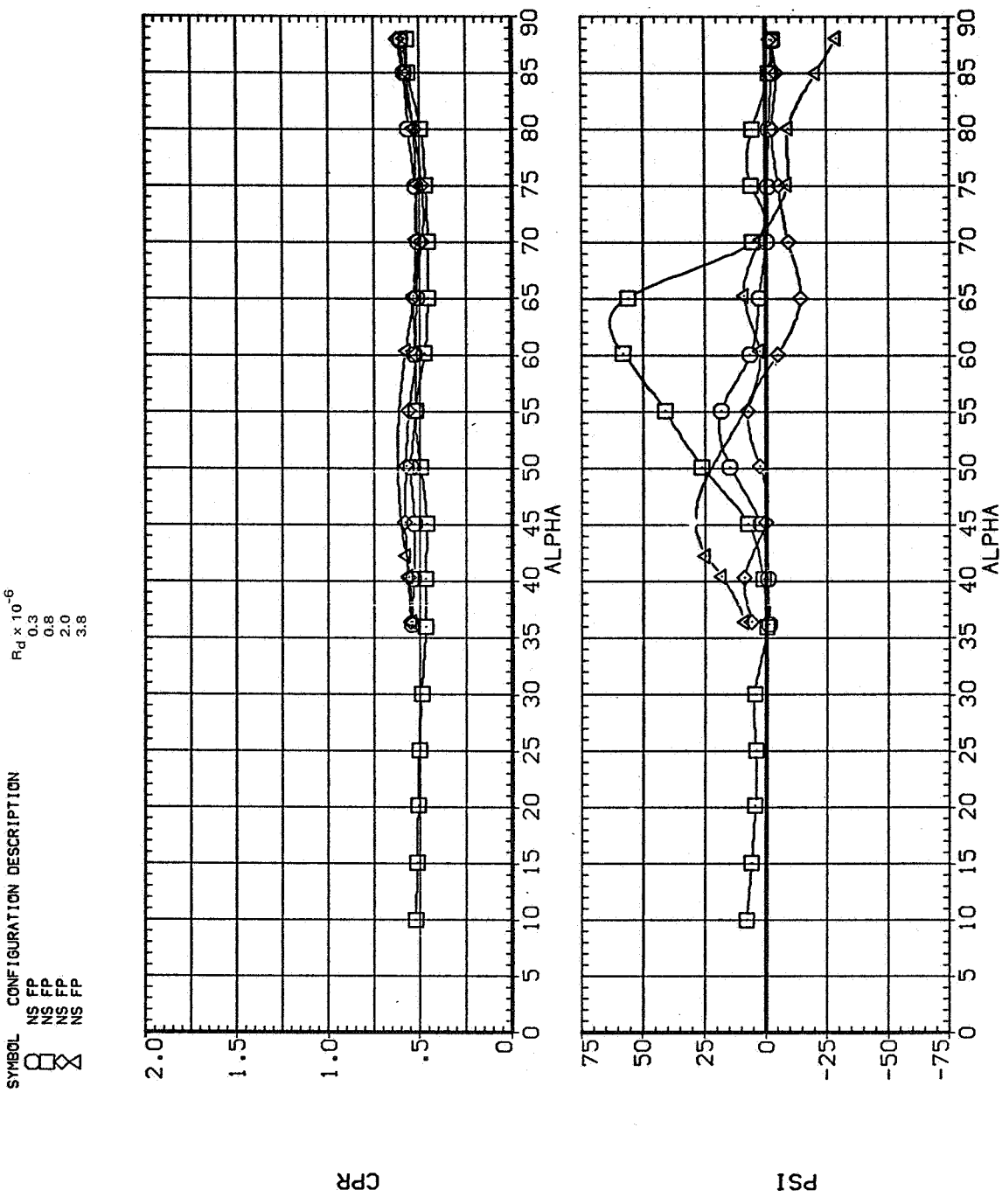

(d) CP_R and Ψ vs α

Figure 20.– Continued.

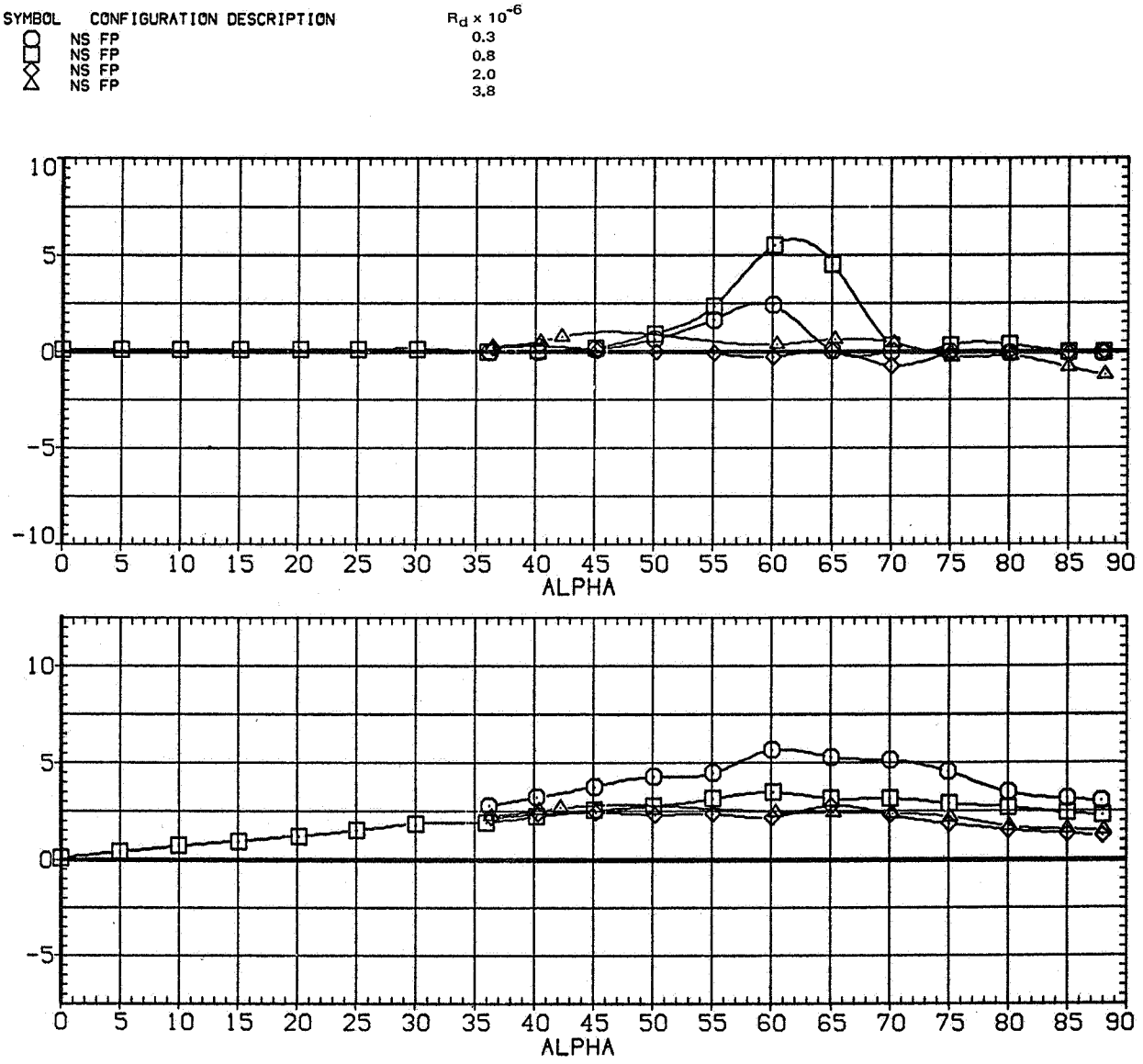

(e) C_n and C_m vs α

Figure 20.– Continued.

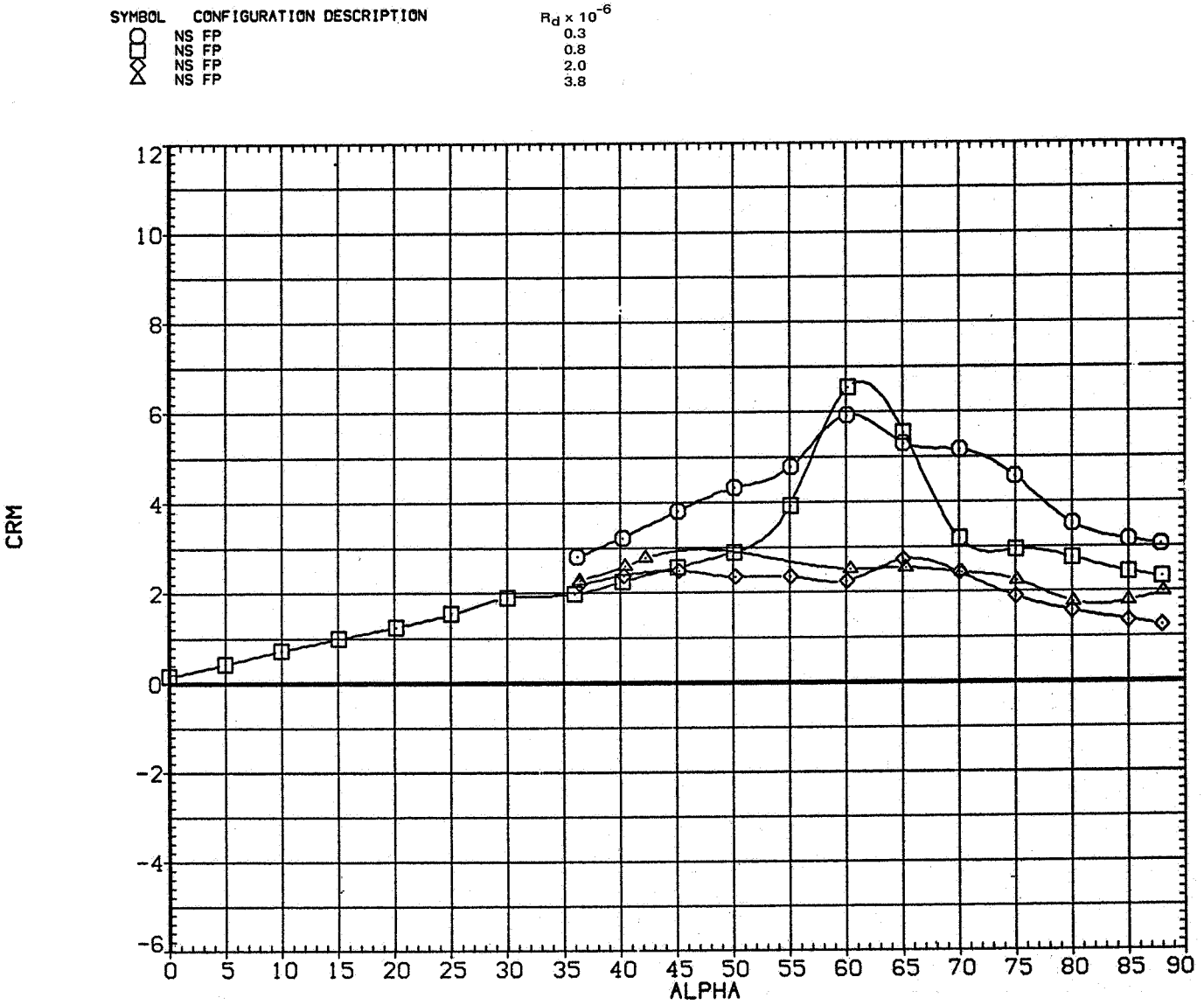

(f) $C_{m,R}$ vs α

Figure 20.– Continued.

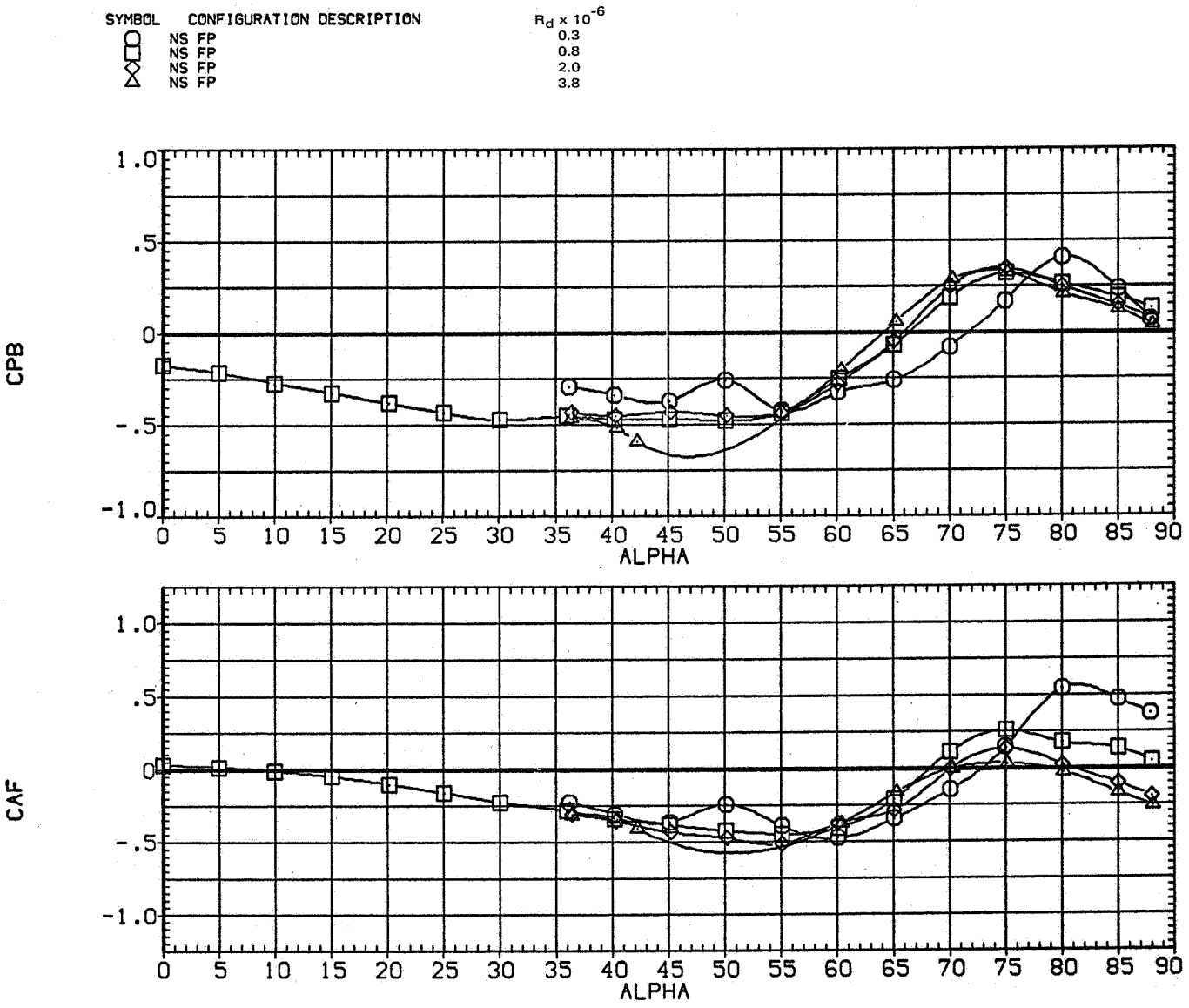

(g) $C_{p,b}$ and C_{AF} vs α

Figure 20.– Concluded.

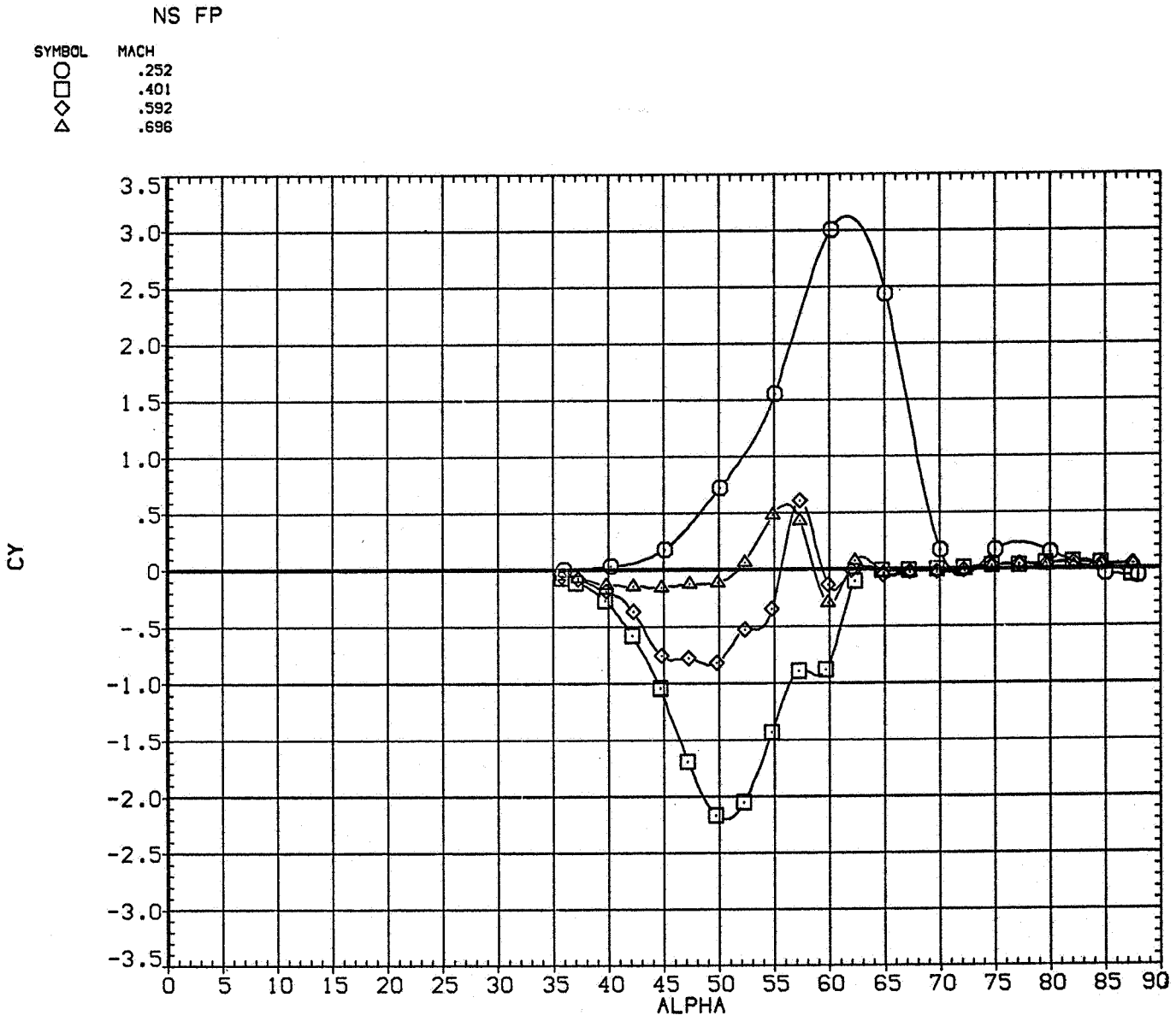

(a) C_Y vs α

Figure 21.– Effect of Mach number for the pointed $\ell/d = 3.5$ paraboloid, $R_d = 0.8 \times 10^6$.

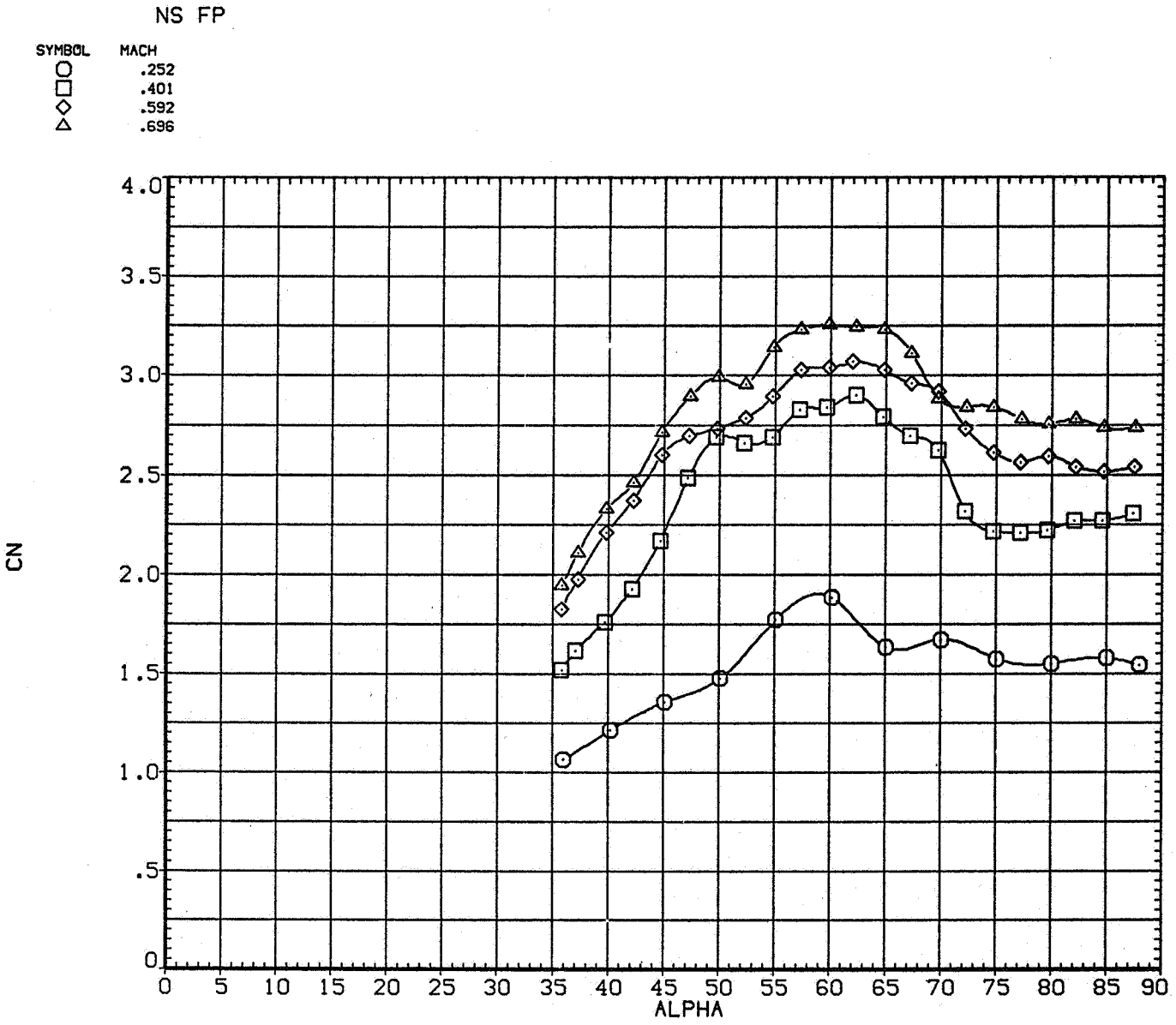

(b) C_N vs α

Figure 21.– Continued.

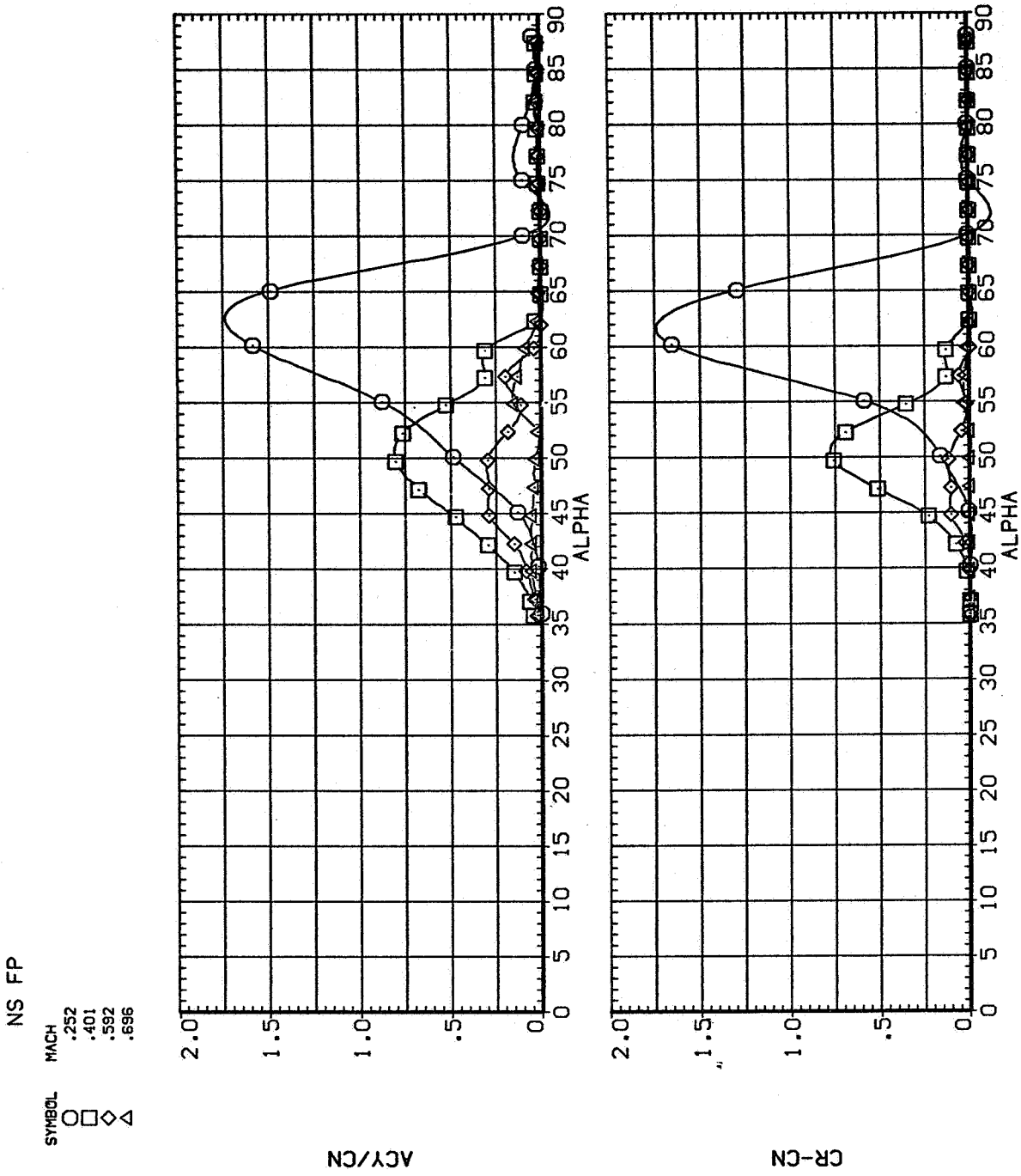

(c) $|C_Y|/|C_N|$ and $C_R - C_N$ vs α

Figure 21.– Continued.

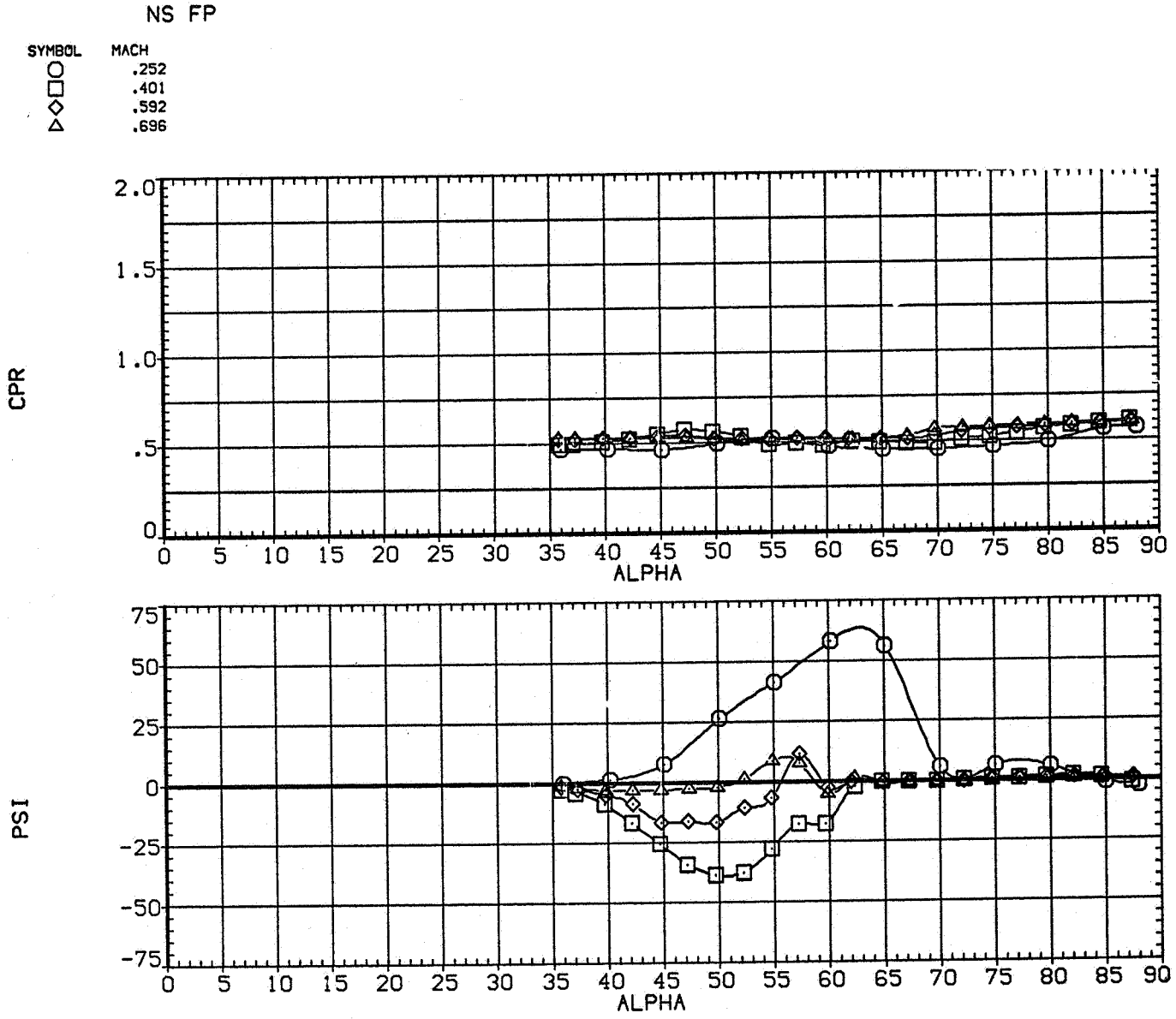

(d) CP_R and Ψ vs α

Figure 21.– Continued.

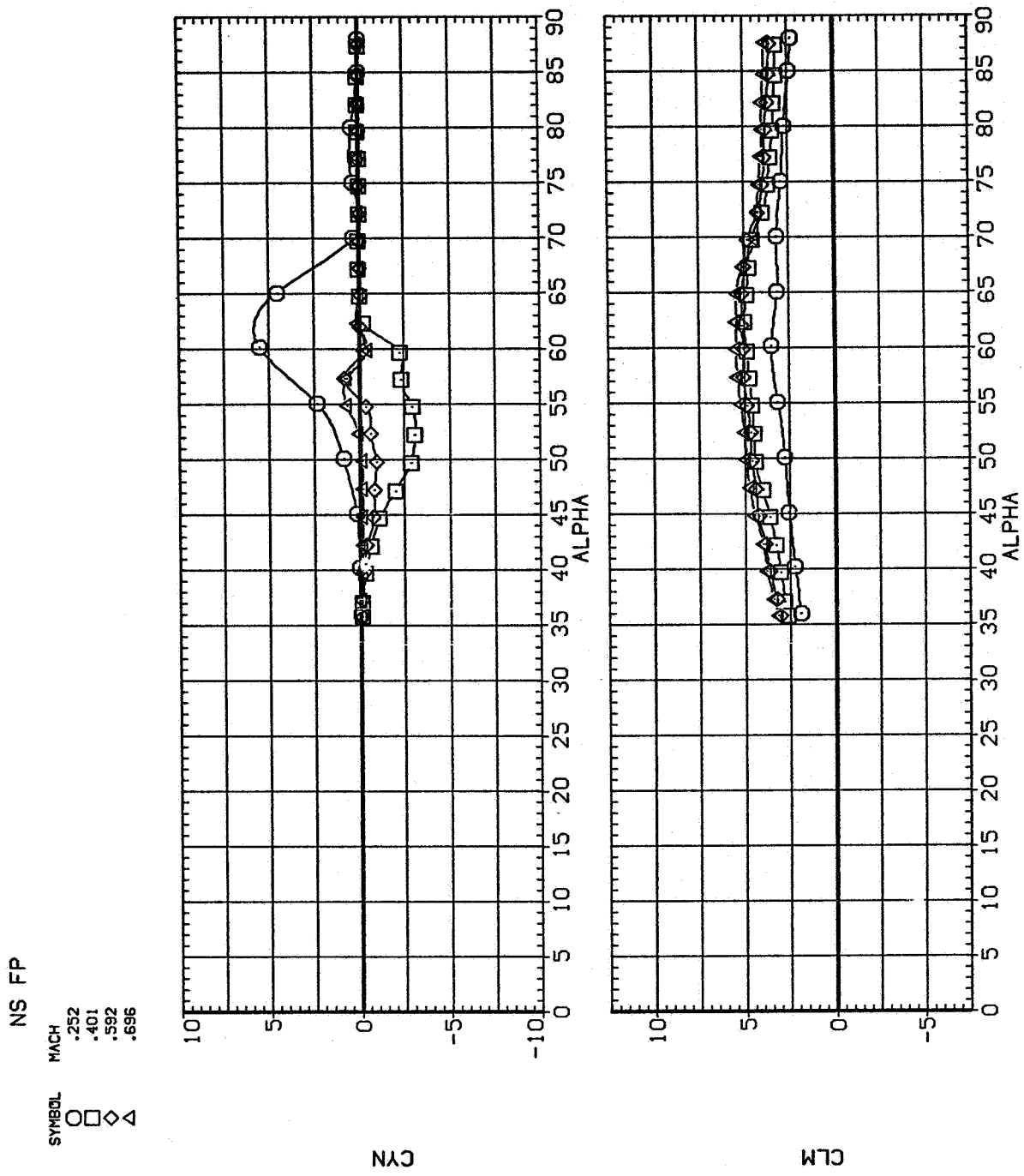

(e) C_n and C_m vs α

Figure 21.– Continued.

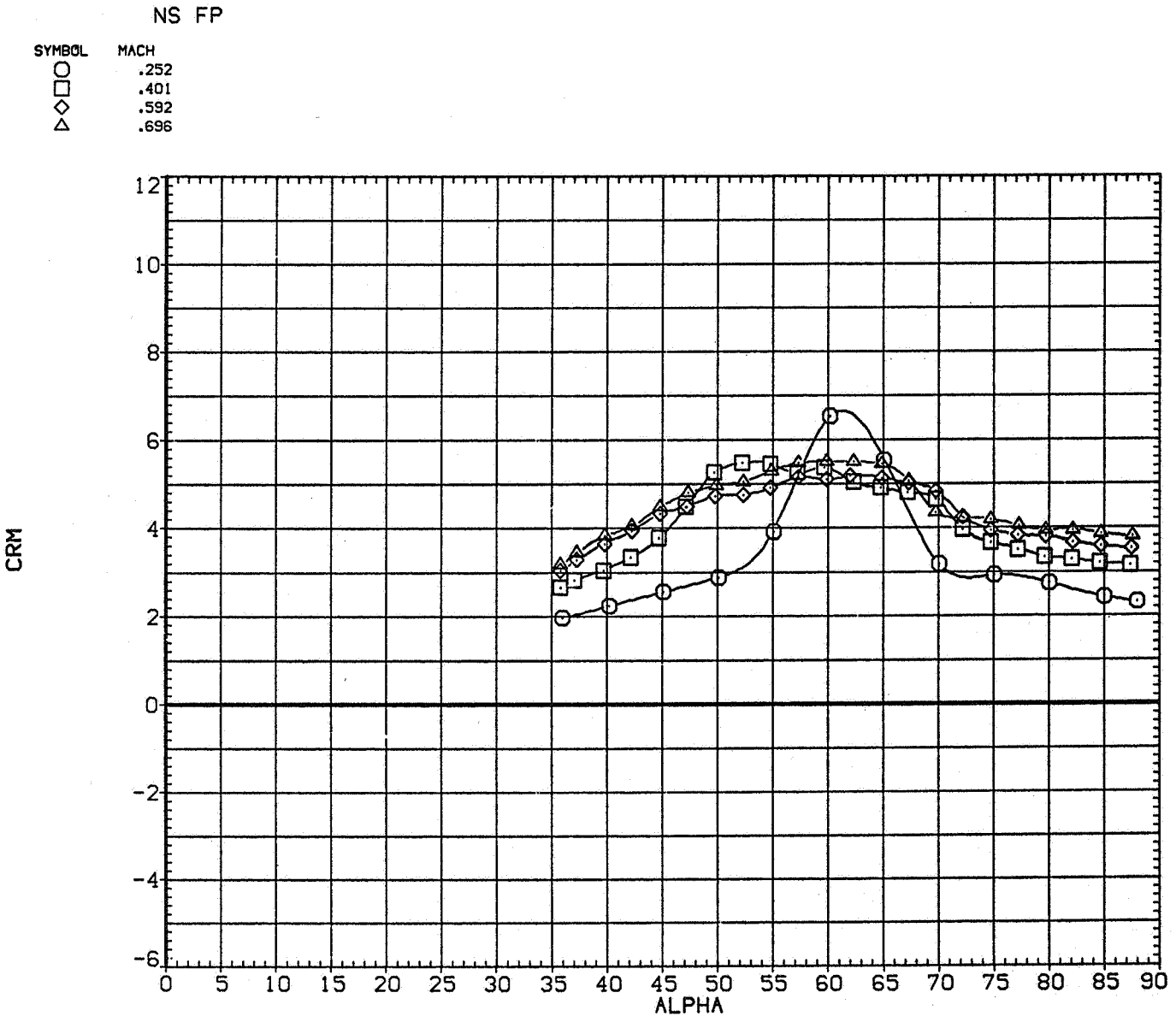

(f) $C_{m,R}$ vs α

Figure 21.– Concluded.

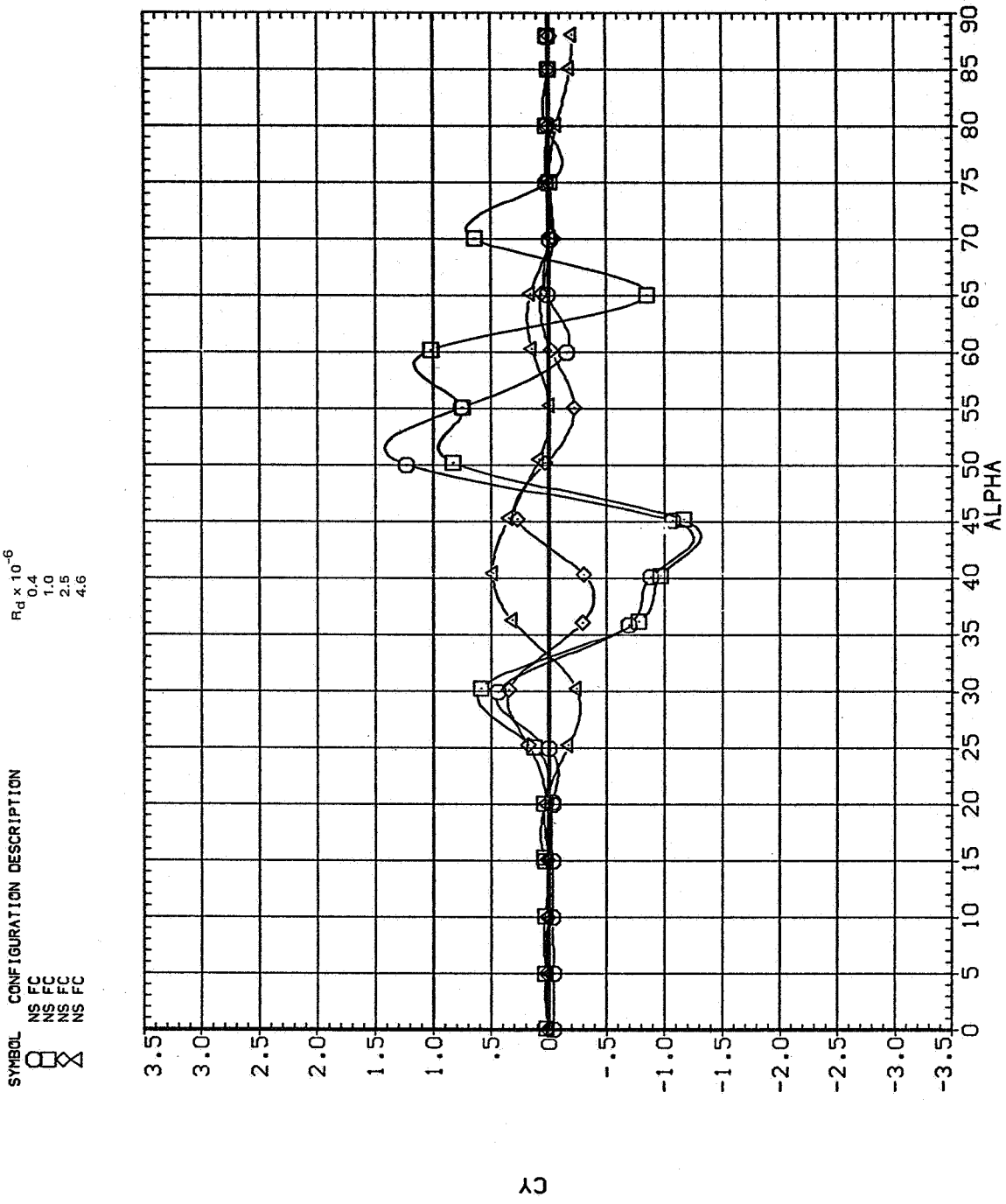

(a) C_Y vs α

Figure 22.– Effect of Reynolds number for the 20° cone, $M = 0.25$.

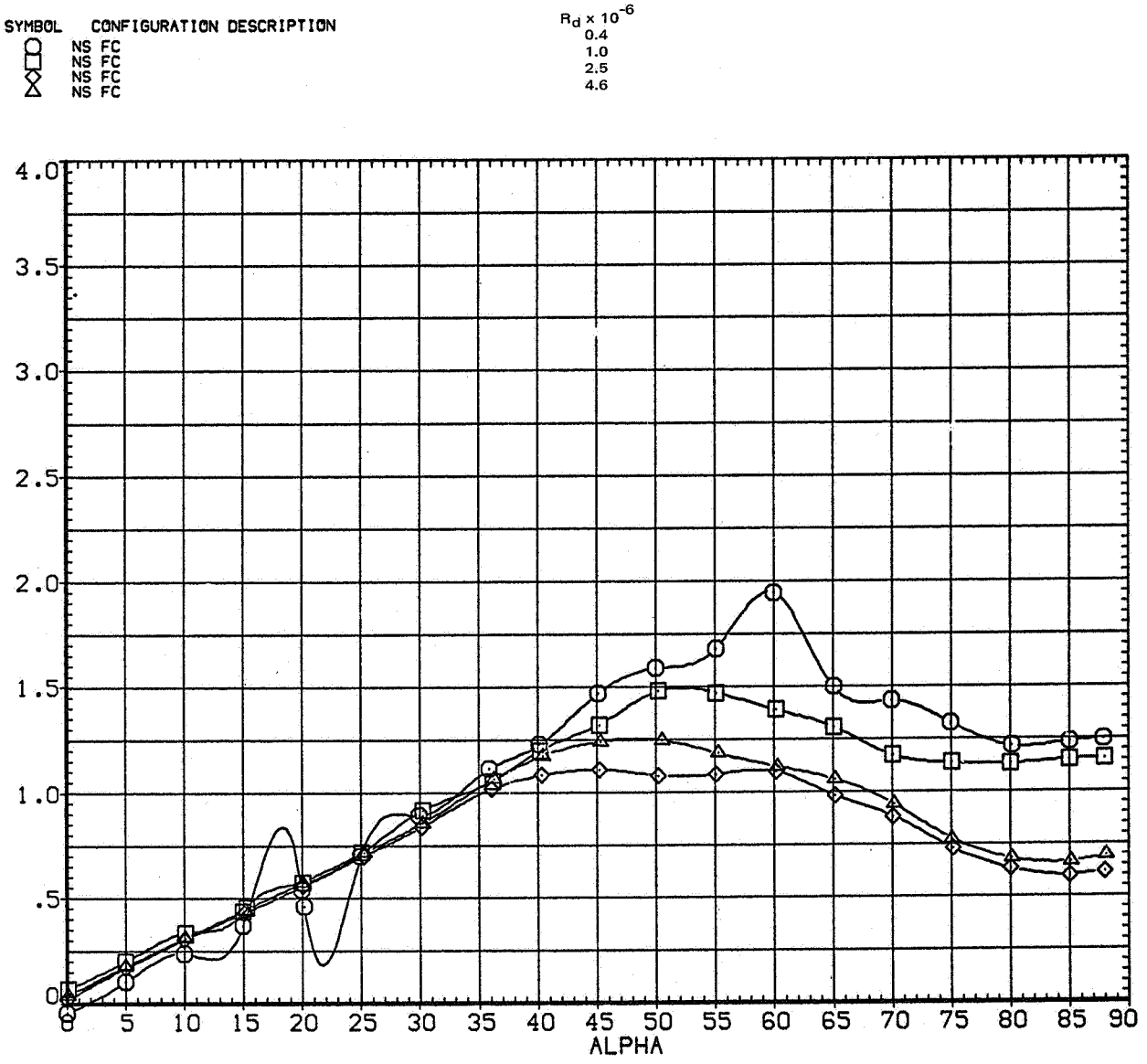

(b) C_N vs α

Figure 22.– Continued.

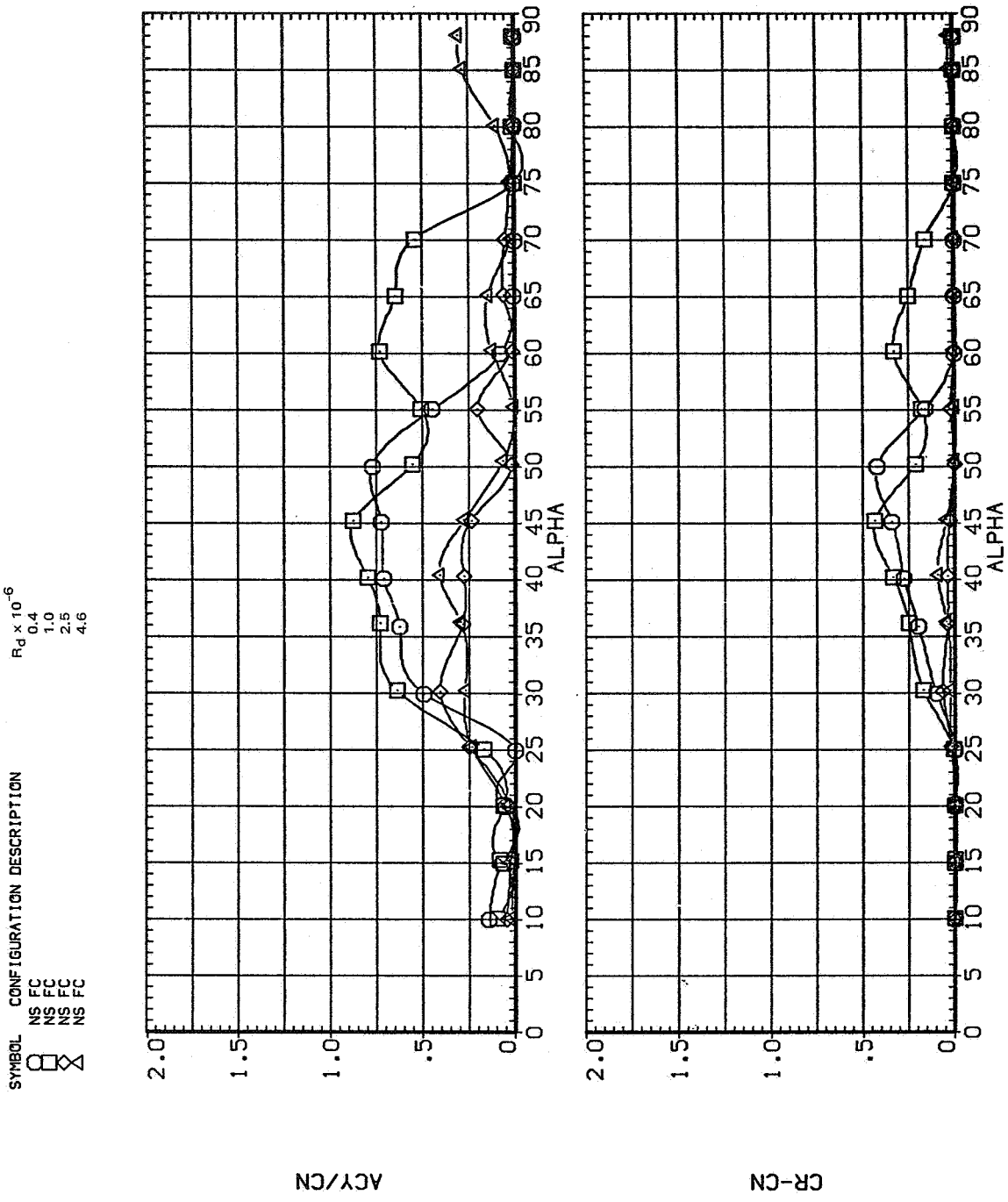

(c) $|C_Y|/|C_N|$ and $C_R - C_N$ vs α

Figure 22.– Continued.

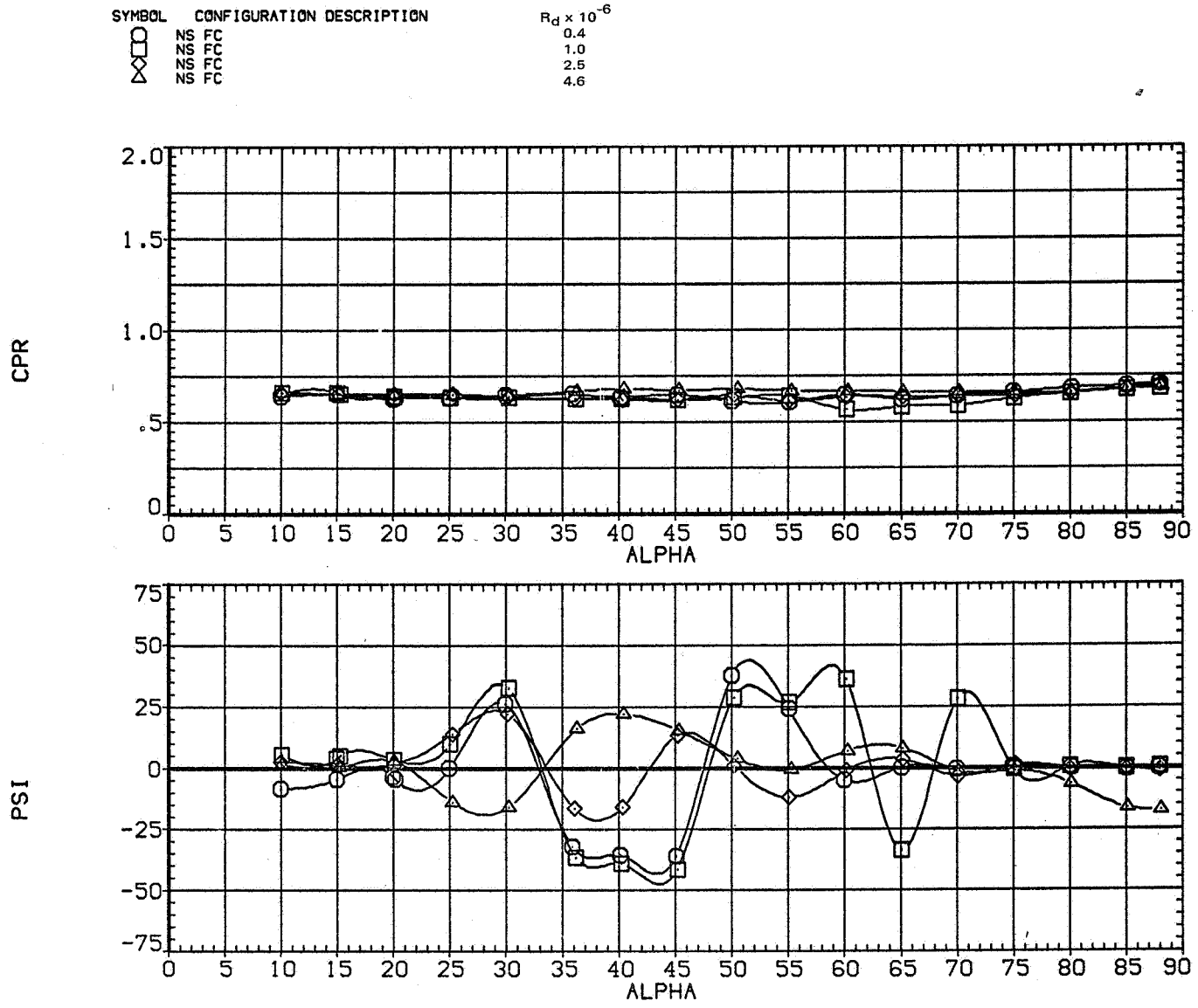

(d) CP_R and Ψ vs α

Figure 22.– Continued.

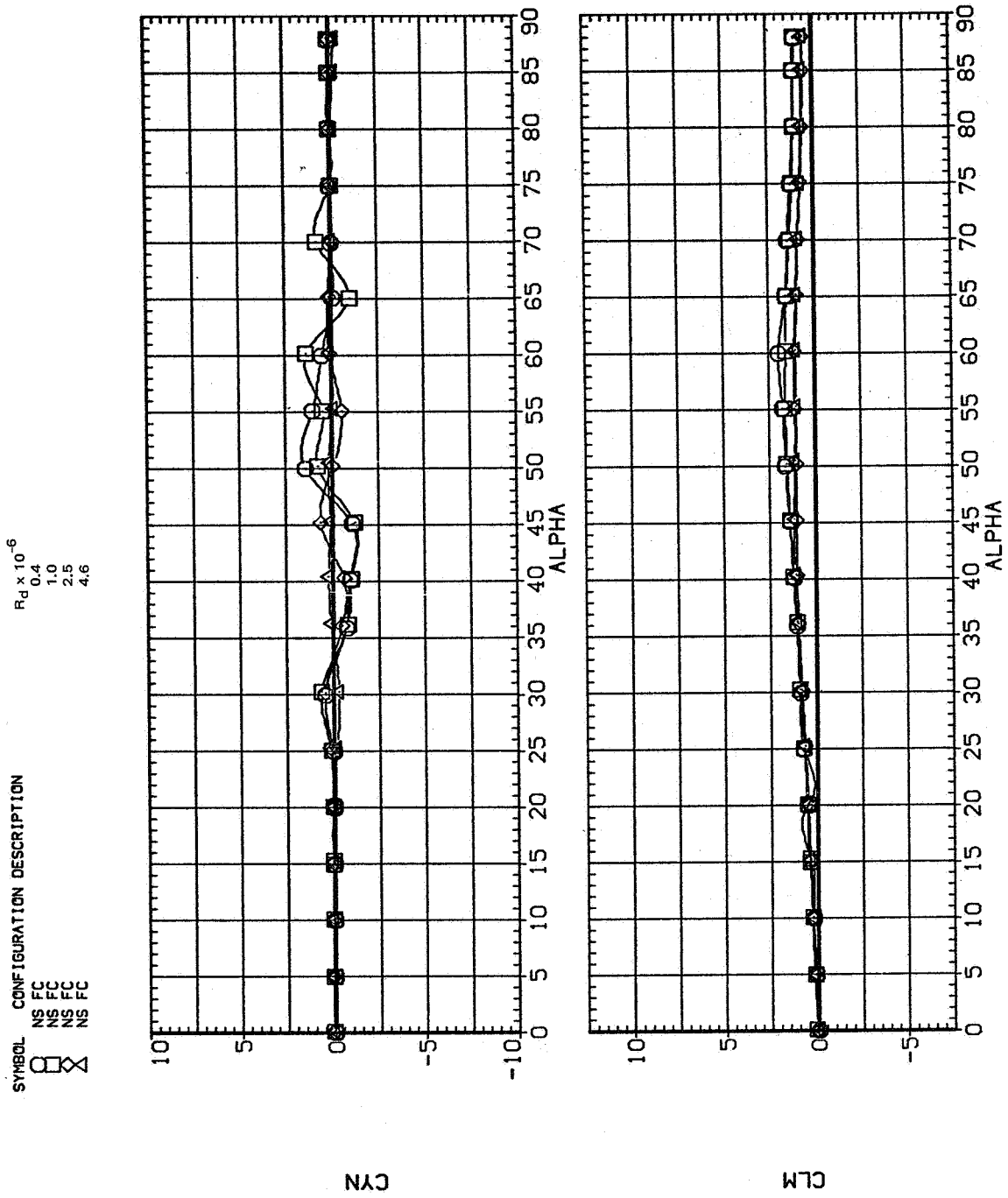

(e) C_n and C_m vs α

Figure 22.– Continued.

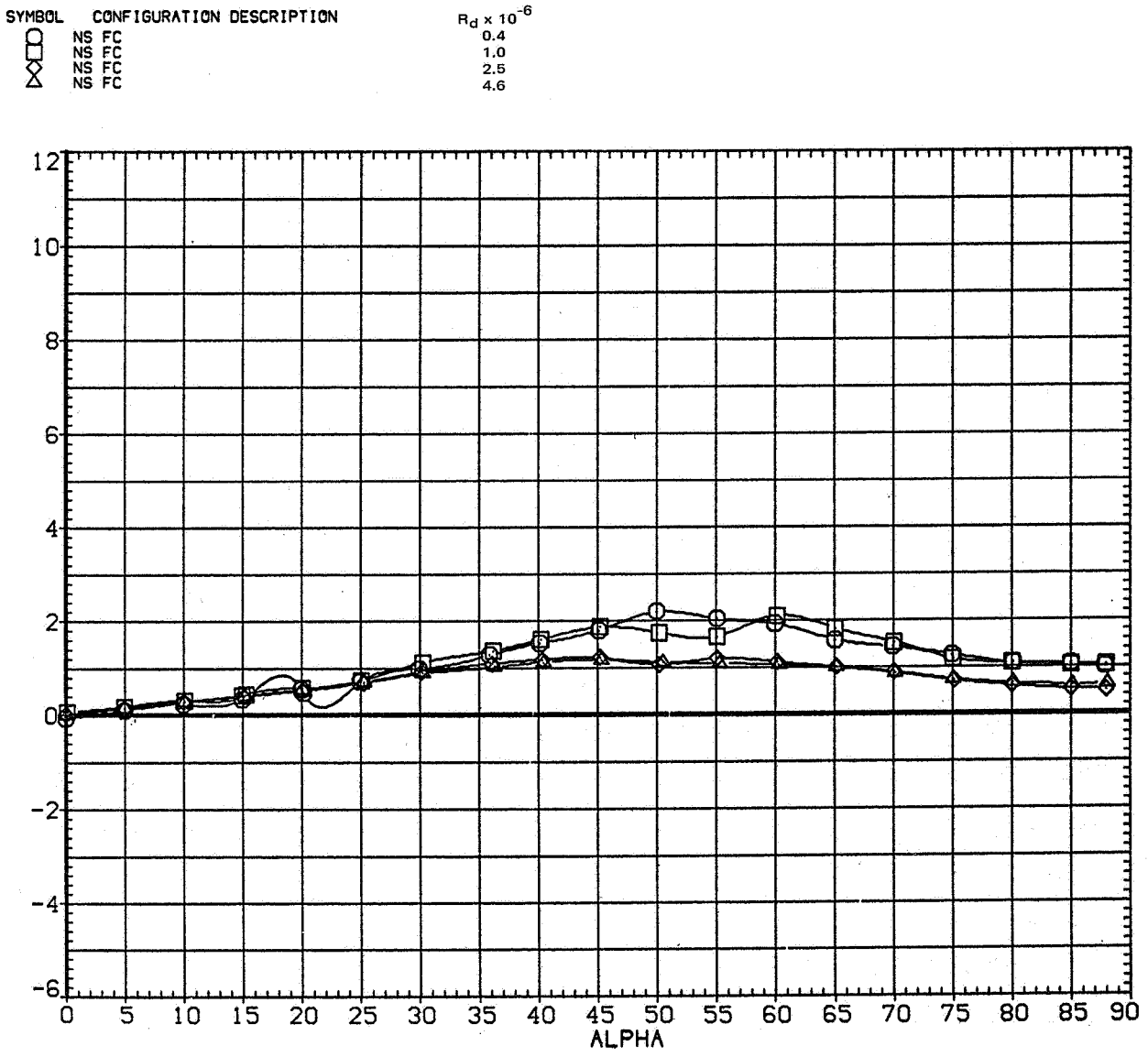

(f) $C_{m,R}$ vs α

Figure 22.– Continued.

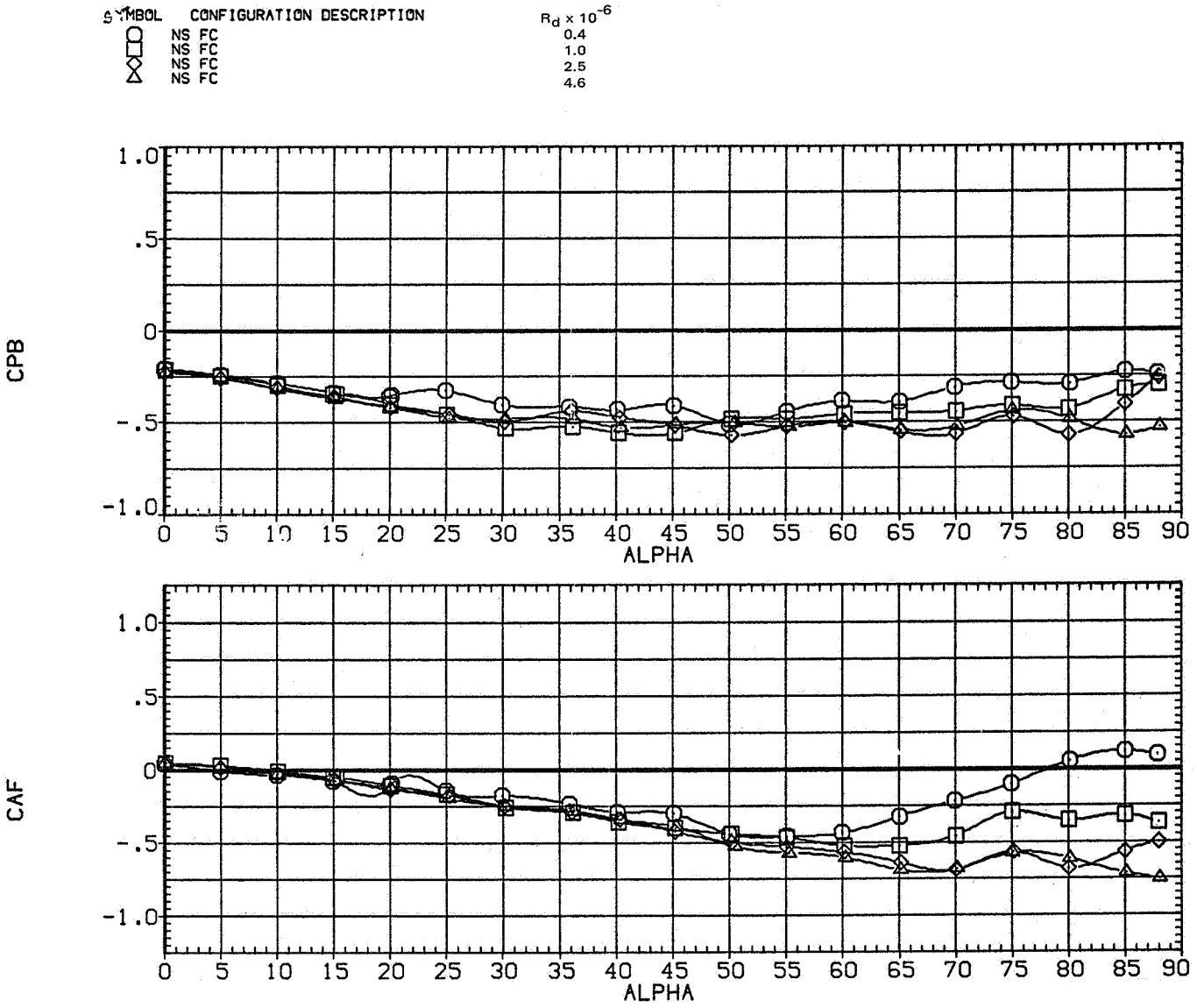

(g) $C_{p,b}$ and C_{AF} vs α

Figure 22.– Concluded.

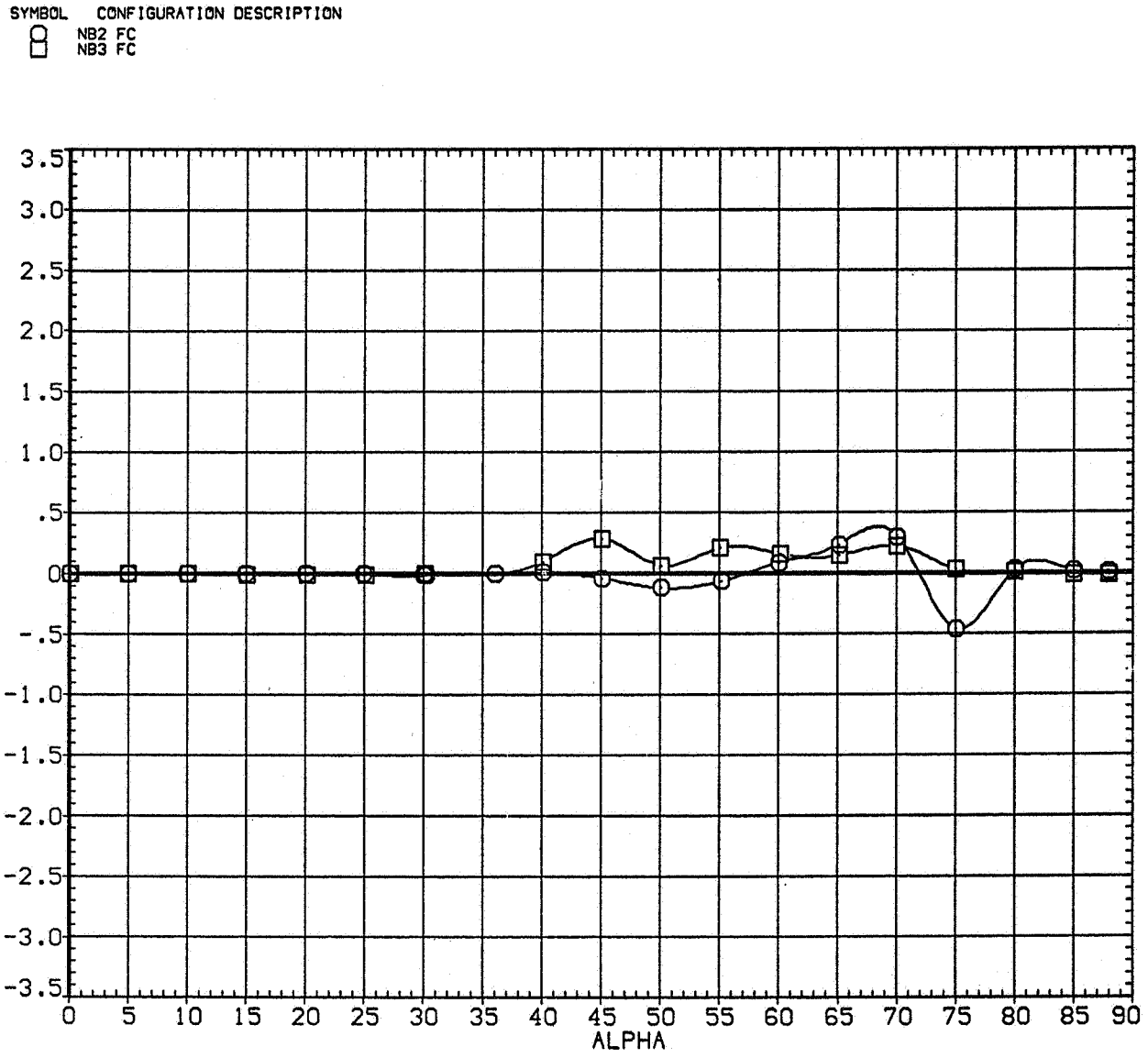

(a) C_Y vs α

Figure 23.– Effect of bluntness for the 20° cone, $M = 0.25$, $R_d = 1 \times 10^6$.

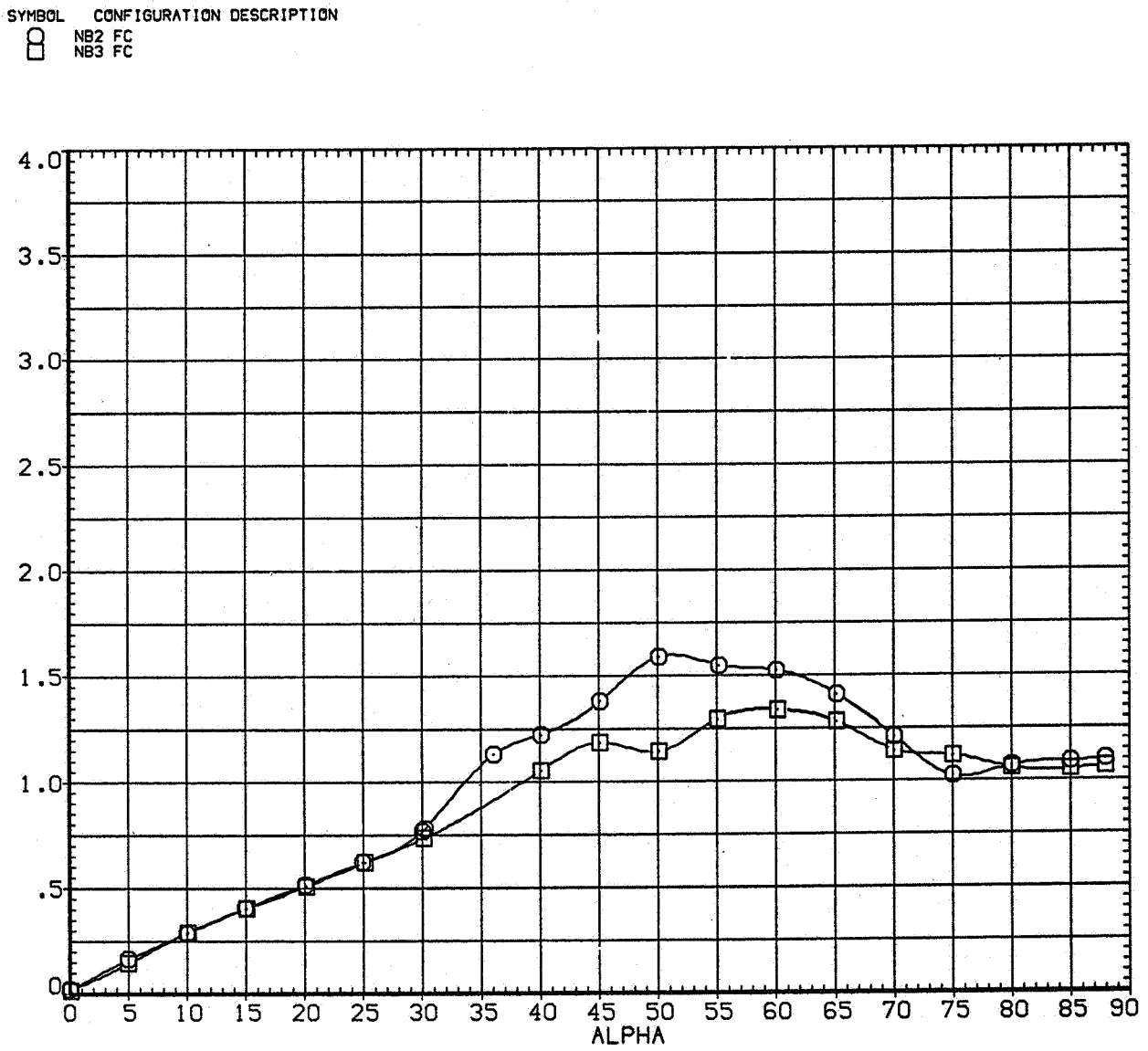

(b) C_N vs α

Figure 23.– Continued.

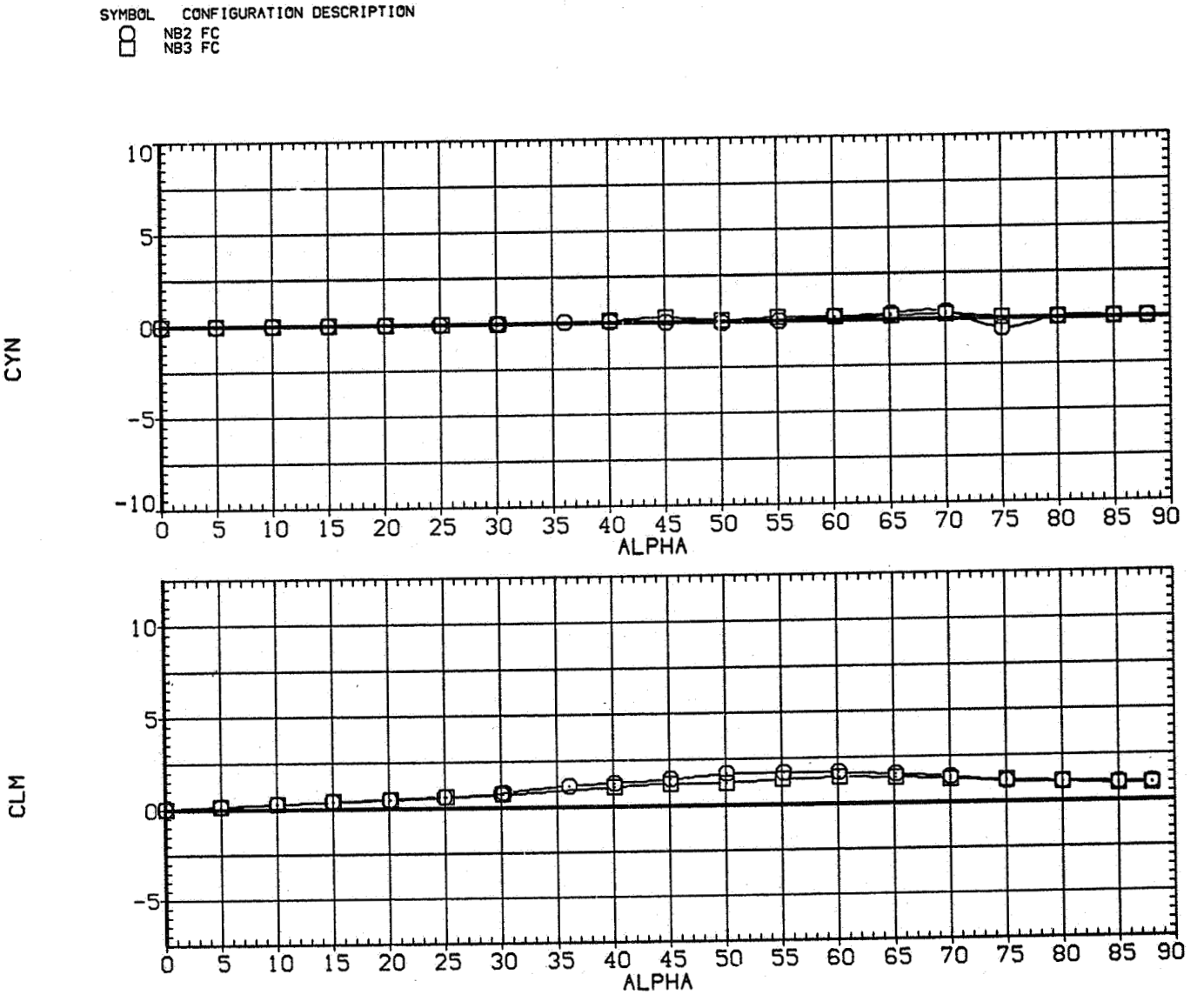

(c) C_n and C_m vs α

Figure 23.– Continued.

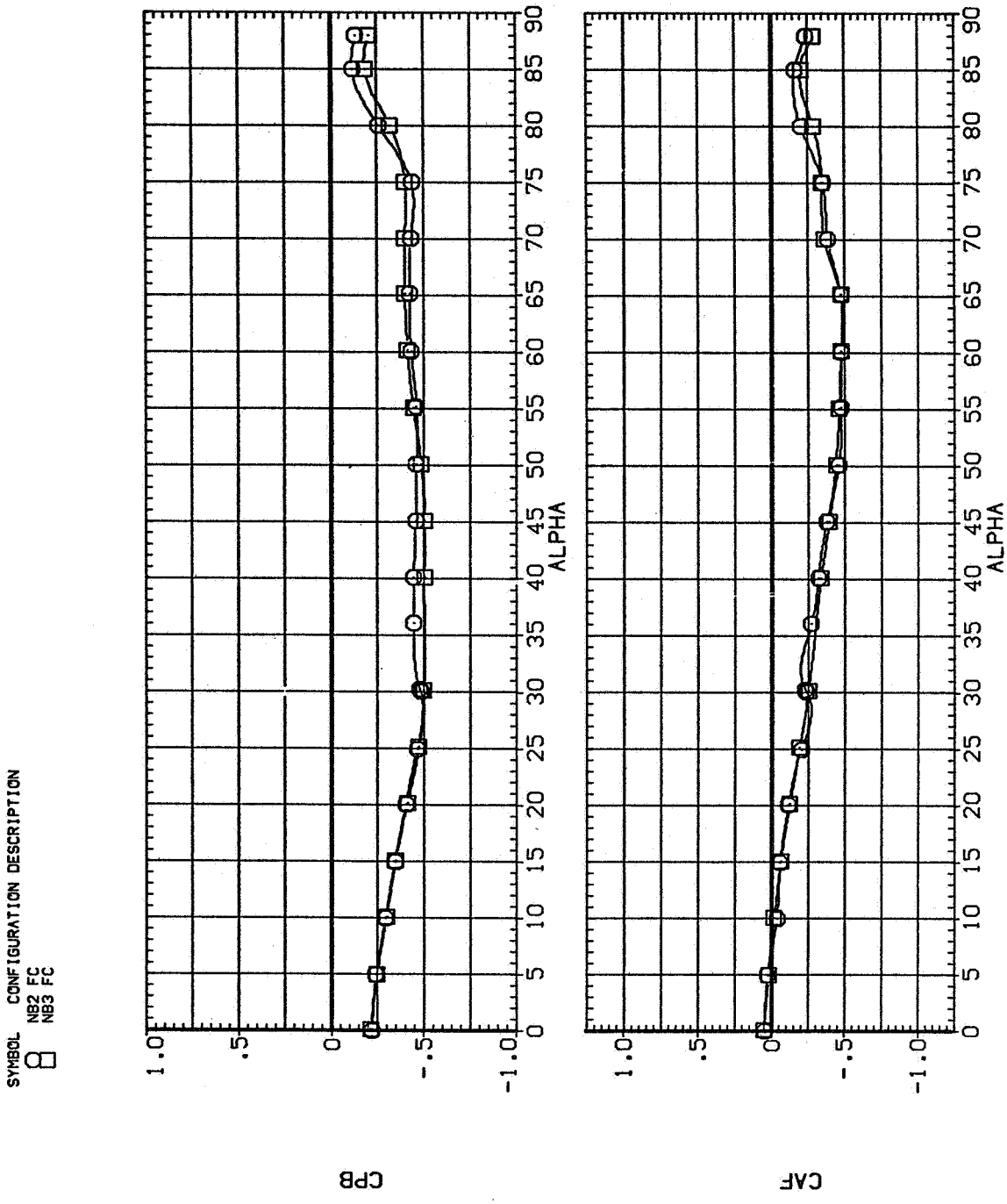

(d) $C_{p,b}$ and C_{AF} vs α

Figure 23.– Concluded.

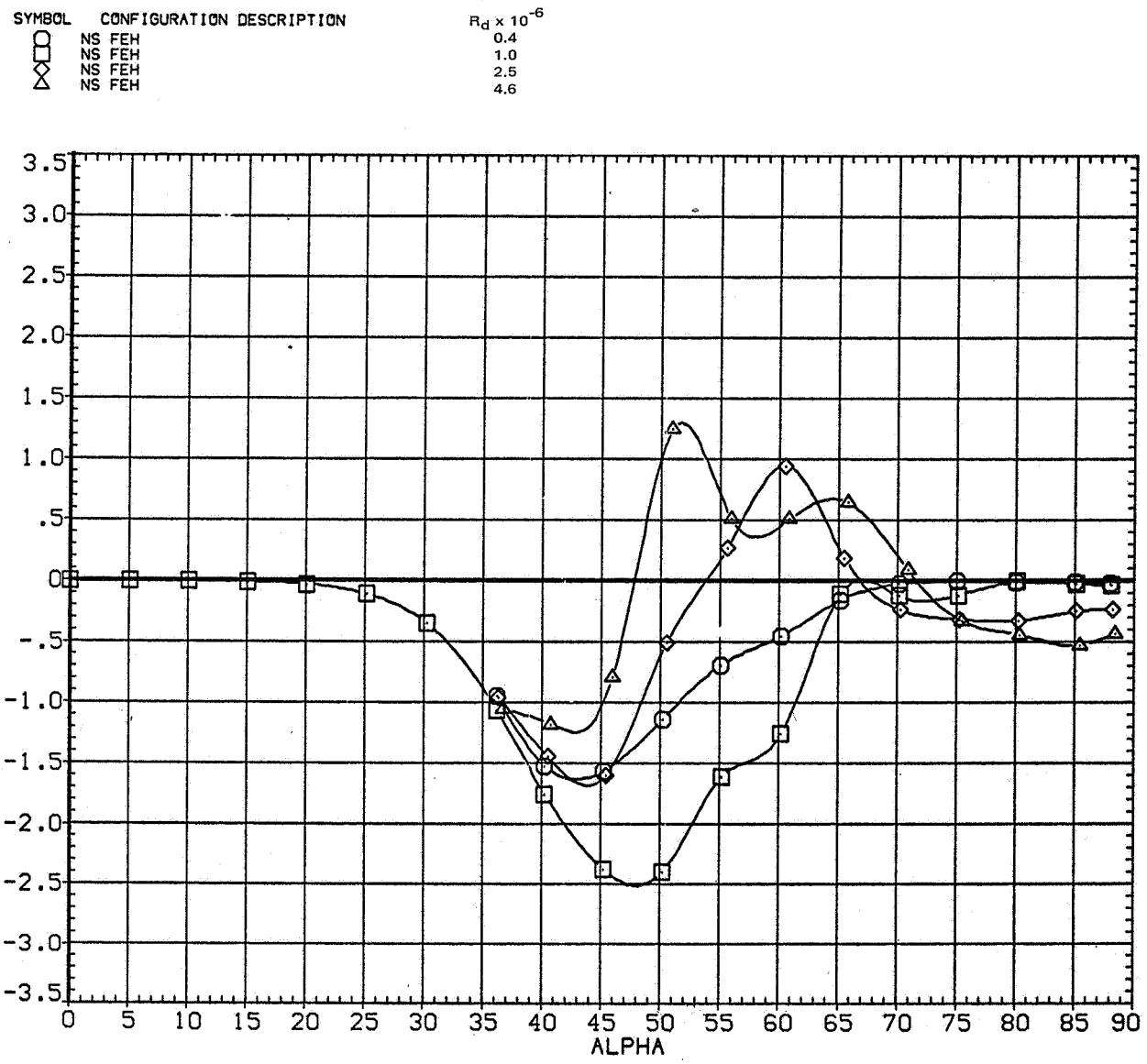

(a) C_Y vs α

Figure 24.– Effect of Reynolds number for the $\ell/b = 3.5$ elliptic tangent ogive, $M = 0.25$.

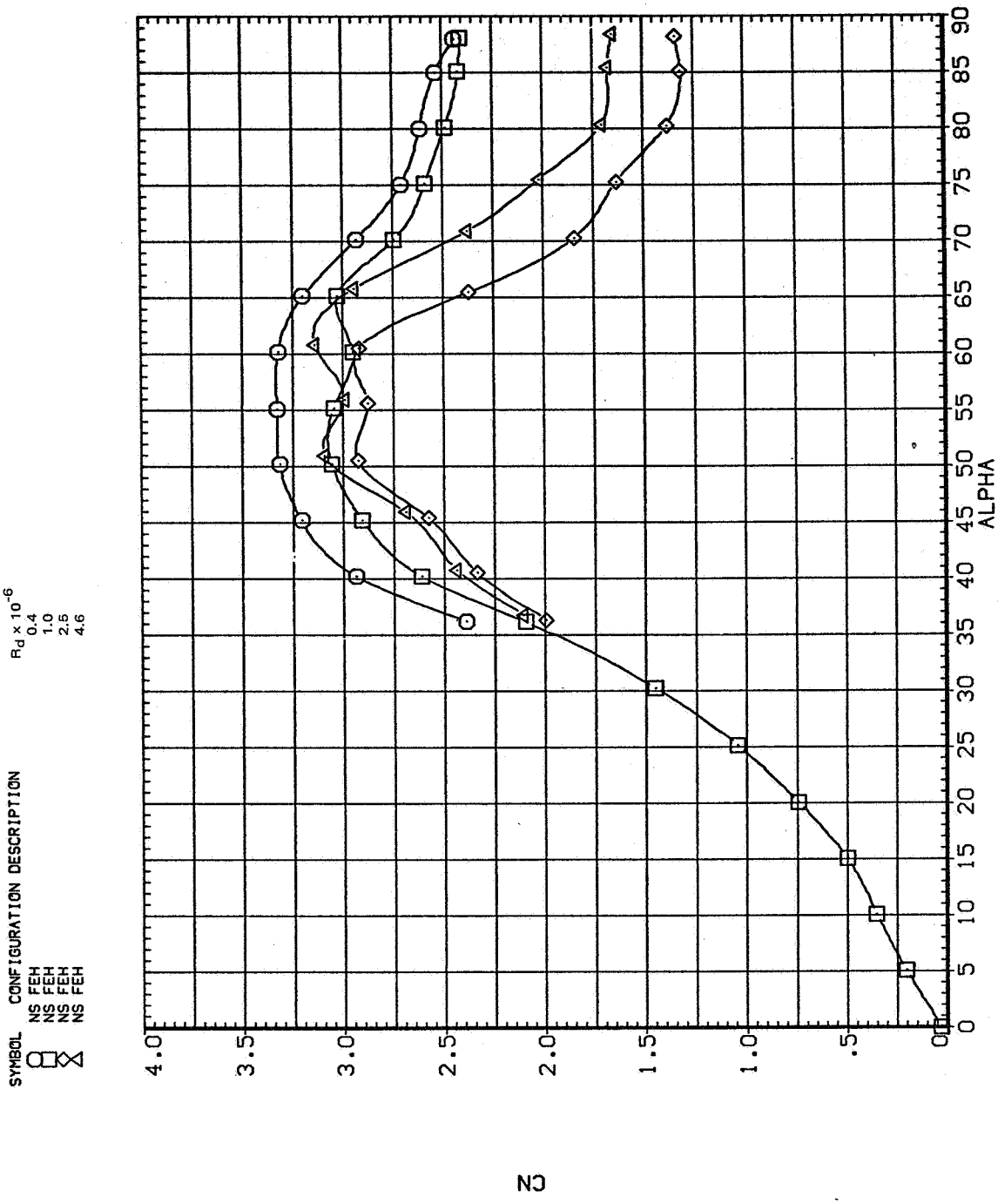

(b) C_N vs α

Figure 24.– Continued.

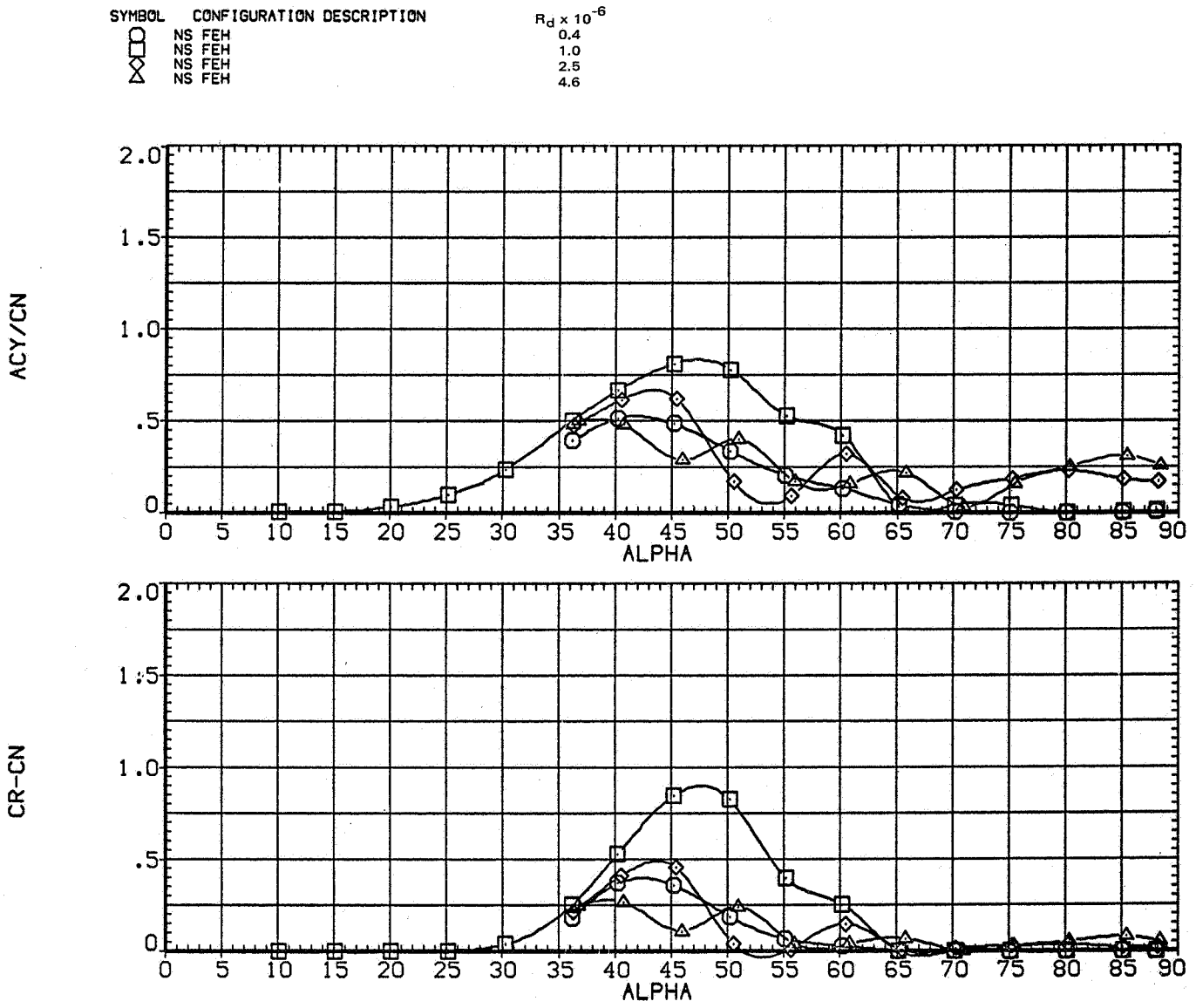

(c) $|C_Y|/|C_N|$ and $C_R - C_N$ vs α

Figure 24.– Continued.

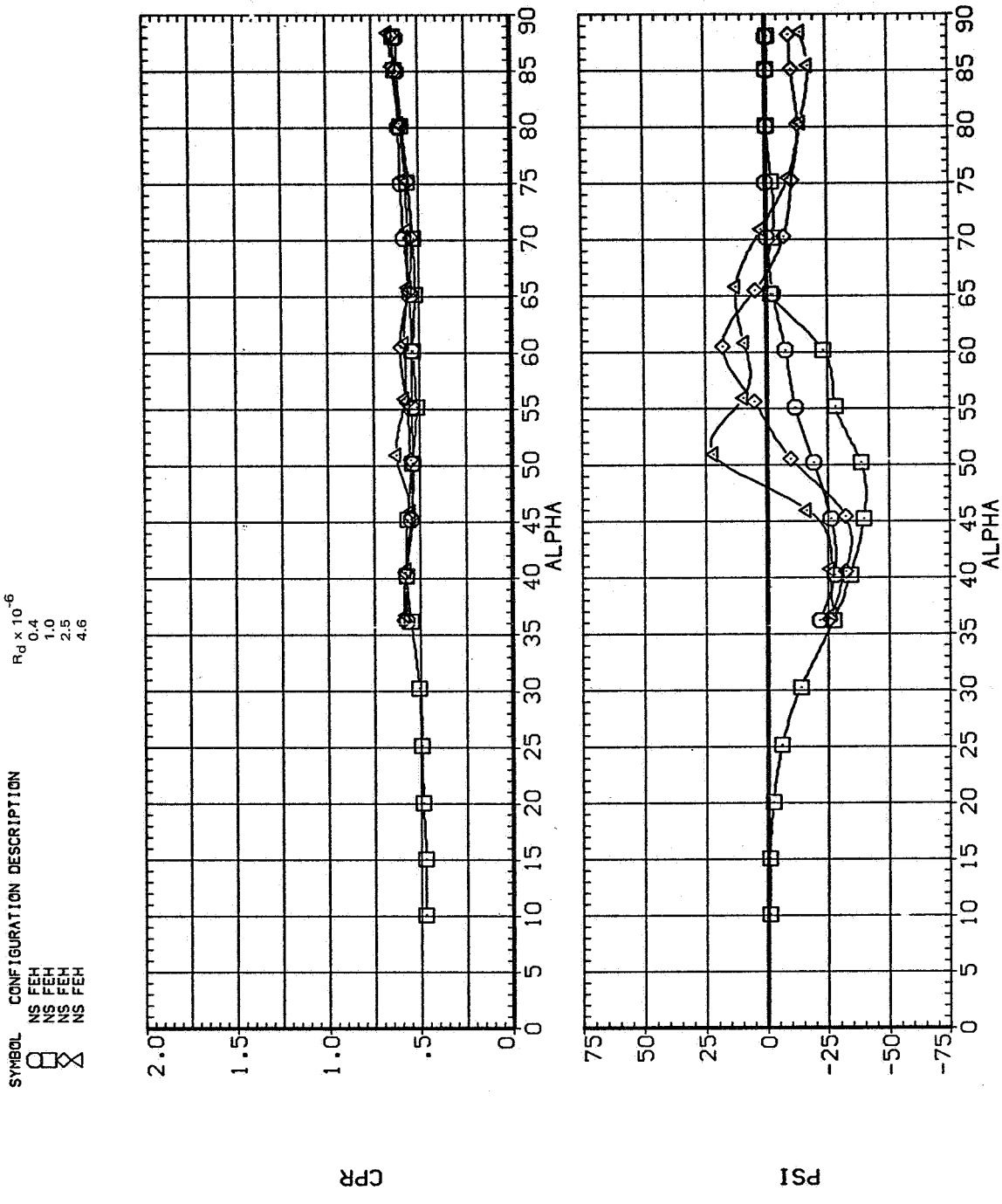

(d) CP_R and Ψ vs α

Figure 24.– Continued.

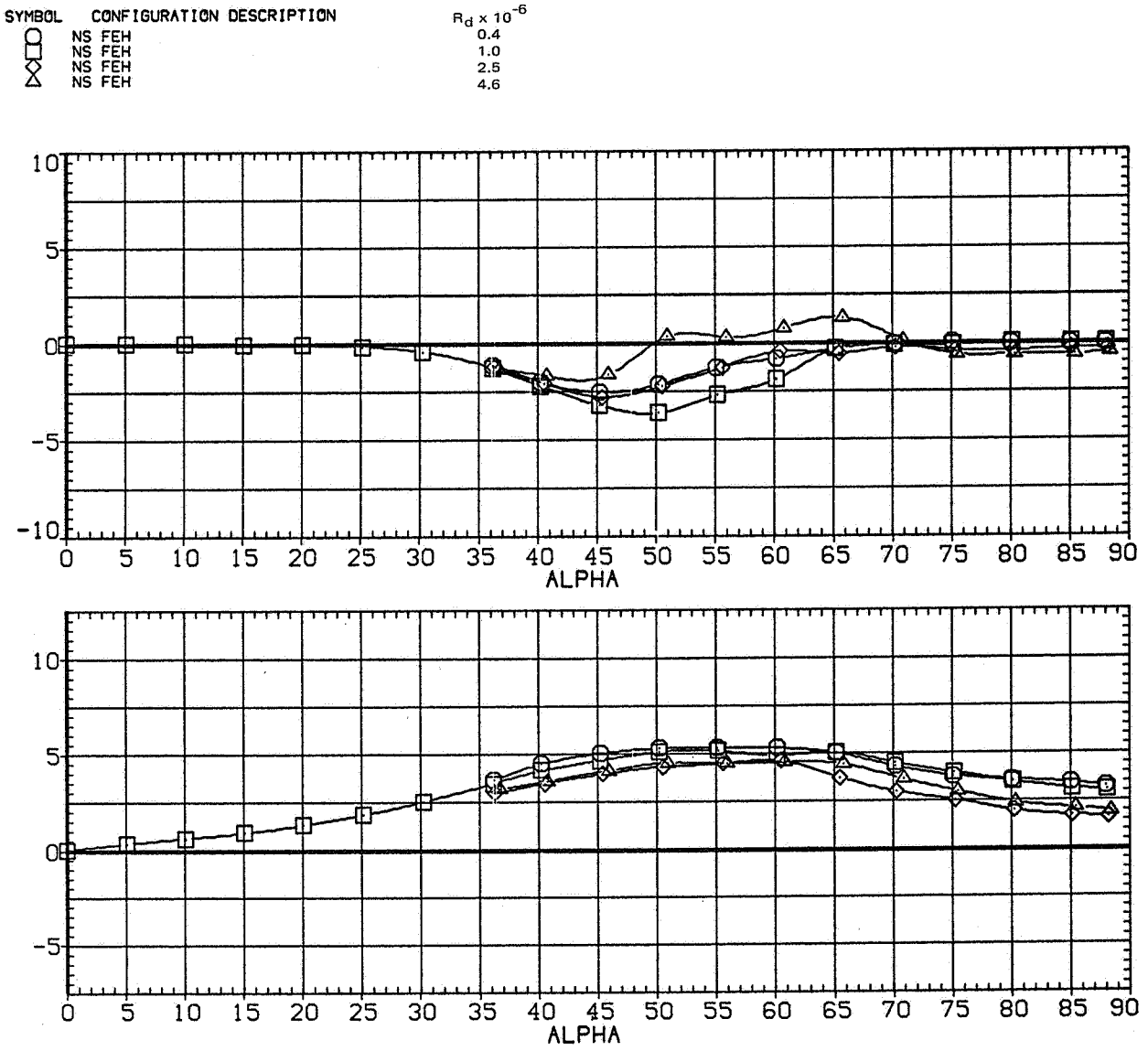

(e) C_n and C_m vs α

Figure 24.– Continued.

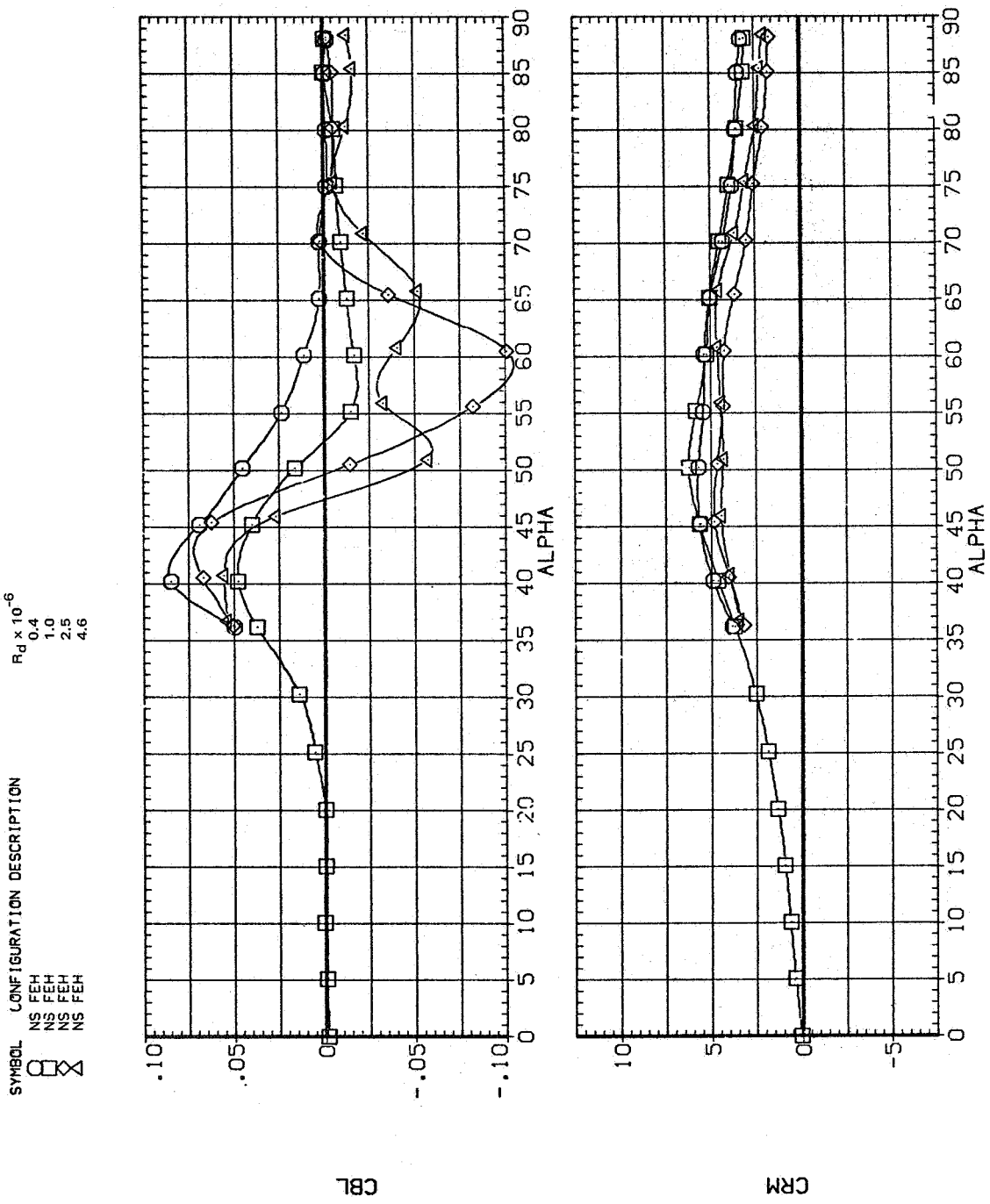

(f) C_{ℓ} and $C_{m,R}$ vs α

Figure 24.– Continued.

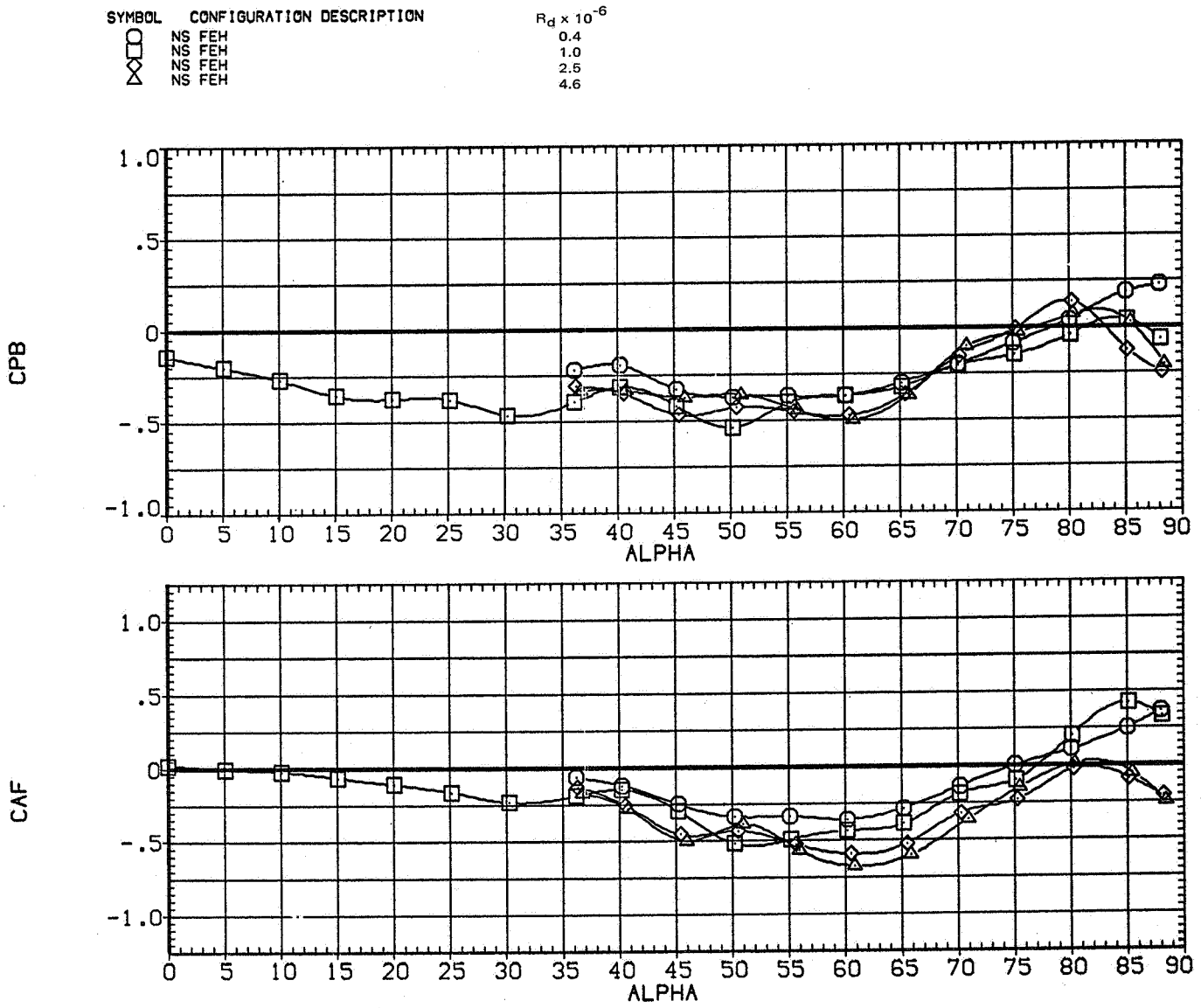

(g) $C_{p,b}$ and C_{AF} vs α

Figure 24.– Concluded.

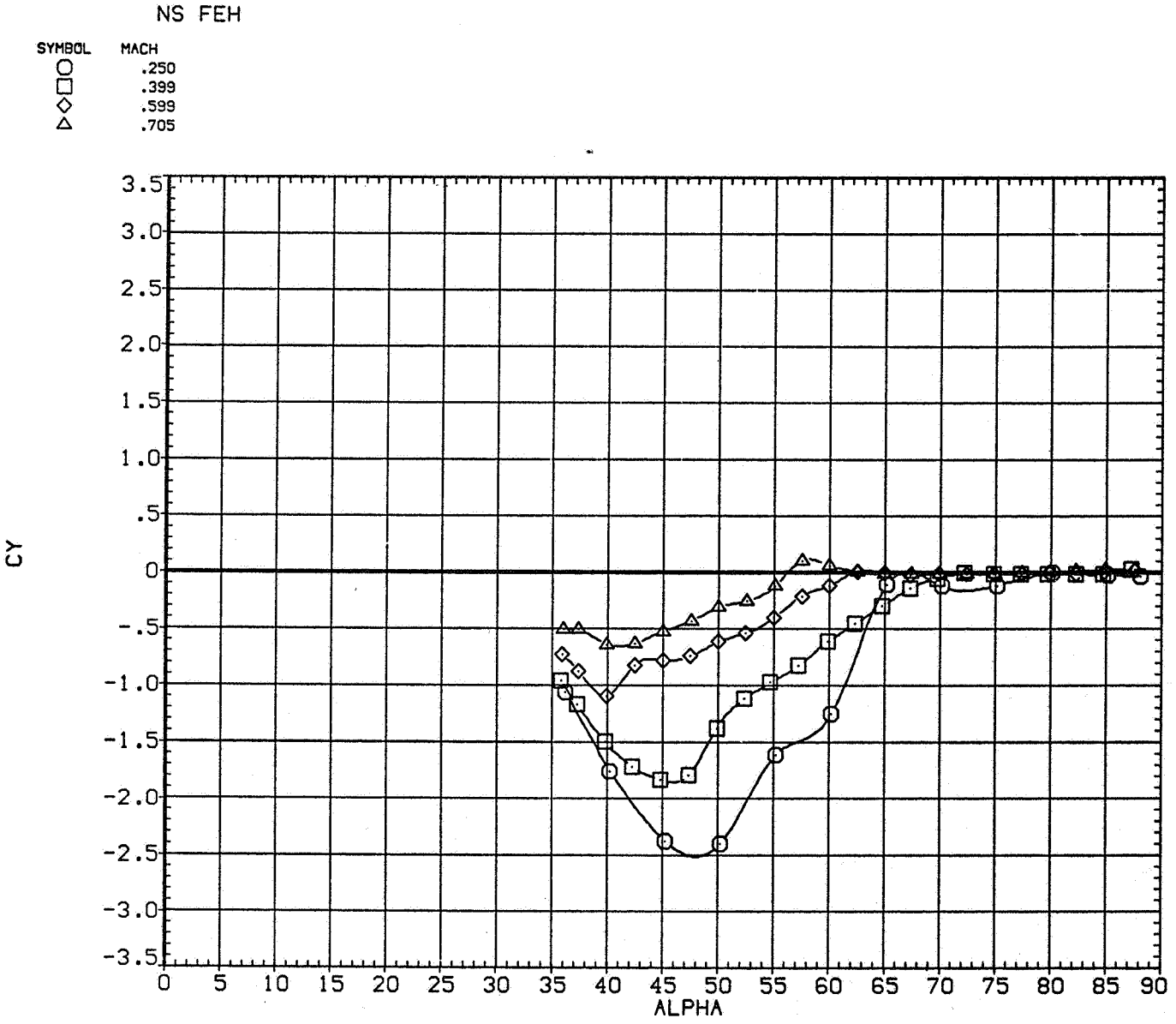

(a) C_Y vs α

Figure 25.– Effect of Mach number for the $\ell/b = 3.5$ elliptic tangent ogive, $R_d = 1 \times 10^6$.

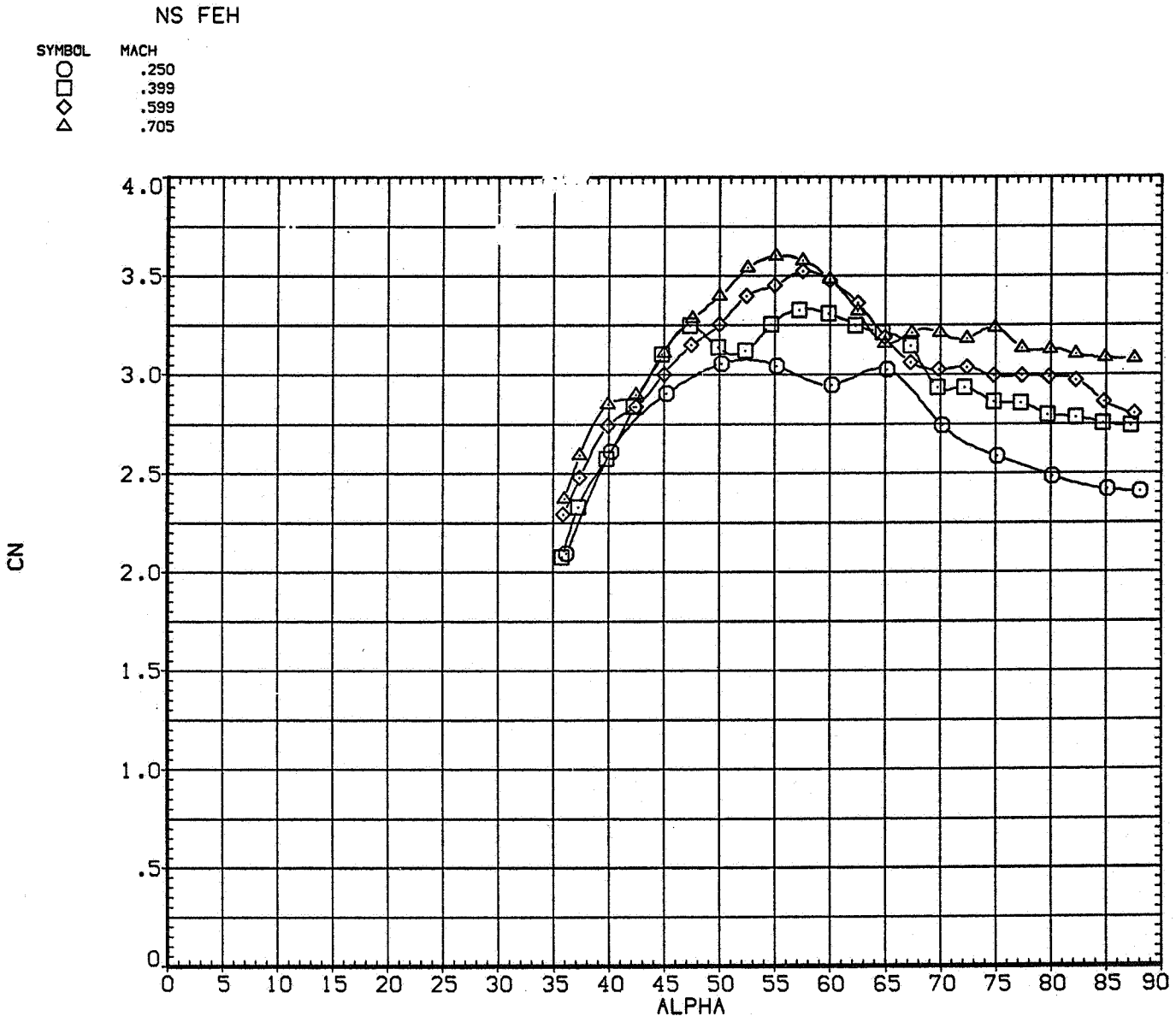

(b) C_N vs α

Figure 25.– Continued.

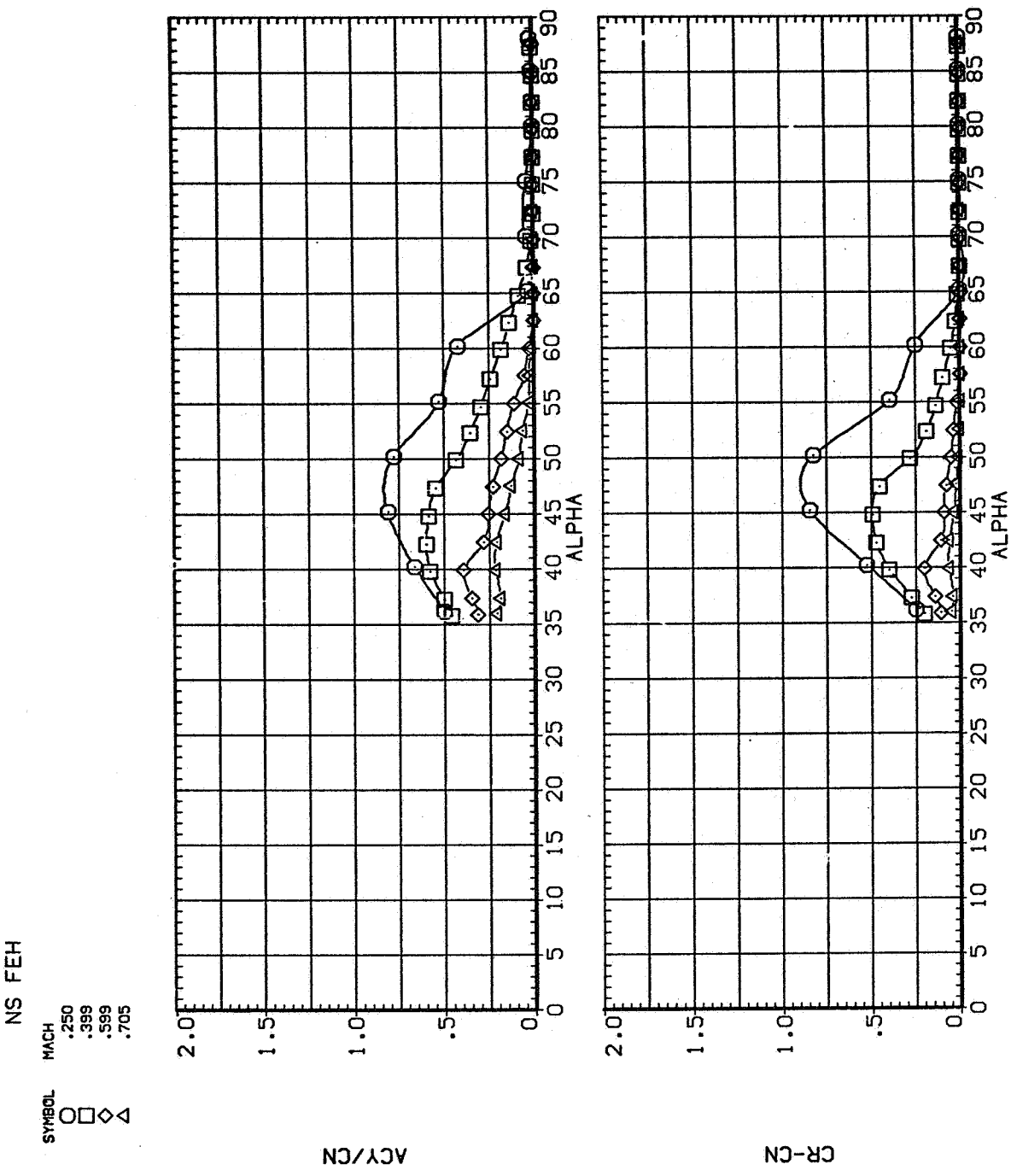

(c) $|C_Y|/|C_N|$ and $C_R - C_N$ vs α

Figure 25.– Continued.

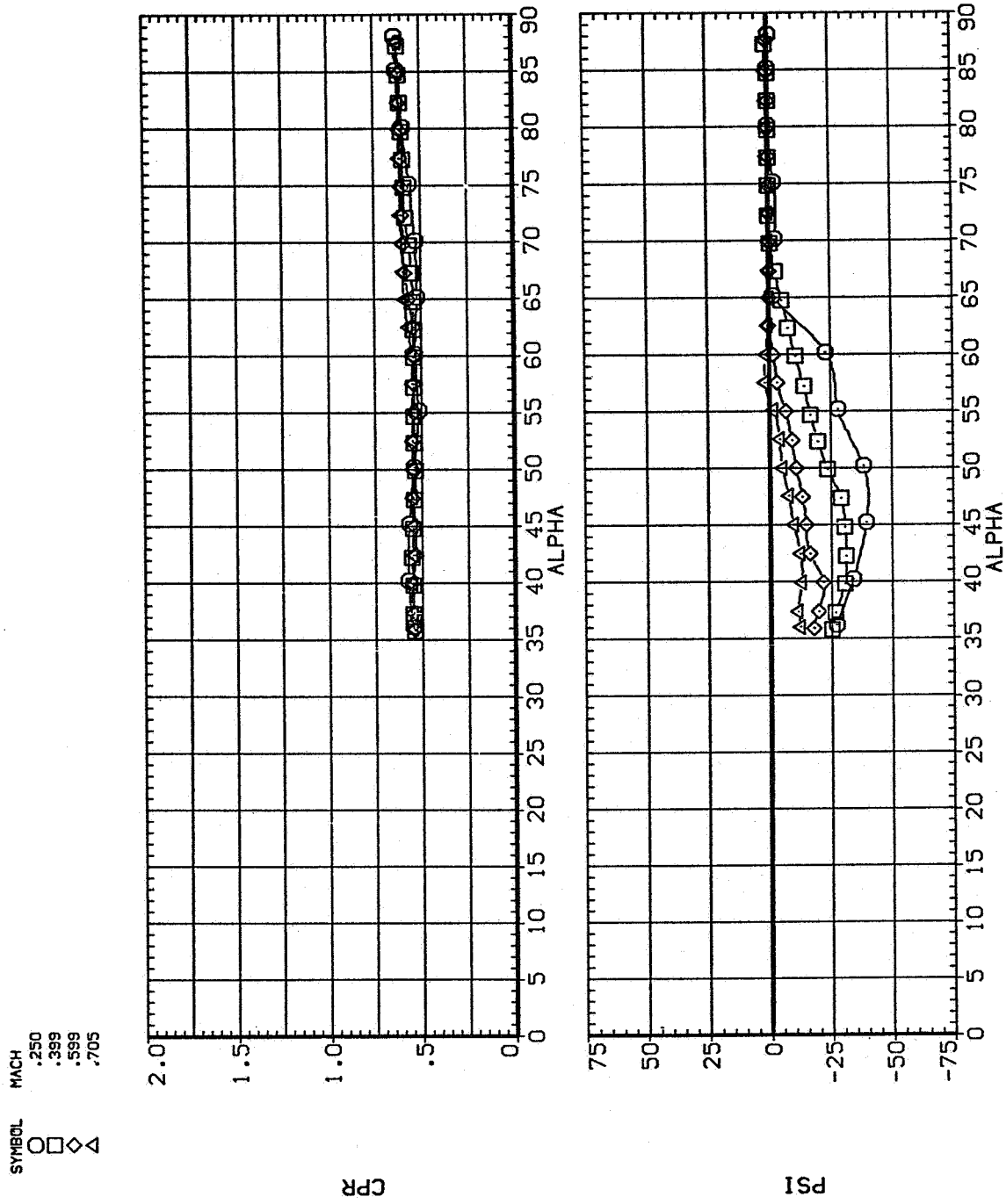

(d) CP_R and Ψ vs α

Figure 25.– Continued.

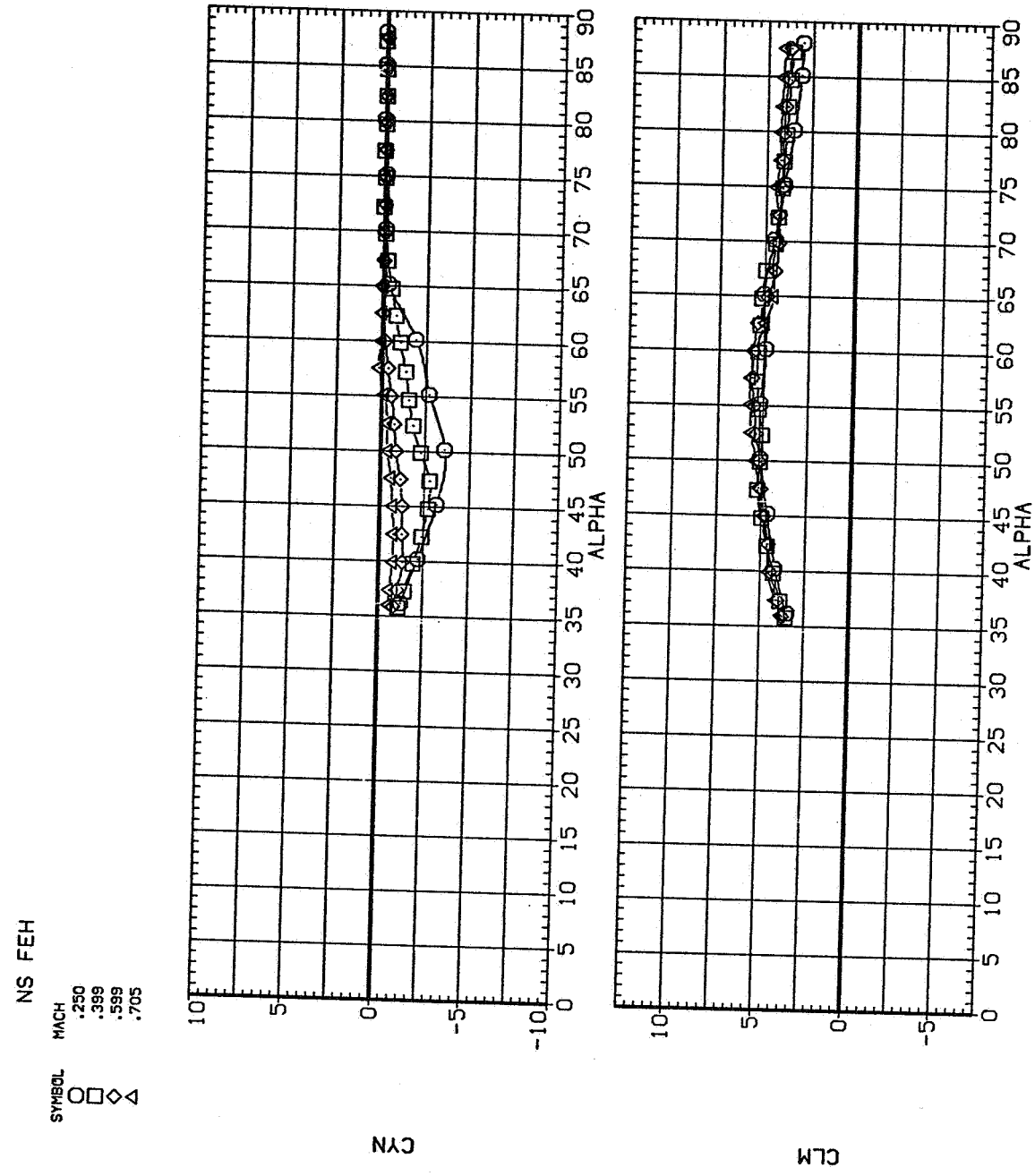

(e) C_n and C_m vs α

Figure 25.– Continued.

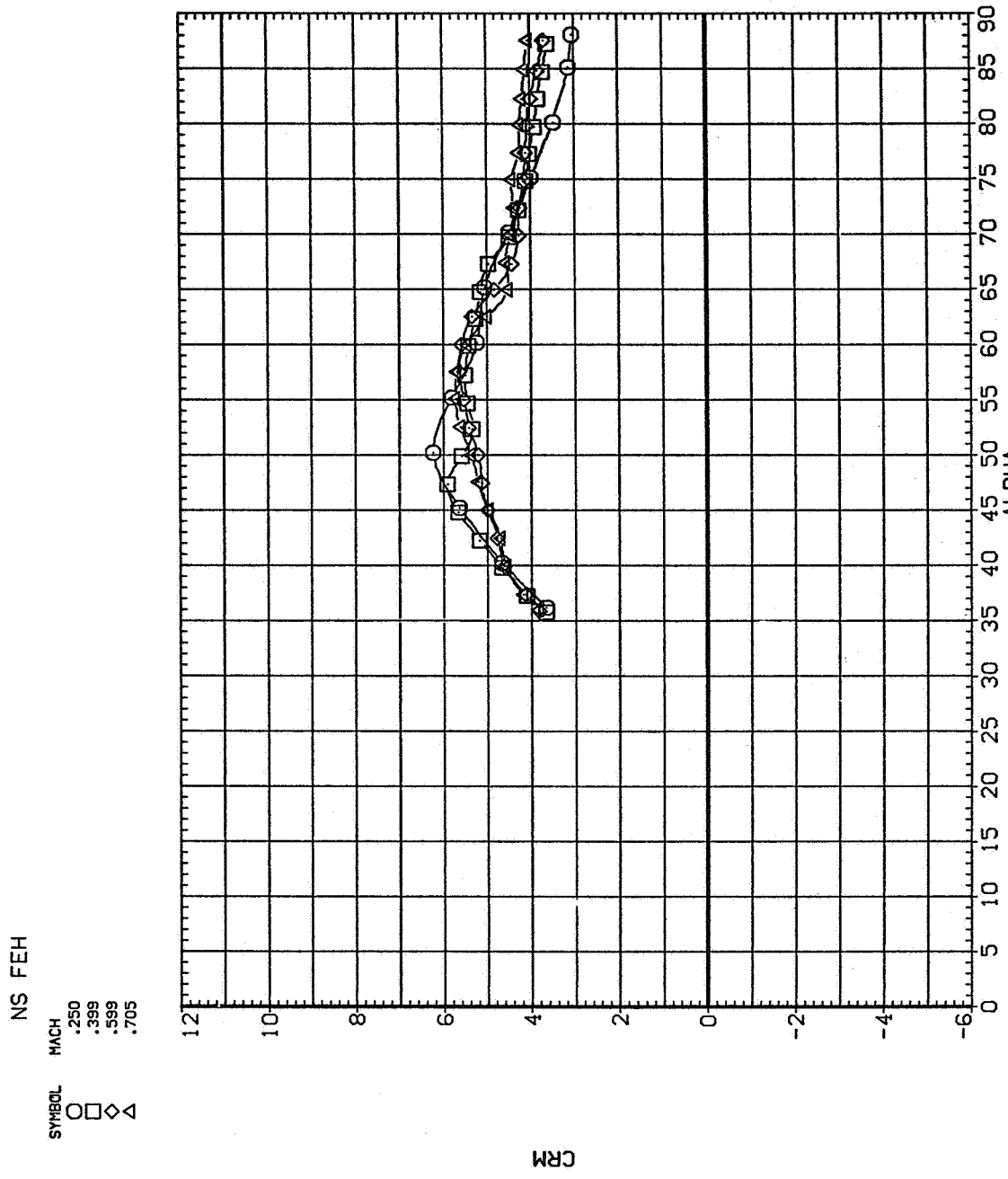

(f) $C_{m,R}$ vs α

Figure 25.– Concluded.

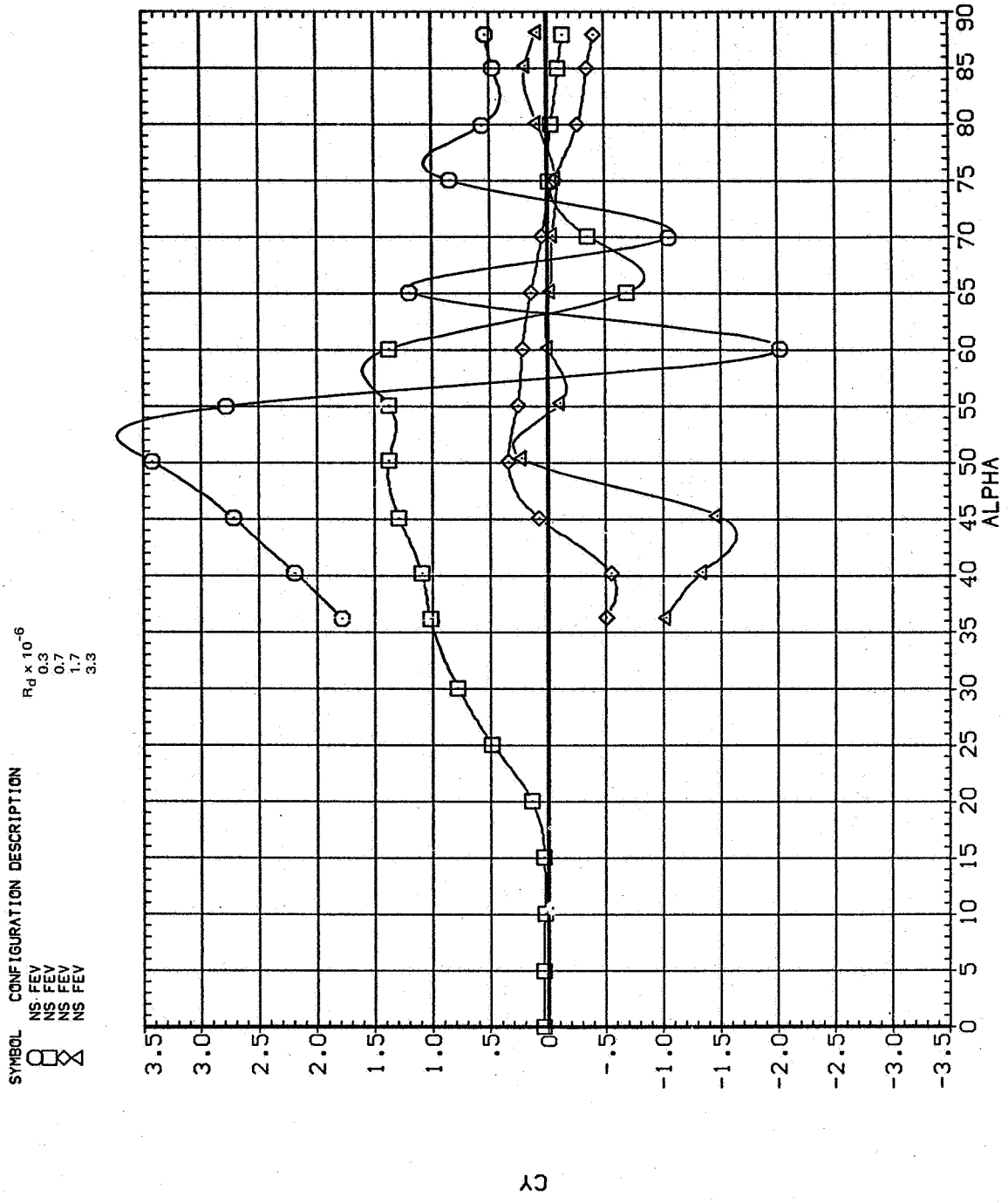

(a) C_Y vs α

Figure 26.– Effect of Reynolds number for the $\ell/b = 3.5$ elliptic tangent ogive, $M = 0.25$.

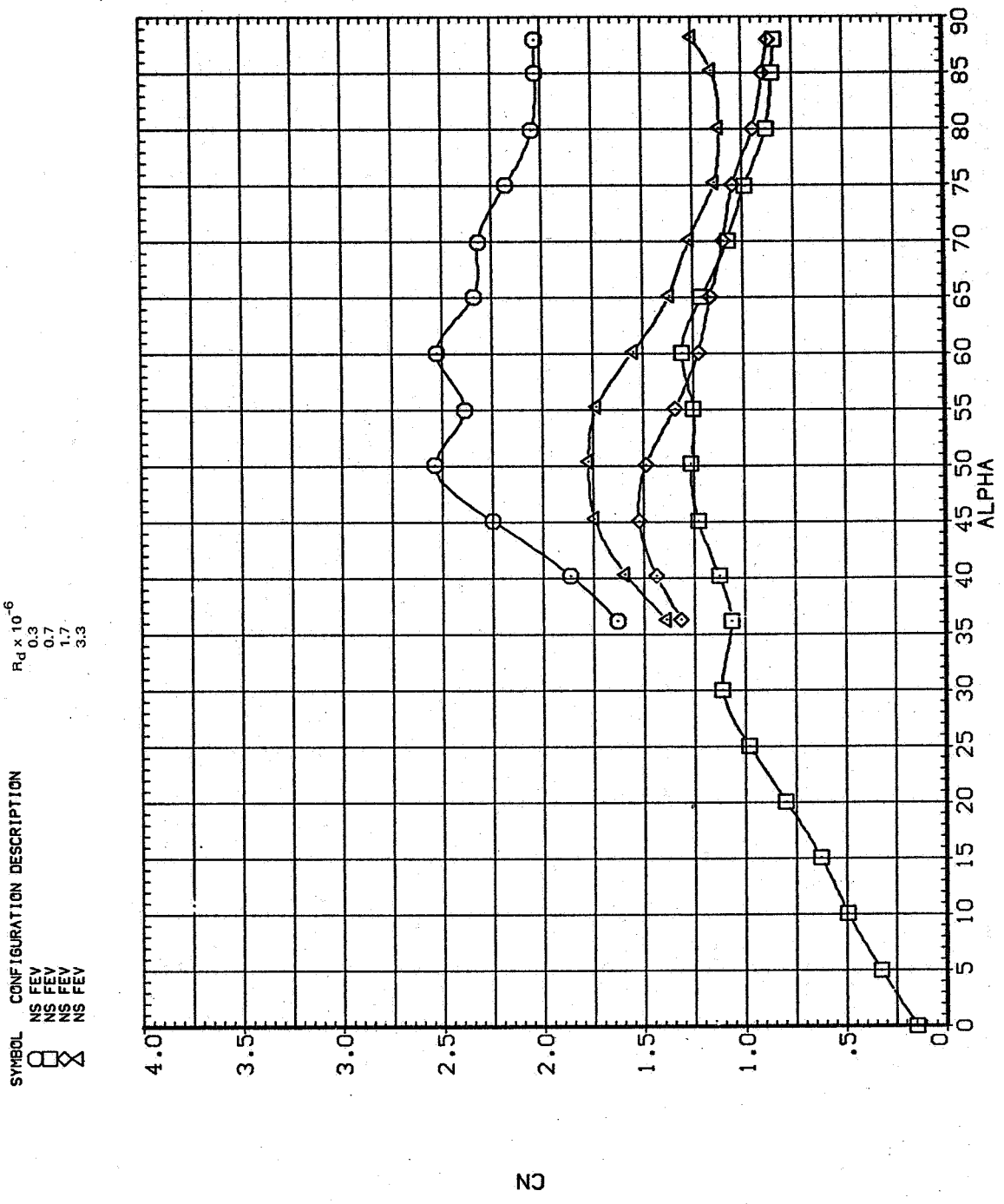

(b) C_N vs α

Figure 26.– Continued.

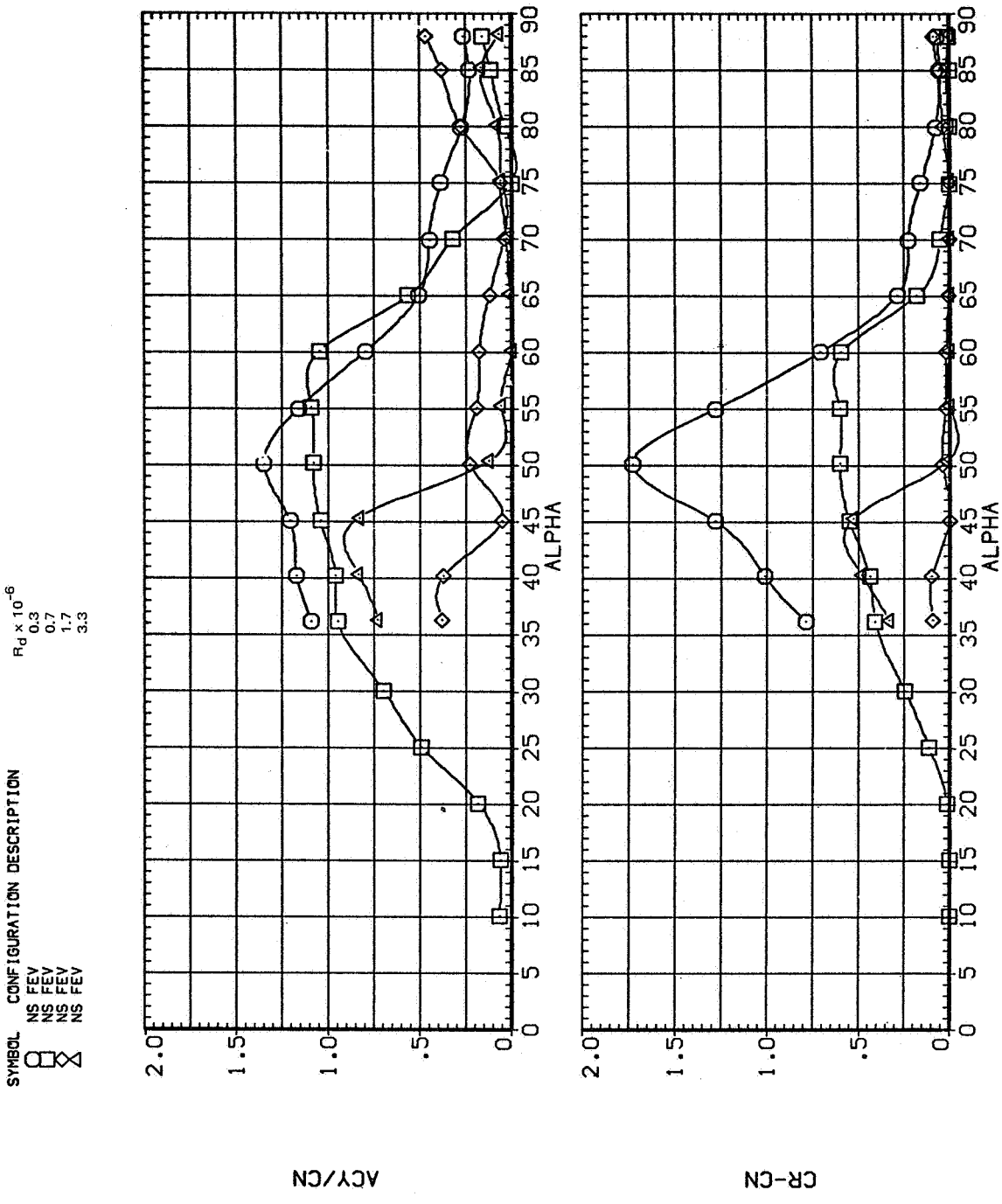

(c) $|C_Y|/|C_N|$ and $C_R - C_N$ vs α

Figure 26.– Continued.

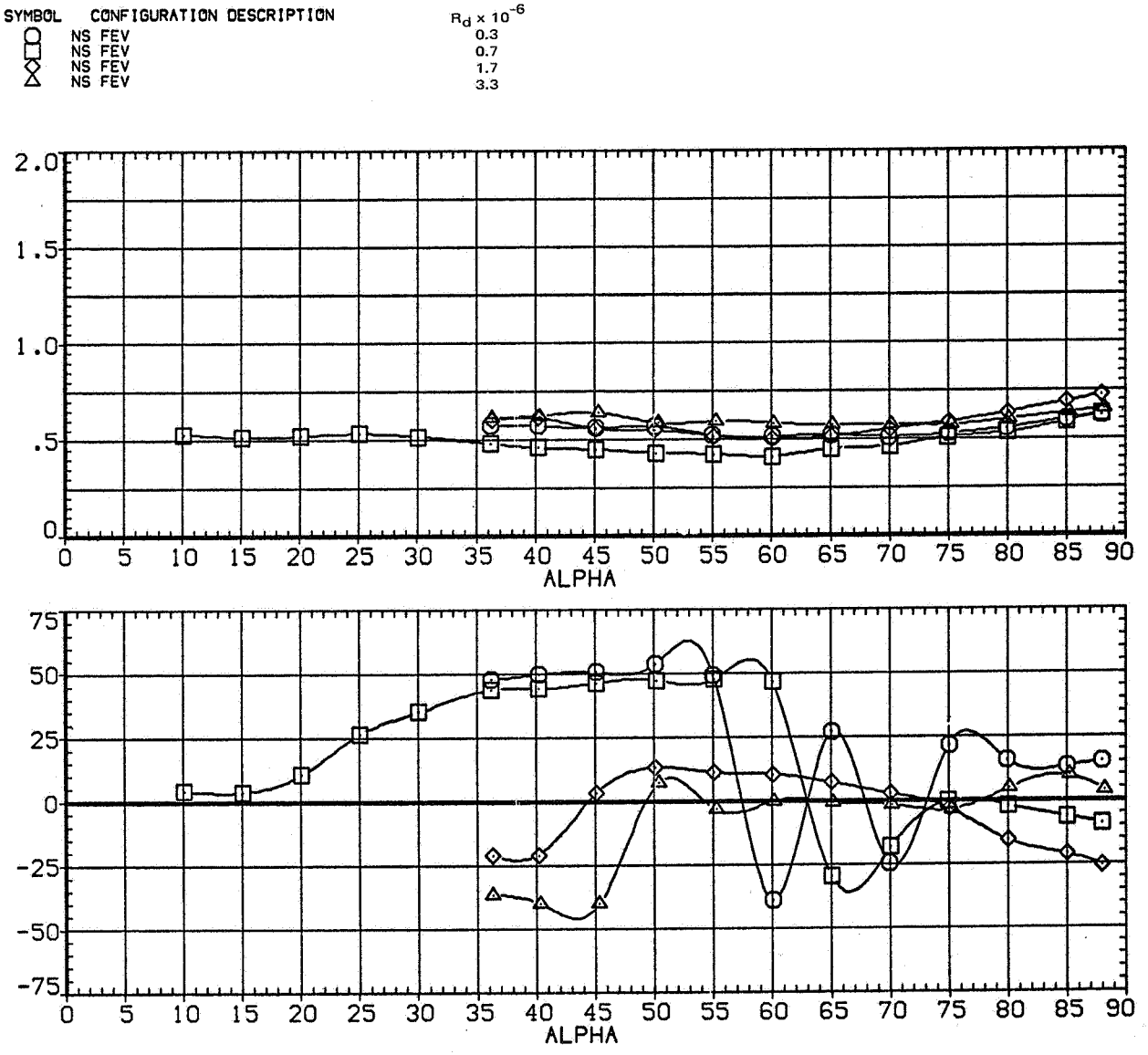

(d) CP_R and Ψ vs α

Figure 26.– Continued.

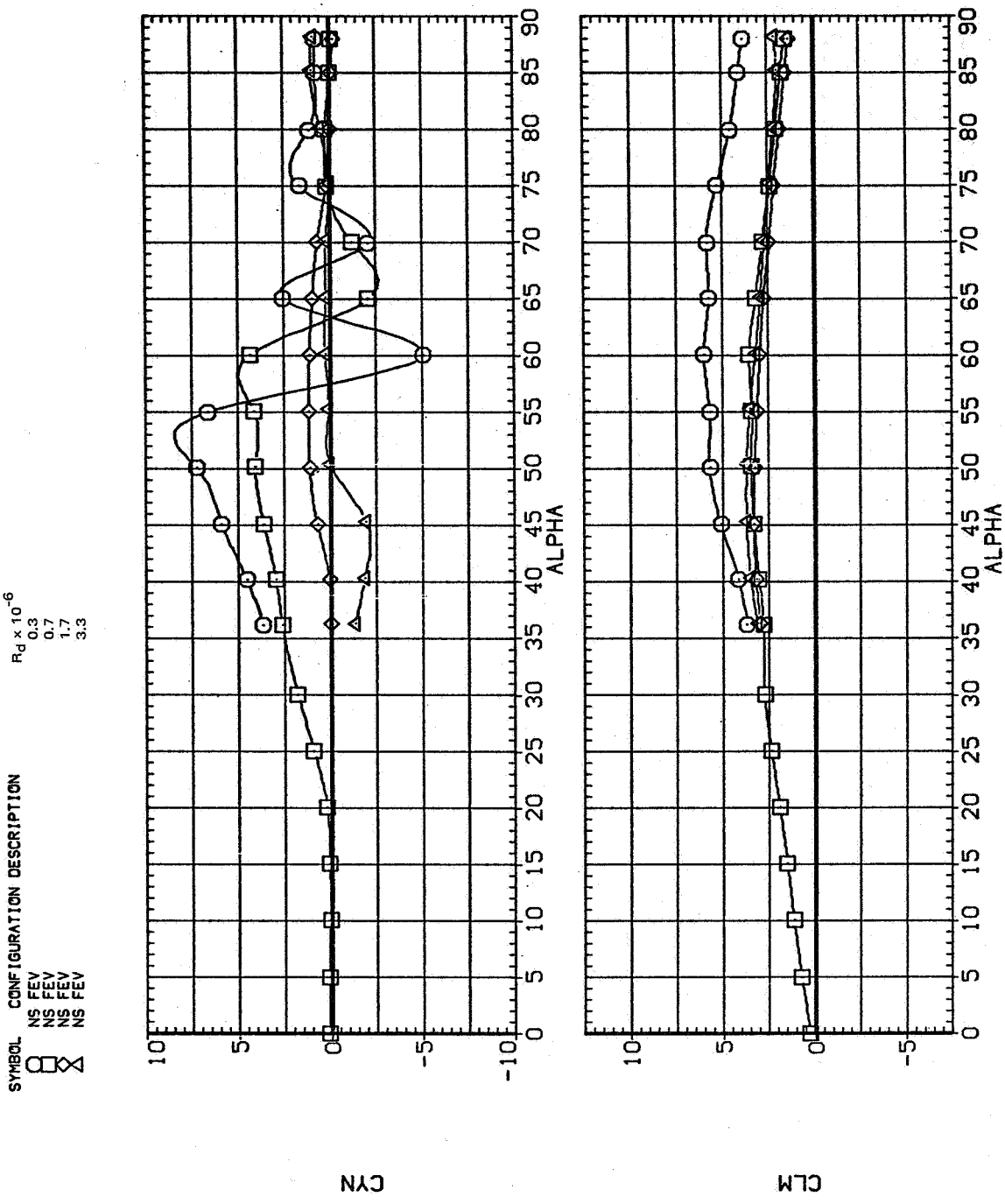

(e) C_n and C_m vs α

Figure 26.– Continued.

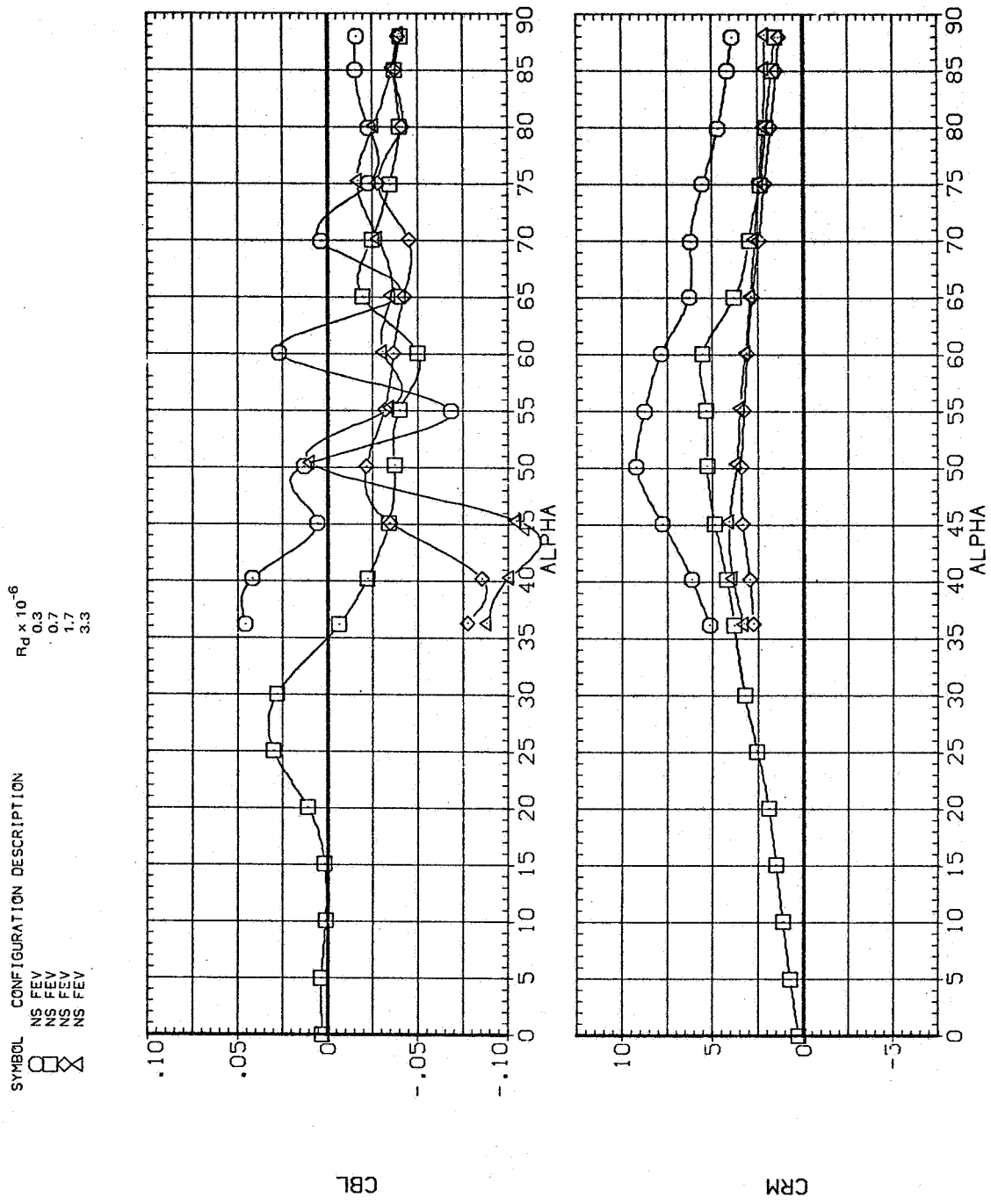

(f) C_{ℓ} and $C_{m,R}$ vs α

Figure 26.– Continued.

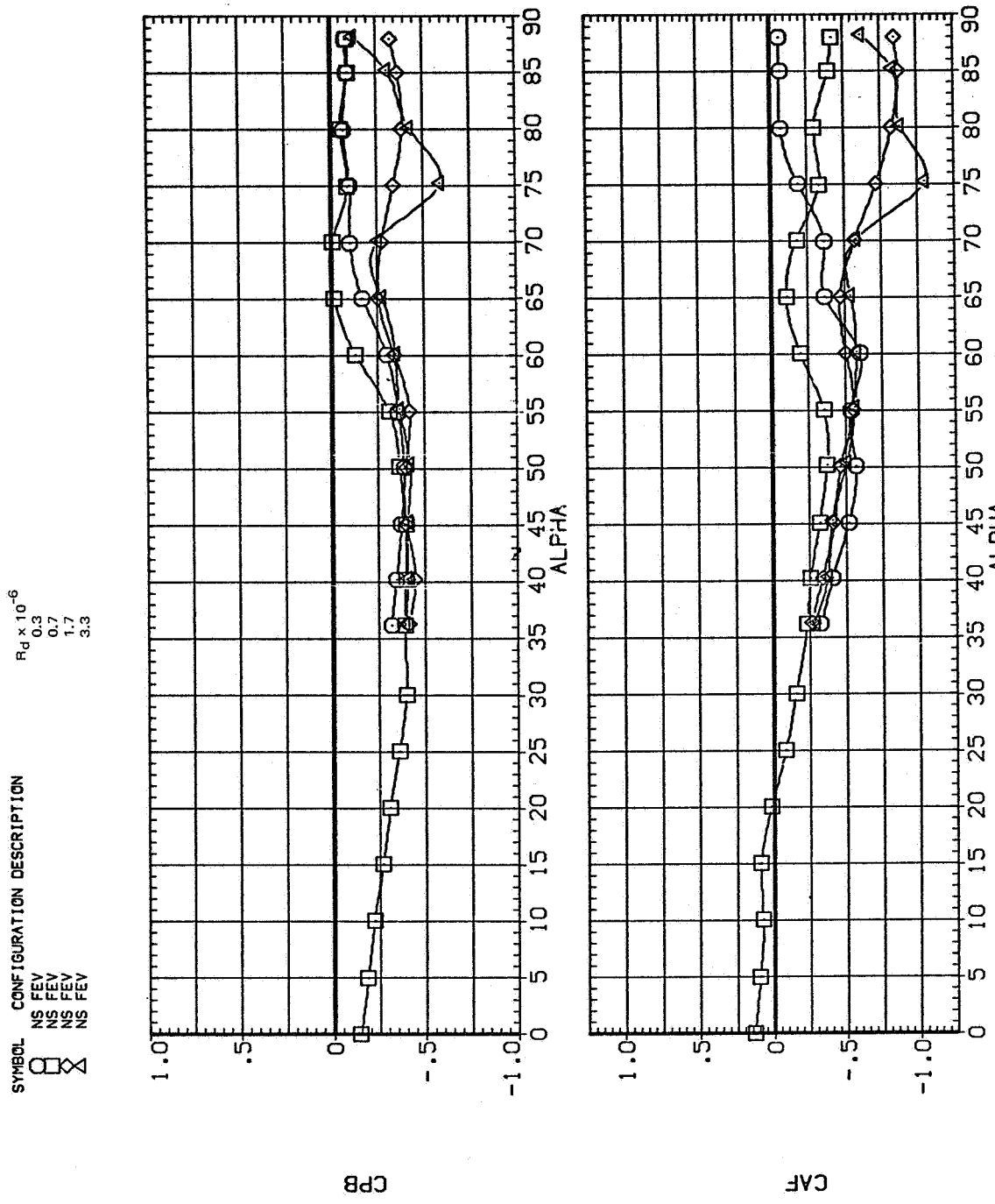

(g) $C_{p,b}$ and C_{AF} vs α

Figure 26.– Concluded.

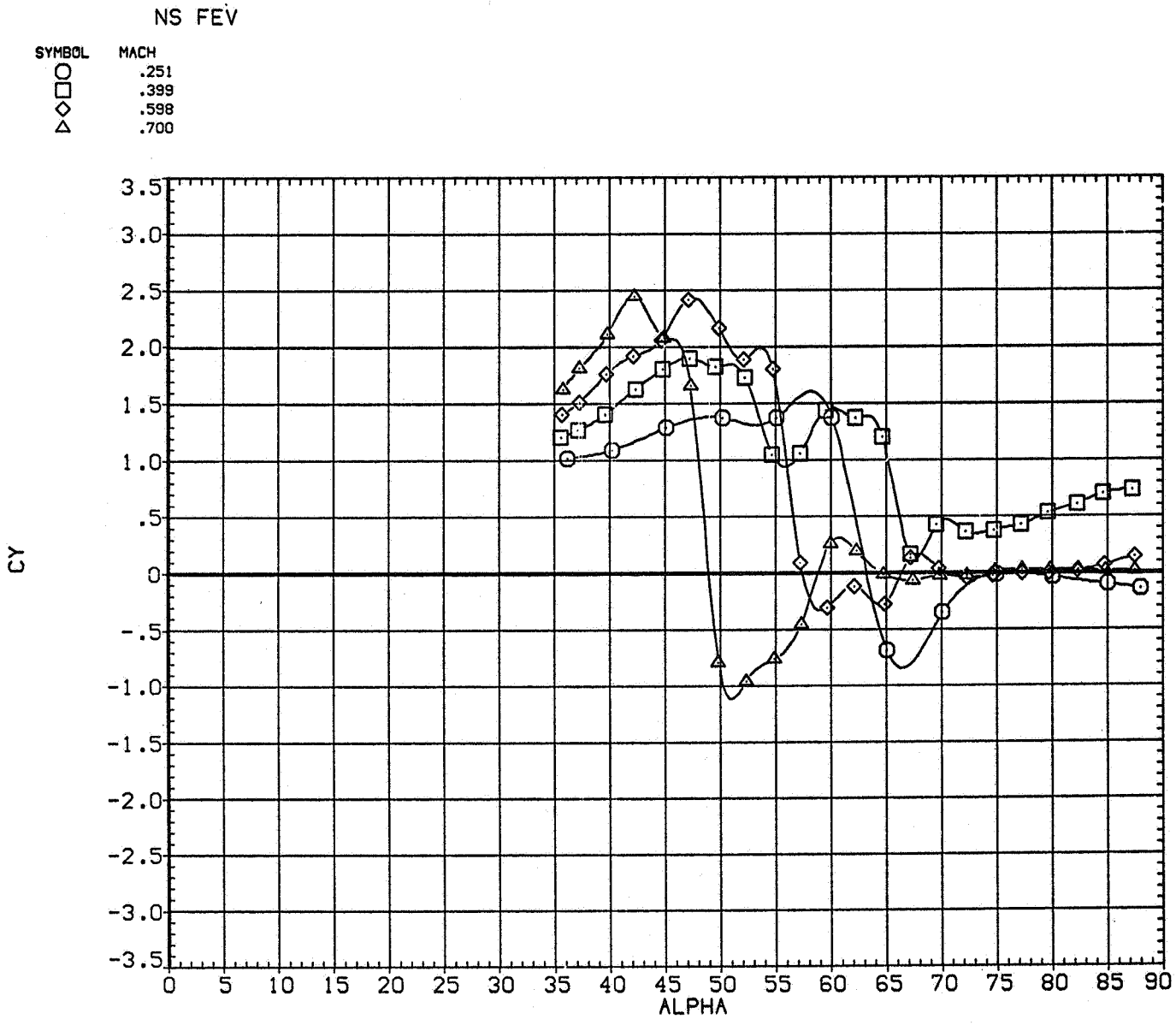

(a) C_Y vs α

Figure 27.– Effect of Mach number for the $\ell/b = 5$ elliptic tangent ogive, $R_d = 0.7 \times 10^6$.

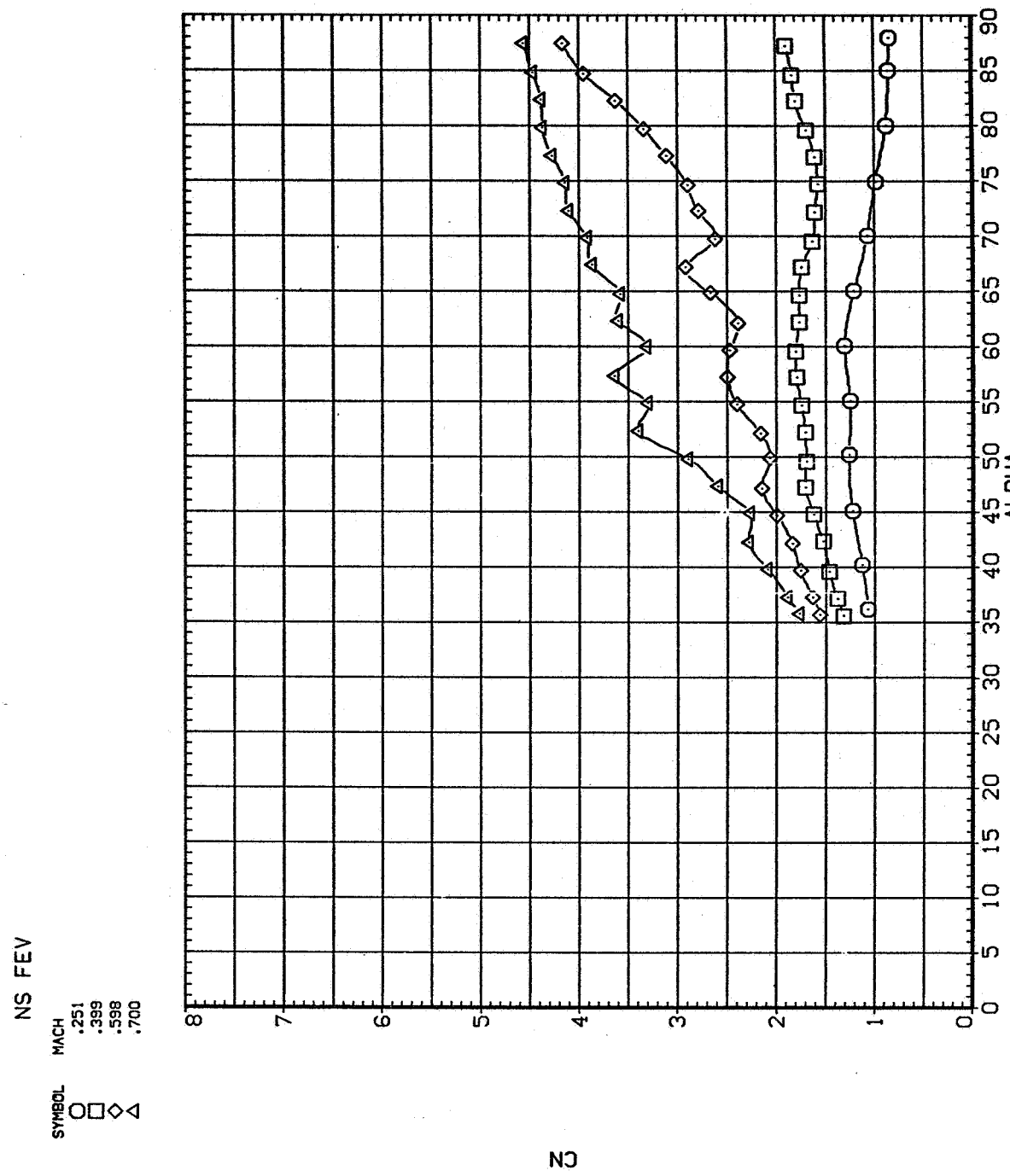

(b) C_N vs α

Figure 27.– Continued.

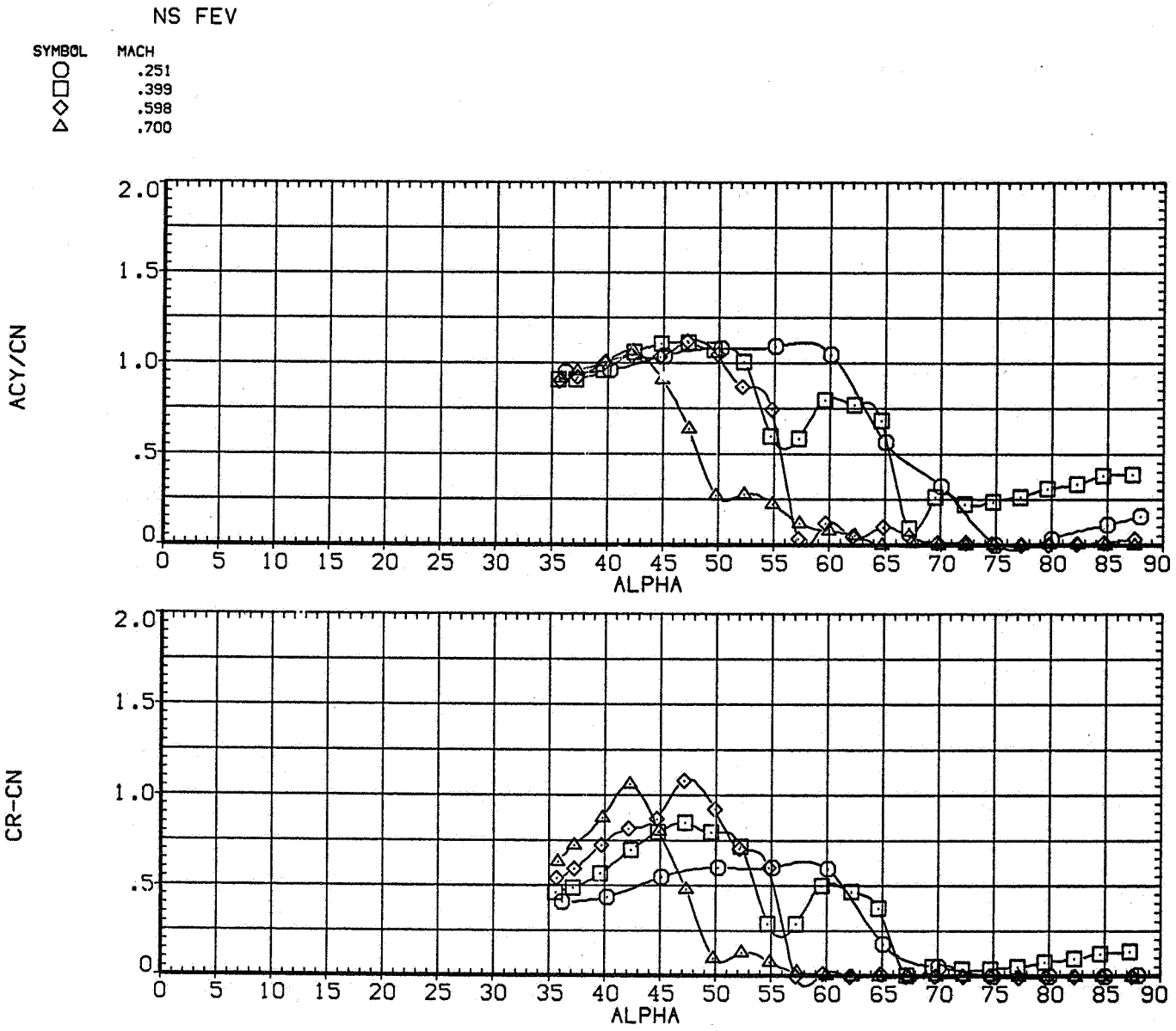

(c) $|C_Y|/|C_N|$ and $C_R - C_N$ vs α

Figure 27.– Continued.

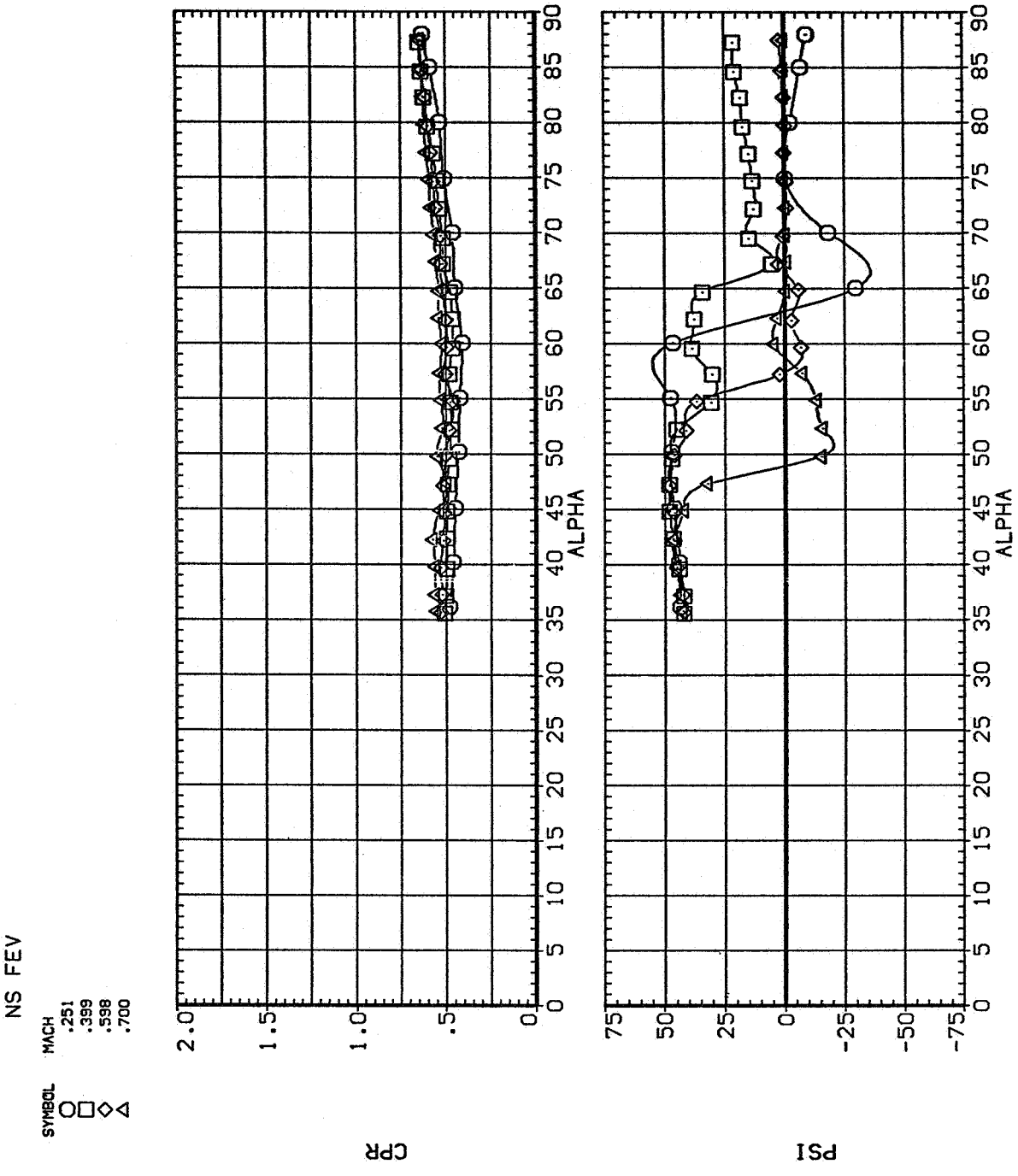

(d) CP_R and Ψ vs α

Figure 27.– Continued.

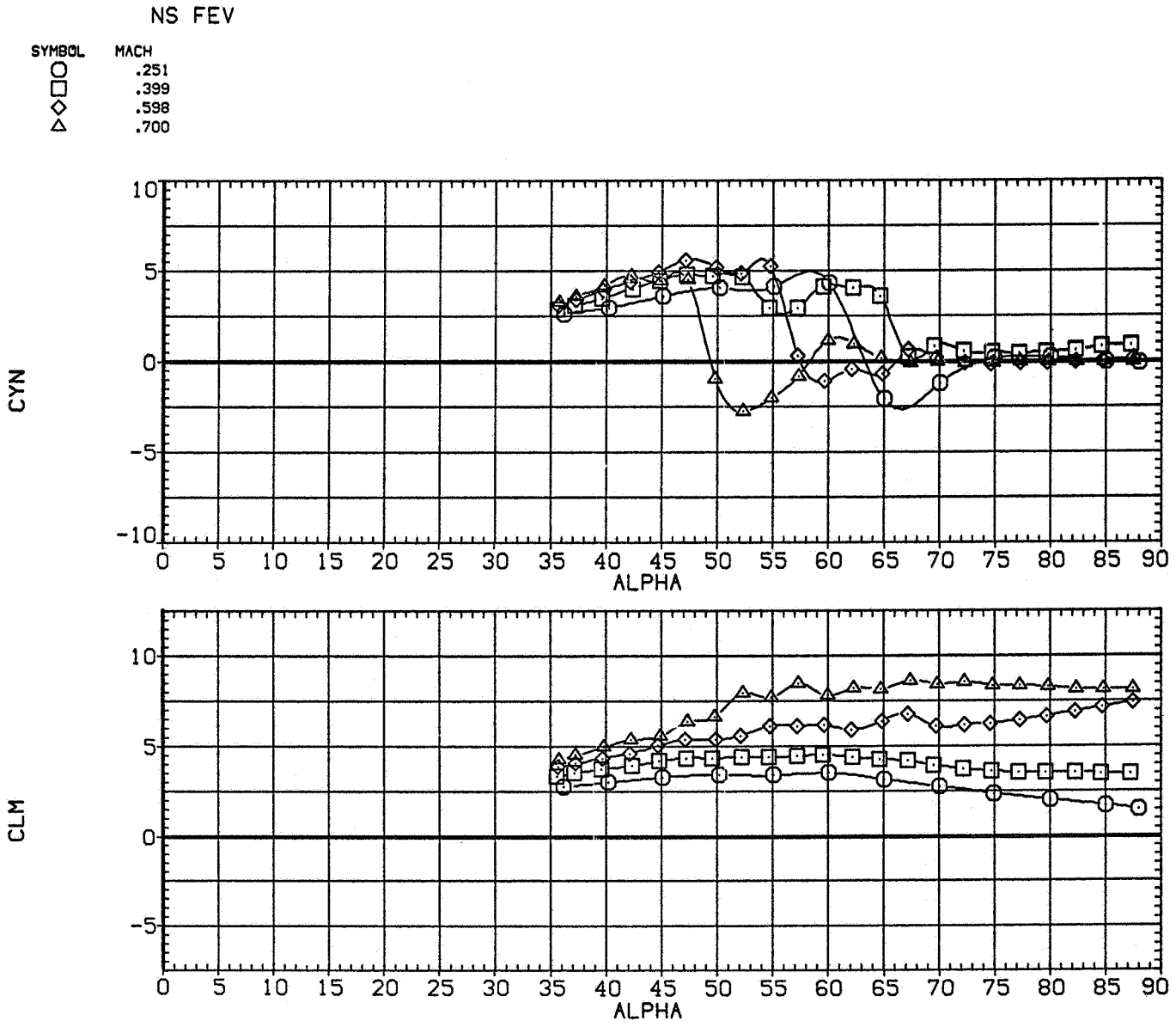

(e) C_n and C_m vs α

Figure 27.– Continued.

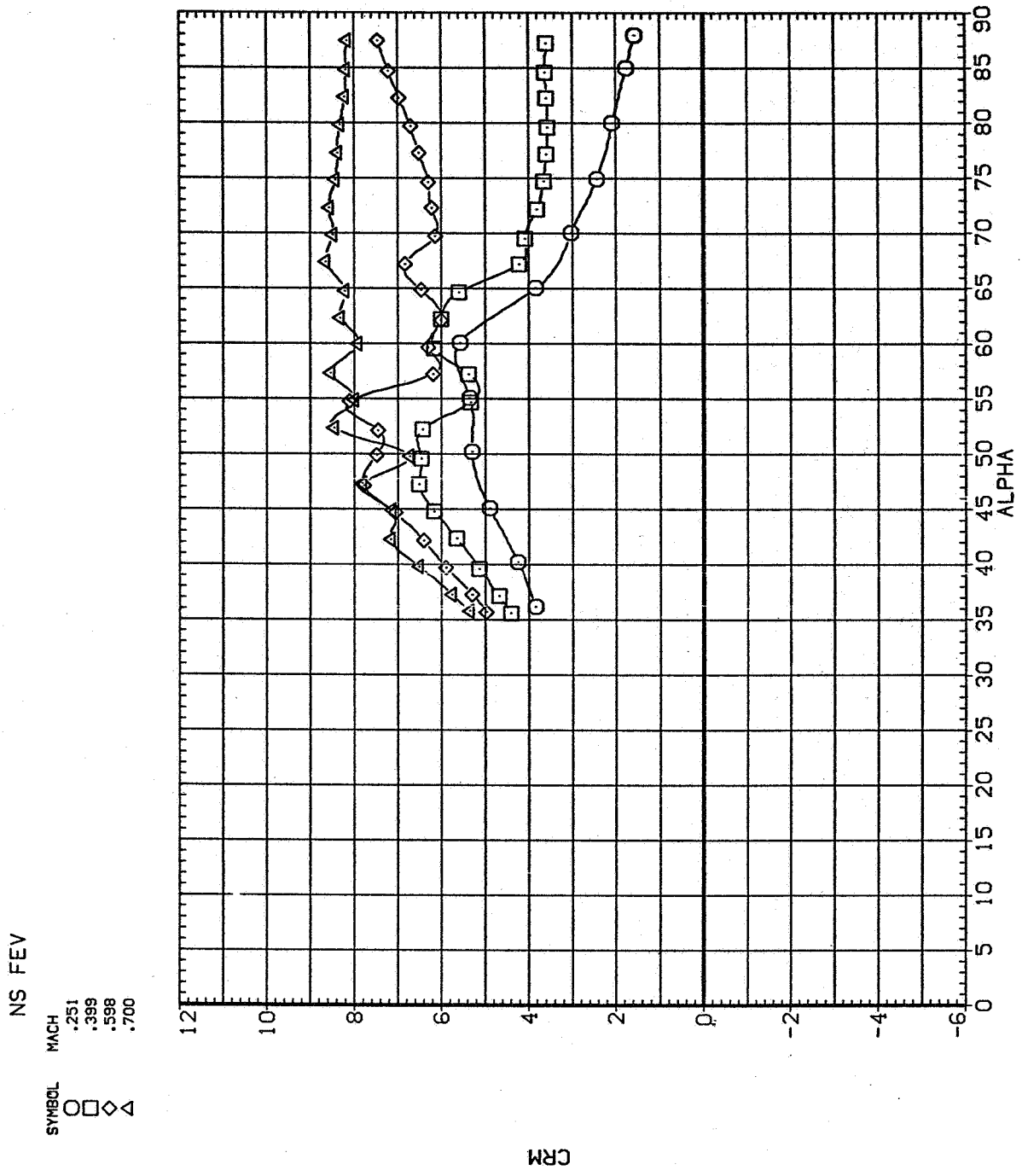

(f) $C_{m,R}$ vs α

Figure 27.– Concluded.